Development of A New Self-centring Low-damage Bracing System for Earthquake Resistant Structures Using Resilient Slip Friction Joints (RSFJs)

Seyed Mohamad Mahdi Yousef-beik

A thesis submitted in fulfilment of the requirement for the degree of Doctor of Philosophy in Structural/Earthquake Engineering, Auckland University of Technology 2021

Supervisors:

Dr Pouyan Zarnani

Prof Pierre Quenneville

September 2021

School of Future Environment, Department of Built Environment Engineering

Auckland University of Technology (AUT), Auckland, New Zealand

Abstract

According to the state-of-the seismic design practice, there are two accepted principles to be obeyed when designing a structure against different levels of earthquakes. The first and the explicit one is that the life-safety of the inhabitants must be assured by sacrificing the fuse elements with the intention of dissipating the input earthquake energy at the time of Ultimate Limit State (ULS) earthquake. The second and the implicit one is that the collapse of the building must be prevented at the time of any event beyond this level (up until the Maximum Considerable Earthquake). Adoption of these principles may bring a number of post-event consequences for the buildings such as structural and non-skeletal damage spreading throughout the structure (such as permanent deformation and storey-drift, strength and stiffness deterioration/loss and so on). Dealing with all of those repercussions on the scale of an urban area or a city with many buildings will put extra burden and demand on the local and national economy in the aftermath of a severe earthquake, which is the most critical time. This may prolong the time of recovery and bring consequent societal and economic short- and long-term impacts.

Low-damage structures, as implied by their name, is referred to those structures whose sacrificial elements can be easily and quickly replaced or repaired, thereby resolving a portion of the above-mentioned complications. However, the problem with the possible permanent drift and accumulation of structural damage may still exist in the low-damage structures. In general, if the permanent drift surpasses a certain limit (normally between 0.2% - 0.5%), complete demolition of the structures or retrofit/realignment program would be required. To tackle this issue, the self-centring low-damage structures seem to be remedial and desirable in terms of eliminating the residual drift in buildings. This would be very crucial for the structures with high importance level (IL) because they shall stay operational after a seismic event to keep providing service for the community.

In this manner, low-damage self-centring braces have the potential to become one of the popular lateral load resisting systems. They can provide not only a large elastic stiffness to control the inter-storey drift when shaking with low-amplitude seismic events (serviceability limit state) but also the passive damping, energy dissipation and self-centring characteristics to meet the resiliency requirements when shaking with large-amplitude seismic events (Design level earthquake or beyond).

This study develops a new self-centring low-damage brace using RSFJ dampers which will act both in tension and compression. As for any element subjected to compression, the main

challenge for design is the considerations for lateral instability and quantification of the ultimate capacity. Thus, the main purpose of this study is that how the brace can be designed and detailed for an intended level of compressive force in a way that the desired performance of such self-centring brace is kept uninterrupted until the intended force and deflection. More specifically, a series of small, large and component-level experimental studies have been conducted in this research program on RSFJ self-centring brace and has shown that the performance of the RSFJ self-centring brace can be interrupted by different failure modes when working in compression. These failure modes are categorized into two groups namely: local and global instabilities. The local (localized) instability is associated with the damper being not able to transfer the axial compression while the global instability is referred to the whole brace assembly being not able to resist the axial compression perfectly. It was found that the local instability is greatly influenced by the boundary conditions of the damper (end support) while the global one is more sensitive to the damper and brace sectional and member properties. The global failure mode, itself, can be of two types, elastic and inelastic, depending on the length, geometry and characteristics of the brace and other components.

In order to quantify and predict the mentioned failure modes, proper analytical frameworks, supported by numerical simulations as well as small- and large-scale experimental tests have been performed throughout the study. Classic structural stability analysis (second-order differential equations of equilibrium) and second-order simplified plastic analysis (which is referred to as simplified collapse analysis – SCMA – in the text) has been employed to quantify the elastic and inelastic global buckling capacity of the brace. After proposing the design guide, the seismic performance of a prototype building equipped with the proposed lateral load resisting system is studied. According to the findings, employing this type of system in a structure will contribute to restricting the displacement demands, reducing the base-shear and floor acceleration and bringing the structure back to its upright position.

Attestation of Authorship

I hereby declare that this submission is my own work and that, to the best of my knowledge and belief, it contains no material previously published or written by another person (except where explicitly defined in the acknowledgements), nor material which to a substantial extent has been submitted for the award of any other degree or diploma of a university or other institutions of higher learning.

Seyed Mohamad Mahdi Yousef-beik

Date: August 2021

Disclaimer

This thesis is prepared by Seyed Mohamad Mahdi Yousef-beik during a four-year PhD program in his best personal capacity and knowledge. Any opinions, findings, conclusions, and recommendations expressed in this material are those of the author and do not necessarily reflect the views of the sponsors. The responsibility of correct employment/accommodation of the opinions, recommendations and formulations of this thesis for the design of RSFJ brace system would fall only and solely on the structural engineer(s) and the involved parties, and the author of the thesis shall not be liable for any design outcome.

Seyed Mohamad Mahdi Yousef-beik

Date: August 2021

Dedication

This thesis is honourably and proudly dedicated to:

My beloved and dearest family

Without their unconditional love, endless sacrifice, infinite compassion and wholehearted support, I could not have come this far.

To Iran

My lovely beautiful home country forming my nature

To New Zealand

For providing me with the opportunity of being nurtured

Acknowledgments

Among many individuals I should be thankful for their contribution to this thesis, I can only name a few due to limited space.

Firstly, I would like to express my profound gratitude to my Supervisors, Dr Pouyan Zarnani and Prof. Pierre Quenneville, for providing me with this great opportunity to pursue my dreams. I am thankful for their continuous and extended support embracing almost all aspects of my life during the study. I am very grateful for insightful guidance, patience and setting high standards to do this study. I cannot find a better place than here to state that I will always reminisce our all-day-long group discussions in our weekly group meetings that I have learnt so much from and have left almost all of them being highly astounded, inspired and motivated.

Secondly, my special thanks and appreciation go to my beloved family for their continuous love, encouragement and support during the course of my PhD. My father, mother and my younger brother who have thought me the value of life, hard work, self-sufficiency, how to be dedicated to work and how to be supportive at any cost.

My sincere appreciation also goes to my workmates and colleagues at Auckland University of Technology, The University of Auckland and Techtonus Ltd, Sajad Veismoradi, Hamed Bagheri, Ashkan Hashemi, Kaveh Sahami and Farhad Mohamadi Darani, Seyed Mohsen Shabankareh, Setu Agarwal and Sriraj Varier with whom I shared memorable times, had pleasant discussions and collaborated on many occasions and topics. The quality and efficiency of the experimental works in this study are deeply beholden to the contributions of Allan Dixon, Andrew Virtue, Dave Craft and Stephen Hartley at the Auckland University of Technology Structural Lab and Mark Byrami at the University of Auckland Structural Test Hall.

I am also very grateful to two leading expert examiners of the thesis: Prof. Ario Ceccotti and Prof. Gregory MacRae, who have carried out the review of the thesis with patience, enthusiasm, and conscientiousness. Their valuable comments and feedbacks have definitely elevated the thesis and are much appreciated.

Finally, the financial supports from the New Zealand Earthquake Commission (EQC) and the Ministry of Business, Innovation and Employment of New Zealand (MBIE) are much appreciated.

Relevant Research Outputs

During my memorable time as a PhD candidate, I had the honour and privilege to work within an active group of talented and experienced researchers. The fruit of these collaborations are the following journal and conference papers that I authored/co-authored:

Journal papers:

1. **Yousef-beik, S. M. M.,** Veismoradi, S., Zarnani, P., Hashemi, A., & Quenneville, P. (2020). Experimental Study On Cyclic Performance Of A Damage-Free Brace With Self-centring Connection. Journal of Structural Engineering, 147(1), 04020299. doi: 10.1061/(ASCE)ST.1943-541X.0002869

2. **Yousef-beik, S. M. M.,** Veismoradi, S., Zarnani, P., & Quenneville, P. (2020). A new self-centring brace with zero secondary stiffness using elastic buckling. Journal of Constructional Steel Research, 169, 106035.

3. **Yousef-beik, S. M. M.,** Bagheri, H., Veismoradi, S., Zarnani, P., Hashemi, A., & Quenneville, P. (2020). Seismic performance improvement of conventional timber brace using re-centring friction connection. Structures, 26, 958-968. doi: 10.1016/j.istruc.2020.05.029

4. **Yousef-beik, S. M. M.**, Veismoradi, S., Zarnani, P., & Quenneville, P. (2021). Effect of second-order actions on the performance of resilient slip friction joints: Analytical and experimental investigation. Structures, 33, 957-970. doi: https://doi.org/10.1016/j.istruc.2021.04.101

5. **Yousef-beik, S. M. M.**, Veismoradi, S., Zarnani, P., & Quenneville, P. Design and Testing of a Self-centring Brace for Compression Ultimate Limit State: Inelastic Buckling (under review of Journal of Constructional Steel Research)

6. Hashemi, A., **Yousef-Beik, S. M. M.,** Darani, F. M., Clifton, G. C., Zarnani, P., & Quenneville, P. (2019). Seismic performance of a damage avoidance self-centring brace with collapse prevention mechanism. Journal of Constructional Steel Research, 155, 273-285

7. Veismoradi, S., **Yousef-beik, S. M. M.,** Zarnani, P., & Quenneville, P. (2021). Development and parametric study of a new self-centring rotational friction damper.

Engineering structures, 235, 112097. doi: https://doi.org/10.1016/j.engstruct.2021.112097

8. Veismoradi, S., **Yousef-beik, S. M. M.,** Zarnani, P., & Quenneville, P. Seismic Strengthening of Deficient RC Frames Using Self-Centering Friction Haunches (under review of Engineering Structures journal)

9. Hashemi, A., **Yousef-Beik, S. M. M**., Zarnani, P., & Quenneville, P. (2021). Seismic strengthening of conventional timber structures using resilient braces. Structures, 32, 1619-1633. doi: 10.1016/j.istruc.2021.03.100

10. Hashemi, A., Bagheri, H., **Yousef-Beik, S. M. M.,** Darani, F. M., Valadbeigi, A., Zarnani, P., & Quenneville, P. (2020). Enhanced Seismic Performance of Timber Structures Using Resilient Connections: Full-Scale Testing and Design Procedure. Journal of Structural Engineering, 146(9), 04020180.

11. Bagheri, H., Hashemi, A., **Yousef-Beik, S. M. M.,** Zarnani, P., & Quenneville, P. (2020). A new self-centring tension-only brace using resilient slip friction joint: experimental tests and numerical analysis. Journal of Structural Engineering.

12. Hashemi, A., Bagheri, H., Darani, F. M., **Yousef-Beik, S. M. M.,** Zarnani, P., & Quenneville, P. (2018). An example procedure for preliminary sizing of resilient slip friction joints (RSFJS) in seismic resistant structures. SESOC Journal, 31(2), 44.

13. Darani, F. M., Zarnani, P., Veismoradi, S., **Yousef-beik, S. M. M**., Hashemi, A., & Quenneville, P. (2021). Resilient slip friction joint performance: Component analysis, spring model and anti-locking mechanism. Structures, 33, 3897-3911. doi:https://doi.org/10.1016/j.istruc.2021.06.075

Conference Papers:

1. **Yousef-Beik, S. M. M.**, Zarnani, P., Darani, F. M., Hashemi, A., & Quenneville, P. (2018). New seismic damage avoidant timber brace using innovative resilient slip friction joints for multi-story applications. Paper presented at the WCTE 2018 - World Conference on Timber Engineering, Seoul, South Korea.

2. **Yousef-beik, S. M. M.**, Bagheri, H., Zarnani, P., Hashemi, A., & Quenneville, P. (2019). Damage-avoidance timber brace using a self-centring friction damper Paper presented at the Pacific Conference on Earthquake Engineering (PCEE), Auckland, New Zealand.

3. **Yousef-beik, S. M. M.**, Zarnani, P., Hashemi, A., & Quenneville, P. (2019). Lateral Instability of Self-centring Braces: Buckling in loading and Unloading. Paper presented at the Pacific Conference on Earthquake Engineering (PCEE), Auckland, New Zealand.

4. **Yousef-Beik, S. M. M.,** Veismoradi, S., Zarnani, P., Quenneville, P., & Hashemi, A. (2020). Self-centring bracing system: avoidance of elastic buckling for braces with one intermediate damper. Paper presented at the annual NZSEE conference, Wellington, New Zealand.

5. **Yousef-Beik, S. M. M.,** Veismoradi, S., Zarnani, P., & Quenneville, P. (2020). Full Scale Quasi-Static Testing of a New Self-centring Damage-Avoidant Timber Brace. Paper presented at the 17th World Conference on Earthquake Engineering (WCEE), Sendai, Japan.

6. **Yousef-Beik, S. M. M.,** Varier, S., Hashemi, A., Zarnani, P., & Quenneville, P. (2021). Proposed Procedure for Design of RSFJ Self-centring Brace for Ultimate Capacity, Paper presented at the annual NZSEE conference, Christchurch, New Zealand.

7. Veismoradi, S., **Yousef-Beik, S. M. M**., Zarnani, P., & Quenneville, P. (2021). Seismic Strengthening of Non-ductile RC Frames Using Resilient Slip Friction Haunches. Paper presented at the NZSEE 2021, Christchurch, New Zealand.

8. Hashemi, A., **Yousef-Beik, S. M. M.,** Bagheri, H., Mohammadi Darani, F., Zarnani, P., & Quenneville, P. (2019). Resilient Slip Friction Joint (RSFJ): A damage avoidance technology for seismic-proofing new and existing buildings. Paper presented at the 12th Canadian Conference on Earthquake Engineering (CCEE).

9. Bagheri, H., Hashemi, A., **Yousef-Beik, S. M. M.,** Zarnani, P., & Quenneville, P. (2019). A self-centring tension-only bracing system for seismic resistant structures using the Resilient Slip Friction Joint (RSFJ). Paper presented at the 12th Canadian Conference on Earthquake Engineering (CCEE).

10. Veismoradi, S., **Yousef-Beik, S. M. M.**, Zarnani, P., & Quenneville, P. (2020). Seismic retrofitting of RC-frames using Resilient Slip Friction Joint toggle-bracing system. NZSEE, Auckland, 2020.

11. Zarnani, P., Valadbeigi, A., Hashemi, A., Darani, F. M., **Yousef-Beik, S. M. M.,** Bagheri, H., & Quenneville, P. (2018). Rotational performance of resilient slip friction joint (RSFJ) as a new damage free seismic connection. Paper presented at the 2018 World Conference on Timber Engineering (WCTE2018).

12. Hashemi, A., Zaboli, B., **Yousef-Beik, S. M. M.,** Zarnani, P., Clifton, G. C., & Quenneville, P. (2018). Seismic performance of resilient slip friction joint (RSFJ) brace with collapse prevention mechanism. Paper presented at the annual NZSEE conference, Auckland, New Zealand.

13. Hashemi, A., Bagheri, H., Quenneville, P., Van Houtte, A., Kemp, M., Newcombe, **Yousef-Beik, S. M. M.,** and Zarnani, P. "Developments and Practical Case Studies for Seismic Resistant Structures Using Resilient Slip Friction Joints (RSFJs)." Paper presented at the annual NZSEE conference, Auckland, 2020.

14. Hashemi, A., Bagheri, H., Quenneville, P., **Yousef-Beik, S. M. M**., Darani, F. M., & Zarnani, P. (2019). Enhanced seismic performance of buildings using tension-only Resilient Slip Friction Joint (RSFJ) braces. Paper presented at the Pacific Conference on Earthquake Engineering (PCEE), Auckland, New Zealand.

15. Hashemi, A., Bagheri, H., Quenneville, P., **Yousef-Beik, S. M. M**., Darani, F. M., & Zarnani, P. (2019b). A robust procedure for analysis and design of seismic resistant structures with flag-shaped hysteretic damping systems. Paper presented at the Pacific Conference on Earthquake Engineering (PCEE), Auckland, New Zealand.

Table of Content

List of Figures

List of Tables

$P_{cr,loading}$	Critical load for after-slip loading
$P_{cr,unloading}$	Critical load for after-slip unloading
$P_{initial}$	Critical load for before-slip;
K_{ABT}	Rotational stiffness of ABT
$(M_{ep})^*$	Bending demand on the endplate
$(M_p)'$	Reduced plastic capacity of the section due to axial load
Δ_{lat}	Lateral displacement of the cap plate
Δ_{max}	Target displacement of RSFJ
$\Delta_{s,max}$	the listed deflection of a disc spring;
Δ_{slip}	Slip displacement of RSFJ
Δ_{ult}	Ultimate displacement of RSFJ
EI_{ABT}	Flexural stiffness of the Anti-buckling mechanism;
EI_{body}	Flexural stiffness of the brace;
f_b	Characteristic bending stress of timber
f_c	Characteristic compressive stress of timber
$F_e\ (P_{cr})$	Euler Load
$F_{in,loading}$	SOE-affected load in damper after activation within the loading phase in in-plane
$F_{in,unloading}$	SOE-affected load in damper after reversed-activation within the loading phase in in-plane
$F_{max,loading}$	Maximum force of RSFJ in loading
$F_{max,unloading}$	Maximum Force of RSFJ in loading phase or Restoring Force of RSFJ (reversed-slip force)
$F_{out,loading}$	SOE-affected load in damper after activation within the loading phase in in-plane

$F_{out,unloading}$	SOE-affected load in damper after reversed-activation within the loading phase in in-plane
F_{pr}	Prestressing force in the stack of disc springs
F_{res}	Residual Force of RSFJ
$F_{restoring}$	Restoring force of the damper;
F_{slip}	Slip force of RSFJ
$F_{u,BRB}$	Ultimate stress of BRB core
$F_{u,s}$	Flat load of a disc springs
F_{ult}	Ultimate Force of RSFJ
$F_{unloading}$	Force in the damper after reversed-activation within the unloading phase
F_y	Yielding stress of Steel
$K_{ax,loading}$	Axial stiffness of the RSFJ for after-slip loading (Post-slip axial stiffness)
$K_{ax,unloading}$	Axial stiffness of the RSFJ for after-slip unloading (Post reversed-slip axial stiffness)
K_d	Initial stiffness of a single disc springs;
K_e	Initial stiffness of a structure
$K_{in,loading}$	Secondary rotational stiffness of loading in in-plane
$K_{in,sec,loading}$	Secondary rotational stiffness of loading (Post-slip rotational stiffness)
K_{pe}	Post-elastic stiffness
K_{st}	Initial stiffness of the stack of disc springs
K_{tan}	Tangent rotational stiffness (can be either of the following three stiffness);
L_1	Distance between pin and middle of the RSFJ
L_{ABT}	Length of the Anti-buckling mechanism;
L_c	Length of the cap plate
L_{con}	Distance between pin and beginning of the damper
L_e	Overlap length between the middle and cap plates
L_{RSFJ}	Total length of the damper

$M_{in,res}$	Residual moment of RSFJ
$M_{in,restoring}$	Restoring moment of RSFJ
$M_{in,slip}$	Slip moment of RSFJ
$M_{in,ult}$	Ultimate moment of RSFJ
M_p	Intact Plastic flexural capacity of the system ($\mathbf{ZF_y}$)
n_b	Number of bolts (or rods) per side of RSFJ
n_d	Number disc springs in a stack
P_{cr}	Elastic (Euler) load of the member
P_n	Squash load ($\mathbf{A_gF_y}$)
P_{ult}	Ultimate strength of the RSFJ brace in compression
R_y	Material overstrength factor
$t_{max,m}$	Thickness of the middle plate at the thickest part
V_u	Additional shear in the brace due to second-order effect and formation of plastic hinge
$\alpha_1 K$	Post-elastic stiffness (secondary) associated with loading for a self-centring system
$\alpha_2 K$	Post-elastic stiffness (secondary) associated with unloading for a self-centring system
β_b	Relative rigidity of ABT
δ_0	Initial imperfection
δ_1	Relative location of the non-continuity region
δ_2	Relative length of ABT
$\delta_{clearance}$	Clearance in the gusset and ABT
δ_{int}	Intersection point between stiffness and strength deterioration curve
Δ_{lat}	Lateral displacement of the damper
θ_0	Initial out-of-inclination at the onset of rotation
θ_g	Angle of grooves
θ_{in}	In-plane rotation

θ_p	Rotation in the plastic hinge
θ_{pr}	Effect of prestressing on SOE-affected path
θ_{slip}	Slip rotation of RSFJ
θ_{ult}	Ultimate rotation of RSFJ
Δ	Axial displacement of the damper
ABT	Anti-buckling tube
b	Width of joint or cap plates
BRB	Buckling-restrained Brace
CTB	Conventional Timber Brace
EI_{ABT}	Flexural Rigidity of the ABT
EBF	Eccentrically Braced Frame
EI	Flexural Rigidity of the brace body
K	Initial stiffness of a structure
L	Total length of the brace
LLRS	Lateral Load Resisting System
m	Modification factor for rotational stiffness of the non-continuity region
MRF	Moment Resisting Frame
RSFJ	Resilient Slip Friction Joint
SC	Self-centering
SCMA	Simplified Collapse Mechanism Analysis
SC-ZSB	Self-centring Zero Stiffness Brace
SDF (SDOF)	Single degree of freedom
SNM	Stiffness Neutralizer Mechanism
SOE	Second-order Effect
S	Elastic Section Modulus
T	Work done by the external load
U	Strain Energy

U	Strain Energy in the plastic hinge
W	Work done by the external load
α	Minimum real positive root of characteristic equation
β	Relative rotational stiffness of the non-continuity region
γ	Prestressing ratio of the stack of disc springs
δ	Lateral displacement
λ	Slenderness of the brace
μ	Coefficient of friction
Z	Plastic Section Modulus

1 Introduction

1.1 Motivation

In pursuit of sustainable development, well-being and inclusive growth of societies, disaster-resiliency is aimed to be achieved for cities of tomorrow. Resilient cities are, indeed, cities that possess the capability to survive, recover and stabilize in the face of sudden emergencies at the earliest possible time. In this manner, Bruneau et al [1] discussed the parameters that may affect the community resilience at the time of a major emergency event. They defined resiliency in a simple manner as the ability of the system to recover quickly when confronted with an abrupt change in the system. Furthermore, they discussed that a system should possess three characteristics to be viewed as a resilient system namely: (a) low probability of failure, (b) not bringing serious consequences from failure and (c) low time for recovery. Such abrupt emergencies can include man-made hazards (terrorist attacks and so on) or natural hazards such as earthquakes, Tsunami, Pandemic and Flood bringing losses and community disruption to the human communities. As a result, the authorities have been in pursuit of taking actions to foster disaster-resiliency against those hazards. An illustration for natural disaster mitigation and resiliency improvement program can be found in the pre-disaster mitigation programs in the United States in the early 2000s [2, 3] where the core mission was to reduce the failure probability, the consequences from the failure and time to recovery.

In this study, when it is referred to resilient, it is merely referred to the "resiliency against earthquake hazard". The resiliency in the form of the general concept and against other hazards is not pursued here. Thus, the main outcome of the study would be to develop a system by which the resiliency of the structures is ameliorated against earthquakes.

1.1.1. *State of the practice in seismic design*

The seismic design approach of most building codes is based on the well-known capacity-design principle in which special sacrificial elements (seismic fuses) are designed and proportioned in a way to be sacrificed at the time of ground shaking in the interest of protecting the whole structure from collapse while safeguarding the inhabitants. The basis of this method of seismic design was

first introduced in 1961 (not with this specific term) by Late Mete Sozen in one of the chapters of the landmark textbook written by Late John A. Blume, Nathan M. Newmark and Leo H. Corning, legends of earthquake engineering, entitled *Design of Multi-storey Reinforced Concrete Buildings for Earthquake Motions* [4]. Later on, John Hollings [5], a prominent structural engineer in New Zealand, extended Sozen's concept to be used for the ductile design of concrete structures. Finally, thanks to Late Tom Paulay, one of the greatest influential figures in earthquake engineering, it was publicized, considerably elevated, developed and found its way into the building codes [5].

This concept possesses two signature rules [4-6]:

First: "The design shear in a concrete beam, column, or bridge pier is calculated from the ultimate moments of the end sections in counter-flexure."

Second: "The sum of ultimate beam moments at the opposite faces of a beam-column joint in a building frame of any material is used as the lower limit to the sum of ultimate column moments at the joint faces – also known as weak beam and strong column principle"

According to this simple but effective principle, all of the global seismic displacement demands are channelled to occur in those members that are designed to be sacrificed during an earthquake while not playing prominent roles in structural integrity and stability. The reason for this can be attributed to the fact that the elastic design of the building may be too expensive while unnecessary given that only a 50-year lifespan is assumed for a building, and the probability of such a major seismic event is low. This is also reported by Late John A. Blume and Newmark in the following context [4]:

"To design for such earthquake by requiring that the structure remains in the elastic range would be grossly uneconomical and would represent the payment of too great a cost to providing for the probability of such an occurrence.[4]"

To list a few examples out of many seismic resisting systems exhibiting such performance, it can be pointed to Moment-Resisting Frames (MRFs) relying on the formation of plastic hinges in beams, Concentrically Braced Frames (CBFs) relying on the post-buckling inelastic behaviour of the brace, Eccentrically Braced Frames (EBFs) relying on the inelastic behaviour of the link element to dissipate the input earthquake energy.

1.1.2. *Need for systems with a higher level of seismic performance*

Such dramatic improvements on the building codes over the past 50 years have successfully increased the safety of the structures and the resiliency of the societies only against the fatality of

the earthquakes. However, recent studies and earthquake events have highlighted the fact that life safety and collapse prevention against an earthquake may not be an adequate measure for resiliency. The imposed direct and indirect cost of rebuilding the damaged city after an earthquake may be a dramatic pressure on the national government requiring a long time for recovery [7]. This is, indeed, opposing the main aim of resiliency, which is quick recovery. The sequence of Canterbury earthquakes in the years 2010-2011 can be taken as an example. Even though most of the buildings and structures in this city were designed according to the modern building codes, and they performed as expected and had successfully safeguarded the inhabitants' lives, a substantial percentage of the Central Business District (CBD) of Christchurch have been or will be demolished [8]. The process of reconstruction of the CBD is still far from completion [8] and is estimated up to 1.5 billion New Zealand Dollars for demolition or reconstruction [7]. It is worth noting that the total damage of the earthquake may reach up to 30 billion New Zealand Dollars if the business interruption, inflation and other parameters are taken into consideration.

Therefore, to increase the resiliency of the societies against those post-event losses, a new framework and method of seismic design seem to be required. Such a framework should include measures to decrease the damage to structures after the earthquakes and also precipitate and facilitate the process of recovering.

1.1.3. *Low-damage (LD) and damage-avoidance (DA) approach for seismic design*

In an attempt to decrease the recovery time, a new method of design has been developed. The low-damage (LD) design philosophy generally refers to a method of seismic design employed by the engineers with the main intention of taking actions to mitigate structural and non-skeletal damage against major seismic events. Considering the structural viewpoint, in this method, the main efforts are placed on minimizing or limiting the structural damage to the members that can be *fully* and *quickly* replaced after the earthquake [9] with minimal functionality interruption. Although engineers may argue that many conventional lateral load resisting systems also fall into this category such as elastic systems, Eccentrically-Braced Frame (EBF) with replaceable links [10, 11], Buckling Restrained Brace (BRB) [12], Base Isolation technologies, Dampers, most of the international efforts, today, have been focused on developing new lateral load resisting systems. Among many low-damage technologies, it can be referred to a number of nationally developed systems in New Zealand namely: sliding-hinge joints [13] and grip 'n' grab [14], rocking timber shear walls [15] and pinching-free-connection (PFC) [16]. Readers are encouraged to see [17-19] for a comprehensive review.

There is another method of seismic design entitled damage-avoidance design, which tends to be very similar to the low-damage concept, but with the difference that in the damage-avoidance approach, more focus and emphasis has been put upon the self-centring, reusable damping mechanism and no post-event maintenance requirement for the intended level of seismic intensity [20, 21]. In this manner, many systems can be classified as both of them. For example, many researchers cited the rocking or self-centring structures as low-damage [22] while another group has reported them as damage-avoidance structures [23-26]. More discussion will be provided on the marginal difference between these design approaches in the following.

1.1.4. *Performance objectives*

John Hare et al [27] provided some practical perspectives for the low-damage systems and discussed some of the main and critical objectives that should be met for a low-damage designed system. They discussed that six parameters should be carefully evaluated and considered when a low-damage system is being designed. These parameters are: (a) Damage mitigation effectiveness, (b) Repairability and self-centring ability, (c) non-skeletal damage, (d) Durability and (e) Affordability.

1.1.4.1. Damage-mitigation effectiveness

Regarding the "Damage-mitigation effectiveness", it is discussed that although the protection of the lateral load resisting system from unrepairable damage is assured with the low-damage systems, the possible damage to the gravity systems and load-paths should be taken into consideration. As an example, it can be pointed to rocking structures where the connection between the rocking elements and the floor systems is still a big challenge [17, 28, 29] to be undamaged. Another example is in the BRB braced frame structures in which the end gusset plates may inevitably yield in the out-of-plane direction [30-32] due to out-of-plane drift. The arrival of such damage can be allowed in the low-damage systems as long as they are limited and can be repaired immediately after the major seismic event. However, when it comes to damage-avoidance design, it may need more detail and careful design considerations so that the probability of damage occurrence is minimized (if not possible to rule out). Furthermore, this demonstrates that a low-damage or damage-avoidance designed building should carefully consider all of the possible scenarios in terms of the appearance of the damage.

1.1.4.2. Reparability, self-centring and post-event maintenance:

The next objective is repairability. Low-damage systems should be easily repaired after the major seismic event, which itself implies that there should exist access to where the sacrificial replaceable seismic fuses are placed. Apart from the access to replace the fuses, the misalignment of the structure is a critical parameter in repairability. Observations from the last earthquakes provided solid evidence to support the possibility of significant residual displacement in case of major seismic strikes [33] and showed that this parameter can perform a key role in the post-event functionality and repairability of the structures. McCormick et al. [34] suggested a threshold of 0.5% residual inter-story drift for the repairability limit of the structures, and most of the building codes are considering or have adopted this value as the maximum limit for the residual drift for the repairability of structures. If the residual drift of a building exceeds this amount, complete demolition and reconstruction is recommended from the economical perspective.

The threshold for citing a building as self-centred tends to be tighter. In this manner, there is no unanimity among scholars for the permissible residual drift for a building to be regarded as *self-centred*. As such, the permissible value is being considered between 0.05% and 0.2%. This will be discussed further in detail in section 1.3.1.2. Overall, having a self-centring system bringing a minimal residual displacement in the post-event time can be a huge benefit for buildings with high importance level or those that must stay continuously functional (eg., hospitals, airports and government buildings. Therefore, a minimal residual drift is one of the desired performance objectives for both the low-damage and damage-avoidance designs.

1.1.4.3. Non-skeletal damage

Another very important parameter that should be taken into design considerations is the non-skeletal element performance. Generally, these elements can be divided into two main groups namely: (a) displacement-sensitive [35] and (b) acceleration-sensitive [36]. The first group includes, for example, the partition walls and cladding elements that are sensitive to inter-story drifts while the latter group includes internal-content of the structures, for example, desk, TV, fridge that are sensitive to floor acceleration. Non-skeletal components usually account for between 70 -85 % of the initial construction cost [37, 38] and are at stake of being severely damaged in much less ground motion intensity as compared to main structural members. Given the recent experiences from Christchurch Earthquakes 2010-2011, the performance of non-skeletal elements falls far behind the structural members [39, 40]. Therefore, having an intact lateral load resisting system

but with destroyed building contents and non-skeletal elements would not seem rational, and it cannot be regarded as a low-damage or damage-avoidance design.

It is worth noting that at the time of writing this thesis, there is an ongoing international program among the University of Auckland, Auckland University of Technology, University of Canterbury and Tongji University entitled Robust Building Systems (ROBUST) [41] partly aiming at enhancing the performance of non-skeletal elements. In this program, a number of low-damage and damage-avoidance systems (including the system under study in this thesis) are planned to be tested and validated on a near full-scale three-storey steel structure using a shake table.

1.1.4.4. Durability and maintenance:

Durability and maintenance are also a matter of debate in the low-damage and damage-avoidance systems. Generally, the lifespan of 50 years is presumed for a building by the international building codes meaning that the performance of the building should not deteriorate or change considerably during this time. Otherwise, a proper design methodology or preventative maintenance protocol to account for the possible repercussions on the performance should be foreseen. The well-known examples of the performance deterioration are corrosion of the steel rebars in concrete structures [42-44], the prestressing loss in the pre-stressed members due to relaxation or creep [45], leakage of the liquid in viscous dampers [46] and etc.

1.1.4.5. Affordability:

The final aspect is affordability. Generally, a marginal increase in the initial cost of the structural elements and construction should be anticipated when designing a low-damage or damage-avoidance system [47], which is due to the deliberate intention of performance improvement. However, this will be paid off within the life span of structures according to a recent study [47]. In that research, a cost-benefit analysis study was performed on a controlled rocking steel braced frame, and it was observed that the self-centring rocking structure was more protected against drift-related damage, which mostly accounts for the earthquake losses.

Another cost that should be foreseen in the cost-benefit analysis of a low-damage structure is the cost for maintenance and monitoring if exist any. As discussed in the previous section, if the low-damage system requires periodic maintenance or monitoring, the cost should be considered in the initial estimation.

1.1.4.6. Conclusion:

As it was discussed in the previous sections, there are several parameters that should be carefully taken into consideration when a building is designed based on the low-damage or damage-avoidance approach. Overall, it can be seen that the expectations from both low-damage and damage-avoidance structures are mostly identical, yet in damage-avoidance design, more emphasis is placed on the reusable damping resource and fully re-centring of the structure. In other words, it can be stated that the damage-avoidance approach tends to be a subset for low-damage while self-centring and reusable damping resource is more highlighted

This section discussed the state-of-the-art seismic design concepts in which the low-damage and damage-avoidance methods of the seismic design were covered. In this respect, the different performance expectations from each of the methods were also discussed in detail, and it was concluded that the damage-avoidance design is almost identical to the low-damage design concept while a stricter emphasis is placed on the self-centring and reusability of the damping mechanism. It is also worth noting that there is not still a clear borderline between the low-damage and damage-avoidance approaches, and a system may be classified as both. An example is the rocking self-centring systems. Although they tend to meet the self-centring objective of the damage-avoidance design, a group of these systems use replaceable seismic fuses with the need for post-event replacement, which such characteristic belongs to low-damage design. On the contrary, the other group uses reusable fuses (eg., friction-based or viscous) which can meet the damage-avoidance criteria. Therefore, the system under study is referred to as a self-centring low-damage brace.

1.2 Description of the low-damage self-centring brace using Resilient Slip Friction Joint (RSFJ)

This research develops a new self-centring brace using the Resilient Slip Friction Joints as a low-damage lateral load resisting system (with a proper design and detailing, also to be damage-avoidance). This brace can be employed in the steel, timber and concrete frames being material-independent. It can offer a high elastic stiffness to limit the inter-story drift while providing energy dissipation and re-entering capabilities. Figure 1.1 shows the possible configurations that the RSFJ damper can be assembled within a brace. The RSFJ brace can have one (Figure 1.1.a) or two locations (Figure 1.1.b) for installation of dampers (in series) to meet either a relatively low or high displacement demand, respectively while it can have a number of RSFJs in parallel at each location to meet the intended force demand (Two in case of Figure 1.1). Furthermore, it can be made up of timber or steel brace. In either of the cases, it has three main components as follows:

1. **RSFJ damper(s):** it is responsible for providing the damping and re-centring capability.
2. **Brace body (Steel or Timber):** it is responsible for providing the high elastic stiffness to limit the inter-storey drift, transferring the axial force and has to remain elastic until the desired level of ground shaking.
3. **Anti-Buckling Tube (ABT):** it is composed of two telescopic steel sections and is responsible for increasing both the elastic and inelastic compression strength of the brace. In another word, these tubes will act in parallel to resist the second-order effects when the brace is working in compression.

1.3 Prior related work and research on Self-centring Braces

1.3.1. *Self-centring systems*

As it was mentioned before, a large portion of international effort has been put into developing new low-damage self-centring lateral load resisting systems although many of the current systems such as the base-isolation or the supplemental dampers also can be classified as low-damage. In this manner, this section focuses on the self-centring structures with more emphasis on the brace-type lateral load resisting systems. Before discussing the self-centring braced frames, a review has been performed on the self-centring systems in general and their performance characteristics.

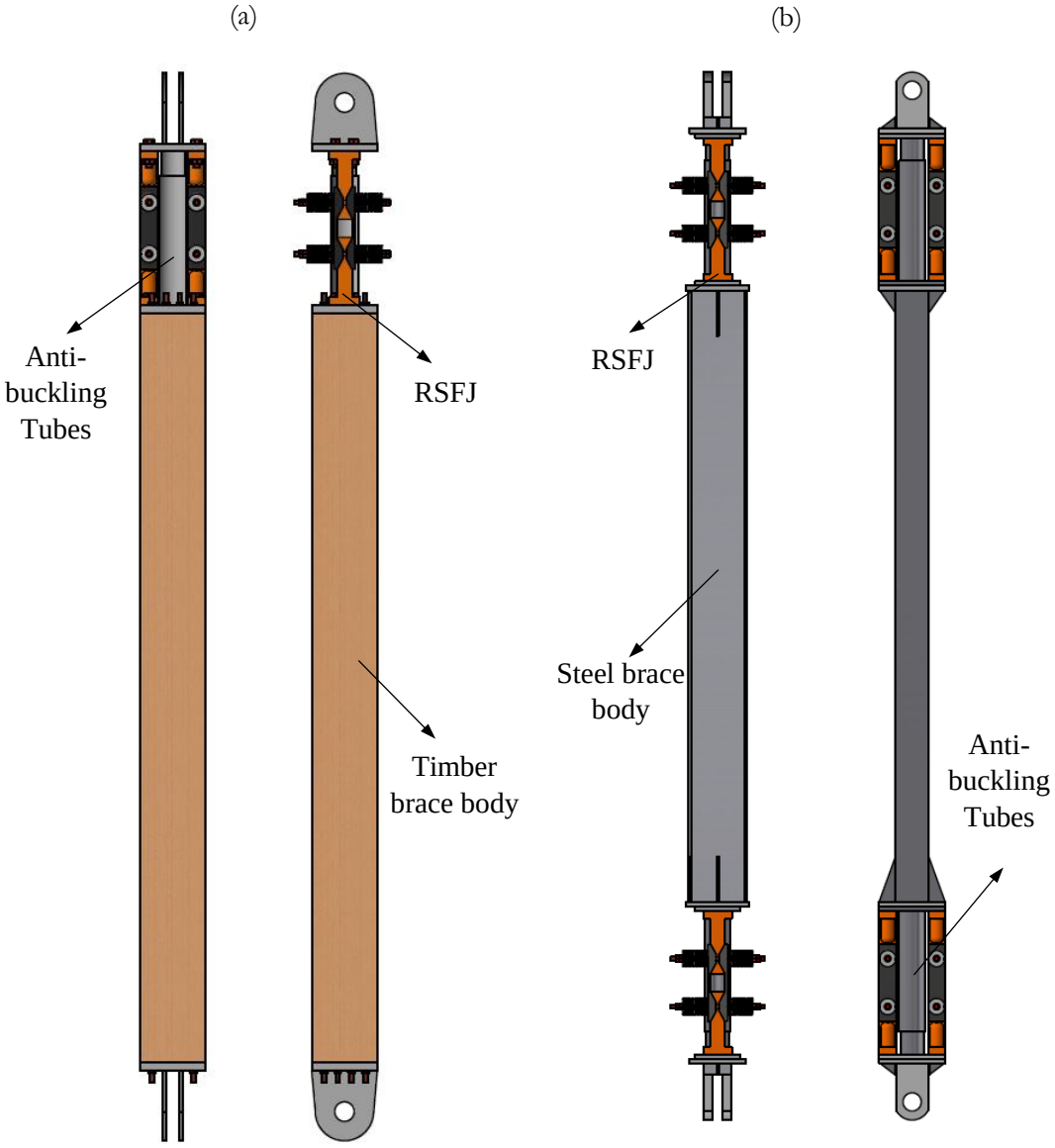

Figure 1.1: RSFJ brace (a) with one damper and timber brace body, (b) with two dampers and steel body

Self-centring systems are often referred to those structures that exhibit a flag-shape hysteresis behaviour, similar to that shown in Figure 1.2 when subjected to a reversed cyclic loading. Depending on the source of damping and the design, it can be categorized as a low-damage or damage-avoidance system (refer to section 1.1.3). The main benefit of these structures is that they can provide a zero (or near-zero) residual displacement when the load is removed. In this type of structure, the factor β (Figure 1.2) is representative of the amount of damping and varies between

zero and two [35]. The advent of low-damage self-centring systems with flag-shaped hysteresis damping dates back to the early 90s [48-50] within the Pre-cast Seismic Structural Systems (PRESSS) program and the application of precast post-tensioned rocking concrete walls [51] and post-tensioned beam-to-column connections [50]. In these systems, post-tensioned tendons are normally used for rocking precast panels to provide the nonlinear elastic response ($\beta = 0$) while the yielding dampers ($\beta = 2$) are used to provide the energy dissipation. These two performances combined together can form the desired flag-shape response. Application of the post-tensioned elements with additional damping resources has been extensively studied in the literature for which it can be referred to [17, 19] for a comprehensive review.

1.3.1.1. Ductility and peak displacement

Christopoulos et al in 2002 [52] studied the nonlinear response of a SDOF self-centring structure with flag-shape behaviour (shown in Figure 1.2) in comparison with a conventional system with bilinear elasto-plastic behaviour. In their study, they included the 5% damping proportional to initial stiffness. The key results of that study were that the performance of the self-centring systems was comparable to that of the conventional one. More specifically, it was found that:

a) The ductility demand of the system is not that much affected by the level of damping ratio though the amount of energy dissipation differs considerably among them.

b) The maximum displacement of SC system can be adjusted to be marginally higher than the bilinear system.

c) The system with flag-shape hysteresis behaviour sustained zero residual displacement.

d) It was found that a SC system with an activation strength of lesser than that of the conventional system and a higher secondary stiffness can outperform the bilinear system in terms of maximum acceleration, peak displacement and residual displacement.

Seo and Sause [53] extended the study by Christopoulos et al. [52] to include the structures with degrading, bilinear elasto-plastic and flag-shape hysteresis response. The parameters of interest were response reduction factor (strength reduction or deamlification factor), level of damping for self-centring system and ductility demand. To do the parametric study, they employed constant-R ductility spectra method [53], the median (not mean) ductility demand. They also used two models to replicate the equivalent viscous damping: (a) initial-stiffness based and (b) secant-stiffness based. According to their parametric study, the following highlights attract more attention:

a) The foremost result from their study was associated with the situation in which the bilinear elasto-plastic and flag-shape system had the same ductility demand for all range of periods. Interestingly and according to their findings, if the damping ratio (β) was around 35% and the post-yield stiffness was at least 5% of the initial stiffness, both systems would have the same ductility demand for the entire range of the period.

b) Ductility demand increased with increasing the response (force) reduction factor value.

c) It was observed that self-centring systems oscillated freely with larger amplitude around zero displacement while bilinear elasto-plastic ones oscillated with lower amplitude but with an offset (residual displacement) after the event.

d) The period range can be divided into groups: (i) the range that ductility demand became equal to reduction factor (R) and independent from the period, normally referred to as equal displacement range, and (ii) where ductility demand was strongly period-dependent. The margin between these two regions varied with the reduction factor and ductility demand.

e) Increasing post-yield stiffness decreased the ductility demand. This was more effective for short-period rather than long-period structures.

f) Increasing the damping ratio decreased the ductility demand. Similar to the post-yield stiffness effect, this was more effective for short-period rather than long-period structures.

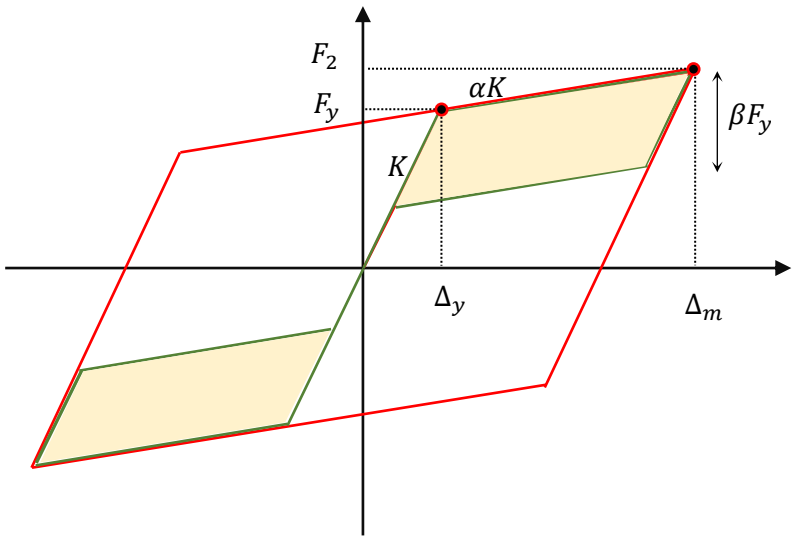

Figure 1.2: Flag-shape hysteretic performance

1.3.1.2. Residual displacement

Ramirez et al. [33] developed a holistic probabilistic framework to account for the effect of residual story drift in the earthquake loss estimation of buildings. Conventionally, the loss was defined to include the economic losses due to either collapse (complete failure of the structure during an event) of the building during a seismic event or essential repairs in the structures without collapsing possibility. They interestingly added the third loss definition to be the obligation to demolish the building after the earthquake due to excessive residual drift and misalignment. They studied both ductile and non-ductile designed concrete frames and concluded that the majority of the economic loss in non-ductile structures was due to the collapse of the structures during the earthquake while in the ductile frames (code-compliant designed), the majority of the loss was due to the post-event demolition as a result of excessive residual drift. Furthermore, they studied the effect of height for loss estimation and finally concluded that, contrary to what many think, the economic loss of the buildings that are designed with respect to new codes (ductile performance) will mostly stem from the demolition of the building due to residual drifts if they are subjected to DBE and MCE level seismic inputs.

In this regard, McCormick et al. [34] studied the permissible level of the residual drift for residential buildings so that they can be regarded as a *repairable* system. They considered three elements namely: (a) functionality of the building after an earthquake, (b) initial construction tolerance and (c) safety. It is worth noting that the building functionality, itself, included the effects of out-of-plumpness of the building on human feelings and their daily lives. According to this study, the residual drifts of 0.006, 0.005 and 0.005 rad were suggested with respect to the three mentioned elements, accordingly. Finally, a single allowable residual drift of 0.005 rad (or 0.5%) was suggested to be employed for the performance-based design of the structures so that a building can be evaluated as either "*repairable"* or "*should be demolished"*.

Eatherton and Hajjar [35] proposed alternative limits based on the cumulative permissible out-of-plumpness of a building and manufacturing tolerance for an individual member as reported in Table 1.1 for an intended building to be regarded as *self-centred*. As can be seen, these permissible values differ based on the height of the structure, and it becomes stricter for taller buildings. Other researchers also reported a value between 0.1% and 0.2% [54-56].

Furthermore, they [35] studied the effect of ambient building conditions on the seismic response of the structures with more focus on the residual drift response of the buildings. The ambient building conditions referred to some aspects that are not modelled typically in the structural model. It includes: (a) semi-rigid connections (simple connections with attachment/detachment

to the floor slab), (b) displacement-sensitive non-skeletal components such as exterior walls, claddings, partition walls, stair stringers, etc. The reason why non-skeletal elements are normally ignored in the structural modelling can be described by:

Table 1.1: Permissible residual drift values for a self-centred building

	3 story	6 story	9 story	12 story
Individual (Maximum out-of-plumpness)	0.20 %	0.20 %	0.20 %	0.20 %
Cumulative (1 inch over height H =12 foot, or 25.4 mm over H = 3658 mm)	0.20 %	0.14 %	0.075 %	0.057 %
Minimum	**0.2 %**	**0.14 %**	**0.075 %**	**0.05 %**

- They normally increase the stiffness and strength just for a limited number of cycles and after a handful of inelastic cycles, they experience a large strength and stiffness degradation.
- Some minor decreases can be seen in the seismic demand, which codes normally neglect.
- Their effect is seen in the damping (partly in 5% for elastic spectra although there are some techniques to reduce their effect [35].

According to their extensive parametric studies, the following results can be remarked:

Effect of system strength:

- Up to the damping ratio of β = 1.5 (shown in Figure 1.3), the residual drift is negligible and within the permissible level (Table 1.1).
- As it was observed, the damping ratio does not have a pronounced effect on the peak drift especially for buildings with stories higher than 6.
- The residual drift is not that sensitive to the "R" factor except for short-period structures.

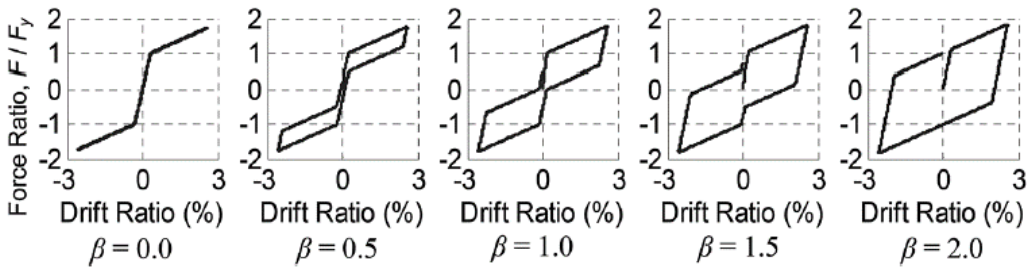

Figure 1.3: Different levels of hysteretic damping for a sample self-centring system [35].

Effect of ambient building resistance:

- At low values of β, more beam-column connections result in larger residual drifts, but as the β approaches 2, more beam-column connections cause a reduction in residual drifts. In other words, the number of semi-rigid connections could bring positive and negative aspects. It favours the building without self-centring, yet disfavours the buildings with self-centring.
- Its effect alleviates with taller buildings or high-period structures.
- Partition walls have less impact as compared to that of the beam-to-column connection.

Effect of stiffness variation:

- It was found that the post-yield stiffness of the system considerably affects the residual drift of the structures especially those with $\beta = 2$ (BRB-type). However, if the self-centring is provided, there would be no need for the post-yield stiffness to be positive. It is worth noting the author of this thesis and his colleagues developed such self-centring brace with zero post-activation stiffness [54], which will be discussed in chapter 8.

Rad et al [57] studied the seismic performance of the steel buildings with initial out-of-straightness and bilinear elasto-plastic behaviour. In this regard, they studied the effect of out-of-straightness on the peak inter-story and residual displacement considering the different response modification factors (R), the different number of stories and a few other factors. According to their findings:

a) The residual drift was heavily sensitive to the initial out-of-straightness.

b) The higher "R" the building was designed for, the more sensitive it was to the initial out-of-plumpness. In other words, the initial out-of-plumpness had more pronounced effects in terms of the peak drift especially on those buildings designed with higher values of R.

c) Generally, a higher "R" factor brought a larger residual drift, yet buildings with an initial tilt were more sensitive.

d) Both peak inter-story and residual drift were on the rise with increasing value of the out-of-plumpness and response modification factor, yet the residual drift was found to be much more sensitive to out-of-plumpness.

e) Finally, they have suggested a number of empirical formulations to predict the peak seismic response for buildings with vertical tilt.

1.3.1.3. Peak floor acceleration demand of self-centring systems

A highly controversial topic associated with the seismic response of the self-centring systems is the acceleration response as it could be indicative of the loss and damage to the non-skeletal components [37, 38, 58] and the diaphragm [59]. Until recently and based on the numerical studies, it was believed that the acceleration response of the self-centring systems tends to be larger than that of the conventional structures and even in some cases might be concerning. Evidence of such opinion was provided by Trembley et al [60] for self-centring braces and by Wiebe et al. [61]. Contrary to the above-mentioned studies, recent shake table studies suggested completely opposing results. The shaking table studies on the rocking steel structures and self-centring braces [62, 63] showed that numerical software may overestimate the acceleration response of the self-centring systems mainly because they lack a smooth transition zone between different zones of the flag-shape hysteresis model. Further studies by Wiebe and Christopoulos [64, 65] revealed that, unlike the displacement and velocity time-history responses, the acceleration time-history response is highly sensitive to the transition zones in the flag-shape response (shown in Figure 1.4). How these transitions are defined may lead to acceleration spikes where the stiffness suddenly changes. According to [64, 65] following remarks can be highlighted for the acceleration response of self-centring systems:

a) Modelling of the flag-shape hysteresis with sharp-corners may lead to the calculation of the acceleration that is not realistic. As shown in Figure 1.4, depending on the roundness of the corners, the acceleration spike may get 10 times bigger.

b) Considerable acceleration spikes are expected in MDF systems when stiffness rapidly increases.

c) The magnitude of the spikes is highly dependent on the roundness or sharpness of the hysteresis curve.

d) Abrupt stiffness change has a negligible and relatively small effect on the peak displacement and velocity response.

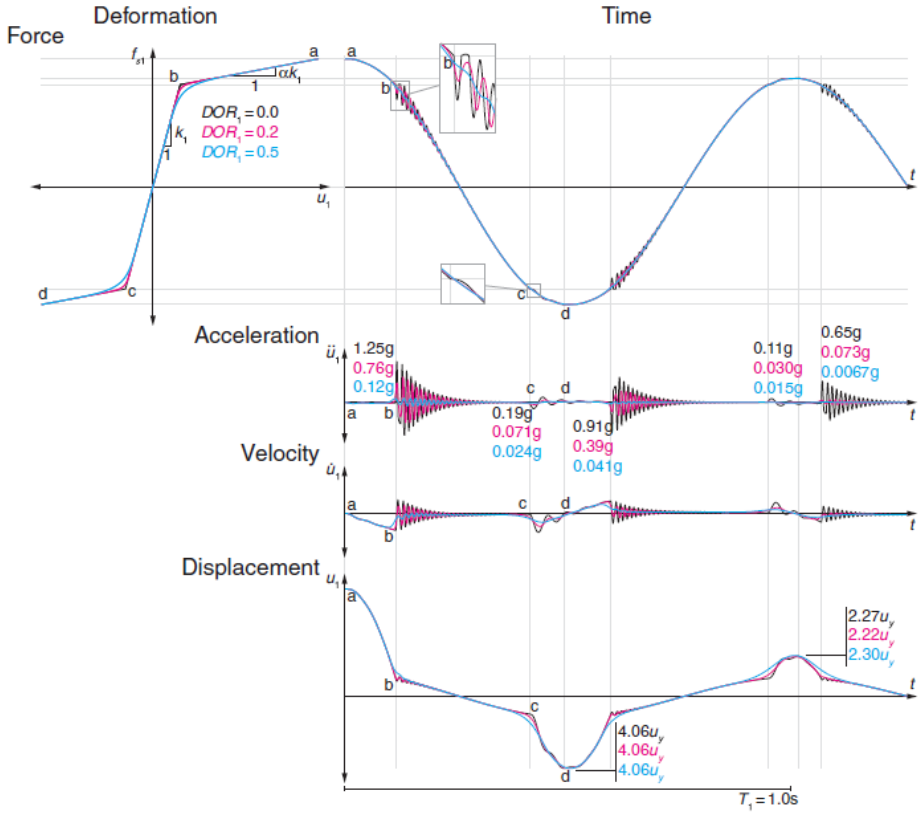

Figure 1.4: Free vibration response of 2DOF system with varying degrees of hysteretic roundness (DOR) [64, 65]

1.3.2. *Rocking steel braced frames*

The rocking steel braced frames (Figure 1.5) are relatively new lateral load resisting systems that have the ability to re-centre the structure back to its upright position after a seismic event and are composed of three main elements. The dampers (seismic sacrificial fuse – red plates shown in Figure 1.5), the main braced frame, which is supposed to remain elastic and the vertical post-tensioning tendons that play the main role in re-centre the building. One possible schematic illustration of this type of system is depicted in Figure 1.5 [66]. Rocking steel braced frames can be used with different combinations of energy dissipation mechanisms or dampers. As an illustration, Trembley et el. [67] used viscous dampers, Wiebe et al [68] employed friction plates, Eatherton et al [69] used steel shear links and Deierlein et al utilized [70] buckling-restrained braces (BRB) as the energy dissipative mechanism.

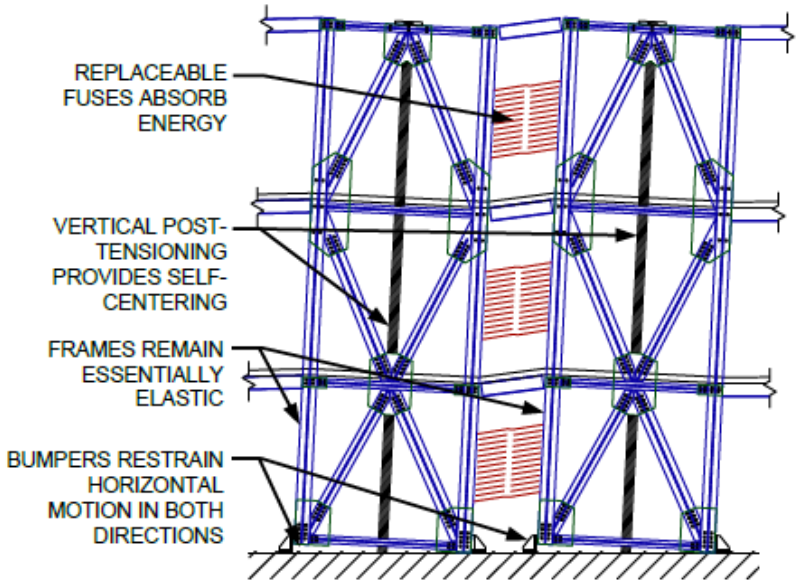

Figure 1.5: Schematic illustration of a rocking steel braced frame [66].

When the structure height increases, the effectiveness of the rocking system will decrease due to the flexibility of the wall and the arrival of the higher mode effects [62]. Researchers have put forth different techniques to solve this problem. Weibe et al [62] proposed two mechanisms to mitigate the higher mode effects in the controlled rocking steel frames. More specifically, they suggested that the multiple rocking joint plus rocking at the base can mitigate the higher mode effects. The other alternative to mitigate the higher mode impact was that a storey (in their study, it was the first storey) can be shear-isolated from the others to limit the base shear. This isolation mechanism in their study was a self-centring brace. In the first approach, the overturning moment was limited by a second rocking joint at the 4th floor resulted in the reduction of the base shear. However, in the second approach, the storey shear was limited by a self-centring brace which resulted in the reduction of the overturning moment. They made an important observation on the impact of columns due to uplift and rocking. According to the shake-table study, the rocking did not affect the peak acceleration or peak force in the column. In 2015, the same researchers established a performance-based design framework for the design of the self-centring rocking steel braces [68, 71]. In order to make the design independent from the initial assumptions in terms of the structural sections, they normalized the variables and performed a parametric study on the different rocking structures. According to their findings, the peak inter-story drift of the structures under investigation was independent of both post-rocking stiffness and the damping ratio of the structures. Furthermore, they concluded that the activation strength (rocking moment) and initial stiffness are governing the seismic demands of the structures. To validate the proposed

framework, they studied two, six and twelve storey prototype buildings. They also applied the previously introduced [62] mitigation techniques for higher mode effects.

Martin et al. [72] developed the capacity design framework for designing the controlled rocking steel frames which explicitly included the higher mode effects into the calculations. The results were close to what Steele and Wieble suggested [73]. They also evaluated the load and resistance factor method (LRFD) to be considered for the design of the members. According to their findings, their proposed capacity design method combined with the safety factors of LRFD method can successfully guaranty that the force-controlled elements (non-fuse) can remain elastic up to the MCE (Maximum Considerable Earthquake). In this regard, Rahgozar et al. [74] investigated how to include the higher-mode effects in the Direct Displacement-Based Design method (DDBD) of the Rocking steel frames.

Kibriya et al. [75] numerically developed a rocking steel brace frame using a buckling-enabled brace using glass-fibre reinforced polymer (GFRP) shells to further improve the response of the rocking steel bracing systems. It was observed that the employment of this system contributed to increasing the lateral resistance and stability of the system, leading to a reduced peak drift and acceleration response although the system did not employ any mechanism for damping. The main benefit of the proposed system was found to be damage- avoidance in case of major seismic events, zero post-rocking stiffness and period lengthening mechanism. The performance of the proposed system can be compared with both the bare rocking and the rocking with post-tensioning as shown in Figure 1.6.

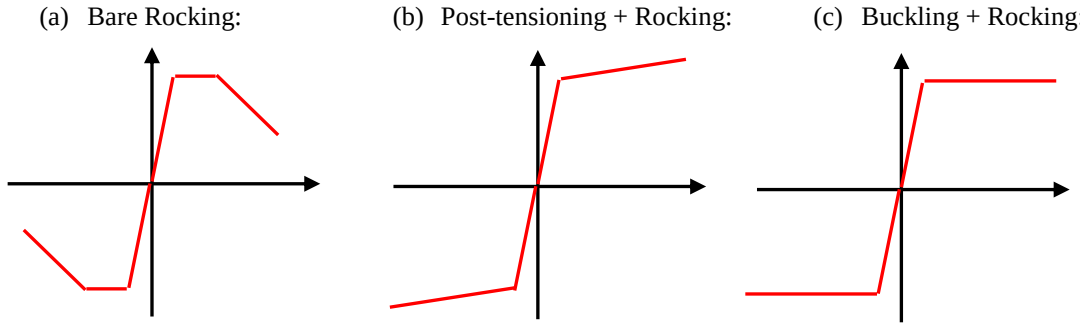

Figure 1.6: Comparison between the different rocking mechanisms: (a) bare rocking of a frame [76], (b) Rocking with post-tensioned elements [51] and (c) Rocking with buckling enabled brace [75].

1.3.3. *Self-centring braces with post-tensioned cables (or rods)*

Christopoulos and Tremblay [60, 77] developed a new self-centring energy dissipative device using two hollow telescopic steel box sections, post-tensioned tendons and friction dampers (shown in Figure 1.7). They also performed quasi-static and dynamic testing on a steel brace sample in order to evaluate the performance of their system. Erochko et al. [78] extended the previous work to increase the displacement capacity of the previously introduced self-centring brace. In that study, they also observed that the end connection, bolted or real-pin, can affect the performance of the self-centring brace. They also observed that in case of the bolted connections for the brace end, a huge bending will be imposed on the connection and column when the frame is pushed to a large displacement, which showed the impact of the end connection. One of the problems that they observed in the results was that the experimentally derived initial stiffness of the brace was considerably less than that of the predicted one with analytical formulations. They explained that the fabrication tolerance was the root cause of this problem, and they developed a model to account for this effect [79]. In this regard, they concluded that the initial stiffness of their developed brace is highly sensitive to manufacturing tolerance. In order to further investigate the application of the brace, they performed a shake table study in 2013 [63]. They used the same seismic response modification factors as BRBs to design a prototype building. According to their findings, the maximum acceleration response of the structure is overestimated if the SAP2000 or OpenSees software is used. They explained that the reason for this phenomenon is the lack of a transition zone between different parts of the flag-shape model in the software. However, the storey shear, storey drifts and other seismic response parameters matched the predictions and numerical studies. Detailed discussion was provided in section 1.3.1.3.

Ping et al. [80] extended the work by Erochko et al. [79, 81] to consider the effect of tendon fracture on the seismic performance of a building equipped with such self-centring braces. In their study, they considered both the single-core and dual-core options (shown in Figure 1.8). In their modelling, the behaviour of the brace was considered to be coming from two decoupled links namely: (a) multi-linear plastic resembling the hysteretic behaviour of the friction damper and (b) multi-linear elastic resembling the hysteretic behaviour of the post-tensioned tendons. As a result, when the tendon fails, the flag-shape performance of the system degrades to a rectangular hysteresis (shown in Figure 1.8). According to their findings, the following points can be highlighted:

a) The risk of collapse is decreased when a dual-core brace is used.

b) The risk of collapse is much higher when the structure is hammered by the near-field earthquakes (events included forward-directivity [82])

c) The tendon failure significantly increased the probability of residual drift

d) Tendon failure seemed to have a limited impact on the floor peak acceleration response though it might contribute to the formation of the weak story due to sudden loss of stiffness.

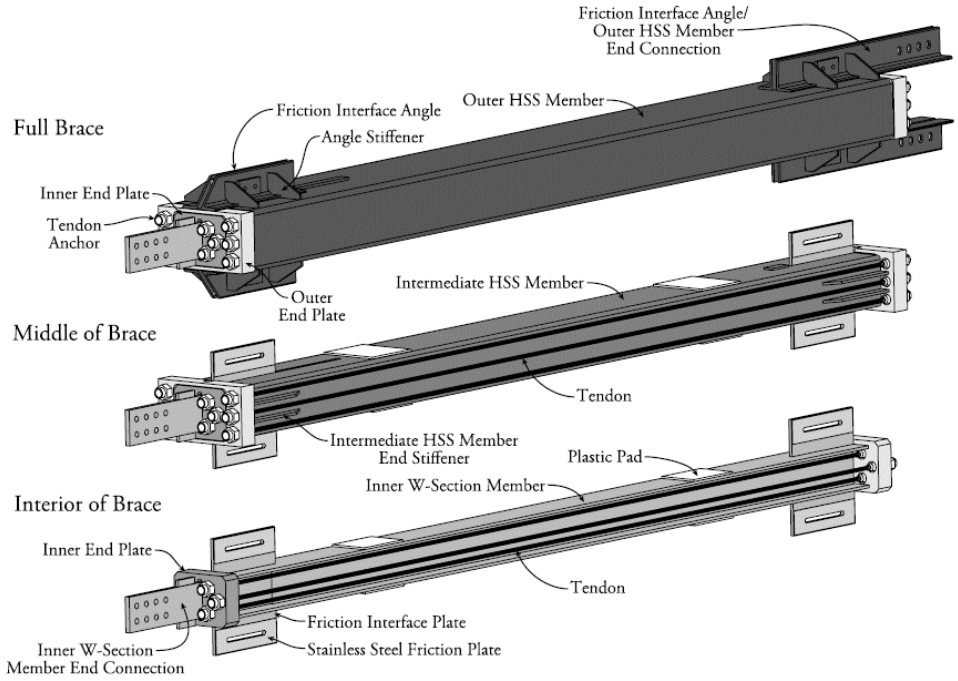

Figure 1.7: Schematic representation of the self-centring brace with post-tensioned tendons [81].

Qing et al. [83] studied the application of post-tensioned composite rods in combination with BRBs to develop a new self-centring brace. In this regard, they evaluated the seismic response of 2 to 16 storey structures subjected to FEMA/SAC suite of ground motion – both near- and far-field - [84] and further validated the previous findings of Eatherton et al. [12, 85] in terms of the fact that the fully self-centring hysteresis performance for a brace may not be necessary for the dynamic self-centring of the structure while considering near-fault effect such as forward directivity. In this sense, they observed that even a system with partial self-centring capability can be re-centred. More specifically, they concluded and recommended that if the ratio of the pretension force to the maximum strength of the BRB falls between 0.6 and 1, one can get the best seismic performance in terms of the peak inter-story drift, residual drift and peak floor acceleration.

(a)

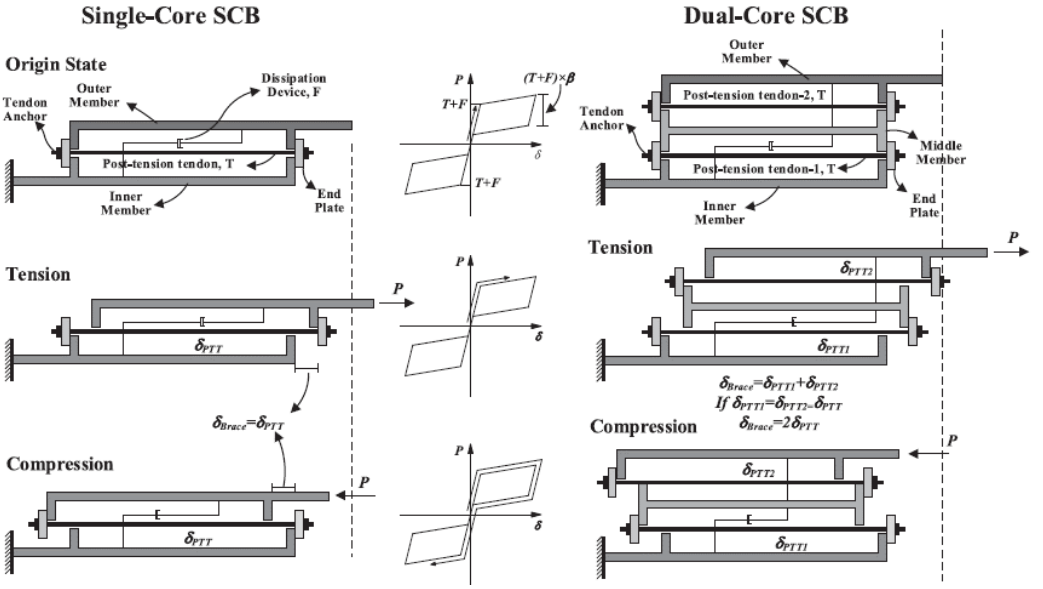

(b)

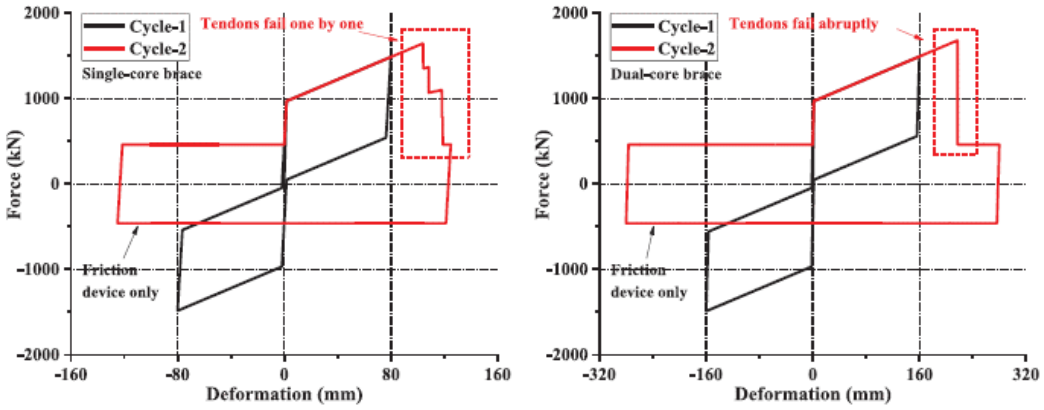

Figure 1.8: self-centring brace with post-tensioned tendons and friction dampers: (a) Single-core and double-core self-centring brace [80] and (b) expected behaviour after tendon failure [80]

1.3.4. *Self-centring braces with Shape Memory Alloy (SMA)*

McCormick et al [86] proposed a tension-compression self-centring brace using SMA (Shape Memory Alloy) bars and presumed that these rebars are encased in a steel jacket so that the SMA rebars do not buckle under compressive loads. They used three and six-story benchmark structures using traditional concentric steel braces [87] as a reference model to be compared with the seismic performance of their proposed system. According to their findings, using the SMA

braces can better distribute the seismic demands throughout the stories while it can also reduce the peak inter-story and residual drifts.

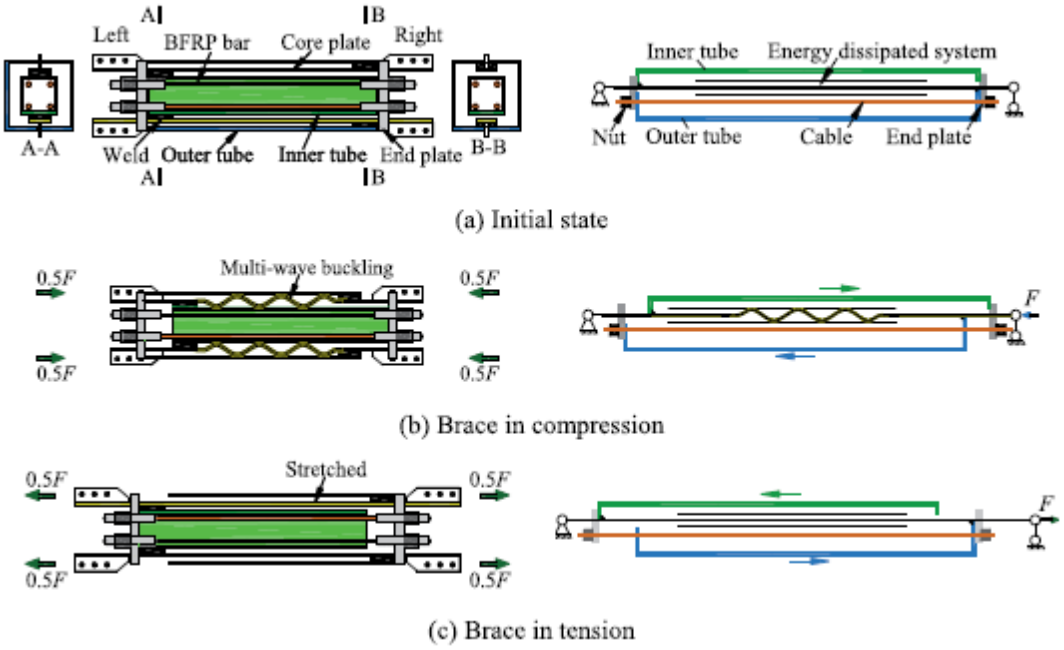

Figure 1.9: Self-centring BRB using pre-tensioned rods [83]

Zhu and Zhang [88, 89] developed a new self-centring brace using SMA tendons for which they suggested a modified constitutive formulation to analyse the brace performance in loading and unloading. In order to optimize the performance of the brace and increase the damping coefficient, they added friction damping to their system using prestressed bolted and clamped steel plates [88]. They performed both the nonlinear pushover and nonlinear time history analyses to validate the performance of an archetype building in comparison with a reference building using BRB braces. In their modelling, they assumed that the activation strength of the brace equals the yielding force of the BRB. According to their findings, the developed brace can have a comparable performance compared to the reference building in terms of peak inter-storey drift and acceleration while it can considerably reduce the residual drift of the structure.

Miller et al. [12] improved the cyclic performance of BRBs using SMA Rods. For this purpose, they used BRB as the energy dissipation mechanism in combination with SMA rods to form a flag-shape response. According to the experimental results, this combination successfully reduced the residual displacement of the BRB to half of the maximum inelastic displacement. Eatherton et al. [85] extended the study on self-centring BRBs and performed a parametric study to propose an optimized design guideline to be used in engineering practice. As it is shown in Figure 1.10, their self-centring system was composed of a BRB brace and 4 SMA rods. Due to the special

arrangement of the end floating plates, the brace could work both in tension and compression while the rods only experienced tension. For the parametric study, the effect of SMA rods, brace capacity, self-centring ratio, initial prestressing of the SMA rods and the ambient building condition were included. According to the parametric studies, the following highlights have been selected:

a) If a minimum damping ratio (the ratio of damped energy by the self-centring-BRB to the bilinear fully elasto-plastic BRB) is about β =25%, the expected ductility demand for both systems is the same.

b) A relative length of greater than 0.4 (the ratio of the SMA rods length to the brace length) will provide an acceptable energy dissipation and enough safety margin against fracture due to the cumulative inelastic strain.

c) Ambient building condition which was considered to be the semi-rigid connection between the beam and column had little effect on the residual response of the building.

d) There is no need to have a fully self-centring brace so that a residual response of the building is achieved. If the initial prestressing force of the SMA rods is equal to half of the BRB capacity in compression, the building will exhibit near-zero residual displacement even in case of the Maximum Considerable Earthquake (MCE) with a probability of exceedance of 2% in 50 years.

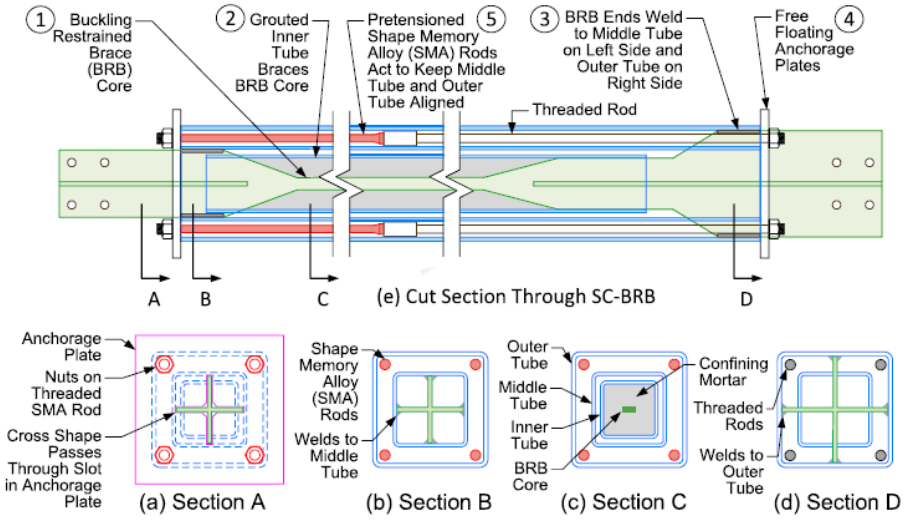

Figure 1.10: Self-centring BRB using SMA rods [12, 85].

Qiu et al. [90] numerically developed a new re-centring brace with a combination of SMA bars and steel plates that were designed to yield in bending (shown in Figure 1.11). They firstly did a

parametric analysis on a single-degree-of-freedom system to come up with the proper parameters so that the seismic response of the proposed brace is relatively similar to those of a BRB frame. They also concluded that by adjusting the post-activation stiffness of the brace and the activation strength, superior performance can be achieved. Further on, they recently did some experimental tests on the subassembly of the brace [91] to further study the performance of the proposed system.

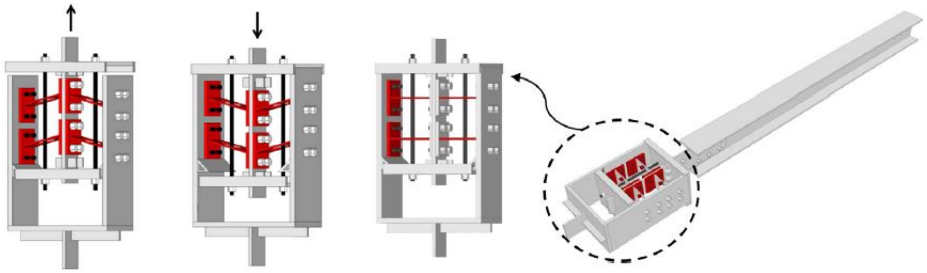

Figure 1.11: Self-centring brace using SMA bars and flexural yielding plates [90, 91]

1.3.5. *Self-centring braces with disc spring and energy dissipation device*

Huang et al. [92] developed a new self-centring steel brace that uses disc springs and the yielding of steel plates for energy dissipation. The steel plate fuse in their study was designed with an initial imperfection so that the secondary moment in the plate assists the formation of the plastic hinge and the energy dissipation.

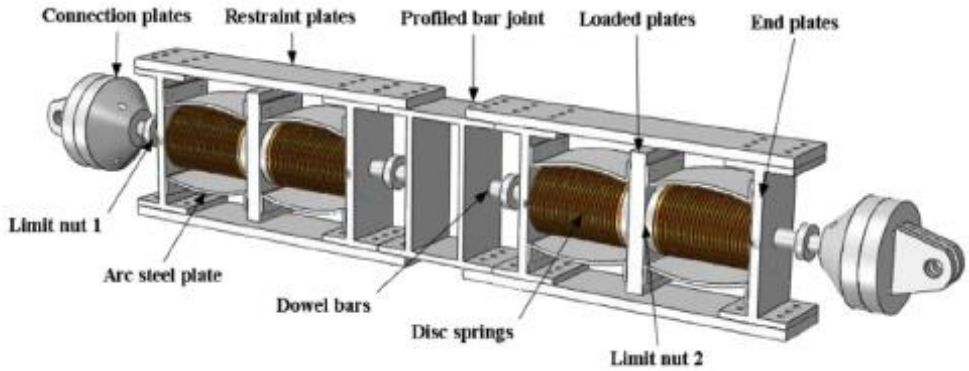

Figure 1.12: Self-centring brace using disc springs and flexural yielding plates [92]

Xu et al. [93] put forth a self-centring brace that was composed of friction pads and pre-pressed disc springs to offer the flag-shape response. They [94] further studied the static and dynamic performances of the brace using different load protocols. More importantly, they observed the global inelastic buckling of the brace when the axial displacement exceeded 2% (shown in Figure

1.13). Xu et al [95] developed a comparable brace and performed a number of destructive tests to observe the failure modes of the proposed brace. They also included and studied the performance of the disc springs and observed that they have some minor internal damping with a marginal difference in loading and unloading stiffness (about 10 %).

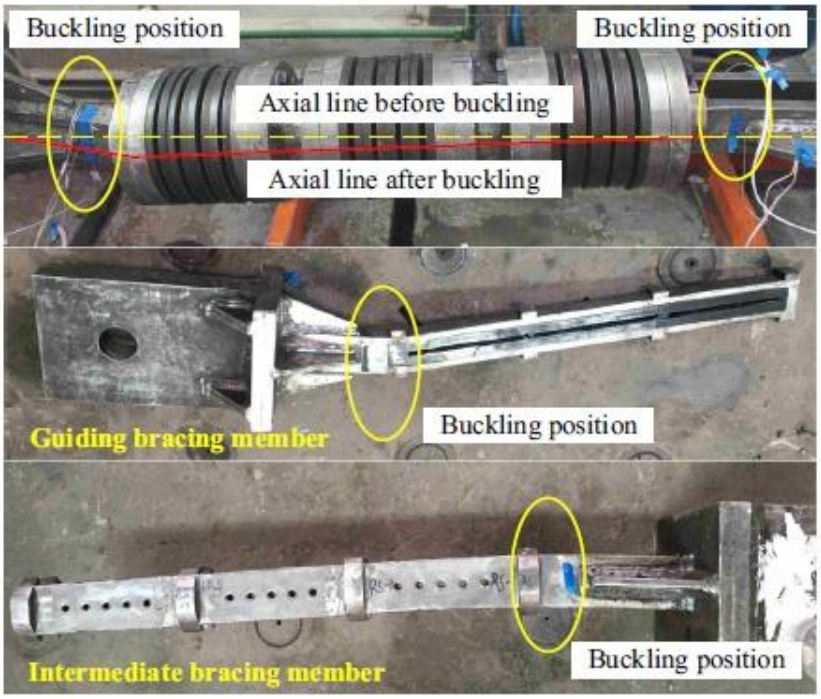

Figure 1.13: Global inelastic buckling of self-centring brace with pre-compressed disc and friction dampers [94]

1.3.6. *Self-centring braces using Friction-ring springs (Ringfeder)*

Issa and Alam [96] developed a new self-centring brace using the Ringfeder friction ring spring device [97] without any prestressing force of the disc spring in the damper. This resulted in the zero activation or slip force and a triangular hysteresis curve rather than a trapezoidal flag-shape. In order to protect the damper from the secondary-order effect, they embedded the damper inside a piston section (shown in Figure 1.14) and tested the brace for different loading rates. According to the experimental results, the loading rate had a minimal effect on the performance of the brace. Furthermore, they conducted a numerical study to compare the seismic performance of a building equipped with two options of Buckling-Restrained Brace (BRB) and the proposed self-centring brace. Interestingly, they found that the displacement demand of the building with their self-centring brace was considerably higher than that of the building with BRB. This tends to be in contrast to findings of similar studies [89, 90, 98, 99] on the self-centring braces and may stem from the fact that they had almost zero slip force or activation strength. It is worth noting that

the activation strength, slip force or rocking moment, was observed to be highly effective in changing the displacement demand [54, 68, 71].

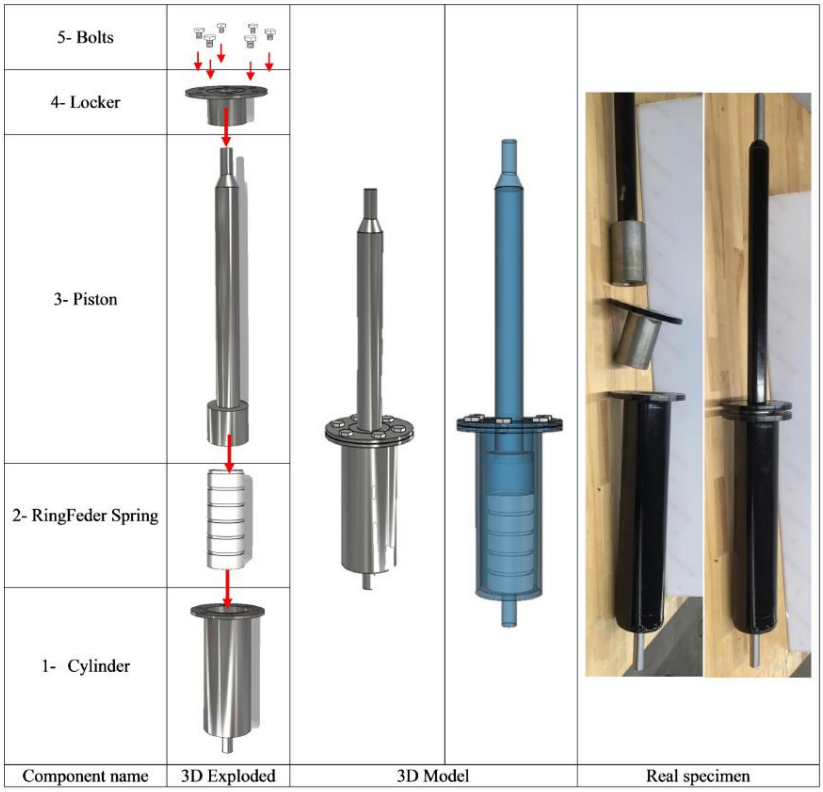

Figure 1.14: Self-centring brace using Ringfeder or friction ring spring device [100]

Hu et al [101-104] developed and evaluated three systems with friction-ring spring dampers namely (a) dual-core rocking steel frame which employed the friction-ring-spring (Ringfeder) as the shear link between the coupled rocking frames, (b) rocking steel frame – which employed the damper as the hold-downs for the rocking core and (c) rocking steel spine -which employed the friction-ring-spring as the diagonal bracing element for energy dissipation and lateral load resistance. These three systems are depicted in Figure 1.15. According to their findings, the following results can be highlighted associated with the three proposed systems:

a) In all three systems, the rocking frame or spine exhibited a rigid body mode which contributed to a better and uniform distribution of inter-story drift. This can assist in avoiding a soft-storey mechanism in case of a major seismic event.

b) All three systems were capable of experiencing 5-6 % inter-storey drift without any structural damage, strength reduction or stiffness deterioration. This can be indicative of the satisfactory performance of the system when a major event, beyond the design level, strikes the buildings.

c) New uniaxial material has been developed for the OpenSees program working environment, which can accurately and precisely predict the performance of the friction-ring-spring damper.

d) A near-full self-centring behaviour was observed for all three systems.

e) Some minor slackness was observed in the experimental result of the systems, which was explained to be induced by the pin connection clearance. Accordingly, a tight-fit pin connection was recommended for real practical applications.

f) Direct Displacement-based Design (DDBD) procedure was developed by which one can design the building accurately with no need for non-linear time history analysis.

1.3.7. *Low-damage braces with replaceable fuse*

Stevens and Wiebe [105] studied and developed a new brace module (shown in Figure 1.16) for the conventional concentrically braced frame which can be easily replaced after a major seismic event. This brace assembly is, in fact, an elevated version of the previously suggested knife plate (Figure 1.16) with added bolted connection proposed by Tsai et al [106]. This brace module had a new gusset plate which was only attached to the beam rather than the beam-column interface. Apart from more constructability and replaceability of the whole system, this new gusset plate had a number of benefits such as reducing the likelihood of the multiple plastic hinges in the gusset plate in the large inter-storey drifts [105]. Additionally, it will encourage the brace to buckle in the in-plane direction, which is more reliable and less destructive than the out-of-plane. According to the experimental program, no special premature failure, unpredictable behaviour was observed, and the connection successfully enforced the buckling to occur in the in-plane direction.

(a)

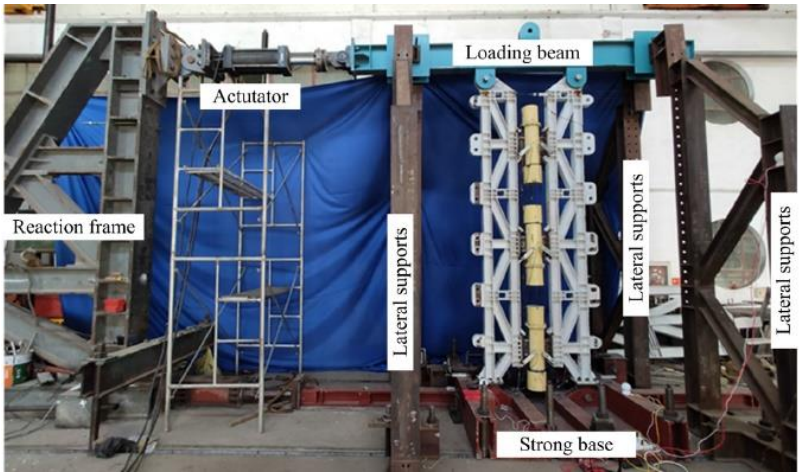

(b)

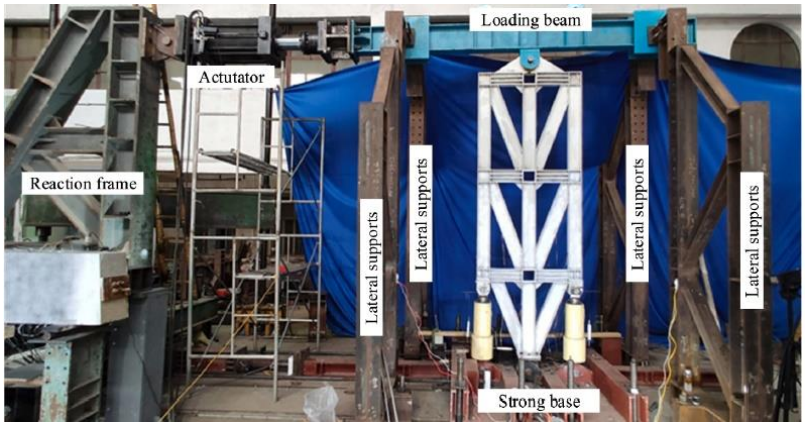

(c)

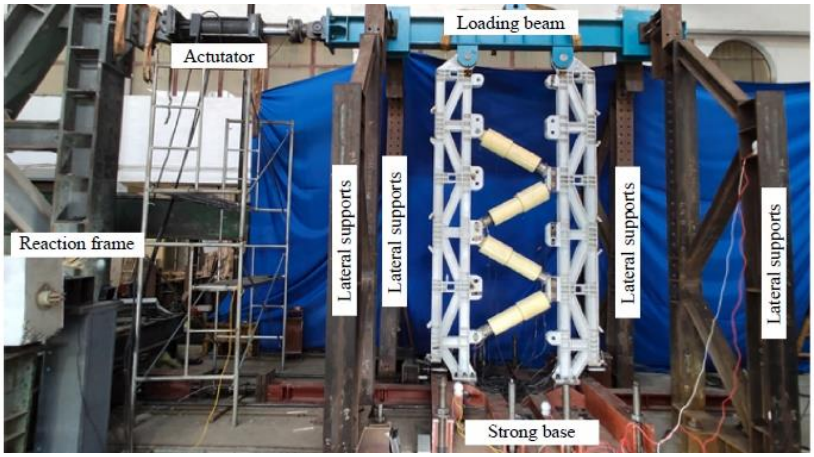

Figure 1.15: Self-centring Rocking Frame: (a) dual-core frame with friction-ring-spring shear link [104], (b) with friction-ring-spring (ringfeder) hold-downs [102] and (c) with rigid steel spines and friction spring dampers (ringfeder) [101]

Mansour et al [10] studied the feasibility of a replaceable shear link for the application of low-damage Eccentrically Braced Frames (EBF) [107] with inverted V configuration. For this purpose, they decoupled the floor beam into two segments: (a) the shear link part and (b) the beam part. Different configurations and methods of instalment were assumed and tested for this replaceable shear link part. The connection of the shear link to the beam was achieved through three methods: (i) Bolted end plate (Figure 1.17.a), (ii) Bolted web connection (Figure 1.17.b) and (iii) welded web connection (Figure 1.17.c). According to their experimental results, minor pinching behaviour was found for the bolted connections through which some additional inelastic rotation capacity of the shear link was observed. Furthermore, they included the repairability of the floor slab in the experimental test and concluded that the common practice in the retrofitting of the slab (for instance methods suggested by the American Concrete Institute- [108] can be viable and sufficient.

Volynkin-Ewens et al [11] extended the previous research into the application of the replaceable shear links in D-type EBF with endplate bolted connection. They also suggested the stocky link elements to be used for this replaceable link given its additional inelastic rotation.

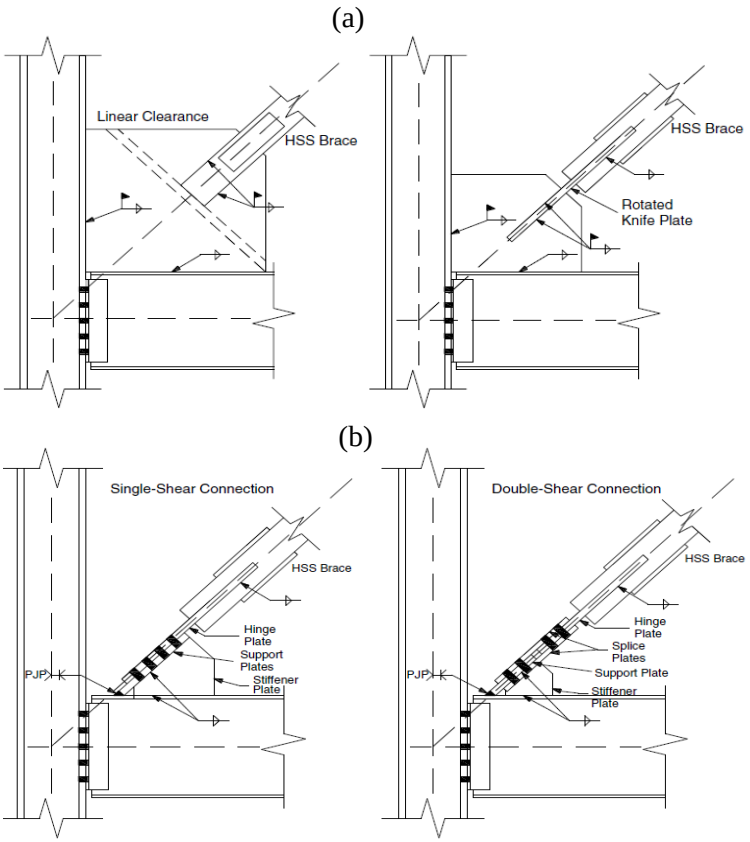

Figure 1.16: (a, b) the conventional and new suggested gusset plate for low damage concentrically braced frames [105]

Clifton et al [109-111] developed a new friction-based replaceable shear link with the web bolted connection (shown in Figure 1.18) for the application of EBFs and concrete coupled shear walls. They used pre-pressed disc springs to provide friction damping. The main benefit of their system was that the performance of the shear link was independent of the length of the link, unlike the conventional yielding-based shear link. Moreover, two frictional surfaces were investigated in the program: (1) Mild steel on abrasion-resistant steel grade Bis-Alloy 400 and (b) Mild steel on mild steel. According to their experimental results, both of the configurations exhibited good performance in terms of the energy dissipation with the difference that the mild-to-mild steel configuration exhibited a hardening behaviour due to galling effect while the mild steel to Bis-alloy 400 configuration exhibited a more repeatable performance with no hardening.

(a)

(b)

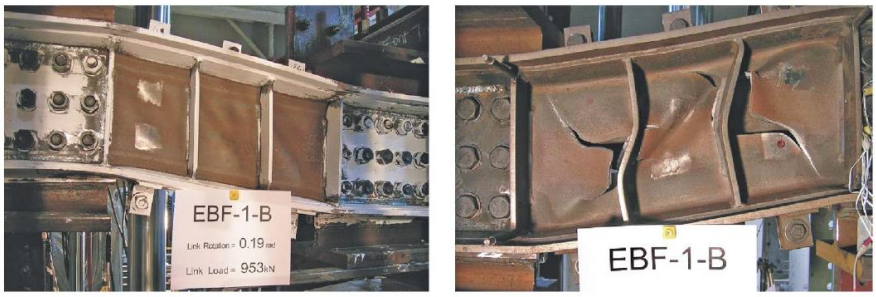

(c)

Figure 1.17: Eccentrically Braced Frames with the replaceable shear link [10]: (a) Bolted end plate, (b) Bolted web connection and (c) welded web connection

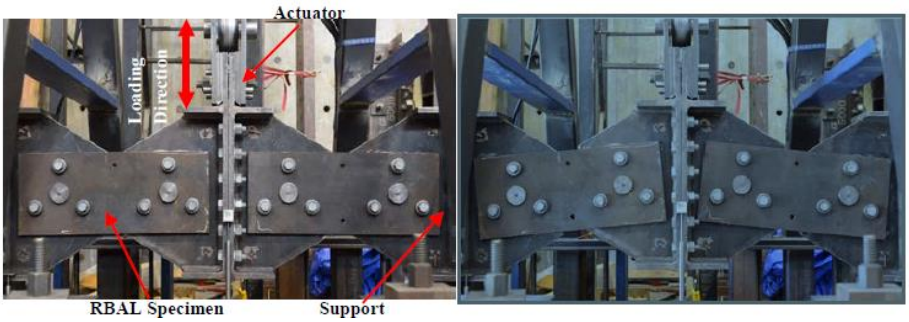

Figure 1.18: Eccentrically Braced Frames with the replaceable frictional shear link [109]

Asymmetrical and Symmetrical Friction connections (AFC and SFC) are among the popular and simple replaceable and low-damage friction connections in New Zealand that can be used in different types of structural systems. The development of the system dates back to the early 1990s when Grigorian et al [112] and Tremblay [113] utilized this connection in the braced frame application in the United States and Canada, respectively. A few years later, Butherworth and Clifton extended the concept for the moment-resisting frame (MRF) structures in New Zealand [114, 115]. Significant efforts have been put into the development of this system and its behaviour on the international scale and within the different lateral load resisting systems. The review in this thesis is mostly limited to the investigations on the low-damage braces. Golondrino et al. [116, 117] studied and tested low-damage braces with both SFC and AFC connection (shown in Figure 1.19). A complete rectangular hysteresis response was observed for both of them, yet 25% and 10% strength degradation were observed for the SFC and AFC braces, respectively. Furthermore, in case of the AFC, due to asymmetrical connection details, the secondary-order moment was more observable resulted in minor asymmetric hysteresis response of the brace in the compression zone.

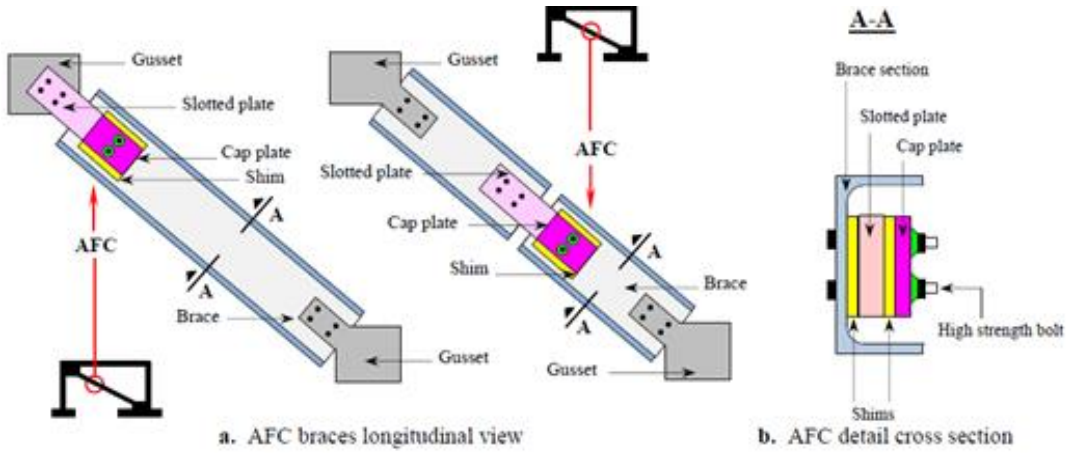

Figure 1.19: Low-damage brace with friction connection [116, 117]

Qu et al. [118] developed and tested a new all-steel Buckling-Restrained Brace (BRB) with replaceable fuse elements. More specifically, their proposed BRB consisted of inner and outer telescoping buckling-restraining elements with intermediate steel plates as the fuse, all of which were assembled using bolted connections and a specific grease as the debonding material. Extensive experimental tests were performed to qualify the employment of such brace. According to their experimental results, accumulative plastic strain capacity and the difference in tension and compression capacity were within the prescription of the codes while it had the main advantage of easy repairability.

1.4 Prior related work and research on the stability of braces

Investigation on the inelastic performance and capacity of the members working under compression would probably date back to the eighteenth century when Engesser [119] noted that the Euler load ($\pi^2 EI/L_e^2$) is only valid for the slender columns. Since then, the topic has been investigated by numerous researchers resulting in the proposal of many different methods [120, 121]. Among those methods, it can be referred to the Tangent Modulus and Double Modulus Theory [122] in which the Euler formulation is used to quantify the inelastic buckling capacity but with the difference that an effective (tangent) modulus of elasticity replaces the elastic modulus of elasticity. Though this large amount of efforts and studies in the nineteenth and twentieth centuries on the calculation of the ultimate strength of the column [121], most of the international building codes now use the approximate empirical curves to calculate the ultimate strength of a column in the interest of simplicity and accuracy. For example, AISC 360 code [123] – American Specification for Structural Steel Design - has adopted a single curve to calculate the ultimate strength of a column for all types of steel sections. However, NZS 3404 [124] – New Zealand Steel Structures Standard – has employed multiple strength curves depending on the steel section type (i.e. RHS, CHS or I-section).

In case of the proposed bracing system, the column strength curve proposed by the codes cannot be used mainly because those curves are mainly developed for prismatic columns (same cross-section over the length). One may argue that the equations that have been developed for stepped columns such as the one depicted in Figure 1.20 [125, 126] can be used in combination with the codes curves (the common practice for the design of stepped columns). It can be argued that this method seems also invalid to be used for RSFJ brace design as it presumes that both sections with EI_1 and EI_2 are transferring the axial force while resisting $P-\delta$ via their flexural stiffness (like the internal force shown in Figure 1.21.a). This is not true when it comes to RSFJ brace assembly. In case of RSFJ brace and at the location where the damper(s) are installed, the axial resistance and the flexural resistance are decoupled in a way that the dampers are transferring the axial load

while the ABTs (Telescopic tubes) are resisting the $(P-\delta)$ via their flexural stiffness (Figure 1.21.b). In this process, it is assumed that the dampers have relatively marginal rotational stiffness as compared to ABTs.

Having said the above-mentioned reasons, neither an empirical column strength curve can be generated (such as those codes prescribe) due to the unavailability of the experimental data nor can the stepped column method be used given the decoupled load distribution among elements.

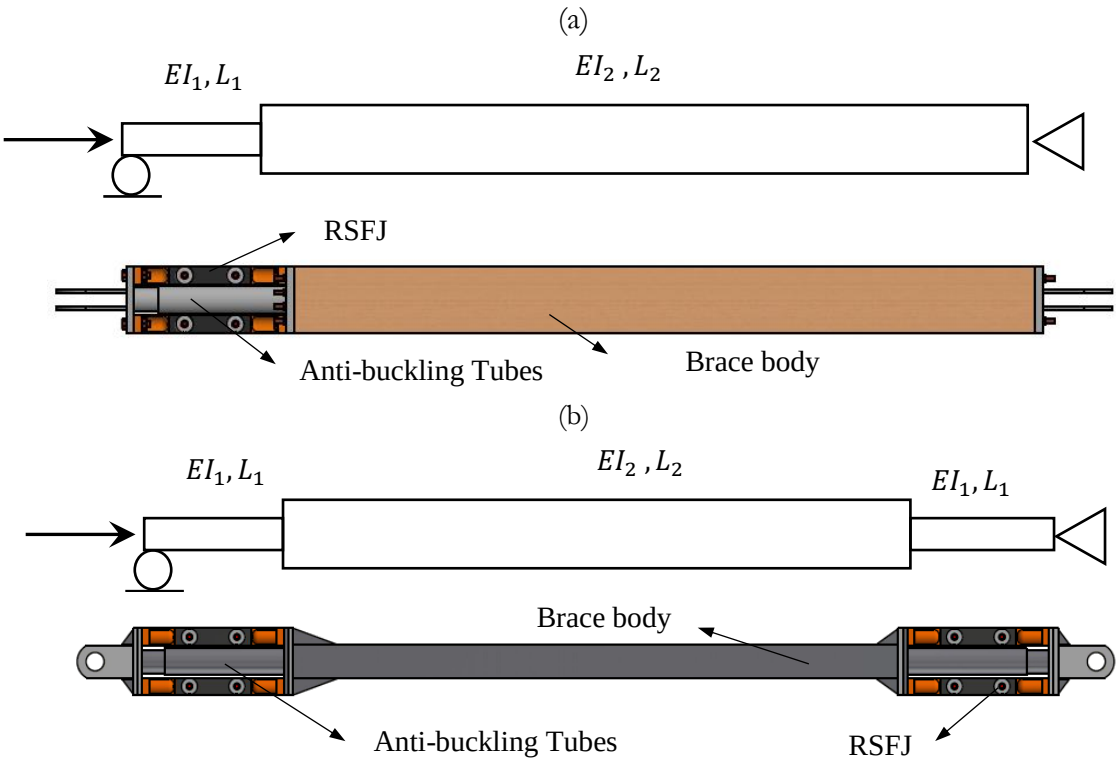

Figure 1.20: Stepped Column Analogy: (a) Column with one stepped section [125] and (b) column with two stepped sections – section 2.14 [126]

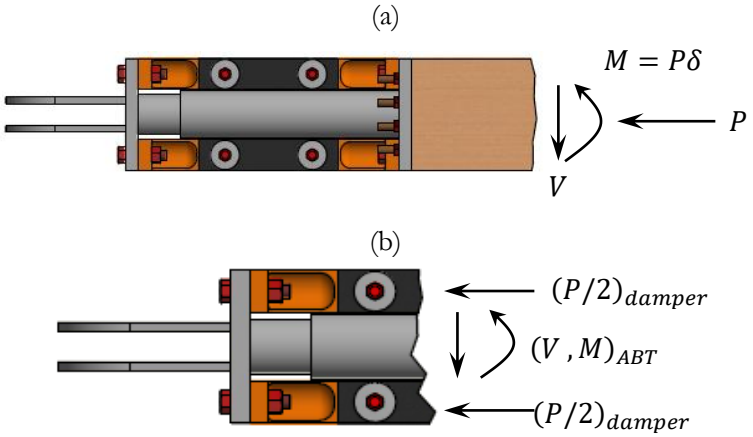

Figure 1.21: Load distribution in brace: (a) internal force in the brace body and (b) decoupled internal force in the ABT and RSFJs

In order to solve the problem and quantify the inelastic buckling load, an approximate method has been suggested by Prof. Bazant [127] entitled "elastic perfectly plastic analysis", which is basically the second-order plastic analysis of structure (see chapter 8 [127]). This is method is generalized and used for the proposed system in chapter 5 (it is referred to as Simplified Collapse Mechanism Analysis). The basis of this method lies in intersecting two curves to spot the inelastic buckling capacity of the member. The first curve is the stiffness deterioration (shown with ascending blue dash-dot line in Figure 1.22) and the reason is that the tangent of the curve, which is the lateral stiffness of the system, is converging to zero as the lateral displacement increases. In other words, the axial load would asymptotically approach the Euler with the incremental increase in the displacement. The second curve is the strength deterioration (shown with the descending red dash-dot line in Figure 1.22). The reason for the title (as implied from Figure 1.22) is that the axial strength of the system would decline if the lateral displacement increases. This is, indeed, due to the combined action rule indicating that the member has a constant capacity against axial and moment combination. If any of them increases, the other must decrease so that their relative summation is kept constant. It is worth mentioning that both strength and stiffness curves are highly sensitive to the boundary conditions and degree of redundancy. This is further discussed in Appendix B – the last part for interested readers.

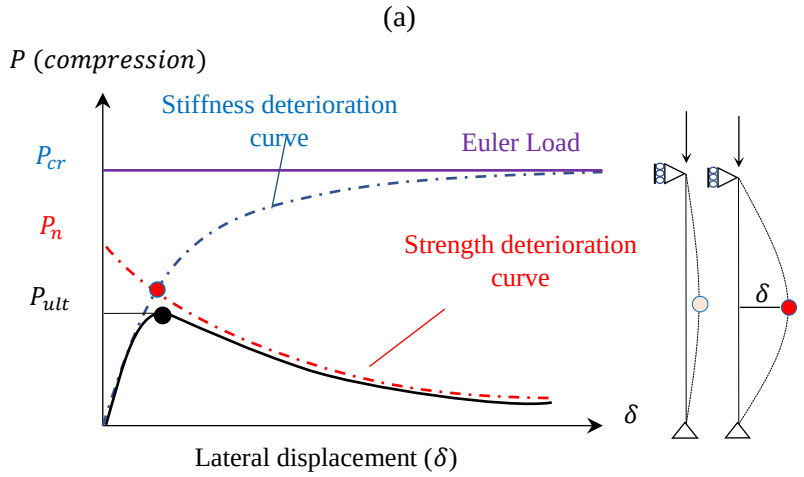

Figure 1.22: Performance of the column subjected to compression force [127]

This method has been successfully implemented to approximate the inelastic buckling capacity of such complex systems as BRBs. The problem observed [128-130] was that although the BRB, itself, is designed to yield in compression, it may fail prematurely if the gusset plates or neck does not have the required strength and stiffness (shown in Figure 1.23.b). Takeuchi et al [31] used the method of elastic perfectly plastic analysis to calculate the inelastic buckling capacity of the BRBs

system as a function of both stiffness and strength of the gusset plates and restrainer zone (Figure 1.23.a). In this regard, they further employed and developed the method to evaluate the BRB stability when it is used in Chevron configuration [32]. The difference with their previous study was that the rotational and of the collector beam was also brought into considerations (Figure 1.23.c). This method is discussed in greater detail in chapter 5 and Appendix B.

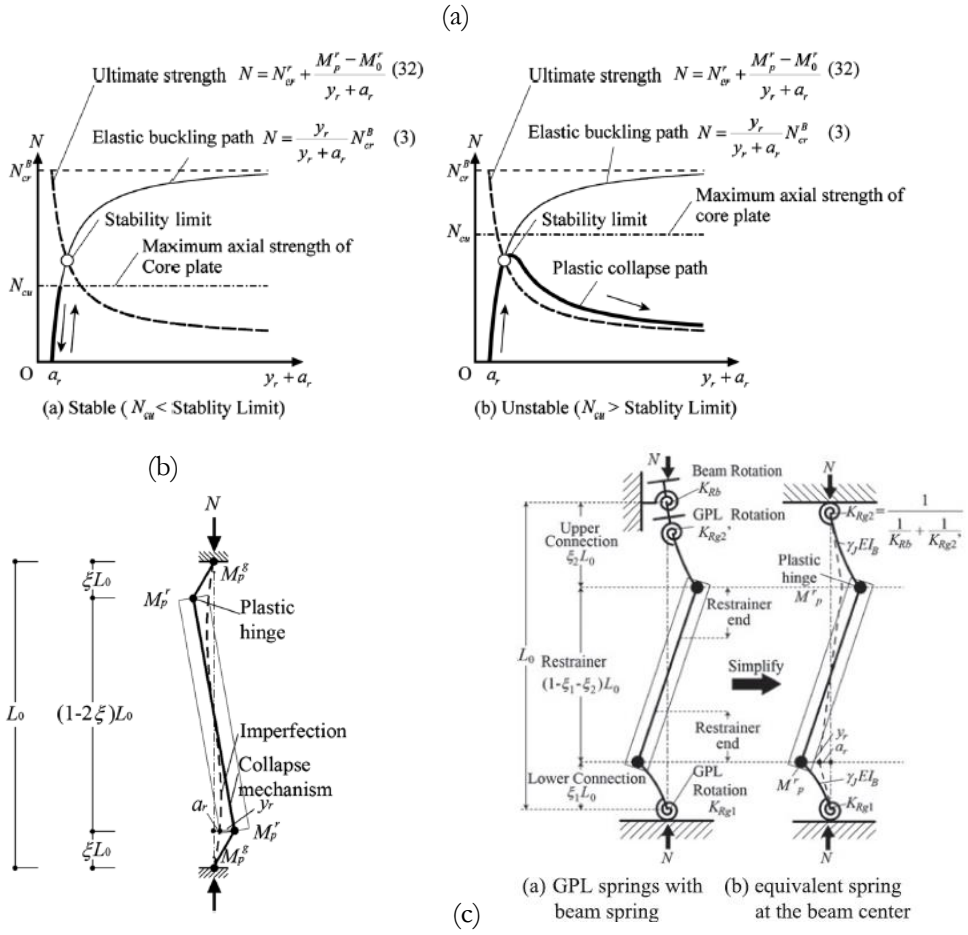

Figure 1.23: Application of elastic perfectly plastic analysis method on BRBs: (a) the convention of intersecting stiffness and strength curves and (b, c) deflected shape at collapse limit state of BRB in X- and Chevron application

1.5 Organisation of this dissertation

- Chapter 1 provides an introduction to the state-of-art practice of earthquake engineering in New Zealand and discusses why there is a need to increase the resiliency of the societies against earthquakes by means of new lateral load resisting systems (low-damage or damage-avoidance). Furthermore, the performance objectives that either a low-damage or damage-avoidance systems should possess or design engineers should take into

account were discussed. Finally, a review of previous research in the field of self-centring structures with more emphasis on the brace-type lateral load resisting systems is provided in this chapter.

- Chapter 2 provides a brief review on the development of the resilient slip friction joint (RSFJ) and more importantly describes the current challenges and concerns of adopting this damper for the tension-compression brace application. In this chapter, the experimental programs have been also outlined.
- Chapter 3 provides analytical and experimental studies on the buckling of the damper, itself, considering different boundary conditions and the axis of installation.
- Chapter 4 provides analytical and experimental studies on the elastic buckling of the RSFJ brace.
- Chapter 5 provides analytical and experimental studies on the inelastic buckling of the RSFJ brace.
- Chapter 6 provides a parametric finite element study to check the accuracy of the proposed analytical model for elastic and inelastic buckling in a range of different design parameters.
- Chapter 7 provides the final proposed framework for the design of the RSFJ braces considering its ultimate limit states in compression. Furthermore, this chapter gives two numerical examples that can be used by engineers and practitioners to grasp a deeper and better understanding of the design procedure.
- Chapter 8 provides a framework to analyse, improve and even retrofit the conventional timber braces using RSFJ damper. A numerical study was performed on a 4-storey prototype building to evaluate the seismic performance of the system.
- Chapter 9 describes a new type of self-centring behaviour by employing the elastic buckling as well as the conventional flag-shape, which will be referred to as "Zero Stiffness Flag-shape". Nonlinear time history analysis was also performed on a prototype building to further investigate the seismic performance of such a system.
- Chapter 10 summarises the findings of the study based on which the main research topics for future studies are recommended.

Finally, it should be noted that there will be some inevitable replications of information such as RSFJ description at the beginning of chapters 2, 3, 4, 8 and 9, which is due to the fact that this thesis is written in the paper-based format.

2 RSFJ as a Damper for Braced Frame Structures

2.1 Abstract:

This chapter gives an introduction to the performance of the RSFJ damper when subjected to different loading in different directions. In this manner, firstly, the performance of the damper will be discussed within its three degrees of freedom (axial, in-plane and out-of-plane rotation) and then its application will be evaluated in the brace-type lateral load resisting systems. Furthermore, the possible failure modes of the RSFJ-brace, as the main scope of the present research, will be qualitatively discussed in this chapter. It will be shown that there might be two possible failure types for the brace namely: (a) local buckling of the damper and (b) global buckling of the brace. In the first case, the damper will buckle independently from the brace; however, in the second case, the whole brace-damper assembly will buckle together. Based on these possible failure modes, the experimental program will be outlined at the end.

2.2 Introduction

Employment of friction dampers in the structures probably dates back to the early 1980s [131, 132] where they were used for steel braced frames and concrete panels by Pall. Later on, Popov et al. [133] and Clifton et al. [134] elevated the concept to be used in the braced frame and Moment Resisting Frames (MRFs), respectively. The first generation of the self-centring friction dampers (Called Ringfeder) was studied and tested by Nims et al. [135] and Filiatrault et al. [136] and then used in the building industry. As one of the more recent developments, a new friction-based damper was introduced in New Zealand [137], known as the Resilient slip friction joint (RSFJ). The RSFJ is a self-centring friction damper that dissipates the input energy through a passive damping and a slip-friction mechanism, applicable to different lateral load resisting systems. Having the self-centring characteristic will contribute to minimizing the post-event maintenance and downtime of the structures after a major seismic event. This chapter mainly deals with the introduction of the RSFJ damper and illustrates its performance subject to different loading procedures. As shown in Figure 2.1, the RSFJ damper is composed of two types of grooved steel

plates namely: outer ones (cap plates) and intermediate ones (slotted or middle plates). These plates are clamped together using high strength rods (or bolts) and prestressed disc springs.

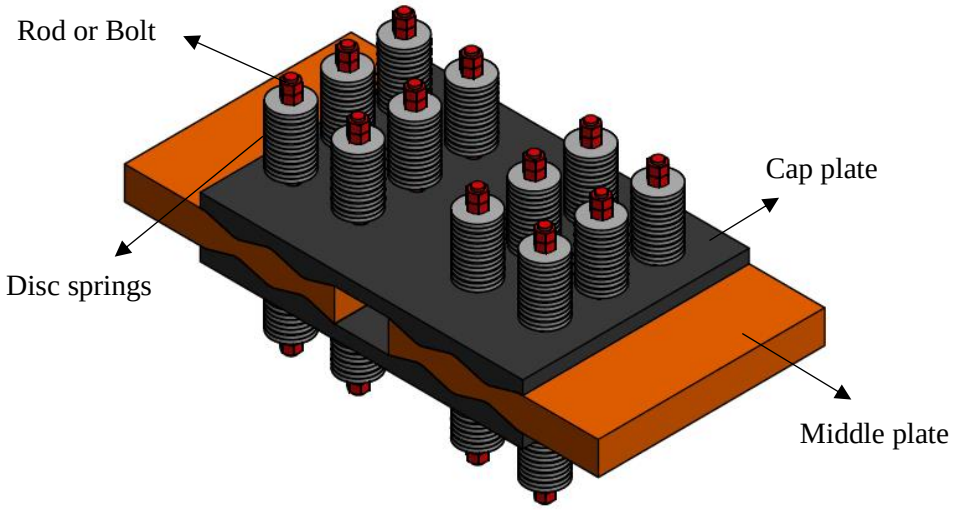

Figure 2.1: RSFJ assembly and its components

2.3 Expected performance

RSFJ damper has six degrees of freedom in total but only three main ones (shown in Figure 2.2) namely: axial, rotation in in-plane (rotation is in-plane of the middle and cap plates) and out-of-plane (rotation is in a plane perpendicular to the in-plane) is studied in this thesis. The performance of the damper considering other degrees of freedom was out of the scope of this study and requires further investigation. In this section, the performance of the damper with respect to each of those three degrees of freedom will be discussed assuming that there is no interaction among them, yet it should be mentioned that the interaction between the axial and rotation degree of freedom will be discussed more in detail in chapter 3.

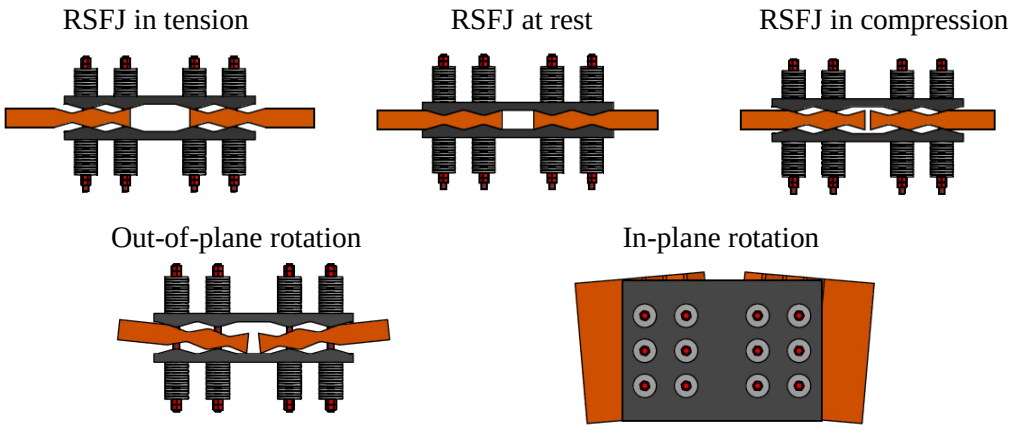

Figure 2.2: Different degrees of freedom for RSFJ damper

2.3.1. *Pure Axial performance*

The centre slotted plates (middle plates) start to slip once the applied axial force overcomes the frictional resistance between the surfaces, which, itself, is coming from the prestressing force in the disc springs. More prestressing of the springs means more frictional resistance and higher slip or activation load. When the pre-stressing is overcome, the cap (outer) plates are pushed to the sides due to the geometry of the grooves. Consequently, this causes more compression in the disc springs. Once unloading starts, the stored elastic energy in the compressed disc springs tends to be released and pushes the cap plates back to their initial position. The reversed-slip will not occur until the frictional resistance is overcome (reversed-slip point in Figure 2.3). The unloading stops when the energy in the disc springs cannot overcome the friction.

The flag-shape performance of RSFJ is depicted in Figure 2.3. In this diagram, the slip force (F_{slip}) is indicative of the force that the damper will start to move. After the slip point, the RSFJ can expand until the disc springs are fully flat. At this point, the axial force is at its maximum and is referred to as the ultimate load ($F_{max,loading}$). Once the unloading begins, the RSFJ does not slip until the frictional resistance is overcome. At this point, the second (reversed) slip point takes place which is known as the restoring point ($F_{max,unloading}$). The point at which the joint will stop moving (shown in Figure 2.3) is referred to as the residual force (F_{res}).

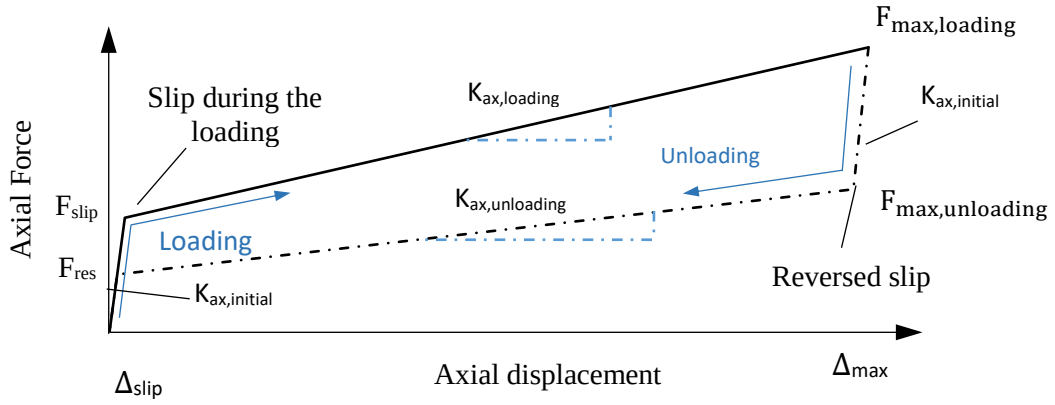

Figure 2.3: Axial performance of RSFJ

The slip (activation) force of the RSFJ (slip force) is given in Eq.22.1 [138]:

$$F_{slip} = 2n_b F_{pr}\left(\frac{sin\theta_g + \mu cos\theta_g}{cos\theta_g - \mu sin\theta_g}\right) \quad 2.1$$

where the angle of grooves is denoted by θ_g; the coefficient of friction is μ. the pre-stressing force is indicated by F_{pr}, and the number of bolts on each splice is shown by n_b (for instance, in Figure 2.1, n_b= 6). Likewise, if the friction acts in the opposite direction, the residual force is determined by:

$$F_{res} = 2n_b F_{pr}\left(\frac{sin\theta_g - \mu cos\theta_g}{cos\theta_g + \mu sin\theta_g}\right) \quad 2.2$$

The ultimate and restoring forces can be determined if F_{pr} is replaced by F_u in F_{slip} and F_{res} equations.

The ultimate axial displacement that the RSFJ can experience during the slip can be calculated from the remaining deflection of the prestressed disk springs to get fully flattened:

$$\Delta_{max} = 2n_d \frac{\Delta_{s,max}}{tan(\theta_g)}(1-\gamma) \quad 2.3$$

where $\Delta_{s,max}$ is the listed deflection of a disk spring, the parameter n_d is the number of disc springs in a stack per each side of the bolt and the parameter $\gamma = \frac{F_{pr}}{F_u}$ is indicative of the pre-stressing ratio.

For a target axial displacement "$\Delta \leq \Delta_{max}$", the characteristic points of flag-shape performance in loading and unloading phases can be calculated using Eq.2.4 and Eq.2.5, respectively:

$$F_{loading} = 2n_b\left(F_{pr} + \frac{k_{st}.\Delta.tan\theta_g}{2}\right)\left(\frac{sin\theta_g + \mu cos\theta_g}{cos\theta_g - \mu sin\theta_g}\right) \quad 2.4$$

$$F_{unloading} = 2n_b\left(F_{pr} + \frac{k_{st}.\Delta.tan\theta_g}{2}\right)\left(\frac{sin\theta_g - \mu cos\theta_g}{cos\theta_g + \mu sin\theta_g}\right) \quad 2.5$$

The post-slip tangent stiffness of the flag-shape hysteresis (in loading) can be calculated by Eq.22.6:

$$K_{ax,loading} = \frac{F_{ult} - F_{slip}}{\Delta_{ult} - \Delta_{slip}} \quad 2.6$$

By re-arranging Eq.2.6, the axial stiffness of the joint after-slip is:

$$K_{ax,loading} = \frac{2n_b(1-\gamma)F_u tan\theta_g\left(\frac{sin\theta_g + \mu cos\theta_g}{cos\theta_g - \mu sin\theta_g}\right)}{2n_d(1-\gamma)\Delta_{s,max}\left(1 - \frac{tan\theta_g \Delta_{slip}}{2n_d(1-\gamma)\Delta_{s,max}}\right)} \quad 2.7$$

Eq.2.7 reduces to Eq.2.8 assuming that $1 - tan\theta_g \Delta_{slip} / \left(2n_a(1-\gamma)\Delta_{s,max}\right) \approx 1$:

$$K_{ax,loading} = n_b K_{st} tan\theta_g \left(\frac{sin\theta_g + \mu cos\theta_g}{cos\theta_g - \mu sin\theta_g}\right) \quad 2.8$$

where K_{st} is the equivalent stiffness for the stack of springs per each side of the bolt (equal to K_d/n_d where K_d is stiffness of a disc spring). A similar procedure can be followed for the unloading phase with the friction force in the opposite direction, which results in:

$$K_{ax,unloading} = n_b K_{st} tan\theta_g \left(\frac{sin\theta_g - \mu cos\theta_g}{cos\theta_g + \mu sin\theta_g}\right) \quad 2.9$$

As can be inferred from Eq.2.8 and Eq.2.9, the after-slip axial stiffness of the RSFJ depends only on the geometry of the damper and the stiffness of the discs.

2.3.2. *Pure Rotational performance*

2.3.2.1. In-plane

The RSFJ damper has also a flag-shape response if it is subjected to an in-plane rotation (Figure 2.4). If an arbitrary in-plane rotation θ_{in} is applied on both ends of the RSFJ in a way that the pre-stressing force of the disc springs is overcome, the disc springs will be further compacted as the cap plates tend to further compress them. The resultant vertical displacement of the disc springs due to the in-plane rotation can be determined by Eq.2.10, with respect to Figure 2.5. In Eq.2.10 and Eq.2.11, it is assumed that the centre of rotation is placed at the centre of the bolts given they are stiff.

$$\Delta_h = \frac{b}{2}\theta_{in} \quad 2.10$$

$$\Delta_v = \frac{b}{2}\theta_{in} tan(\theta_g) \quad 2.11$$

in which the width of the damper is denoted by *b*. During the in-plane rotation, the disc springs will be more compacted as the grooves will climb on top of each other (as shown in Figure 2.5). Therefore, the reaction forces in the stacks of springs also increase due to this vertical displacement (Eq.2.11) and will be added up to the pre-stressing forces.

The increased force in the springs due to the in-plane rotation can be determined as:

$$F'_{pr} = F_{pr} + K_{st}.\Delta_v \qquad 2.12$$

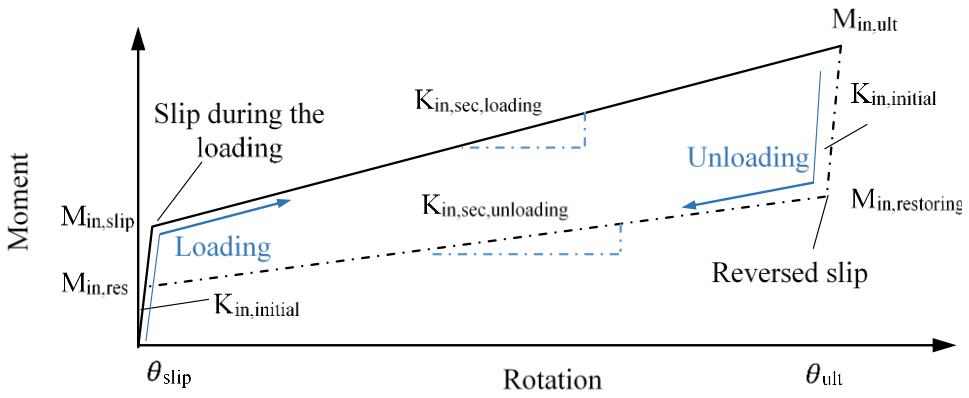

Figure 2.4: In-plane performance of the RSFJ

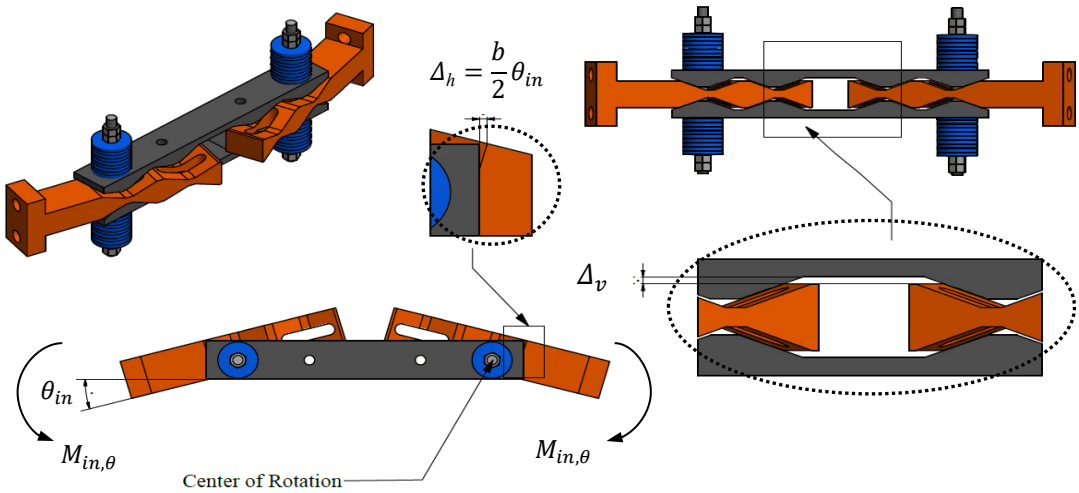

Figure 2.5: Deformation compatibility in case of the in-plane rotation

The rotation can continue until the disc springs become fully flattened. In the diagram shown in Figure 2.5, the slip moment ($M_{in,slip}$) is indicative of the force at which the joint will start to rotate. The maximum in-plane moment is denoted by $M_{in,ult}$. Once the unloading begins, the RSFJ does not slip until the frictional resistance is overcome. This point is, in fact, the second (reversed) slip point taking place when the joint is unloading in rotation, which will be referred to as the restoring moment ($M_{in,restoring}$). From this point onward, the joint slips rotationally to release the energy absorbed in the disc springs. The slip will continue till a point that the restoring force is not high enough to overcome the friction. At this point, the joint will stop rotating. This is shown in Figure 2.4 and will be referred to as the residual moment ($M_{in,res}$). The slip moment of the RSFJ can be calculated as:

$$M_{in,slip} = n_b F_{pr} b \frac{(sin\theta_g + \mu cos\theta_g)}{(cos\theta_g - \mu sin\theta_g)} \quad 2.13$$

The residual in-plane moment ($M_{in,res}$) is determined when the direction of the friction force is reversed:

$$M_{in,res} = n_b F_{pr} b \frac{(sin\theta_g + \mu cos\theta_g)}{(cos\theta_g - \mu sin\theta_g)} \quad 2.14$$

The ultimate and restoring moments can be determined if F_{pr} is replaced by F_u in $M_{in,slip}$ and $M_{in,res}$ equations. The post-slip tangent stiffness of the flag-shape related to the loading phase (secondary rotational stiffness of the loading) will be:

$$K_{in,sec,loading} = \frac{M_{in,ult} - M_{in,slip}}{2\theta_{ult}} = \frac{K_{st}.n_b.b^2}{2} tan\theta_g \frac{(sin\theta_g + \mu\, cos\theta_g)}{(cos\theta_g - \mu sin\theta_g)} \quad 2.15$$

By further simplifying Eq. 2.15 with respect to Eq. 2.8:

$$K_{in,sec,loading} = \frac{b^2}{2} K_{ax,loading} \quad 2.16$$

Eq.2.16 expresses the relation between the axial and rotational post-slip stiffnesses of the RSFJ. Similarly, the secondary rotational stiffness in the unloading phase can be determined as:

$$K_{in,sec,unloading} = \frac{M_{in,restoring} - M_{res}}{2\theta_{ult}} = \frac{K_{st}.b^2}{2} tan\theta_g \frac{(sin\theta_g - \mu cos\theta_g)}{(cos\theta_g + \mu sin\theta_g)} \quad 2.17$$

Or alternatively as a function of post-slip axial stiffness (with respect to Eq. 2.9):

$$K_{in,sec,unloading} = \frac{b^2}{2} K_{ax,unloading} \quad 2.18$$

As inferred from Eq.2.15 and Eq.2.17, the after-slip rotational stiffness of the RSFJ depends only on the geometry of the damper and the stiffness of the discs.

2.3.2.2. Out - of - plane

The same procedure can be followed for the out-of-plane performance of the RSFJ. If the damper is subjected to an out-of-plane rotation, the vertical movement of the cap plate due to the deformation compatibility (Figure 2.6) can be derived as:

$$\Delta_v = \frac{(l_e + t_{max}\, tan\theta_g)\theta_{out}}{2} \quad 2.19$$

This can be divided into two terms. The first and the larger portion of the vertical displacement is due to the lever arm L_e, the length of the area that the middle plate and cap plate are in contact with when the joint is at rest (Figure 2.6). The second and smaller portion of the vertical displacement is due to the thickness of the middle plate (the thickest part as it is in contact with the two side cap plates). The resultant force in the disc spring due to the vertical displacement of the cap plates and in the presence of an initial prestressing will be the summation of the prestressing force and the incremental increase in the force due to vertical displacement:

$$F'_{pr} = F_{pr} + \frac{K_{st}(l_e + t_{max}\, tan\theta_g)\theta_{out}}{2} \quad 2.20$$

By satisfying the equilibrium of the free body diagram of the cap and middle plates with the recognized forces in the disc springs, the characteristic point of the flag-shape performance will be determined:

$$(M_{slip})_{out} = n_b F_{pr} t_{max}\left(\frac{sin\theta_g + \mu cos\theta_g}{cos\theta_g - \mu sin\theta_g}\right) + n_b F_{pr} l_e \quad 2.21$$

$$(M_{res})_{out} = n_b F_{pr} t_{max}\left(\frac{sin\theta_g - \mu cos\theta_g}{cos\theta_g + \mu sin\theta_g}\right) + n_b F_{pr} l_e \quad 2.22$$

The ultimate and restoring moments can be determined if the F_{pr} is replaced by the F_u in the M_{slip} and M_{res} equations.

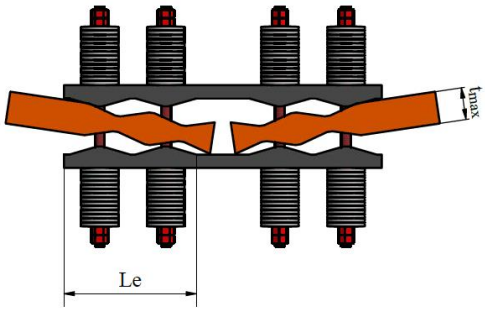

Figure 2.6: Deformation compatibility in case of the out-of-plane rotation

The ultimate out-of-plane rotation that the RSFJ can experience during the slip can be calculated from the remaining deflection of the prestressed disk springs to get fully flattened (re-arranging Eq.2.20):

$$\theta_{out,ult} = 2\left[\frac{F_u - F_{pr}}{K_{st}\left(l_e + t_{max}tan\theta_g\right)}\right] \quad 2.23$$

The after-slip rotational stiffness of the RSFJ can be calculated as below:

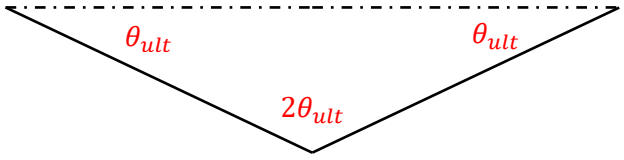

Figure 2.7: Idealized deformed shape of the RSFJ

$$K_{out,sec,loading} = \frac{M_{out,ult} - M_{out,slip}}{2\theta_{ult}} = \frac{n_b K_{st}\left(l_e + t_{max}tan\theta_g\right)}{4}\left[t_{max}\left(\frac{sin\theta_g + \mu cos\theta_g}{cos\theta_g - \mu cos\theta_g}\right) + l_e\right] \quad 2.24$$

$$K_{out,sec,unloading} = \frac{M_{out,restoring} - M_{out,res}}{2\theta_{ult}} = \frac{n_b K_{st}\left(l_e + t_{max}tan\theta_g\right)}{4}\left[t_{max}\left(\frac{sin\theta_g - \mu cos\theta_g}{cos\theta_g + \mu sin\theta_g}\right) + l_e\right] \quad 2.25$$

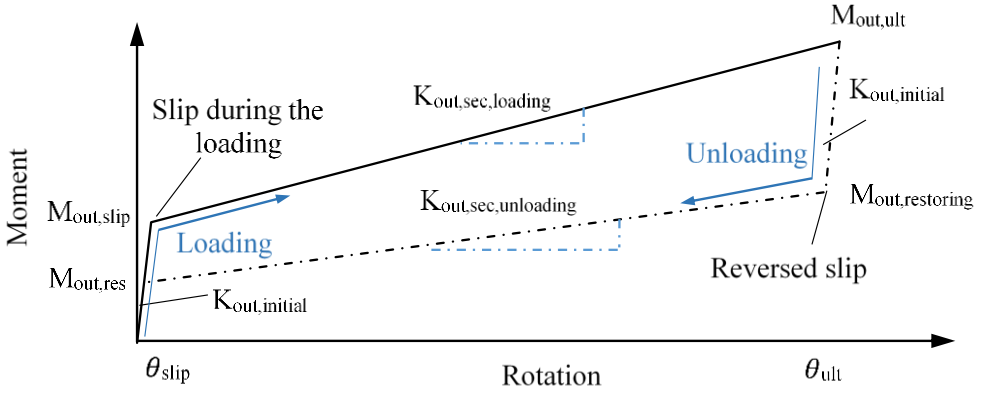

Figure 2.8: Out-of-plane performance of RSFJ

2.3.2.3. Finite Element Verification

The axial behaviour of the RSFJ has been experimentally verified within the previous studies [139], but the rotational performance either in in-plane or out-of-plane has not been tested. This section provides a numerical validation for the rotational performance of the RSFJ, which later in the next section will be used to analyse the interaction between the different degrees of freedom.

The RSFJ for the numerical study was composed of two middle and cap plates prestressed up to 10 kN using high-strength bolts, as shown in Figure 2.9. In order to validate the predicted analytical flag-shape for the in-plane and out-of-plane cases, three different numbers of disc springs (25, 15 and 11) were used where the stiffness and the flat load of a single disc were assumed to be 33.3 kN/mm and 30 kN, respectively. The study was performed within the ABAQUS software environment (V.2019) where the steel material was modelled using an eight-node linear three-dimensional solid element (C3D8R) with a modulus of elasticity of 200 GPa. In order to reduce the computational efforts, only half of the joint was modelled in the software while the proper constraints were employed to replicate the symmetry. The friction between middle and cap plates were modelled using surface-to-surface contact using tangential and normal behaviour with a coefficient of friction of 0.18 to resemble the reality. The disc springs were also modelled using the link element with the proper stiffness. For the purpose of analysis, two steps of loading were assumed. In the first step, the prestressing was applied using an equivalent distributed load while in the second step, the main loading protocol was applied.

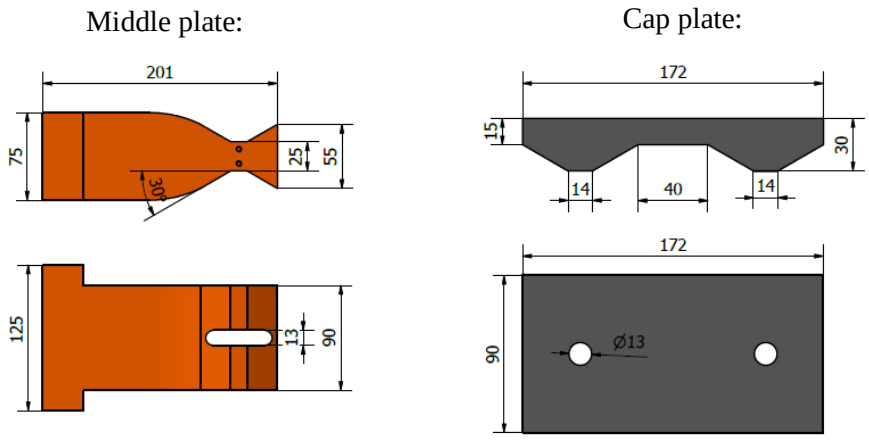

Figure 2.9: RSFJ dimensions for numerical study in ABAQUS

The moment-rotation diagram resulting from ABAQUS is illustrated in Figure 2.10 and Figure 2.11 for in-plane and out-of-plane cases, respectively. For the validation of the performance in ABAQUS, one cycle in one direction up to the intended rotation was considered to minimize the

computational effort. As can be seen, the analytical predictions are in good agreement with the numerical results.

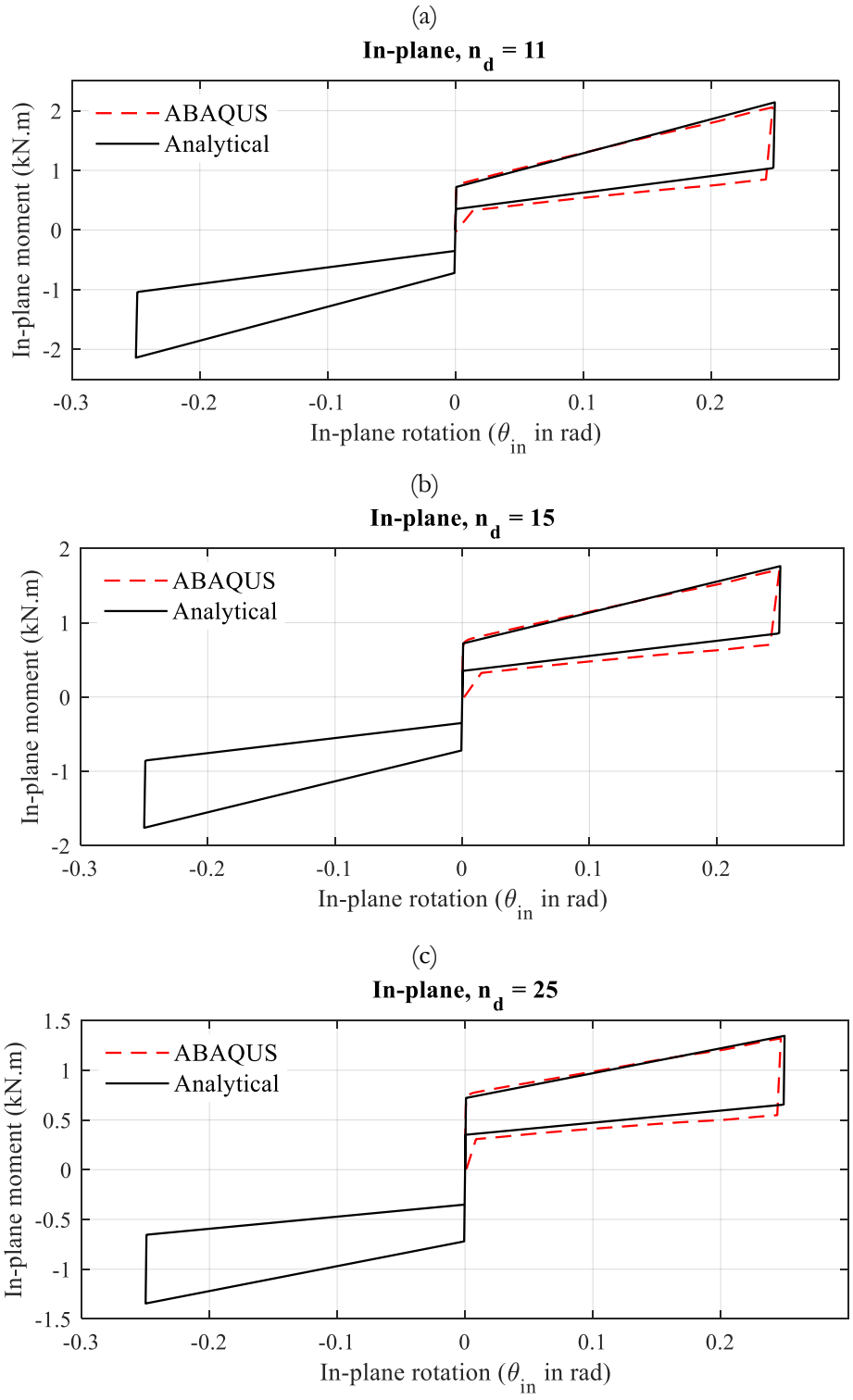

Figure 2.10: Analytical Vs Numerical performance of RSFJ in in-plane direction, (a) n_d = 11, (b) n_d = 15 and (c) n_d = 25

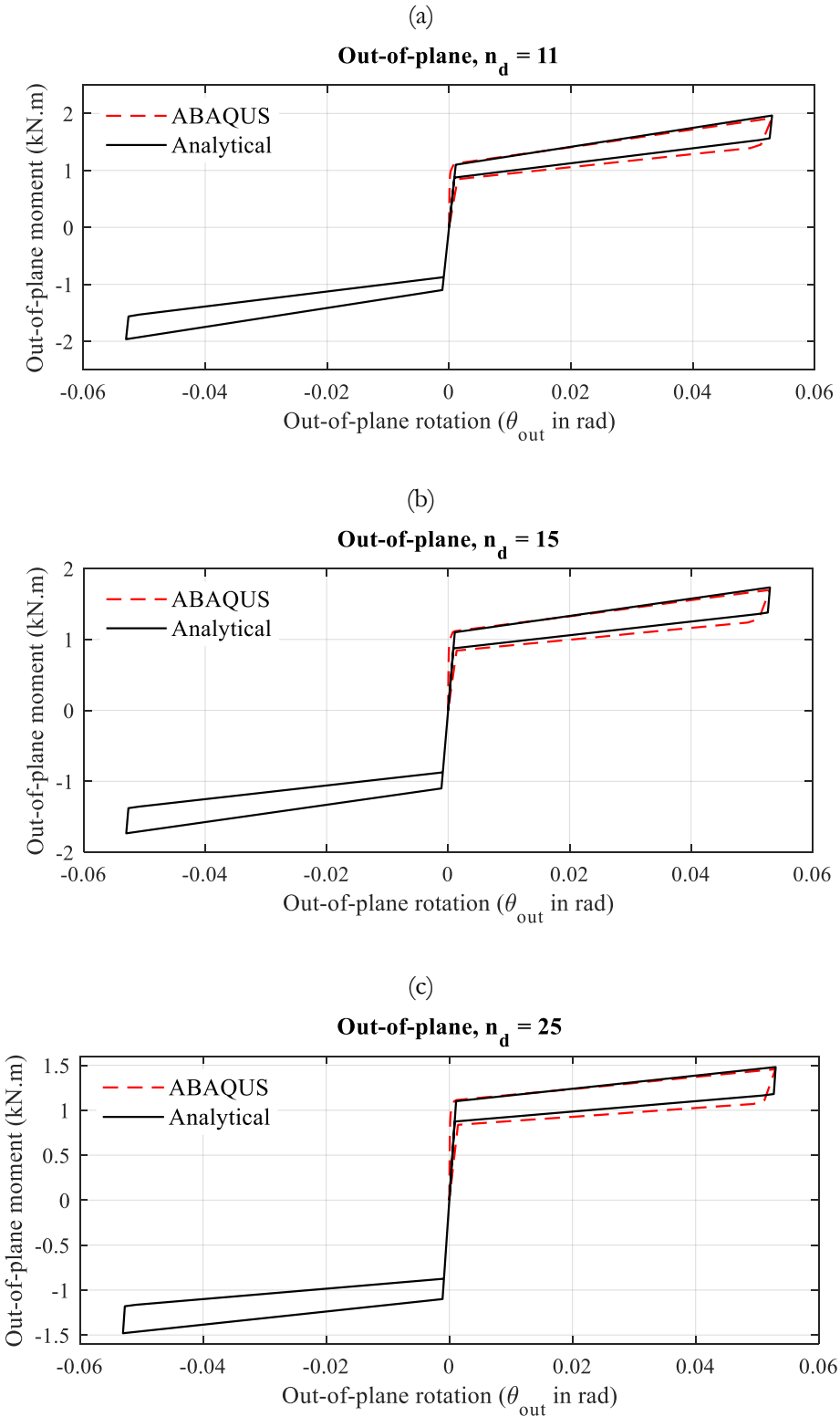

Figure 2.11: Analytical Vs Numerical performance of RSFJ in out-of-plane direction, (a) n_d = 11, (b) n_d = 15 and (c) n_d = 25

The other point to be discussed is the difference in the amount of damping for in-plane and out-of-plane rotation. As can be inferred from Figure 2.10 and Figure 2.11, the out-of-plane behaviour of the RSFJ does not provide as much damping as the in-plane case. The reason for this is rooted in Eq.2.24 and Eq.22.25. More specifically, the formulation for characteristic points of the out-of-plane flag-shape involves a part that does not involve any friction (the second part in parenthesis in Eq.2.24 and Eq.2.25). This part is constant in both the loading and unloading phase and attempts to cancel out the effect of the part with friction. For example, if the ratio of l_e/t_{max} is considerable, the amount of damping in the out-of-plane direction would tend to become zero.

2.4 Possible failure modes of the RSFJ-brace

As it was discussed in the previous section, the RSFJ damper has two rotational degrees of freedom in in-plane and out-of-plane directions, which can be viewed as rotational flexibility or an intermediate weakening for the brace. This intermediate weakening can trigger two possible failure modes for the brace. The first scenario is the damper buckling independent of the brace body (Figure 2.12.a). This failure is entitled as *local buckling* mainly because it is similar to the local buckling of the steel sections in which a portion of the member would buckle independently of the adjacent parts. The second scenario is the *global buckling* which can be of elastic or inelastic type. It should be also mentioned that both the global and local buckling should be evaluated during the design procedure in the in-plane and out-of-plane scenarios separately given that the RSFJ performance differs in each of those directions. In any cases of buckling, the performance of the brace may be interrupted and so needs to be avoided. In this regard, chapter 3 will discuss the local buckling of the damper with different boundary conditions while respecting the in-plane and out-of-plane conditions. An extensive experimental campaign is provided in this chapter to highlight the effectiveness of the analytical predictions. Chapter 4 will discuss the global elastic buckling of the RSFJ-brace when it is not strengthened with the ABT. A series of small- and full-scale experiments are also provided in this chapter to put more light on the elastic buckling and static performance of the brace. Chapter 5 will discuss the global inelastic buckling of the RSFJ-brace. In this chapter, three specimens are tested by which the dynamic performance and inelastic buckling of the brace are evaluated.

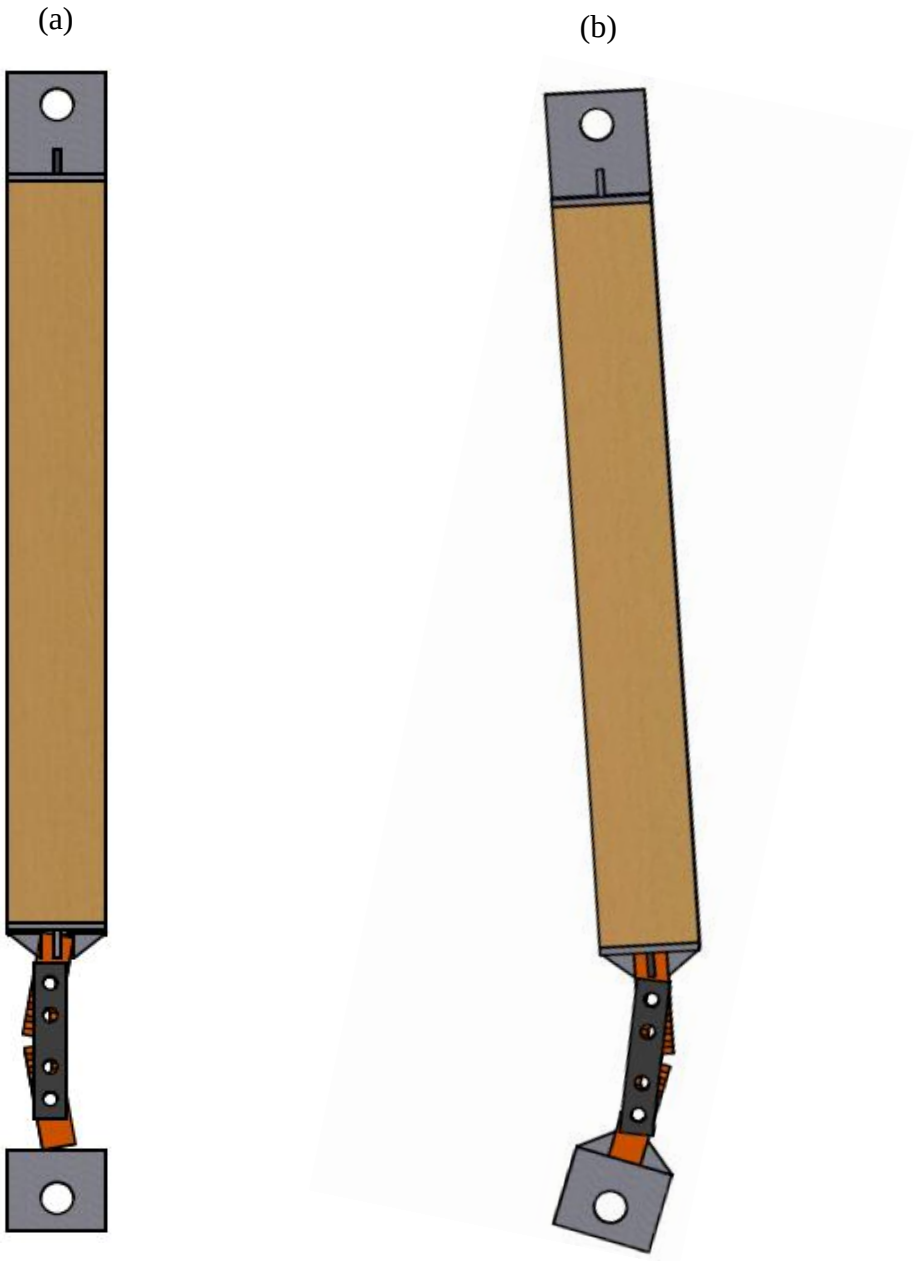

Figure 2.12: Possible failure modes of the RSFJ-brace, (a) Local (Damper) Buckling and (b) Global (brace) Buckling

3 Manuscript.1 - Local Buckling of the RSFJ Damper in In-plane and Out-of-plane Direction ($P-\Delta$ effect on the damper performance)

Based on the article published on 2021/10/1 by peer-reviewed "Journal of Structures", Volume 33, page 957-970

3.1 Abstract

At the end of the previous chapter, it was indicated that there are two possible instability modes (local and global) associated with the RSFJ brace when it is subjected to compression. As mentioned, one of them was the local instability of the damper, itself. This chapter provides an in-depth study of the damper instability and its degraded performance due to second-order effects (SOE) or $P-\Delta$.

The Resilient Slip Friction Joint (RSFJ) is a relatively new friction damper developed and introduced in New Zealand. It is used in structures to dissipate the earthquake energy with the advantage of re-centring the structure back to its upright position. This chapter investigates the experimental behaviour of the RSFJ when it is subjected to second-order effect (SOE) both in the joint *in-plane* and *out-of-plane* cases. The main consequence of SOE is the reduction of the axial force capacity and stiffness of the damper in compression. From the design perspective, it is ideal if the damper is only loaded axially with no bending transfer at the supports. As such, in some applications, a pin-pin support condition would be required to release the deformation compatibility requirements between the damper and the structure. The experimental investigation has shown that the impact of SOE on the RSFJ with the pin-pin end condition is more critical on the joint in-plane direction as compared to the out-of-plane. Furthermore, the analytical expressions are developed to account for the SOE, validated by the experimental results. Also, some recommendations are provided to limit the adverse effects of second-order actions on the RSFJ performance.

3.2 Introduction and background

The second-order effect (SOE) – or normally referred to as $P-\Delta$ effect – is normally referred to those additional actions appearing as a result of the geometrical nonlinearity when the system of interest is in equilibrium under the deformed shape. As a result of SOE, the lateral stiffness of

the system will reduce due to flexural deformation. This phenomenon is usually ignored in the first-order linear elastic analysis of structures, yet its effect is considered as an amplification factor for the first order actions as per building codes [140]. The structure of interest can be either an element such as a brace, column or a sacrificial seismic fuse (in this study) or the entire structure. In both cases, if the structure is not properly designed for the additional actions and deformations, the performance of the system may be disrupted or in an extreme case, the system may become unstable. The SOE, normally referred to as the P-delta effect (*P*-Δ) in the literature, adversely affects both the initial elastic and post-elastic stiffnesses of the system (Figure 3.1.a); however, it has a more significant impact on the post-elastic stiffness of the system as it is much lower than the initial one [140-143].

At the structural level, flexible structures such as Moment Resisting Frames (MRFs) are more prone to the *P*-Δ effects as they will exhibit more lateral displacement contributing to amplification of the SOE due to the gravity force. In some cases, this effect may induce a negative post-yield tangent stiffness, which itself may increase the potential side-way collapse of the structures due to ratcheting [142, 144]. A numerical study by MacRae [141] on the bilinear single-degree-of-freedom system, showed that the *P*-Δ effects can contribute to increasing of the fundamental period and more importantly, the possibility of cumulative inelastic deformation in a single direction, which is indicative of a large residual displacement or sideway collapse. The out-of-plumpness, initial imperfections and erection errors can even worsen the *P*-Δ effect and make the structure more sensitive to second-order actions [57, 145]. Rad and colleagues [57] studied the seismic performance of the steel buildings with initial out-of-straightness with bilinear elasto-plastic hysteresis behaviour. In this regard, they studied the effect of out-of-straightness on the seismic response. Their study revealed that: (i) the residual drift is heavily sensitive to the initial out-of-straightness, and (ii) the higher "R" (response modification factor) the building is designed for, the more sensitive it is to the initial out-of-plumpness.

Likewise, at the element level, the SOE will affect the performance of the element and will be exacerbated by the initial imperfection or the out-of-plumpness [145]. A good illustration can be the bracing elements under compression that are supposed to resist the earthquake lateral loads in the structures. In Buckling-Restrained Braces (BRBs), for instance, if the gusset plates fail to provide the required stiffness, the whole brace-gusset assembly may buckle in a compressive force less than what the brace is designed for [31, 32, 146] due to SOE. In other words, the BRB will experience a premature failure due to the formation of a plastic mechanism though it was supposed to yield in compression. In this regard, a number of stiffness and strength requirements for the gusset plates have been proposed [31, 32, 146]. Another example can be Concentrically Braced Frames (CBFs) which are supposed to behave similarly to what is depicted in Figure 3.1.b.

Because of the SOE, the lateral displacement of the brace will increase as the axial force within the brace rises. In case of stocky brace members (red line in Figure 3.1.b), after a relatively small displacement and before the axial load hits the Euler load, a plastic hinge will form within the brace and the resisting force will diminish with a negative stiffness. In the case of slender braces (green line in Figure 3.1.b), the axial force may hit the Euler and then experience a plastic mechanism and becomes unstable. If the SOE was absent for these elements, the performance in compression could be the same as the tension. The SOE can be beneficial in some special cases if the design details are carefully taken into account. A new self-centring brace with a zero post-elastic tangent stiffness is developed and introduced by[54] where the SOE was employed to reduce the post-elastic stiffness. Another example can be found in [75] where Kibriya et al.2020 developed a rocking steel brace frame using a buckling-enabled brace made up of the glass-fibre reinforced polymer (GFRP) shells.

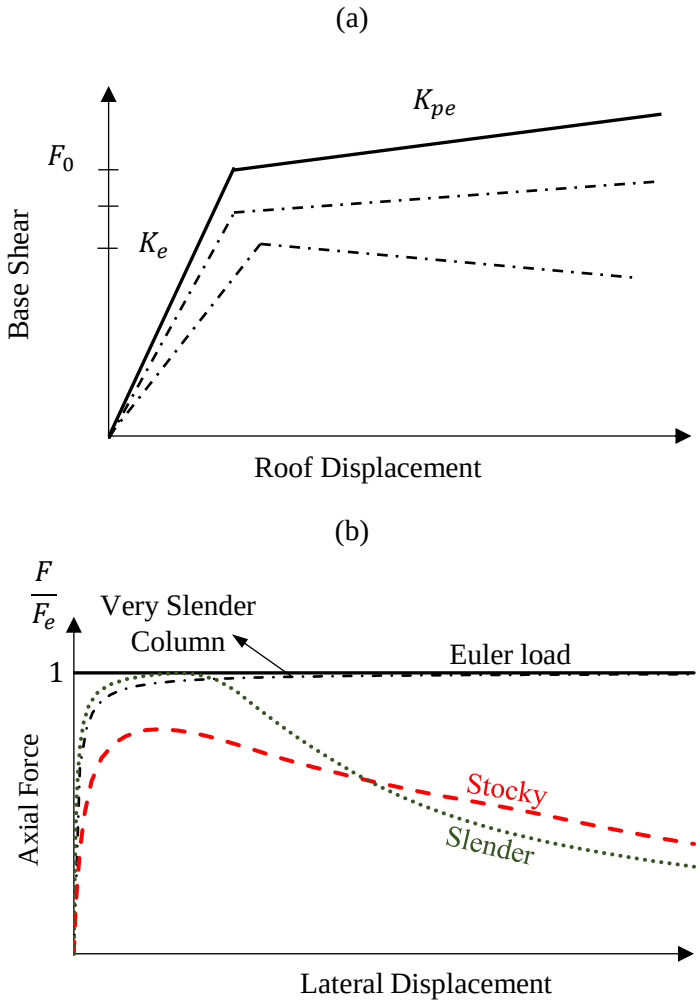

Figure 3.1: effect of P-Δ on: (a) Base shear Vs roof displacement and (b) behaviour of compressive members (very slender, slender and stocky member).

Employment of friction dampers in the structures probably dates back to the early 1980s [131, 132] where they were used for steel braced frames and concrete panels by Pall. Later on, Popov et al. [133] and Clifton et al. [134] elevated the concept to be used in the braced frame and Moment Resisting Frames (MRFs), respectively. Furthermore, Latour et al [147-151] studied the behaviour of semi-rigid connections using prestressed bolted and slotted connections.

The first generation of the self-centring friction dampers (Called Ringfeder) was studied and tested by Nims et al. [135] and Filiatrault et al. [136] and then used in the building industry. For more information regarding the friction dampers, readers are referred to [152-154]. The Resilient slip friction joint (RSFJ) is relatively a new self-centring friction damper that dissipates the input energy through a passive damping and a slip-friction mechanism [137], which can be applied in different lateral load resisting systems. Among several applications, it can be referred to the self-centring tension-compression braces [54, 98, 99, 155, 156], self-centring tension-only braces [157, 158], rocking timber or concrete shear walls [159, 160], rocking steel braced frames with shear links [161] and MRFs [162]. Figure 3.2 shows some of the real applications of RSFJ in the industry [163].

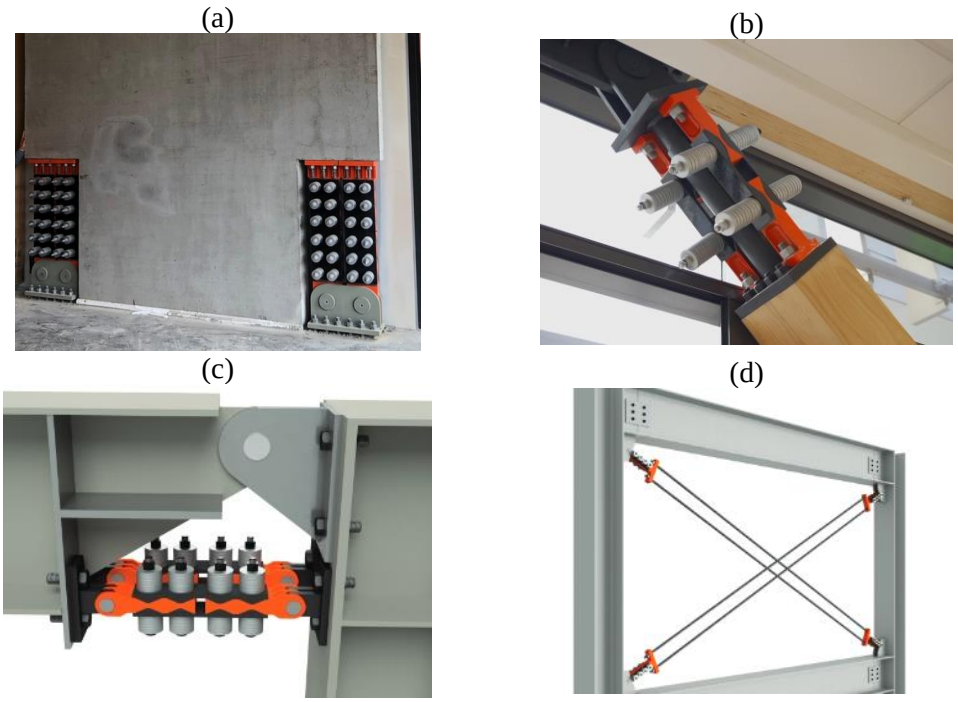

Figure 3.2: RSFJ damper installation in various structural systems [163] (a) Hold-down for Rocking Shear walls (pinned-fixed), (b) Self-centring brace (fixed-fixed), (c) Moment Resisting Frame (pin-pin) and (d) Tension-only Brace

The past experimental studies [157, 164] have shown that in those structural applications (such as tension-compression brace) where the RSFJ is supposed to experience a compressive force, there

is a possibility of buckling occurrence due to SOE. This results in reducing the compression capacity although it might be of elastic damage-free type. The fact is that the rotational flexibility of the RSFJ both in the *in-plane* and *out-of-plane* makes it more susceptible to SOE. Accordingly, the main focus of this paper is placed on the evaluation of the RSFJ performance in the presence of SOE. More importantly, the paper presents the critical conditions in which such SOE might appear as well as the measures that should be taken to either avoid it or design for it. For this purpose, several design parameters have been included in the study such as: (a) different end conditions (pin and fixed), (b) different prestressing force and (c) different number of disc springs. An extensive experimental program was conducted with over 70 tests. This paper also provides the analytical expressions to predict the second-order affected performance of the damper.

3.3 Damper performance in the presence of SOE (second-order effect)

The desired uninterrupted performance of the damper is the flag-shape type depicted in Figure 3.3.b which shows the performance of the damper when working only axially. This behaviour is developed through the geometrical nonlinearity of the RSFJ components in the form of a frictional sliding between a series of clamped grooved steel plates. When the disc springs are pre-compressed, a frictional resistance will be formed and therefore, a certain amount of force is required to activate the damper. This force is referred to as the slip force (F_{slip}) in Figure 3.3.b. The loading can continue to a target displacement until the disc springs get flat. When the unloading starts, the frictional force will act in the opposite direction, and the joint will not slip until the reversed slip force. After this point, the unloading phase with slippage continues until reaching the residual force where the slippage stops. The flag shape behaviour of the RSFJ with and without the prestressing force is shown in Figure 3.3.c and Figure 3.3.d [157]. For a target axial displacement "$\Delta \leq \Delta_{max}$", the performance points of the flag-shape hysteresis in loading and unloading phases, as a function of axial displacement, can be calculated using Eq.3.1 and Eq.3.2, respectively [98]. These values are bounded below and above by $\left(F_{slip}\ ,\ F_{max,loading}\right)$ for the loading part and by $\left(F_{res}\ ,\ F_{max,unloading}\right)$ for the unloading part:

$$F_{loading} = 2n_b\left(F_{pr} + \frac{k_{st}\Delta tan\theta_g}{2}\right)\left(\frac{sin\theta_g + \mu cos\theta_g}{cos\theta_g - \mu sin\theta_g}\right) \quad 3.1$$

$$F_{unloading} = 2n_b\left(F_{pr} + \frac{k_{st}\Delta tan\theta_g}{2}\right)\left(\frac{sin\theta_g - \mu cos\theta_g}{cos\theta_g + \mu sin\theta_g}\right) \quad 3.2$$

In Eq.3.1 and Eq.3.2, if the target axial displacement is equal to zero, the slip (F_{slip}) and residual forces (F_{res}) will be determined. Accordingly, by considering the maximum allowable displacement as an input, the maximum load in loading ($\mathrm{F_{max,loading}}$) and unloading ($F_{max,unloading}$) phases will be determined. In the aforementioned equations, the angle of grooves is represented by "θ_g"; the coefficient of friction is indicated by "μ", and the stiffness of stack of disc springs is denoted by "k_{st}". The parameter "n_b" indicates the number of bolts on each middle plate (Figure 3.1.a, $n_b = 2$), and "F_{pr}" represents the prestressing force in the disk springs. The maximum axial displacement (Δ_{max}) that a RSFJ can experience during the slip can be calculated from the remaining deflection of the pre-stressed disk springs before getting fully flattened and is formulated as:

$$\Delta_{max} = 2n_d \frac{\Delta_{s,max}}{tan\theta_g}(1-\gamma) \qquad 3.3$$

where "n_d" is the number of disk springs per side of a bolt and "$\Delta_{s,max}$" is the maximum deflection capacity of a single disk spring. The parameter "$\gamma = F_{pr}/F_{u,s}$" is indicative of prestressing percentage and "$F_{u,s}$" is the flat load of a disc spring.

This desired flag shape behaviour may deteriorate as a result of SOE and additional rotation that may occur for the damper. This is mainly due to the impaired contact between the middle and cap plates in the *in-plane* and *out-of-plane* and is always accompanied by a relative rotation between the middle plates and cap (Figure 3.3.e and Figure 3.3.f). The behaviour shown in Figure 3.3.c and Figure 3.3.d with the red lines is the deteriorated performance which has less axial force capacity in compression but involves considerable lateral movement (rotation) either in the *in-plane* (shown in Figure 3.3.f) or *out-of-plane* (shown in Figure 3.3.e). It is worth noting that the degradation of the flag-shape depends on several parameters including the end conditions (pin or fixed), the geometry of the plates, prestressing force, number of disc springs and angle of grooves. This will be more discussed in detail in the next sections. Once the damper is experiencing SOE, additional bending and shear actions will be induced, and if the middle and cap plates are not properly designed for these additional forces, they may yield and endanger the integrity of the structures.

3.1 Experimental program

For the evaluation of the damper performance in the presence of SOE, a RSFJ damper was designed and manufactured composed of mild steel plates with an elastic modulus of 200 GPa

and yield stress of 340 MPa. The middle plate of the RSFJ had a width of 90 mm at the thin part and 125 mm at the thick part. At its end part, two 25 mm holes were considered so that it can be either attached to the machine as a fixed end or bolted to another intermediate plate (pin end 1 or 2) to provide pin support. The angle of the grooves was considered to be 30 degrees. A slotted hole with 57 mm length was also considered in the middle plate so that enough room is provided for the axial travel of the damper. The cap plate of the RSFJ was 172 mm long and it had the same width as the middle plate. Two 13 mm holes were also considered to accommodate two 12 mm rods in the cap plates. Further information regarding the dimensions of the plates is provided in Figure 3.4.a. The assembly of the damper with different end conditions in the *in-plane* and *out-of-plane* is also illustrated in Figure 3.4.b. It should be noted that only the pin-pin and fixed-fixed end conditions are depicted in Figure 3.4.b, yet the pin-fixed condition could be also employed with a different arrangement of the end plates. As it is shown in Figure 3.4.b, the maximum possible axial travel of the RSFJ in compression is the lesser of the free distance between two middle plates (40 mm) and the remaining displacement capacity of the prestressed disc spring stack (Eq.3.3). The MTS Universal Testing Machine with 300 kN capacity was used to perform the tests.

Table 3.1: The testing program

Direction	Boundary Conditions	Specimens	Number of tests
In-plane	Pin – Pin	DPPI15/2.5, DPPI15/10, DPPI25/0, DPPI25/5	25
	Fixed – Fixed	DFFI25/0, DFFI25/14, DFFI48/12	3*
	Pin – Fixed	DFPI48/0	14*
	Pin – Pin (with additional plates for rotation restriction)	DPPI25/0	4**
Out-of-plane	Pin – Pin	DPPO48/0, DPPO56/2.5	25
	Fixed – Fixed	DFFO25/0, DFFO25/14, DFFO48/12	3*

* in these cases, SOE was restrained due to end condition.

** in this case, SOE was hindered by additional plates.

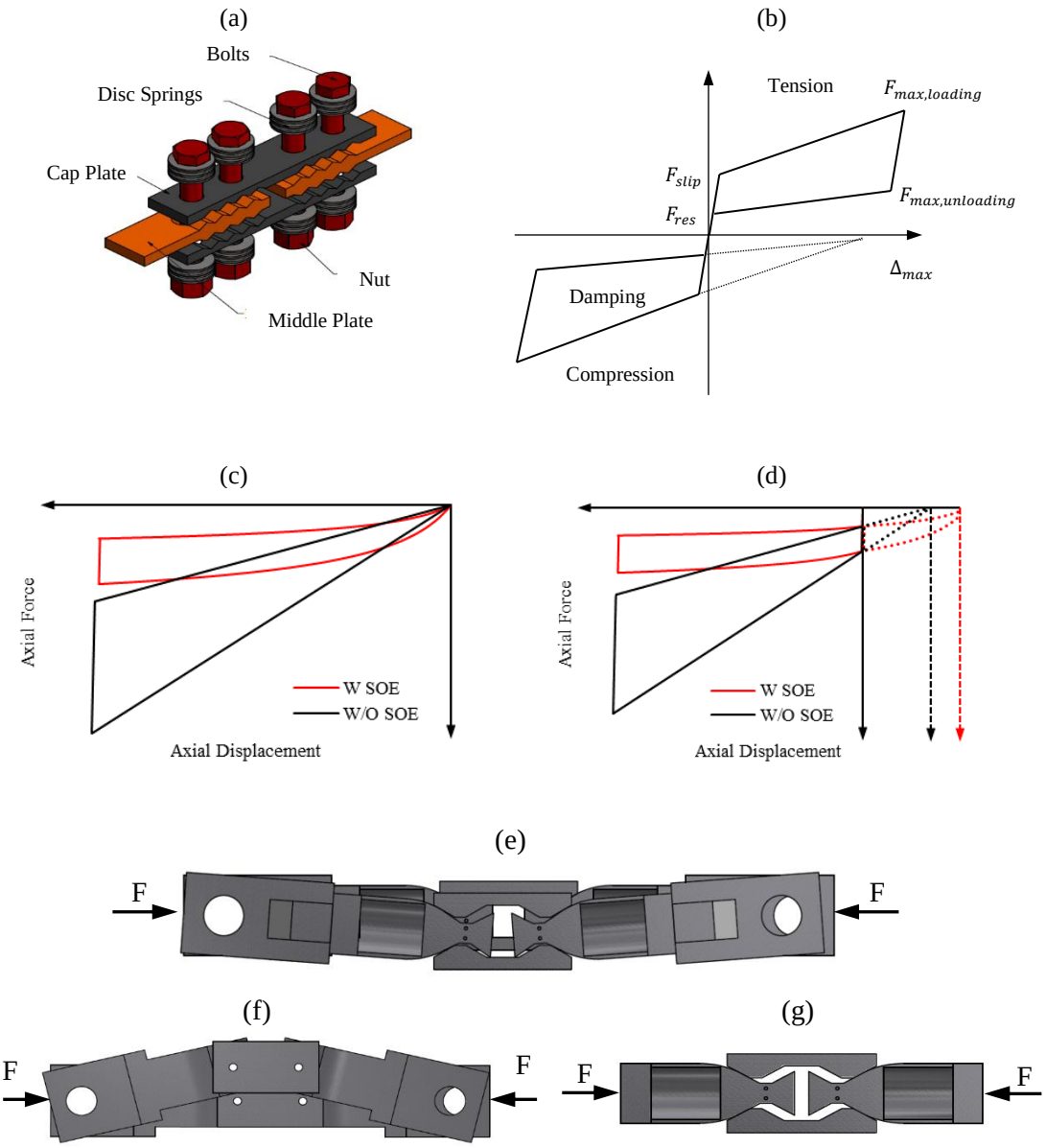

Figure 3.3: Sample RSFJ and its hysteresis performance: (a) assembly and components, (b) desired flag-shape with no SOE, (c) effect of SOE on performance without prestressing, (d) effect of SOE on performance with prestressing, (e) deformed shape in out-of-plane due to SOE, (f) deformed shape in in-plane due to SOE, (g) deformed shape in the absence of SOE

Table 3.1 summarizes the specimens that were considered in the program and are labelled by D (damper), FF, PP or FP (fixed-fixed, pin-pin or fixed-pin end condition), I or O (in-plane or out-of-plane), the number of discs per side of the rod (n_d) and the prestressing force (F_{pr}) expressed in kN. As it will be discussed in the following sections, a certain amount of imperfection was required to activate and capture the SOE. Therefore, for each configuration of the specimens, the testing was repeated with an increase in imperfection until the SOE was observed. In this regard,

the last column of Table 3.1 shows the total number of tests (including the repetitions) for each group of specimens with specific boundary conditions.

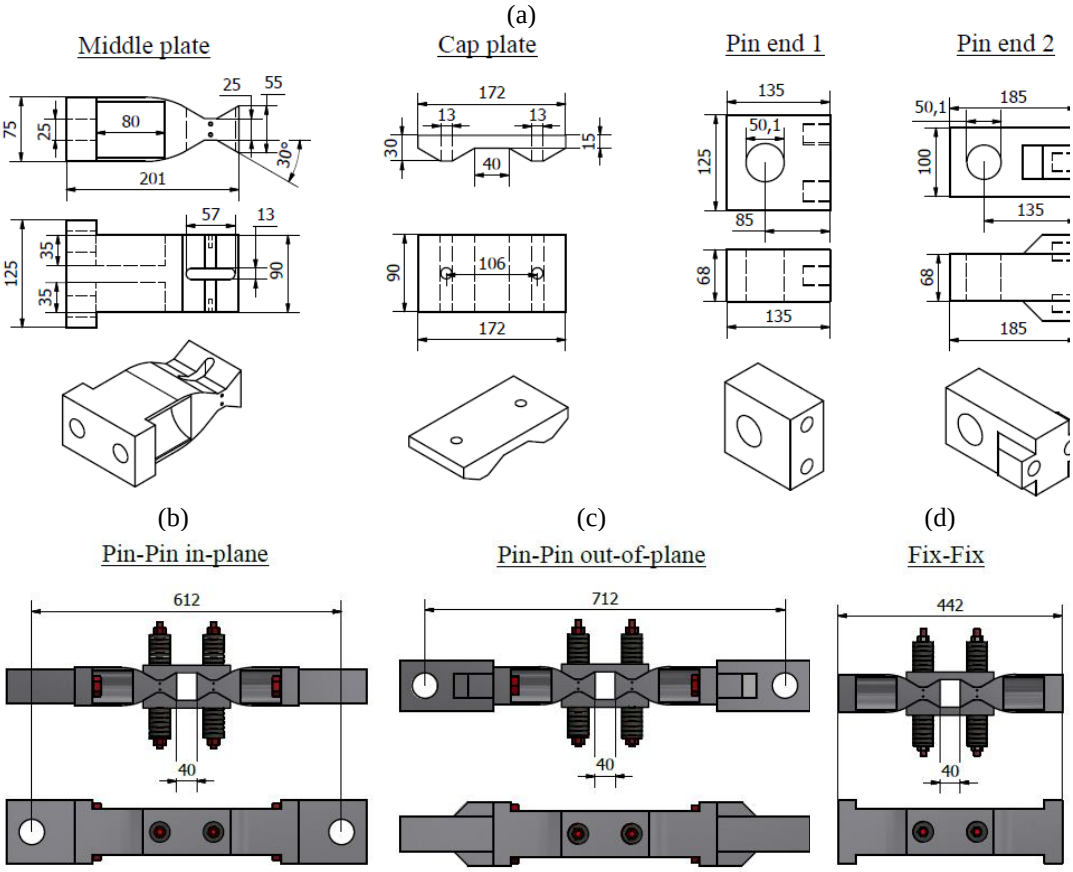

Figure 3.4: The RSFJ designed for testing: (a) middle and cap plates, (b) assembly with pin-pin end in in-plane, (c) assembly with pin-pin end in out-of-plane, (d) assembly with fixed – fixed end

3.1.1. *Experimental Test on disc spring*

As shown in Figure 3.5, the stiffness of the disc changes with the amount of prestressing force in the disc springs. Furthermore, it was shown that all the derived expressions are functions of the stiffness of the stack of the disc. Therefore, in order to accurately predict the response, the stiffness of the disc as a function of prestressing force is needed. Accordingly, this section is dedicated to the force-control cyclic tests on the stack of disc springs with a different number of discs and different prestressing forces. As shown in Figure 3.5.d, for safety reasons, a steel sleeve was used to embrace the stack and act as the support when the axial load was applied. Two stacks with 9 and 15 disc springs were used with zero, 5 kN, 10 kN and 15 kN prestressing forces. It should be also noted that the upper limit of the force was taken to be 20 kN as it was the flat load of a single disc.

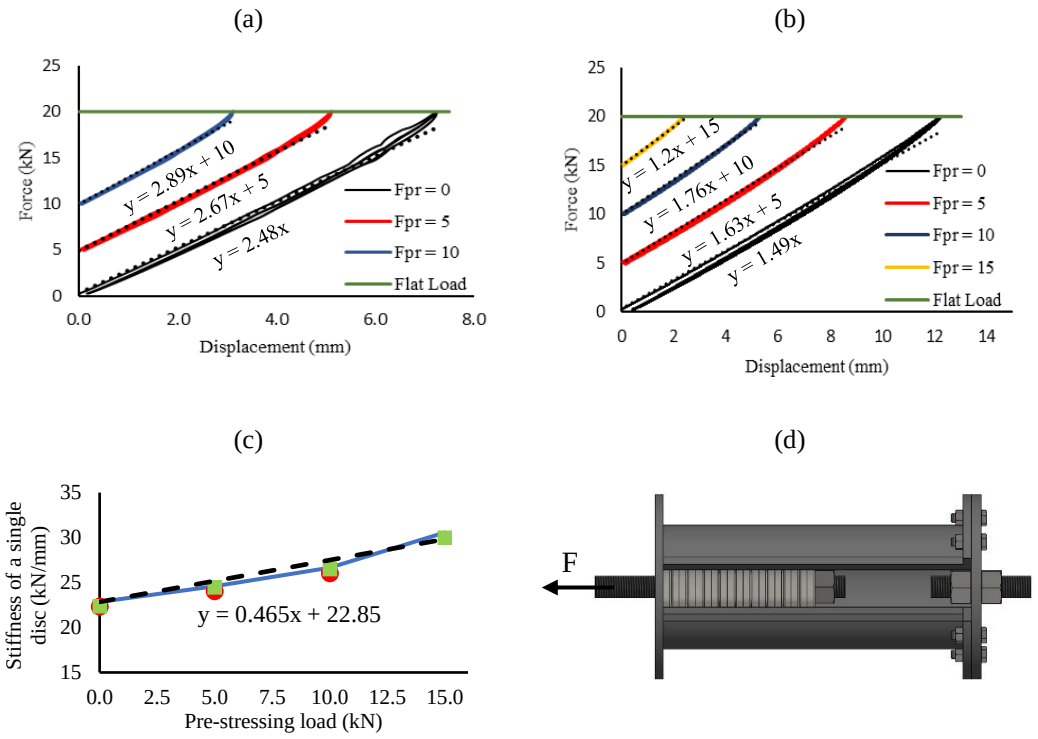

Figure 3.5: Force-control Experimental test on the stack of disc springs (a) stack with 9 discs, (b) stack with 15 discs, (c) stiffness of a single disc (d) set-up used for test

The experimental results of the testing are depicted in Figure 3.5.a and Figure 3.5.b for the stacks with 9 and 15 discs, respectively. The behaviour of the stack of discs could be idealized with a linear line in which the increasing of the prestressing force slightly raised the initial stiffness of 22.85 kN/mm (in the case of zero prestressing). After performing a regression analysis on the data, the stiffness of the single-disc was calculated as a function of prestressing load, as shown in Figure 3.5.c. By Eq.3.4, the stiffness of a stack of the disk can be determined as a function of prestressing force and the number of disc springs used. It should be noted that the following formulation is only applicable to the discs employed in this experimental program.

$$K_{st} = \frac{1}{n_d}\left(0.465F_{pr} + 22.85\right) \qquad 3.4$$

3.1.2. *Calibration of friction coefficient with reversed cyclic test*

The coefficient of friction (μ) is another important design parameter that should be properly quantified to predict the performance of the damper. Past studies [157] have shown that this parameter may differ in a range between 0.13 to 0.18. In this respect, a number of reversed cyclic tests were performed on the RSFJ joint with fixed-fixed end conditions so that the coefficient of friction can be quantified. It is worth noting that in this part of the program, the SOE was absent

mainly because the end conditions were fixed, and any rotation or lateral movement for middle plates were almost impossible assuming rigid motion for the plates. The test was also performed both in tension and compression with 5mm increments in the displacement amplitudes (i.e., 5mm, 10mm, 15mm, 20mm, etc.). The prestressing force was applied using a special hydraulic device (as shown in Figure 3.6) which had a loadcell at its end so that the amount of prestressing force in the disc springs can be tracked. Each stack of the disc was prestressed to the desired level of force and then the experiment was conducted up to the target displacement. Table 3.2 presents the specimens that were recruited for this part of the experimental program. According to the experimental test, the coefficient of friction was calibrated to be between 0.15 to 0.17 for the best fit of the analytical predictions to the experimental data with respect to Figure 3.7. The analytical predictions were calculated using Eq.3.1-Eq.3.3 using the target displacement reported in Table 3.2. The stiffness of the stack was also calculated using Eq.3.4.

Table 3.2: Details of RSFJ dampers for fixed-fixed end condition test

Specimen	F_{pr} (kN)	n_d	n_b	θ_g (degree)	K_{st} (kN/mm)	Δ_{max} (mm)
DFF25/0	0	25			0.914	40
DFF25/14	14	25	1	30	1.187	30
DFF48/12	12	48			0.587	35

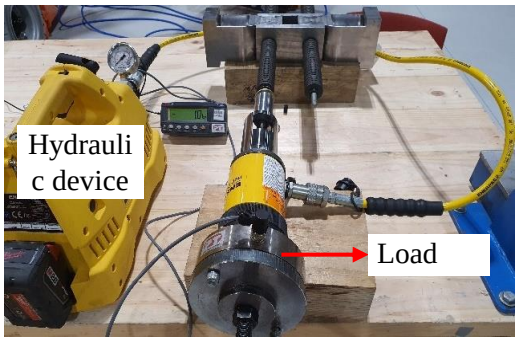

Figure 3.6: Hydraulic device for prestressing the stack of disc springs

3.1.1. *In-plane testing with pined-pined end condition*

When the RSFJ is affected by the SOE in the in-plane direction, the frictional sliding and consequently passive damping are still present (Figure 3.3.f). It has already been demonstrated that the RSFJ possesses a flag-shape moment-rotation behaviour in the in-plane direction [54].

Therefore, the entire RSFJ assembly can be idealized and treated as a rigid column with two segments and an intermediate nonlinear rotational spring (Figure 3.8.e) in which each segment is representative of a middle plate and the rotational spring is representative of the performance of the cap plates when an in-plane rotation occurs. According to the classical stability analysis [54, 127], when the second-order in-plane rotation is involved, the behaviour of the RSFJ in the loading phase can be calculated using Eq.3.5 based on the assumption that it has a pin-pin end and the tangent rotational stiffness will govern the stability [54]. In this equation, the first part ($4K/L$, which can be derived from Eq 4.20 if $L_1 = L_2 = L/2$ – further info regarding the proof can be found in Appendix B) indicates the Euler elastic buckling load of the equivalent spring model while the second part indicates the effect of initial out-of-straightness and prestressing:

$$F_{in-plane,loading} = \frac{4K_{in,loading}}{L}\left(\frac{\theta + \theta_{pr} - \theta_0}{sin(\theta + \theta_{pr})}\right) \quad 3.5$$

where L is the total length of the RSFJ, θ is the in-plane rotation, θ_{pr} is the effect of prestressing offsetting the force axis (as shown in Figure 3.3.d), and θ_0 is the initial out-of-inclination (at the onset of rotation). Both parameters can be calculated using Eq.3.6 and Eq.3.7:

$$\theta_{pr} = \frac{2F_{pr}}{K_{st}btan(\theta_g)} \quad 3.6$$

$$\theta_0 = tan^{-1}(\frac{b}{2l_b}) \quad 3.7$$

where l_b is the distance between the pin and the centre of disc springs (or rod) and *b* is the plate width. The parameter $K_{in,loading}$ is the post-slip tangent rotational stiffness of the RSFJ in the in-plane direction and can be calculated as [54]:

$$K_{in,loading} = \frac{K_{st}n_b b^2}{2} tan\theta_g \frac{(sin\theta_g + \mu\, cos\theta_g)}{(cos\theta_g - \mu\, sin\theta_g)} \quad 3.8$$

Eq.3.5 can reduce to Eq.3.9 with respect to Eq.3.8:

$$F_{in-plane,loading} = 2n_b b^2 K_{st}\left(\frac{2sin^2\theta_g + \mu\, sin2\theta_g}{2cos^2\theta_g - \mu\, sin2\theta_g}\right)\left[\frac{\theta + \theta_{pr} - \theta_0}{Lsin(\theta + \theta_{pr})}\right] \quad 3.9$$

Accordingly, on the unloading phase, the behaviour of the RSFJ involving an in-plane rotation (as a SOE) can be determined by considering the reversed direction of friction:

$$F_{in-plane,unloading} = 2n_b b^2 K_{st} \left(\frac{2sin^2\theta_g - \mu\, sin2\theta_g}{2cos^2\theta_g + \mu\, sin2\theta_g}\right)\left[\frac{\theta + \theta_{pr} - \theta_0}{Lsin(\theta + \theta_{pr})}\right] \quad 3.10$$

(a)

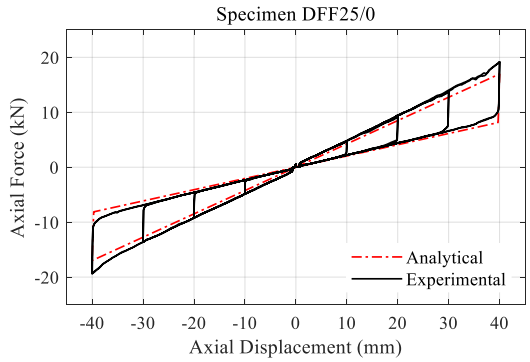

(b)

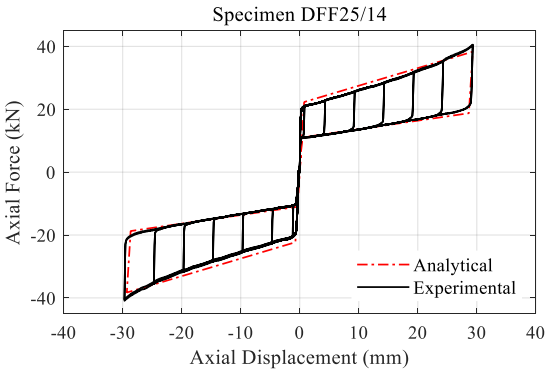

(c)

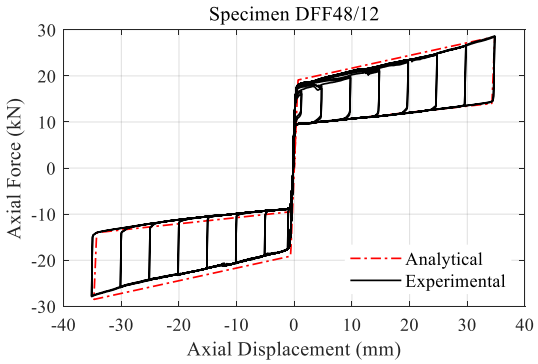

Figure 3.7: Results of reversed cyclic tests of RSFJ with fixed – fixed end condition: (a) specimen DFF25/0, (b) specimen DFF2514, (c) specimen DFF48/12

The correlation between the axial displacement (Δ), the lateral movement of the RSFJ (Δ_{lat}) and the in-plane rotation (θ) can be estimated by use of trigonometry:

$$\Delta = L[cos(\theta_0) - cos(\theta)] \leq \Delta_{max} \quad 3.11$$

$$\Delta_{lat} = \frac{L}{2}[tan(\theta) - tan(\theta_0)] \quad 3.12$$

In order to validate the above-mentioned equations, a number of experimental tests have been performed as it is shown in Figure 3.8 and tabulated in Table 3.3. Each test included two or three cycles up to the target displacement. Furthermore, to trigger the SOE, an artificial imperfection moment was applied for which lightweight washer plates were used (each plate weighted about 30 N). This will be further discussed in the final section of the paper. It should be noted that the imperfection conditions created for these tests in the laboratory environment could be similar to the reality given the axial loads might be slightly eccentric due to erection errors or manufacturing tolerances. For the purpose of data acquisition, a drew wire was attached to the middle plate to measure the lateral movement and the LVDT (linear variable differential transformer) readings from the MTS machine was used to measure the axial displacement.

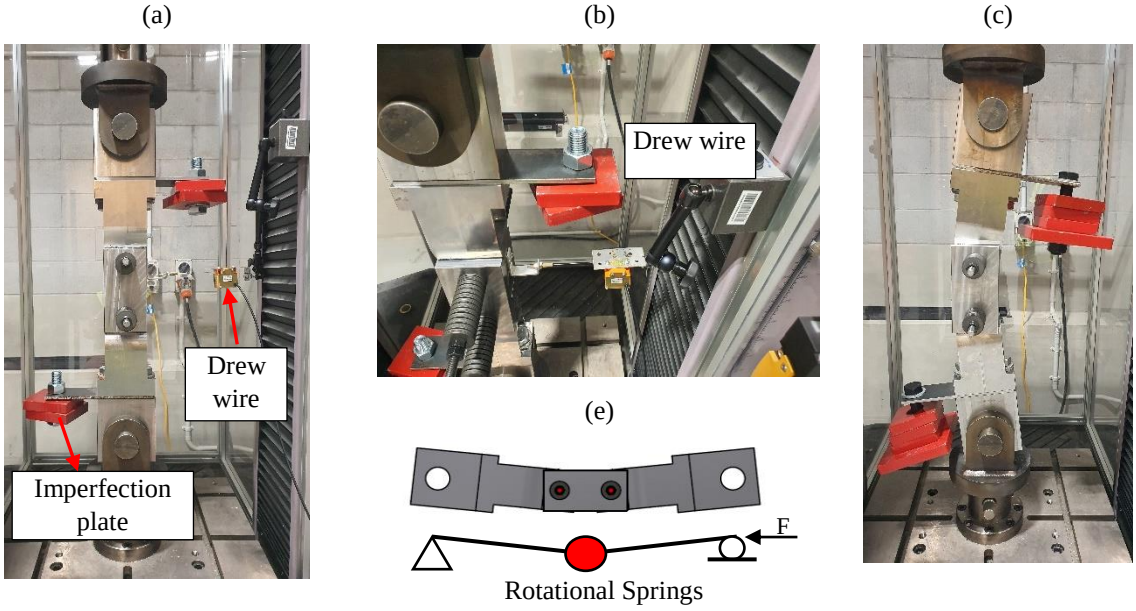

Figure 3.8: (a) in-plane testing setup, (b) instrumentation, (c) deformed shape of RSFJ due to SOE and (e) Idealized SDOF spring model for RSFJ in in-plane

Table 3.3 presents the specimens that were employed for this part of the experimental program. Two variations of discs number (15 and 25) with 4 different prestressing forces were considered.

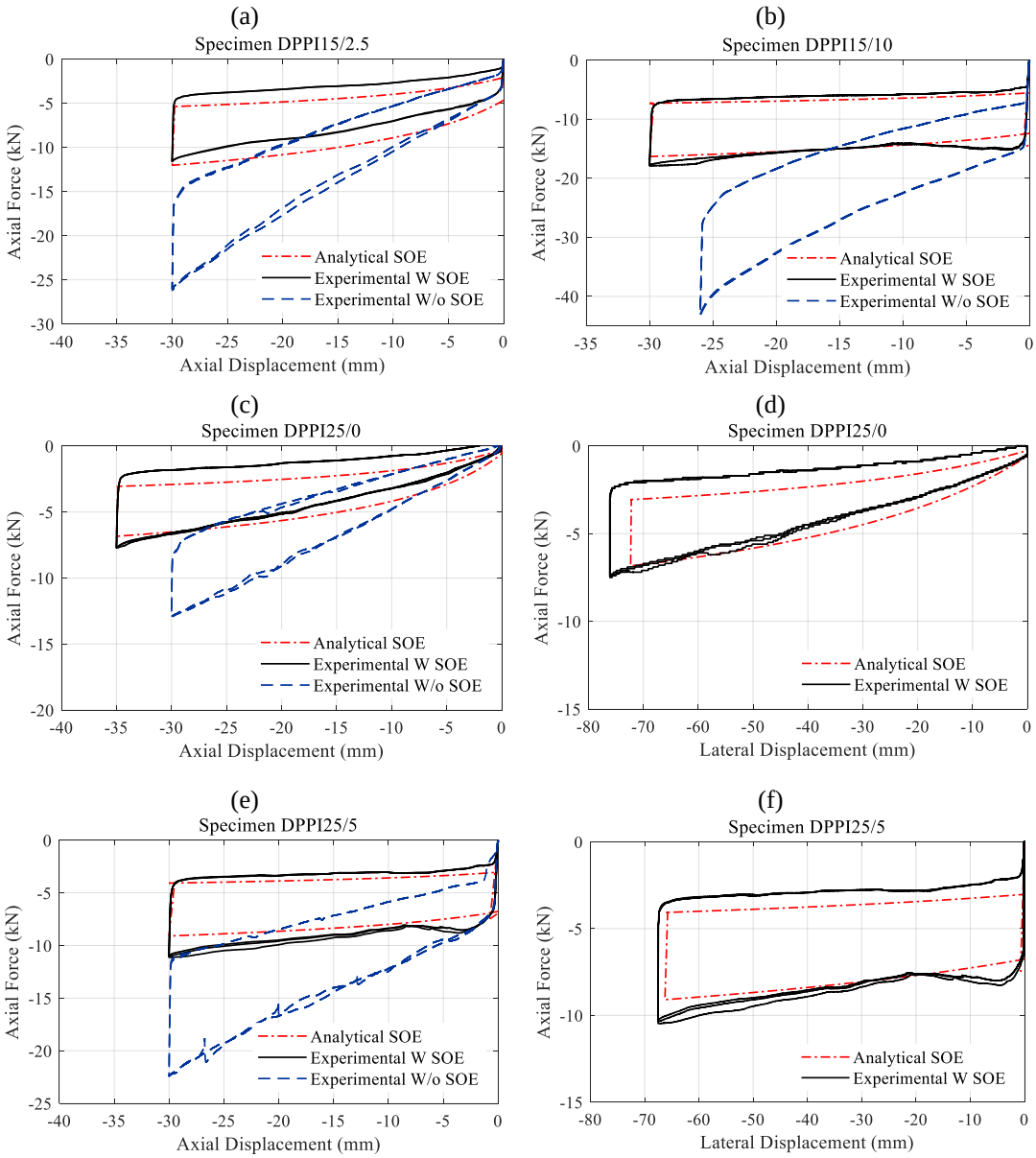

Figure 3.9: Experimental results vs analytical predictions of RSFJ under SOE in in-plane: (a) axial displacement vs axial load for specimen DPPI152.5, (b) axial displacement vs axial load for specimen DPPI1510, (c) axial displacement vs axial load for specimen DPPI250, (d) lateral displacement vs axial load for specimen DPPI250, (e) axial displacement vs axial load for specimen DPPI255 and (f) lateral displacement vs axial load for specimen DPPI255

Table 3.3: Details of RSFJ damper for pin-pin end condition for in-plane testing

Specimen	F_{pr} (kN)	n_d	n_b	θ_g (degree)	K_{st} (kN/mm)	Δ_{max} (mm)
DPPI15/2.5	2.5	15	1	30	1.555	30
DPPI15/10	10	15			1.754	30
DPPI25/0	0	25			0.916	35
DPPI25/5	5	25			0.974	30

Figure 3.9 illustrates the experimental results in which the red lines show the analytical prediction (discussed in this section), and the black and blue lines show the experimental performance in the presence and absence of SOE, respectively. In all of the cases, the effect of SOE was not detectable for the before-slip phase of the experiment while it was significant for the post-slip phase. The intact post-slip axial stiffness of RSFJ (blue dashed lines) – both in loading and unloading – experienced a considerable drop as a result of the *in-plane* rotation (Figure 3.9). This resulted in the reduction of the maximum force to about half (in all of the cases). Figure 3.9.d and Figure 3.9.f demonstrate the lateral deflection of the RSFJ under the influence of SOE. The maximum lateral displacement of the damper was around twice the maximum axial displacement. This large lateral movement may have led to the yielding of the plates if it was not properly factored in the design. However, as the plates were intentionally designed for the combined actions (bending and axial force), no yielding of the material was observed. It should be noted while there was no failure in the damper due to rotation, however, in real applications the large lateral movement of the damper and the increasing drift of the structure could damage the non-skeletal elements and claddings if not considered in the design.

3.1.2. *Out–of–plane testing with pined-pined end condition*

Similar to the in-plane behaviour, the analytical expression for the out-of-plane behaviour in the presence of SOE can be acquired. By considering the free body diagram of the system in the deflected (rotated) shape in a pin-pin condition, the equilibrium of forces yields Eq.3.13 (after mathematical simplifications) – the proof is provided in the appendix:

$$F_{out,loading} = 2n_b k_{st}\left(\frac{sin\theta_g + \mu cos\theta_g}{cos\theta_g - \mu sin\theta_g}\right)\left[B(1-cos\theta) + A\theta + 2\frac{F_{pr}}{k_{st}}\right]\left[\frac{\sigma}{\sigma + t_{max,m} sin\theta_g}\right] \quad 3.13$$

where $t_{max,m}$ is the thickness of the middle plate at the thickest part and σ, A and B are defined as follows:

$$\sigma = 2L_e\left(cos\theta_g - \mu sin\theta_g\right)(1-\mu\theta) + (L - L_c)\theta sin\theta_g \quad 3.14$$

$$A = L_e + t_{max,m}.tan(\theta_g) \quad 3.15$$

$$B = 0.5(L - L_c + 2L_e).tan\theta_g \quad 3.16$$

in which L, L_c and L_e are the total length, cap plate length and the overlap length between the middle and cap plates, respectively (shown in Figure 3.10.d). The correlation between the axial displacement, lateral movement and the out-of-plane rotation of the RSFJ can be estimated as follows by simple trigonometry:

$$\Delta = \frac{2B(1-cos\theta)+A\theta}{tan(\theta_g)} \leq \Delta_{max} \quad 3.17$$

$$\Delta_{lat} = \frac{B}{tan(\theta_g)}\theta \quad 3.18$$

Table 3.4 presents the specimens that were employed for this part of the experimental program. Two variations of discs number (48 and 56) with two different prestressing forces were considered.

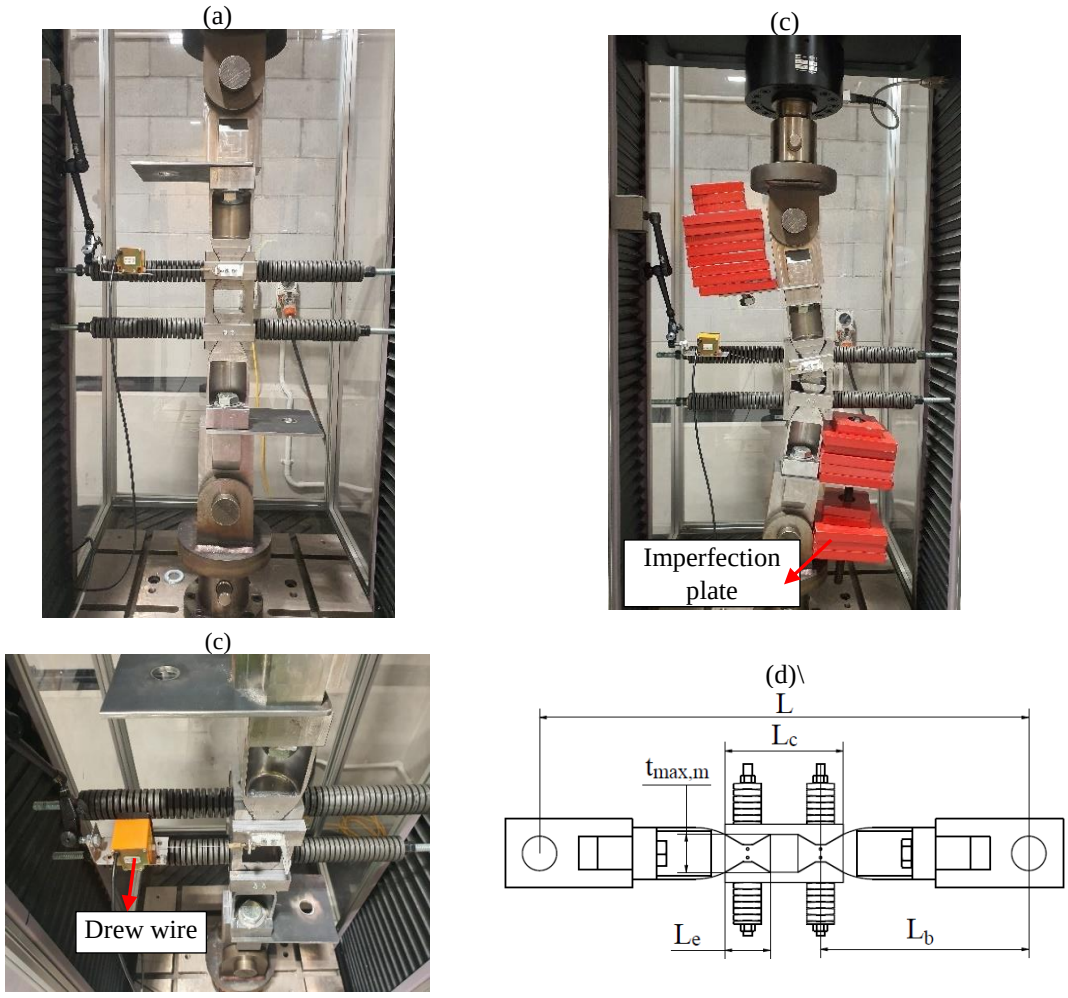

Figure 3.10: (a) Test-set up for the out-of-plane testing program, (b) deformed shape of RSFJ due to SOE, (c) instrumentation and (d) parametric dimensions

Table 3.4: Details of RSFJ damper for the pin-pin end condition in the out-of-plane direction

Specimen	F_{pr} (kN)	n_d	n_b	θ_g (degree)	K_{st} (kN/mm)	Δ_{max} (mm)
DPPO48/0	0	48	1	30	0.478	35
DPPO56/2.5	2.5	56			0.419	35

Figure 3.11 illustrates the results of the out-of-plane test in which the red lines show the analytical prediction presented in this section, and the black and blue lines show the experimental performance in the presence and absence of SOE, respectively. As for the specimen DPPO15/10, it can be seen that the SOE had a marginal impact on the initial (elastic stiffness). The specimen DPPO48/0 had no initial stiffness as it was not prestressed. On the other hand, the post-slip tangent stiffness witnessed a drop both in loading and unloading, yet it was not as significant as the in-plane case.

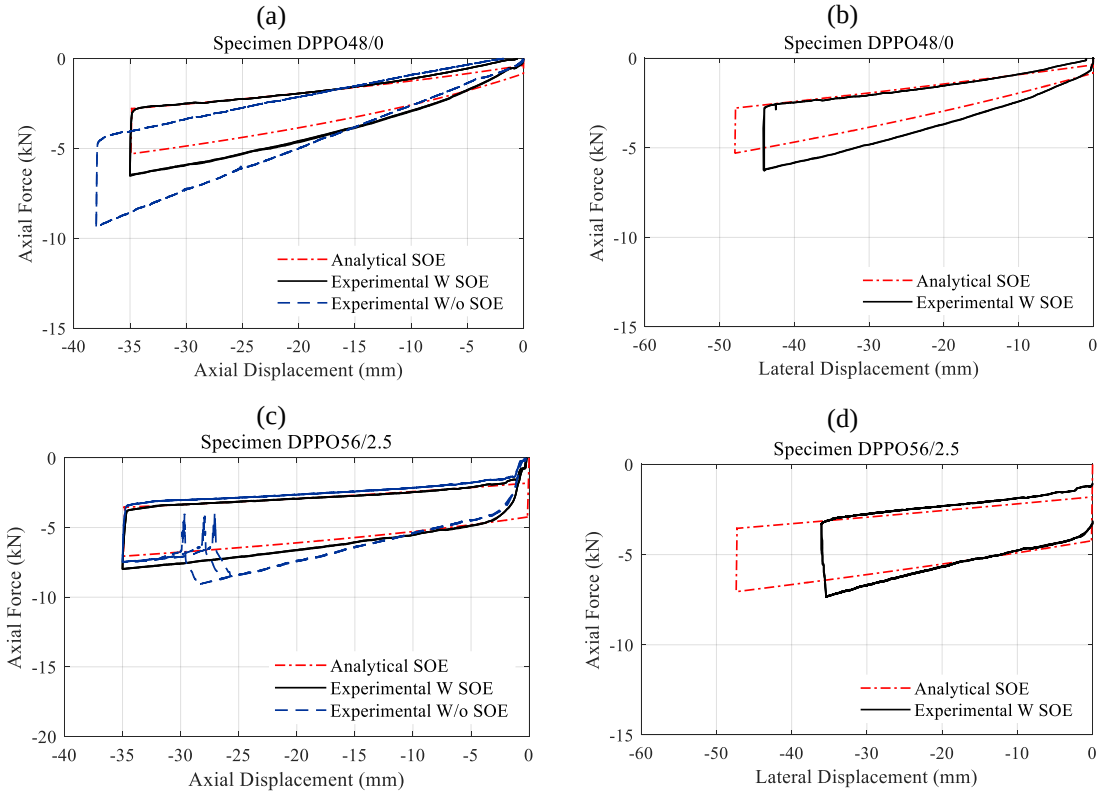

Figure 3.11: Experimental results vs analytical predictions of RSFJ under SOE in out-of-plane (a) axial displacement vs axial load for specimen DPPO480, (b) lateral displacement vs axial load for specimen DPPO480, (c) axial displacement vs axial load for specimen DPPO562.5 and (d) lateral displacement vs axial load for specimen DPPO562.5

In case of the specimen DPPO56/2.5, the results of the axial-only loading (without SOE) was not available; therefore, the result of the specimen with a slight degree of SOE was used so that the discrepancy between different behaviours can be distinguished. In the results and within the blue line, a new phenomenon can be observed. The test included 3 cycles up to 35 mm in compression, and in all of them, there was a sudden drop with a negative stiffness showing the transition from the blue line to the red one. This is, in fact, an instability or transition that occurred during the test and lied in the imperfection acting on the joint. The same was observed for the other scenarios in the in-plane and will be discussed in the next section. The maximum lateral displacement of the damper was nearly equal to the maximum axial displacement. This large lateral movement may contribute to the yielding of the RSFJ component; however, as the plates were intentionally designed to stay elastic in this testing even after rotation, no yielding of the material was observed. There was a 30% difference between the analytical prediction and the experimental observation for the lateral displacement of the specimen DPPO56/2.5. This difference was negligible for the specimen DPPO48/0.

3.1.3. *In-plane and out-of-plane with pined-fixed condition*

In the previous two sections, it was observed that when the damper is pinned at the supports, it is highly prone to experience a decline in capacity. According to the test results, the impact of SOE on the in-plane direction was even more significant as compared to the out-of-plane case. For example, for the damper used in this study, the impact of the in-plane SOE was twice the out-of-plane. As another possibility affecting the performance of the RSFJ, the behaviour of the damper is studied and discussed with pin-fixed end conditions in this section.

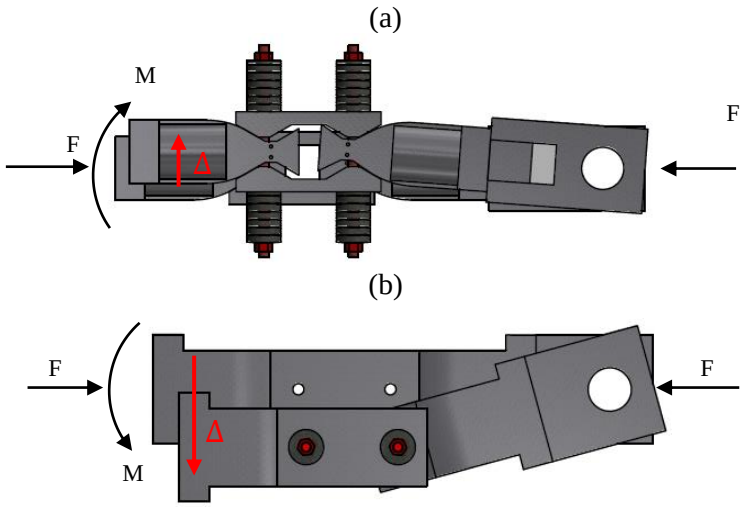

Figure 3.12: Imaginary deformed shape of RSFJ due to SOE with pin – fixed end condition (a) out-of-plane and (b) in-plane

According to Figure 3.12, the deformed shape of the damper (including the additional rotation due to SOE) is depicted for both *in-plane* and *out-of-plane* directions in which one end is pinned while the other is fixed with released shear deformation degree-of-freedom (DOF). As can be seen, the deformation compatibility of the damper (Figure 3.12.a and Figure 3.12.b) necessitates that the left middle plate (with no rotational DOF) displaces as the slave of the cap plate to one side (Figure 3.12.a and Figure 3.12.b) by considering the displacement as a rigid motion. Therefore, if the shear deformation DOF is fixed, it can be concluded that the damper could be unsusceptible to the SOE because of the deformation compatibly constraint. This was experimentally observed for the specimen DFPI48/0, which was pin-pin in in-plane, had zero prestressing force and had a high number of disc springs. This combination made it the most prone case to SOE, yet no trace of degradation was found according to the experimental result depicted in Figure 3.13.b even with the maximum number of imperfection plates (Figure 3.13.a).

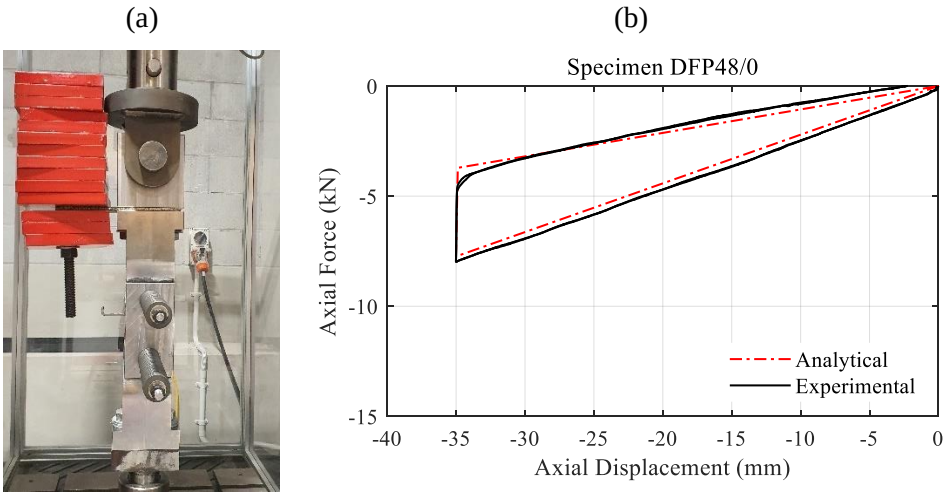

Figure 3.13: Test set-up for RSFJ test with pin – fixed end condition (Left) and Experimental results vs analytical predictions for specimen DFP48/0 (Right)

3.2 Further discussion:

As previously mentioned, an artificial and small imperfection moment was employed during the testing program with the intention of triggering the SOE. Imperfection was applied to the damper using washer plates. The imperfection was increasing from zero (with no plate) until an instability or transition was observed in the damper performance due to the SOE when compared to the axial-only behaviour. It should be noted that if the imperfection moment was larger than this critical imperfection (i.e., activation-imperfection), the damper followed the SOE path in the testing program. Table 3.5 presents the specimens that were discussed in the *in-plane* testing section

but with the difference that it reports the imperfection at which the transition (instability) occurred. The results of the tests during which the SOE was triggered are shown in Figure 3.14. Among them, the result of specimen DPPI15/5 (Figure 3.14.a) shows that the SOE was activated during the loading path at an imperfection of 0.002 kN.m where the damper experienced a peak around 14 kN in loading and immediately after that it saw a sudden drop with negative stiffness to the SOE affected path. For the other three specimens, the instability occurred during the unloading with a negative stiffness just after the reversed slip point.

Table 3.5: Details of RSFJ damper with pin-pin end condition and the imposed imperfection to activate the SOE

Specimen	F_{pr} (kN)	n_d	n_b	θ_g (degree)	Imperfection (kN.m)	Δ_{max} (mm)
DPPI15/5	5	15	1	30	0.002	30
DPPI25/0	0	25			0.004	35
DPPI25/5	5	25			0.004	30
DPPI25/10	10	25			0.038	30

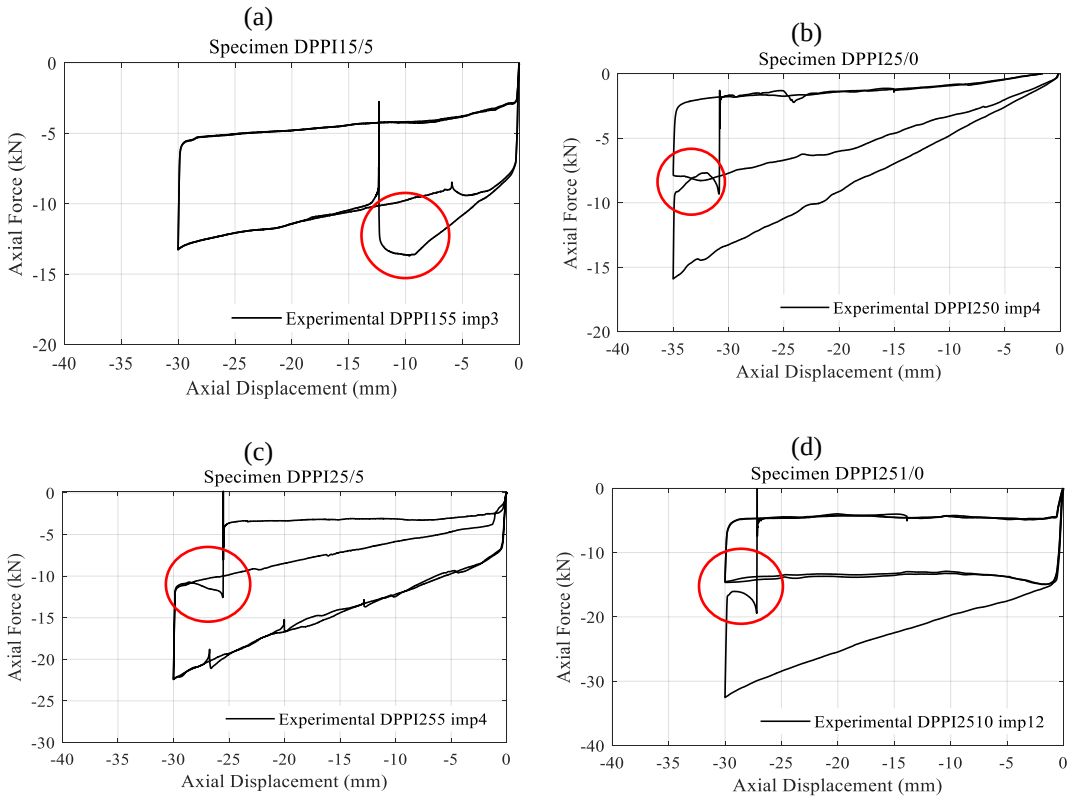

Figure 3.14: Transition from pure axial performance of RSFJ to the SOE affected path (a) Specimen DPPI15/5, (b) Specimen DPPI25/0, (c) Specimen DPPI25/5 and (d) Specimen DPPI25/10

Figure 3.15.a shows the imperfection required for each specimen to activate the SOE. Generally, it can be seen that the amount of imperfection moment required to trigger the SOE will increase with the amount of prestressing force in the disc springs; however, it is inversely correlated with the stiffness of the stack. The blue and red trend lines in Figure 3.15.a are illustrative of this fact as the red line (for $n_d = 25$) tends to be lower than the blue line (for $n_d = 15$). As for the out-of-plane, it required a considerably higher amount of imperfection moment as compared to the in-plane though the stiffness of stack for the out-of-plane direction was much less. In general, it can be concluded that if the imperfection is less than the activation-imperfection, the damper will follow the axial-only performance while if the imperfection is higher than the activation-imperfection, the damper follows the SOE path. Quantifying the activation-imperfection requires further study to include the effect of several parameters such as manufacturing method, installation tolerance, prestressing force, the direction of SOE (in-plane and out-of-plane), etc. Thus, the observed activation-imperfection in this study might not be valid for the other dampers with different designs. Figure 3.15.b shows the disassembled middle and cap plates at the end of the testing program. According to the observations, there were some scratches on the middle and cap plates, however, they were minor and shallow which is common in case of friction dampers.

(a) (b)

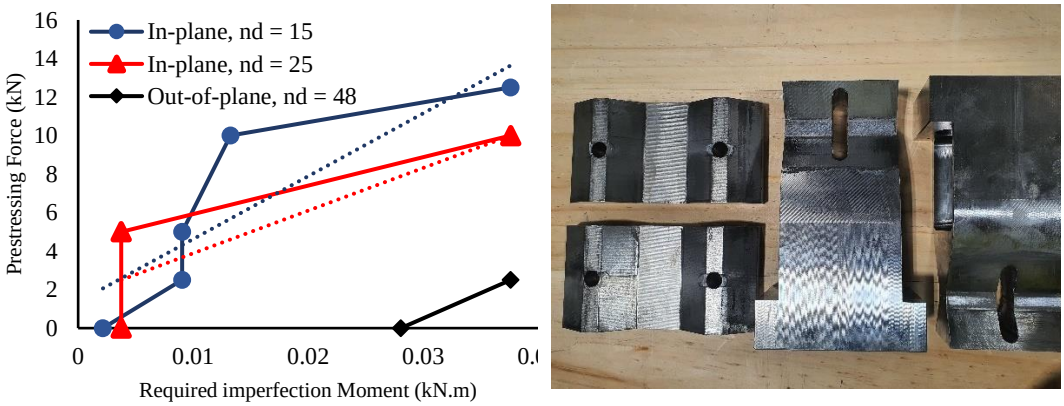

Figure 3.15: (a) correlation between the required imperfection for SOE activation and prestressing force and number of disc springs, (b) photo of RSFJ components after testing completion

As discussed, the ideal situation to design the components of the damper is when it has a pin-pin end condition as there would be no bending transfer or deformation compatibility requirements between the structure and the damper. However, as it was demonstrated in this paper, the pin-pin end condition is the most vulnerable case to experience degradation due to SOE.

3.3 Recommendations

Given the outcome of the study and the experimental observations, the following recommendations are proposed:

1. If a damper is installed with the pin-pin end conditions, it is suggested to be designed once for axial-only behaviour and once for SOE affected performance, and the critical demands to be considered. This might lead to a damper with thicker plates as the plates should be designed once for axial load and once for both axial and bending.

2. A simple remedial solution to make the damper less sensitive to *in-plane* SOE is the usage of some stopper plates bolted (or welded) to the middle plate as shown in Figure 3.16.a. In the case of the casting method of manufacturing, these plates can be simplify considered in the mould and manufactured as part of the middle plates in one piece. By using these plates, the relative rotation between the middle and cap plates will be hindered, and as a result, the damper will not be affected by the *in-plane* SOE. This solution was experimentally tested, and the performance was free of the SOE (Figure 3.16.c).

3. The other recommendation is to use the pin-fixed end conditions for the damper. As it was discussed earlier, changing one of the supports to fixed, can rule out the possibility of SOE in the direction in which the support is fixed. An illustration of this approach can be found in a real project in New Zealand in which the RSFJ was used as the hold-downs for rocking concrete shear walls with pin-fixed end condition in both *in-plane* and *out-of-plane* (swivel - fixed) [163]. Having a pin-fixed end condition has also an advantage over the fixed-fixed case. Although the fixed-fixed end condition is the best approach to cancel out the SOE, the additional bending that would be transferred to the damper from both ends as a consequence of deformation compatibility might be significant. Therefore, the pin-fixed situation could be an ideal condition for the damper from both SOE considerations and damper design perspectives.

4. There might be some cases that RSFJ needs to be installed in a fixed-fixed situation due to stability considerations. An illustration of this is the tension-compression braces, which are naturally vulnerable to SOE due to the large compression force and the pinned ends. For this case, the RSFJ is used as fixed-fixed and a telescopic male/female tubes can be put in parallel to the damper (Figure 3.16.b) to not only reduce the SOE on the damper but also reduce the SOE on the brace. As the performance of the braces is more complicated in the presence of SOE, a separate study is being performed at the time of writing this paper [165].

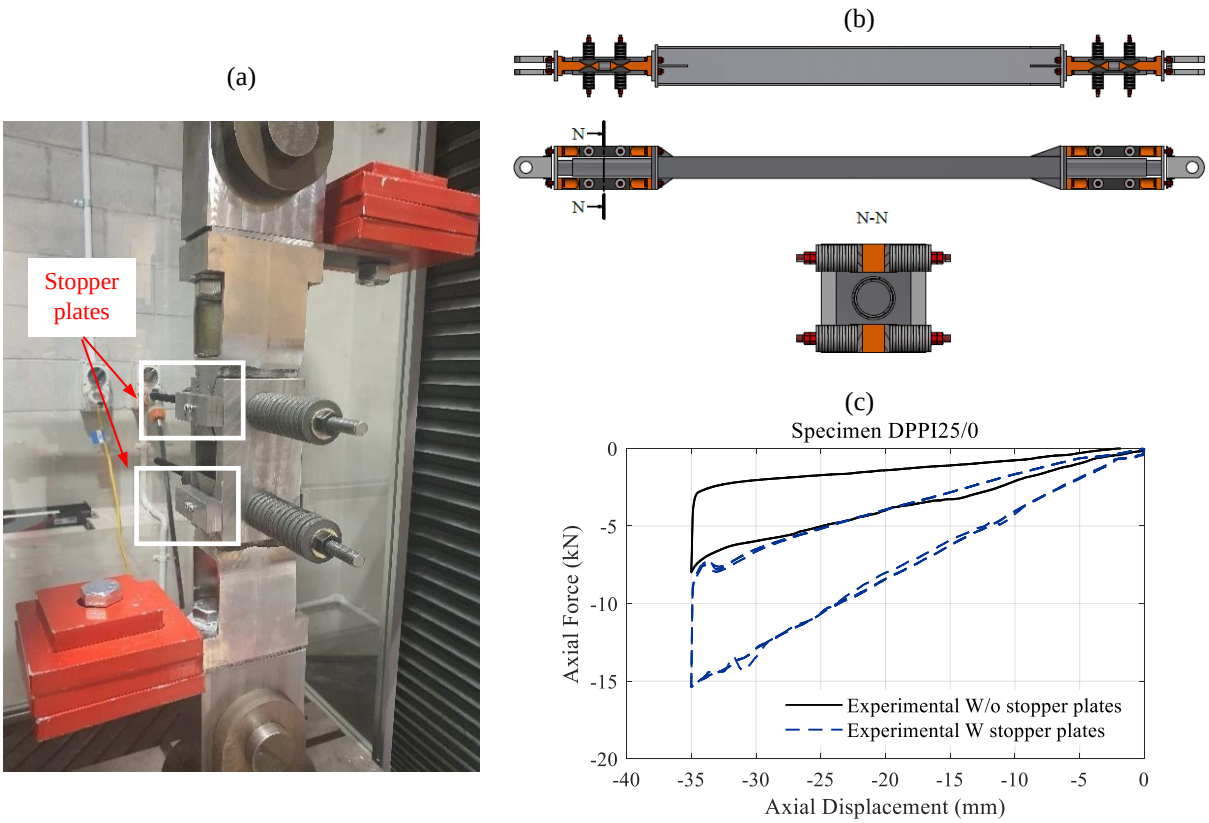

Figure 3.16: (a) RSFJ assembly with additional plates mounted on the middle plate to limit the in-plane SOE rotation, (b) RSFJ brace assembly with telescopic tubes parallel to RSFJ and (c) Experimental results when additional plates were used on the middle plates

3.4 Summary and Conclusion

Extensive experimental tests (more than 70) and analytical studies were conducted in this research project focusing on the effect of second-order actions on the RSFJ damper performance. It has been revealed that the pin-pin end condition is the most critical situation for the damper for both *in-plane* and *out-of-plane* although this boundary condition is desired because there would be no extra bending and shear force demands on the damper. The analytical expressions to predict the performance of the damper in the presence of second-order actions have been also developed and validated with the experimental data. Therefore, in case that the damper is expected to be affected by the second-order actions, its performance can be predicted accurately and the damper can be designed for the additional actions. Furthermore, it has been discussed that a certain amount of imperfection is needed for the damper to follow the degraded performance due to second-order actions. This imperfection was artificially applied during the testing program;

however, it may exist inherently in reality due to manufacturing errors or erection tolerances. In addition, it was observed that the activation-imperfection of the in-plane qualitatively was less than that of the out-of-plane. The amount of imperfection was also on the rise with an increasing amount of prestressing force in the disc springs. Quantifying the activation-imperfection requires further study and experimental testing to consider the effect of manufacturing methods, installation tolerances, prestressing force, the direction of SOE (in-plane and out-of-plane), etc.

In order to control the SOE, it has been suggested that the pin-fixed end condition be used in real applications such as the hold-downs for rocking shear walls. In some cases, it might be necessary to use the fixed – fixed end condition due to the large amplitude of SOE and stability considerations of the system (such as in tension/compression braces). Finally, the feasibility study of using some additional plates to be attached to the middle plate was also found to be effective to exclude the in-plane SOE.

4 Manuscript.2 - Global Elastic Buckling of the RSFJ-Brace

Based on the article published on 2021/1/1 by peer-reviewed "Journal of Structural Engineering", Volume 147, issue 1, page 04020299

4.1 Abstract

This paper investigates the experimental behaviour of a self-centring (SC) timber brace that employs the Resilient Slip Friction Joint (RSFJ) for energy dissipation. Due to the inherent characteristics of the RSFJ, mainly rotational flexibility, it was observed that the brace is susceptible to lateral instability. As will be shown experimentally, the demerit to this lateral instability is the reduction of the brace capacity in compression though it is of elastic type and recovers at the end of unloading. Therefore, this paper aims to prevent the instability issue in the RSFJ-brace system. To do so, a proper framework to predict and quantify the instability is developed, and then a quasi-static test is performed on a small-scale (1:3) specimen to evaluate the accuracy of the proposed framework. In order to address the instability problem, the Anti-buckling Tubes (ABT) concept with associated stiffness requirements is introduced in the second part, whose effectiveness is assessed using a quasi-static test on a full-scale specimen. Results indicate that the utilization of the ABT will rule out the possibility of instability.

4.1 Introduction

The advent of low-damage Lateral Load Resisting System (LLRS) with flag-shaped hysteresis performance dates back to the Pre-cast Seismic Structural Systems (PRESSS) program and application of precast post-tensioned rocking concrete shear walls [51] where precast concrete panels with post-tensioned tendons were used with yielding dampers to reduce the displacement demand. Application of post-tensioned elements with additional damping was generalized to moment-resisting frames (MRFs) by [166] and [167]. The application has been also extended to rocking timber shearwalls by Buchanan et al. and Palermo et al. [15, 168]. Application of friction dampers has been studied by other researchers as a low-damage system [13, 26, 153, 169]. The combination of post-tensioning and dampers has been also extended to steel braces [77, 79, 170, 171]. Various novel self-centring LLRS systems that utilize the post-tensioned tendons with

yielding dampers [172] have been introduced, and readers are encouraged to see [17] for a comprehensive review.

Generally, a flag-shape hysteresis response can be achieved from a combination of a damping device with a nonlinear elastic spring, and it has been shown that they can be utilized in buildings to reduce the acceleration and displacement demands [77]. The Resilient Slip Friction Joints (RSFJ) [137] is, indeed, the extended version of the conventional friction spring dampers [136, 137] which can provide self-centring and damping in one single device. The joint has been utilized in a number of LLRSs including rocking timber shear walls, tension-only braces, self-centring braces and so on [98, 157, 160, 165]. It should be noted that there is a concern regarding the performance of this damper when it is loaded in compression in terms of lateral instability. Nearly in all of the above-mentioned applications, RSFJ was either working completely in tension or partially in compression as the performance of the RSFJ was under investigation in the time. However, for the first time in this study, a self-centring (SC) timber brace using RSFJ is introduced and is expected to work both in tension and compression.

Similar to other bracing systems, the buckling and instability need to be studied and investigated to see if they can function as a barrier to attain the intended performance in compression. The root cause of the instability in the proposed brace lies in the arrival of rotational flexibility [99, 156] where the RSFJ is positioned. This problem is not limited to the proposed SC brace. Such an analogous problem has been observed and reported for the Buckling-Restrained Braces (BRB), which, in fact, takes place as a result of either the inadequately-designed gusset plates or neck zone [31, 129]. More specifically, although the BRB is designed to yield in compression, it may fail prematurely if the gusset plates or neck does not have the required strength and stiffness [30-32, 130]. In order to tackle the problem, Takeuchi et al. [31, 32] used energy methods to put forth some stability criteria based on boundary conditions and geometry of the BRB. According to experimental results and the failure observed, they advised two stability limits, one for stiffness and one for strength, to ensure the perfect performance for BRB. In this regard, comparable stability criteria have been suggested [30] based on the formation of a plastic mechanism and the notational load method. An identical path was followed for the proposed brace in this study. In the first part of the paper, a framework is established in which both approximate and exact formulas are developed to quantify the buckling load. This framework is then validated via reversed cyclic test, performed on a small-scale specimen. Thereafter, in the second part of the paper, an Anti-buckling Tube concept (ABT) using two sliding tubes is introduced and suggested to function as a local strengthening to increase the buckling load to the desired level, whose efficiency is experimentally tested and validated via full-scale quasi-static test.

4.2 Damper performance

4.2.1. *Axial Performance*

As shown in Figure 4.1, the RSFJ is composed of two types of grooved steel plates namely: outer ones (cap plates) and inner ones (slotted or middle plates). These plates are clamped together using high strength bolts and prestressed disc springs. Centre slotted plates (middle plates) start to slip once the applied axial force overcomes the frictional resistance between the surfaces, which itself is a function of how much the disc springs are prestressed. More pre-compressing of the springs means more frictional resistance and higher slip load. When the pre-stressing is overcome, the cap (upper) plates are pushed to the sides, which consequently causes more compression in the disc springs. Once unloading starts, the stored elastic energy in the compressed disc springs will be released and pushes the cap plates back to their initial position and similarly pushes or pulls the middle plates to their initial position. Hence, these plates can slide on each other repeatedly during cyclic loading, thereby dissipating the input energy.

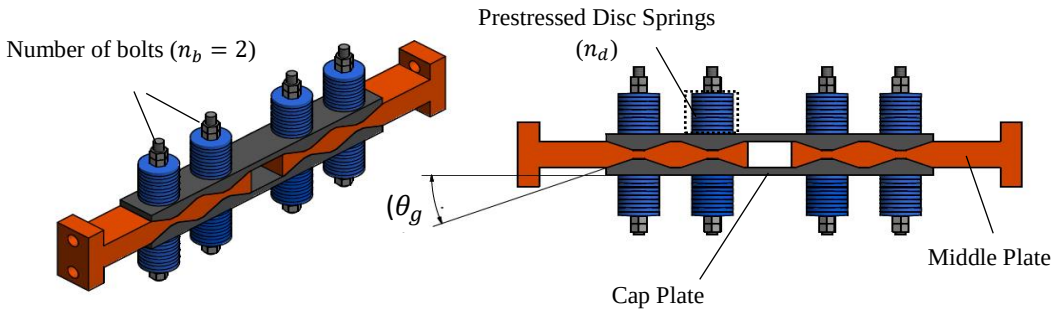

Figure 4.1: RSFJ assembly and components

The flag-shape performance of RSFJ is depicted in Figure 4.2. In this diagram, the slip force (F_{slip}) is indicative of the force that the joint will start to move. After the slip point, the RSFJ can expand until the disc springs are fully flat. At this point, the axial force is at its maximum and is referred to as the ultimate load (F_{ult}). This is shown in Figure 4.2. Once the unloading begins, RSFJ does not slip until the frictional resistance is overcome. At this point, the second (reversed) slip point takes place which is known as the restoring point ($F_{restoring}$). From this point onward, the joint will be slipping to release the absorbed energy in the disc springs until a point that axial force is not high enough to overcome friction. At this point, the joint will stop moving (shown in Figure 4.2) and is referred to as the residual force (F_{res}).

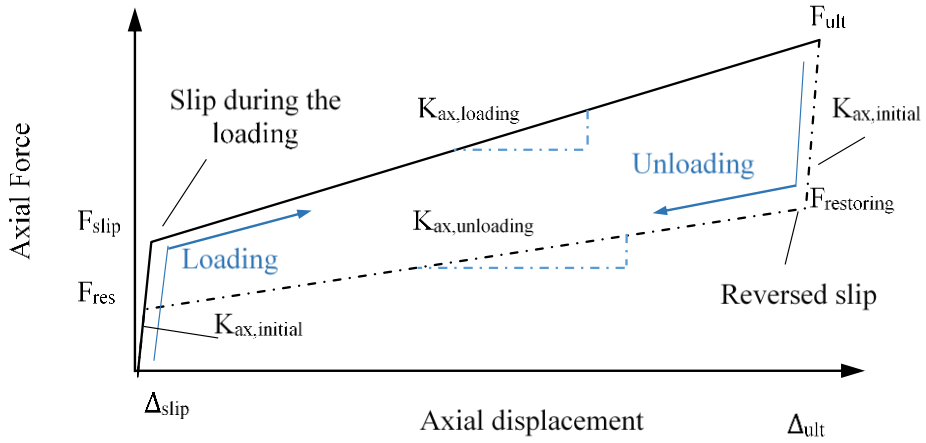

Figure 4.2: Passive self-centering hysteretic axial response of RSF joint (flag-shaped hysteresis)

The activation force of the RSFJ (slip force) is given in Eq.4.1 [138]:

$$F_{slip} = 2n_b F_{pr}\left(\frac{sin\theta_g + \mu cos\theta_g}{cos\theta_g - \mu sin\theta_g}\right) \quad 4.1$$

where the angle of grooves is denoted by θ_g; the coefficient of friction is μ. the pre-stressing force is indicated by F_{pr}, and the number of bolts on each splice is shown by n_b (for instance, in Figure 4.1, n_b= 2). Likewise, if the friction acts in the opposite direction, the residual force is determined:

$$F_{res} = 2n_b F_{pr}\left(\frac{sin\theta_g - \mu cos\theta_g}{cos\,\theta_g + \mu sin\theta_g}\right) \quad 4.2$$

The ultimate and restoring forces can be determined if F_{pr} is replaced by F_u in F_{slip} and F_{res} equations.

The ultimate axial displacement that the RSFJ can experience during the slip can be calculated from the remaining deflection of the prestressed disk springs to get fully flattened:

$$\Delta_{ult} = 2n_d \frac{\Delta_{s,max}}{tan(\theta_g)}(1-\gamma) \quad 4.3$$

where $\Delta_{s,max}$ is the listed deflection of a disk spring, the parameter n_d is the number of disc springs in a stack per each side of the bolt and the parameter $\gamma = \frac{F_{pr}}{F_u}$ is indicative of the pre-stressing ratio. The post-slip tangent stiffness of the flag-shape hysteresis (in loading) can be calculated by:

$$K_{ax,loading} = \frac{F_{ult} - F_{slip}}{\Delta_{ult} - \Delta_{slip}} \quad 4.4$$

By re-arranging Eq.4.4, the axial stiffness of the joint after-slip is:

$$K_{ax,loading} = \frac{2n_b(1-\gamma)F_u tan\theta_g \left(\frac{sin\theta_g + \mu cos\theta_g}{cos\theta_g - \mu sin\theta_g}\right)}{2n_d(1-\gamma)\Delta_{s,max}\left(1 - \frac{tan\theta_g \Delta_{slip}}{2n_d(1-\gamma)\Delta_{s,max}}\right)} \quad 4.4a$$

Eq.4.4a reduces to Eq.4.5 assuming that $1 - tan\theta_g \Delta_{slip}/\left(2n_d(1-\gamma)\Delta_{s,max}\right) \approx 1$:

$$K_{ax,loading} = n_b K_{st} tan\theta_g \left(\frac{sin\theta_g + \mu cos\theta_g}{cos\theta_g - \mu sin\theta_g}\right) \quad 4.5$$

where K_{st} is the equivalent stiffness for the stack of springs per each side of the bolt (equal to K_d/n_d where K_d is stiffness of a disc spring). A similar procedure can be followed for the unloading phase with the friction force in the opposite direction, which results in:

$$K_{ax,unloading} = n_b K_{st} tan\theta_g \left(\frac{sin\theta_g - \mu cos\theta_g}{cos\theta_g + \mu sin\theta_g}\right) \quad 4.6$$

As inferred from Eq.4.5 and Eq.4.6, the after-slip axial stiffness of the RSFJ depends only on the geometry of the damper and the stiffness of the discs.

4.2.2. *In-plane Rotational Performance:*

The RSFJ damper has also a flag-shape response [165, 173] if it is subjected to in-plane rotation (Figure 4.4). If an arbitrary in-plane rotation θ_{in} is applied on both ends of the RSFJ in a way that the pre-stressing force of the disc springs is overcome, disc springs will be further compacted as the cap plates tend to further compress them. The resultant vertical displacement of the disc springs due to the in-plane rotation can be determined by Eq.4.8, with respect to Figure 4.3. In Eq.4.7 and Eq.4.8, it is assumed that the centre of rotation is placed at the centre of the bolts given they are stiff enough not to slip (move laterally).

$$\Delta_h = \frac{b}{2}\theta_{in} \quad 4.7$$

$$\Delta_v = \frac{b}{2}\theta_{in}tan(\theta_g) \quad 4.8$$

In which the width of joint or cap plates is denoted by b. During the in-plane rotation, the disc springs will be more compacted as the grooves will climb up each other (as shown in Figure 4.3). Therefore, the reaction forces in the stacks of springs also increase due to this vertical displacement (Eq.4.9) and will be added up to the pre-stressing forces.

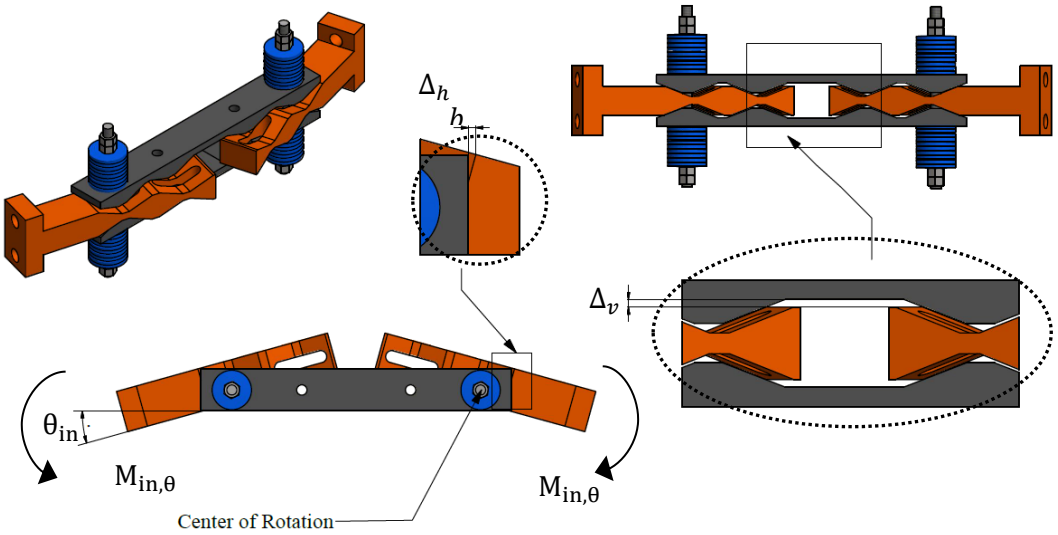

Figure 4.3: In-plane rotation of the RSFJ with one bolt per splice

The increased force in the springs due to the in-plane rotation can be determined as:

$$F'_{pr} = F_{pr} + K_{st}.\Delta_v \quad 4.9$$

$$F'_{pr} = F_{pr} + K_{st}.\frac{b}{2}\theta_{in}tan(\theta_g) \quad 4.9a$$

The rotation can continue until the disc springs become fully flattened. In this diagram, slip moment ($M_{in,slip}$) is indicative of the force at which the joint will start to rotate. The maximum in-plane moment is denoted by $M_{in,ult}$. Once the unloading begins, the RSFJ does not slip until frictional resistance is overcome. This point is, in fact, the second (reversed) slip point taking place when the joint is unloading in rotation, which will be referred to as restoring moment ($M_{in,restoring}$). From this point onward, the joint slips rotationally to release the energy absorbed in the disc springs. The slip will continue till a point that the restoring force is not high enough to overcome friction. At this point, the joint will stop rotating. This is shown in Figure 4.4 and will

be referred to as the residual moment ($M_{in,res}$). The slip moment of the RSFJ can be calculated as:

$$M_{in,slip} = n_b F_{pr} b \frac{(sin\theta_g + \mu cos\theta_g)}{(cos\theta_g - \mu sin\theta_g)} \quad 4.10$$

The residual in-plane moment ($M_{in,res}$) is determined when the direction of the friction force is reversed:

$$M_{in,res} = n_b F_{pr} b \frac{(sin\theta_g + \mu cos\theta_g)}{(cos\theta_g - \mu sin\theta_g)} \quad 4.11$$

The ultimate and restoring moments can be determined if F_{pr} is replaced by F_u in $M_{in,slip}$ and $M_{in,res}$ equations. The post-slip tangent stiffness of the flag-shape related to the loading phase (secondary rotational stiffness of the loading) will be:

$$K_{in,sec,loading} = \frac{M_{in,ult} - M_{in,slip}}{2\theta_{ult}} = \frac{K_{st}.n_b.b^2}{2} tan\theta_g \frac{(sin\theta_g + \mu\, cos\theta_g)}{(cos\theta_g - \mu sin\theta_g)} \quad 4.12$$

Where θ_{ult} can be derived from Eq 4.9 if F'_{pr} is replaced by F_u (flat load of the disc springs). By further simplifying Eq.4.12 with respect to Eq.4.5:

$$K_{in,sec,loading} = \frac{b^2}{2} K_{ax,loading} \quad 4.13$$

Eq.4.13 expresses the relation between the axial and rotational post-slip stiffnesses of the RSFJ. Similarly, the secondary rotational stiffness in the unloading phase can be determined as:

$$K_{in,sec,unloading} = \frac{M_{in,restoring} - M_{res}}{2\theta_{ult}} = \frac{K_{st}.b^2}{2} tan\theta_g \frac{(sin\theta_g - \mu cos\theta_g)}{(cos\theta_g + \mu sin\theta_g)} \quad 4.14$$

Or alternatively as a function of post-slip axial stiffness (with respect to Eq.4.6):

$$K_{in,sec,unloading} = \frac{b^2}{2} K_{ax,unloading} \quad 4.15$$

As inferred from Eq.4.12 and Eq.4.14, the after-slip rotational stiffness of the RSFJ depends only on the geometry of the damper and the stiffness of the discs.

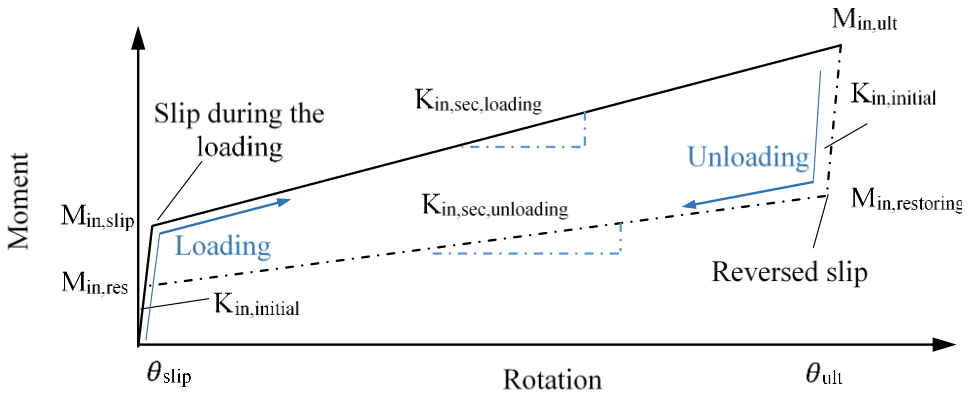

Figure 4.4: Passive self-centring hysteretic rotational response of RSF joint (flag-shaped hysteresis)

4.3 Lateral Instability of the Brace

4.3.1. *Buckling Load Quantification*

As in any member subjected to compressive forces, the main phenomenon that may interrupt the performance of the intended brace is the buckling during which the brace may fail due to sideway deflections rather than being axially compacted. Besides having an axial flag-shape behaviour, the RSFJ damper possesses a flag-shape moment-rotation behaviour when it is subjected to an in-plane moment. This implies a nonlinear rotational spring with passive damping. Placing this nonlinear rotational spring along the brace body will make it susceptible to lateral instability given that the secondary stiffness of RSFJ both in loading and unloading are considerably less than that of the brace body (shown in Figure 4.6). It is worth noting that the moment-rotation behaviour of RSFJ described in section 2.3.2 is based on the premise that equal bending moments are acting at both ends of the joint while it is not the case for brace application with RSFJ at the ends. However, this assumption can be valid if the length of the RSFJ is considerably less compared to the length of the brace. Furthermore, this assumption reduces the complexity of the analysis, yet estimates the buckling loads with acceptable accuracy. If it is assumed that the instability load of the brace with a nonlinear rotational spring (shown in Figure 4.6) is a function of the tangent rotational stiffness of the spring (refer to [127], the tangent rotational stiffness of the RSFJ ($K_{initial}$, $K_{in,sec,loading}$ and $K_{in,sec,unloading}$) can be put in the partial differential model developed and suggested in [174]. According to this model, the buckling load of a compressive member with a rotational spring can be calculated as:

$$P_{cr} = \alpha \frac{EI}{L^2} \qquad 4.16$$

where parameter L is the total length of the brace, EI is the flexural rigidity of the brace body and α is the minimum of nonzero real roots of the following algebraic-trigonometric equation [174] – proof can be found in Appendix B:

$$f(\alpha) = \beta tan(\delta_1\sqrt{\alpha}) - tan\left(\sqrt{\alpha}(1-\delta_1)\right)\left[\sqrt{\alpha}tan(\delta_1\sqrt{\alpha}) - \beta\right] \quad 4.17$$

In this equation, β is the relative stiffness of the RSFJ to flexural stiffness of the brace body, which differs for different phases of loading. The parameter δ is indicative of the relative position of the rotational flexibility (RSFJ):

$$\beta = \frac{K_{tan}.L}{EI} \quad 4.18$$

$$\delta_1 = \frac{L_1}{L} \quad 4.19$$

In which K_{tan}.is the rotational tangent stiffness ($K_{initial}$, $K_{in,sec,loading}$ and $K_{in,sec,unloading}$ for initial, post-slip loading and post-slip unloading stiffness, respectively) and L_1 is the distance between the pin and middle of the RSFJ as shown in Figure 4.6. For the relative positions of $\delta_1 =$ 0.1, 0.2, 0.3, 0.4 and 0.5, Eq.4.17 is solved by the nonlinear solver function of MATLAB software [175], and the numerical results of α are illustrated in Figure 4.5. As can be witnessed, increasing β results in higher values of α, implying a larger critical load. This increase will slow down gradually until α reaches a plateau ($\beta \to +\infty$) and converges to the Euler (elastic) buckling load for a simply supported column ($\pi^2 EI/L^2$), i.e., $\alpha = \pi^2$. Apart from that, by comparing different values of α and δ_1, it can be concluded that the larger δ_1 results in a lower buckling load for the same value of β. Therefore, the worst position for RSFJ is the middle of the brace while the best position seems to be at the end. Hence, the RSFJ is positioned at the end of the brace in the experimental campaign to be discussed in section 4.40 and section 4.5.

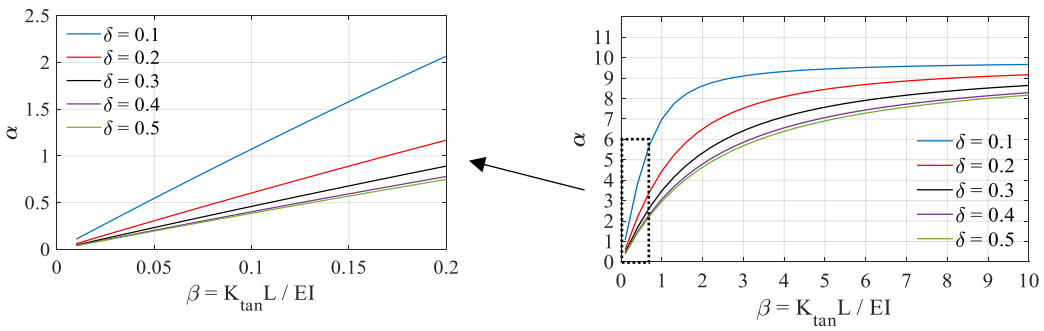

Figure 4.5: Different values of α based on different relative position and stiffness

Based on Figure 4.5, if β is small (lower than 0.2), the solution of Eq.4.17 α can be approximated by linear interpolation as $\alpha = \beta/\delta_1(1-\delta_1)$ – proof has been provided in Appendix B. Substituting it in Eq.4.16, the critical load can be estimated by Eq.4.20:

$$P_{cr} = \frac{K_{tan}L}{L_1 L_2} \tag{4.20}$$

By substitution of the tangent rotational stiffness of the RSFJ (Eq.44.12-15) into Eq.4.20, the following two approximate critical loads can be computed:

$$P_{cr,loading} = \frac{n_b b^2 L K_{stack}}{2L_1 L_2}\left(\frac{2sin^2\theta_g + \mu sin2\theta_g}{2cos^2\theta_g - \mu sin2\theta_g}\right) \tag{4.21}$$

$$P_{cr,unloading} = \frac{n_b b^2 L K_{stack}}{2L_1 L_2}\left(\frac{2sin^2\theta_g - \mu\, sin2\theta_g}{2cos^2\theta_g + \mu\, sin2\theta_g}\right) \tag{4.22}$$

where $P_{cr,loading}$ and $P_{cr,unloading}$ are the approximate buckling loads in the loading and unloading phase, respectively. The only difference between Eq.4.21 and Eq.4.22 is the sign of friction force. Therefore, it can be deduced that the buckling associated with unloading - $P_{cr,unloading}$ - can be interpreted as the restoring force if the brace has buckled in loading. Furthermore, it should be noted that there are supposed to be three types of buckling loads with respect to the rotational behaviour of the spring (moment – rotation response). Two stiffnesses are affiliated with the post-slip (low stiffness) phase of the flag-shape – $P_{cr,loading}$ and $P_{cr,unloading}$– and one is associated with elastic (high stiffness) parts of flag-shape hysteresis – $P_{cr,initial}$. The latter case is not considered in this study as it is much higher than those related to the flexible parts, and it is very unlikely for a brace to hit that force in the before-slip phase.

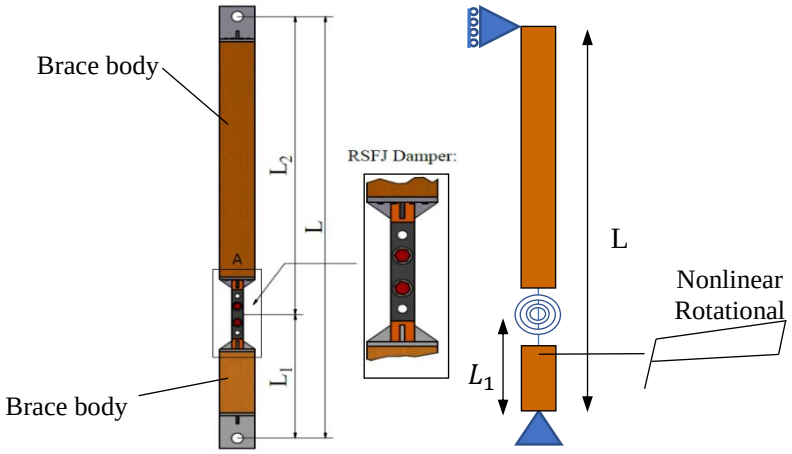

Figure 4.6: Analytical model for stability of the RSFJ brace

4.3.2. *Different Types of Brace Behaviour in Compression:*

According to a general stability rule [127, 176], when the axial load in a member approaches the buckling load, two equilibrium situations (known as the bifurcation in equilibrium) can exist for the member in the vicinity of the buckling load. The first situation is that the member buckles and the additional bending is resisted by the flexural strength of the member while in the second situation, the member does not buckle, and the additional axial load is resisted by the axial strength of the member. The first situation is referred to as stable equilibrium while the second is referred to as unstable equilibrium. This phenomenon is normally cited as the *bifurcation* theory [176]. In case of the RSFJ-brace assembly and due to the presence of the pre-stressing force in the RSFJ, this bifurcation point can appear at a different level of axial load (assuming that the sign convention is negative for compression and positive for tension). More specifically, depending on whether or not the slip force (F_{slip}) is higher than the critical load ($P_{cr,loading}$), there can be two different behaviours associated with the brace. In the first case, if the pre-stressing of the disc springs is relatively low in a way that the slip force is less than the critical load (shown in Figure 4.7.a), will be referred to as *low pre-stressed brace*, the bifurcation point (black filled circle) appears after-slip and is located at the intersection between $P_{cr,loading}$ and the flag-shape hysteresis curve (dark black line). At this specific point, the brace can follow two equilibrium paths. The first one (the continuous line) is the primary path (flag-shape), which is unstable (ball on a concave gravity field) after the buckling load and the RSFJ gets axially compacted in an unstable fashion. On the other hand, the second path is the dashed line during which the brace has a zero-lateral stiffness, so it exhibits a considerable lateral displacement, yet is stable (ball on a straight gravity field).

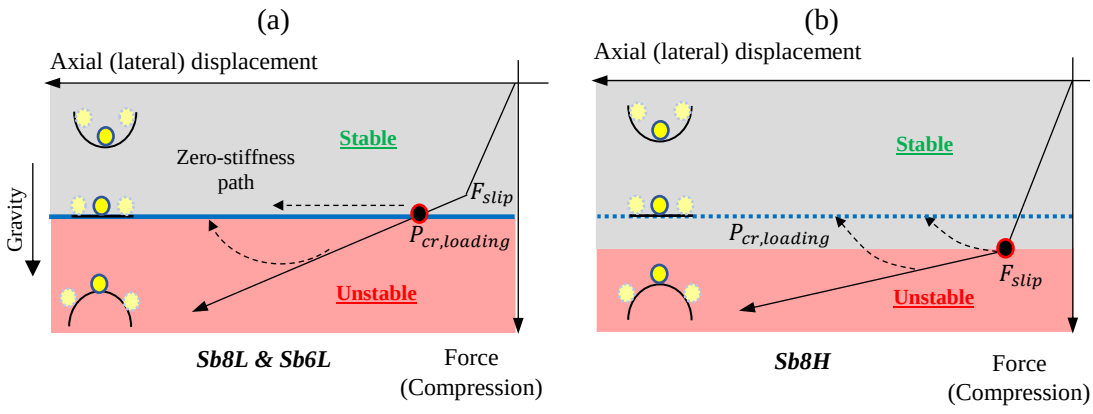

Figure 4.7: Different behaviour of brace: (a) When Slip force is less than critical load, (b) when Slip force is higher than the critical load

In the second case (Figure 4.7.b), if the pre-stressing of the disc springs is relatively high in a way that the slip force is higher than the critical load ($F_{slip} > P_{cr,loading}$), the bifurcation point is not located at the intersection between $P_{cr,loading}$ and the flag-shape hysteresis curve (dark black line) and may appear exactly at slip force or any higher force, which itself, depends on the imperfection of the system. The reason is that the prestressing force in the damper hinders the buckling and will postpone it to the after-slip situation. The difference to the previous case is that the system is always unstable (ball on a concave gravity field) after-slip because the force at any load after-slip is already beyond the buckling load. Secondly, there would be no zero-stiffness path, and any instability is accompanied by a strength degradation with minus stiffness [127]. A more detailed discussion has been provided in [164] regarding the brace performance in the loading and unloading phase.

4.4 Small-scale experimental test

A one third scaled timber brace from a real under-construction project in New Zealand was considered and tested under reversed cyclic loading to validate the formula developed for quantification of the buckling load. The test specimen was composed of a timber LVL grade 11 with an elastic modulus of 11 GPa. The cross-section of the specimen was square-shaped with 150 mm width. The tension and compression strength of the timber body was 600 kN and 810 kN parallel to the grain. An RSFJ that has already been tested [138] was attached at the end of the brace to act as the energy-dissipation mechanism. As it was discussed earlier, the end of the brace was picked as it is the best position in terms of decreasing the buckling possibility. The RSFJ dimensions are provided in Figure 4.8.c. The damper was attached to the timber body using eight self-tapping screws of 180 mm long and 7 mm diameter parallel to the grain to be able to resist a tensile capacity of the RSFJ. To track the damper displacement, two displacement gauges were installed on the sides of the RSFJ. Furthermore, to record the lateral displacement of the brace, two Linear Variable Differential Transformers (LVDTs) were employed. The experimental test setup including the instrumentations is portrayed in Figure 4.8.a and Figure 4.8.b. The employed specimens and their related characteristics are tabulated in Table 4.1 in which a different number of disc springs and pre-stressing force were used. The specimens are labelled as Sb (Small-scale brace), n_d (number of disc springs), L or H (Low or high pre-stressed). The low pre-stressed brace means that the slip force was less than the buckling load ($F_{slip} < P_{cr,loading}$) while the high pre-stressed brace means that the slip force was higher than the buckling load ($F_{slip} > P_{cr,loading}$). That a brace is a low or high pre-stressed determines the expected behaviour and the

type of instability. The expected brace performance in these situations was discussed in section 3.2.

The cyclic loading regime for the small-scale test is depicted in Figure 4.9 and had a maximum displacement of 9 mm, comparable to 1.4% drift of the scaled frame (assumed to be presentative of the design level earthquake).

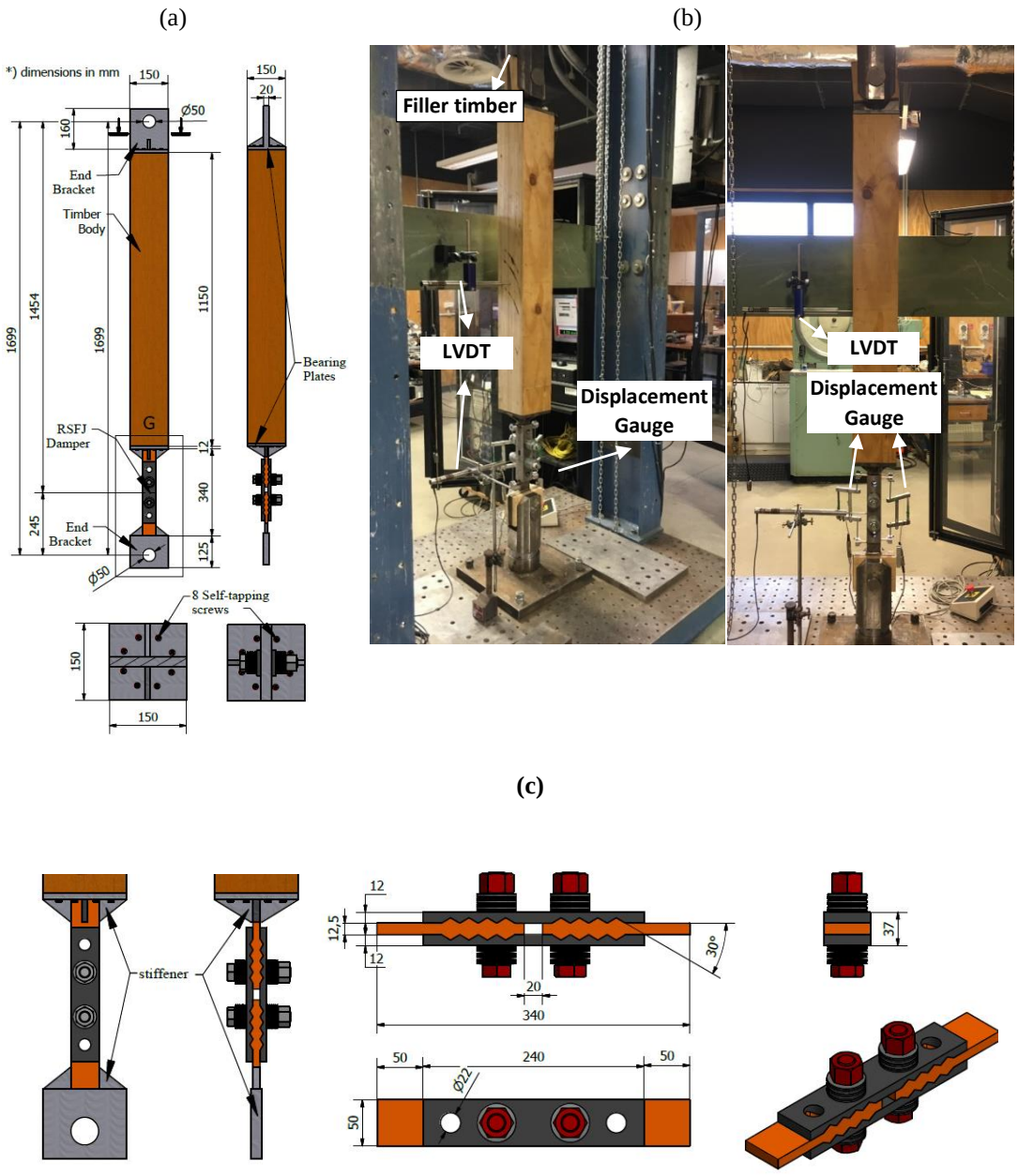

Figure 4.8: In-plane testing of the brace: (a) test specimen dimensions, (b) specimen in the testing apparatus, and (c) recruited RSFJ damper

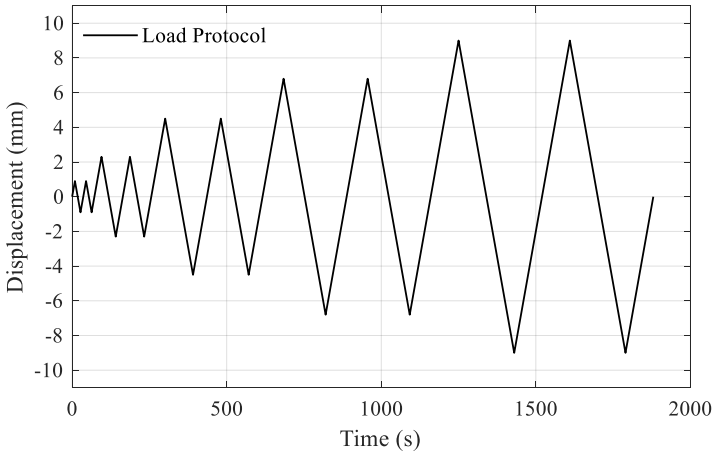

Figure 4.9: The loading protocol

Table 4.1: Test configurations for small-scale test

Specimen	n_d	F_{pr} (kN)	F_{slip} (kN)	F_{res} (kN)	F_{ult} (kN)	$F_{restoring}$ (kN)	K_{st} (kN/m)	$K_{in,sec,unload}$ (kN.m)	$K_{in,sec,load}$ (kN.m)	$\frac{EI_{body}}{L}$ (kN.m)	$P_{cr,load}$ (kN)	$P_{cr,unload}$ (kN)
Sb8L	8	5.3	8.5	4.2	24.7	12	4.3	1.21	2.48	144	11.7	5.7
Sb6L	6	5.7	9.1	4.4	32	15.6	6.4	1.8	3.7	144	17.5	8.5
Sb8H	8	10.3	16.4	8	31.6	15.4	4.3	1.21	2.48	144	11.7	5.7

4.4.1. *Small-scale test results*

Figure 4.10 and Figure 4.11 show the test results of the small-scale test. The first two tests were performed on the specimens Sb8L and SB6L while the last test was performed on the specimen Sb8H. The possible response of the samples Sb8L and Sb6L was discussed and explained in section 3.2 and indicated in Figure 4.7.a. However, the possible response of the sample Sb8H was the one indicated in Figure 4.7.b. It should be noted that no intentional imperfection (or eccentricity of the applied load) was imposed on the system, yet the inherent imperfections of the brace such as out-of-plane crookedness were inevitable. The buckling loads were calculated using the approximate expressions (Eq.4.21 and Eq.4.22) as β was smaller than 0.2. The flag-shape hysteresis loops for specimens Sb8L and SB6L were obtained and are shown in Figure 4.10.b-e. The left figures show the axial displacement versus the axial load, and the right figures show the lateral displacement of the brace (output of bottom LVDT) versus the axial load. As can be seen, the tension part of the experimentally obtained diagrams was in good agreement with the

predicted analytical flag-shapes (the black dashed line) while in the compression, the results differed considerably with the predicted flag-shape (black dashed line) due to buckling occurrence.

For sample Sb8L, the situation was low pre-stressed implying that the critical load corresponding to the loading phase ($P_{cr,loading}$) was 11.7 KN and was higher than the slip force (8.5 KN). Therefore, the first case explained in section 4.3.2 (Figure 4.7.a) governed the brace behaviour. It is after the fourth cycle that the bifurcation appeared where the flag-shape (the primary path) was intersected by the buckling load (the secondary path). Surprisingly, the system followed the unstable path in the ninth cycle and did not buckle. However, after this cycle, the system followed the stable zero-stiffness path after the bifurcation point and buckled during the loading for the rest cycles. That the brace did not buckle up to the ninth cycle was indicative of the fact that the second-order effect due to the inherent imperfections was negligible. However, after the ninth cycle, the secondary order effect became larger as the axial load increased and contributed to encouraging the brace to buckle. It should be also noted this could not be properly quantified as it depends on the manufacturing, erecting of the structure, test setup and may differ case by case.

A similar type of behaviour (Figure 4.7.a) was expected for Specimen Sb6L as it was low prestressed. Regarding this sample, the slip force (F_{slip}) and the buckling force corresponding to loading ($P_{cr,loading}$) was estimated to be 9.1 kN and 17.5 kN, respectively. As it can be seen, the brace buckled at the predicated buckling load ($P_{cr,loading}$) for all cycles. In the unloading phase, the brace is restored at the buckling load corresponding to unloading ($P_{cr,unloading}$).

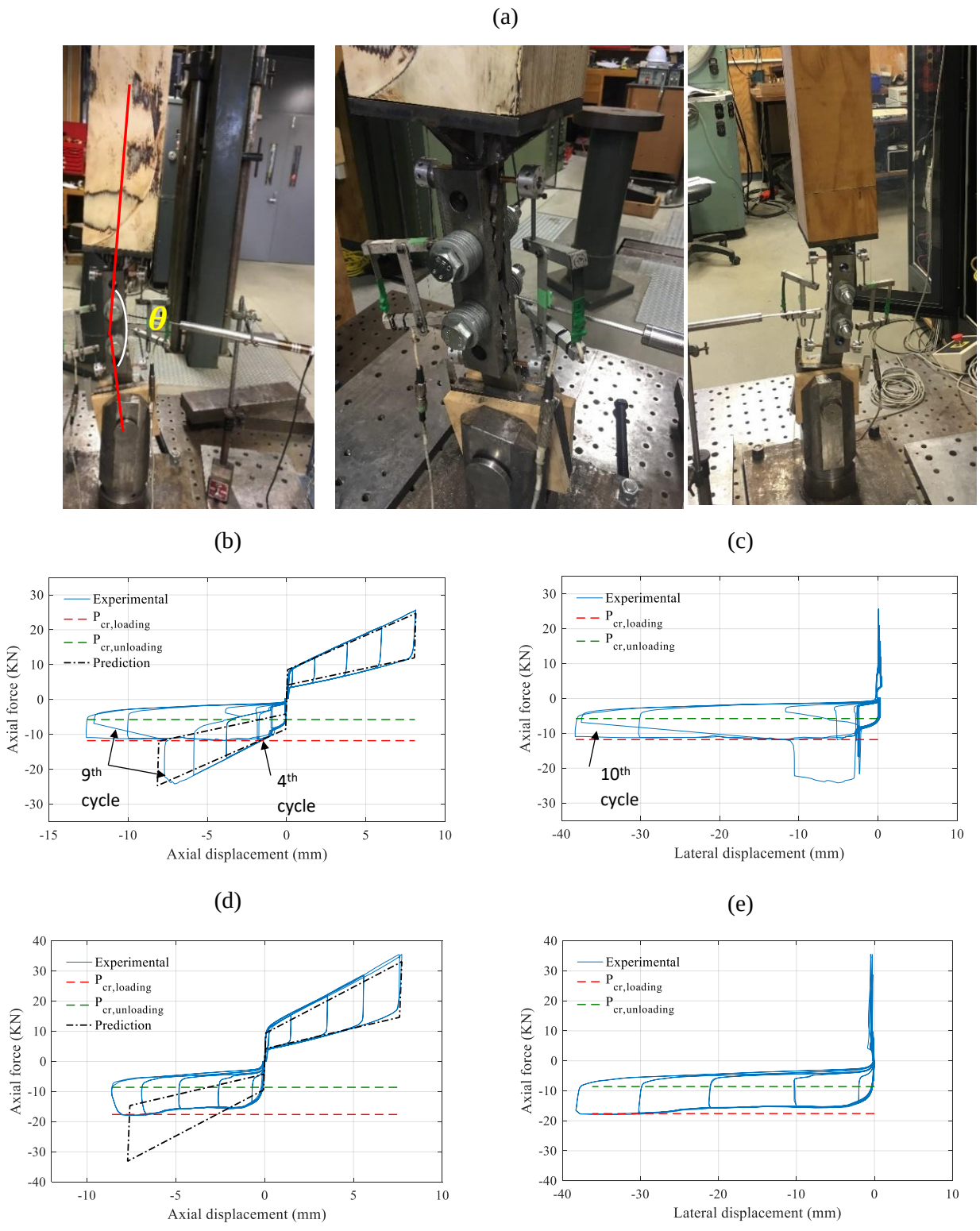

Figure 4.10: Test results for low pre-stressed RSFJs: (a) the in-plane buckling mode shape, (b) hysteresis curve for configuration 1, (c) lateral displacement vs axial force for configuration 1, (d) hysteresis curve for configuration 2, (f) lateral displacement vs axial force for configuration 2

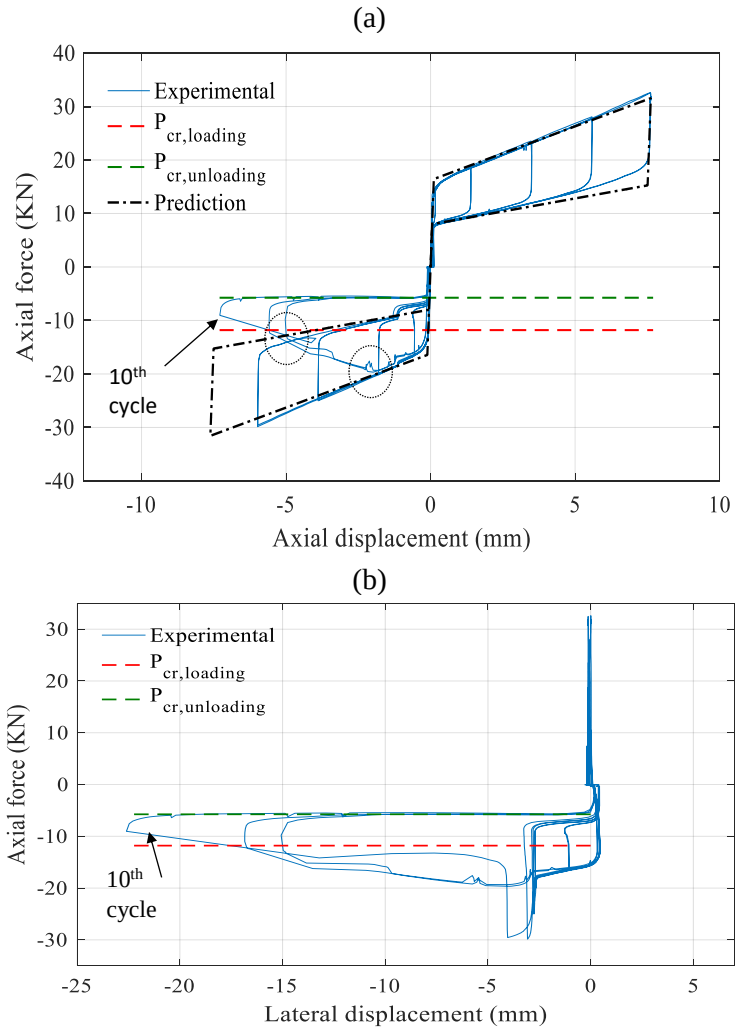

Figure 4.11: Test results for high pre-stressed RSFJs: (a) hysteresis curve for configuration 3, (b) lateral displacement vs axial force for configuration 3

The high pre-stressed model behaviour was explained in section 4.3.2 and shown in Figure 4.7.b and it was the expected behaviour for the sample Sb8H. The acquired hysteresis curve is shown in Figure 4.11.a. The slip (F_{slip}) and buckling load ($P_{cr,loading}$) for this system were predicted to be 16.4 kN and 11.7 kN, respectively. When the slip force is higher than the buckling load (Figure 4.11.b), the system becomes unstable as soon as it slips, and the axial load in the brace may degrade to $P_{cr,loading}$ with minus stiffness. It is worth to mention that no instability was witnessed until the 4th cycle, yet for the rest cycles, the axial load firstly peaked at around 20 kN and then fell to $P_{cr,unloading}$ to unload.

In conclusion, the developed buckling formulas managed to predict the instabilities for both low pre-stressed and high pre-stressed specimens. Furthermore, although the instability was damage-

free and restored each time, it reduced the brace compressive strength. Thus, it is preferred to avoid it. The next section discusses how this can be attained.

(a)

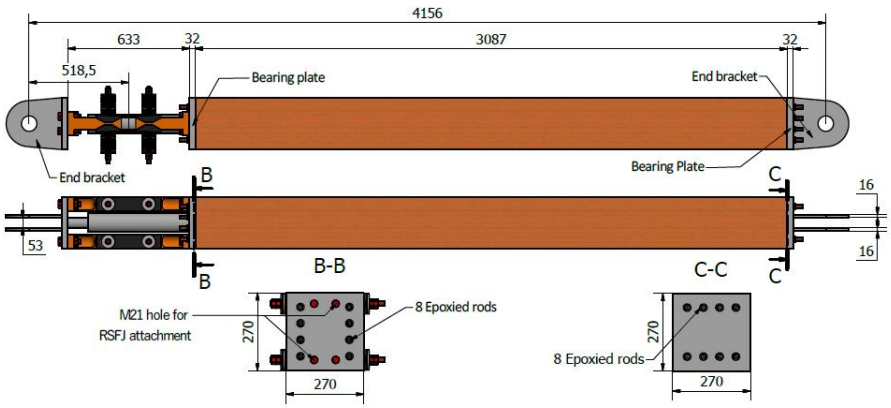

(b)

(b)

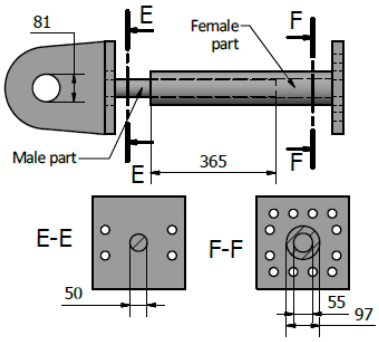

(c)

(d)

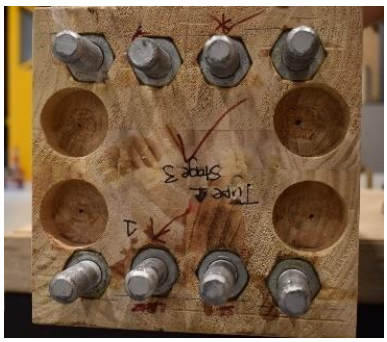

(e)

Figure 4.12: (a) drawing for timber brace, (b) drawing for Anti-buckling tubes for ABM, (c and d) Epoxied rods and (e) real employed ABT

4.5 Full-scale Experimental test:

The root cause of lateral instability of the brace is the rotational flexibility that appears within the brace due to the installation of the damper (RSFJ). Therefore, local strengthening of the brace where the damper is located seems like one of the effective solutions. To do so, a telescopic configuration using two sliding tubes is used to increase the rotational stiffness of the brace where the RSFJ is located (shown in Figure 4.12.a). The important point that should be taken into consideration is that these two sliding tubes should possess the required stiffness and strength so that the global buckling load is higher than the force demand in the brace. In order to quantify this, the same model explained in section 4.3.1 can be used based on the premise that the Anti-buckling Tubes (ABT) and damper(s) act in parallel. Therefore, the input rotational stiffness into the stability model is assumed to be the summation of the dampers' rotational stiffness and ABM rotational stiffness. The force and displacement demand was assumed to be 400 kN and 50 mm for the full-scale brace.

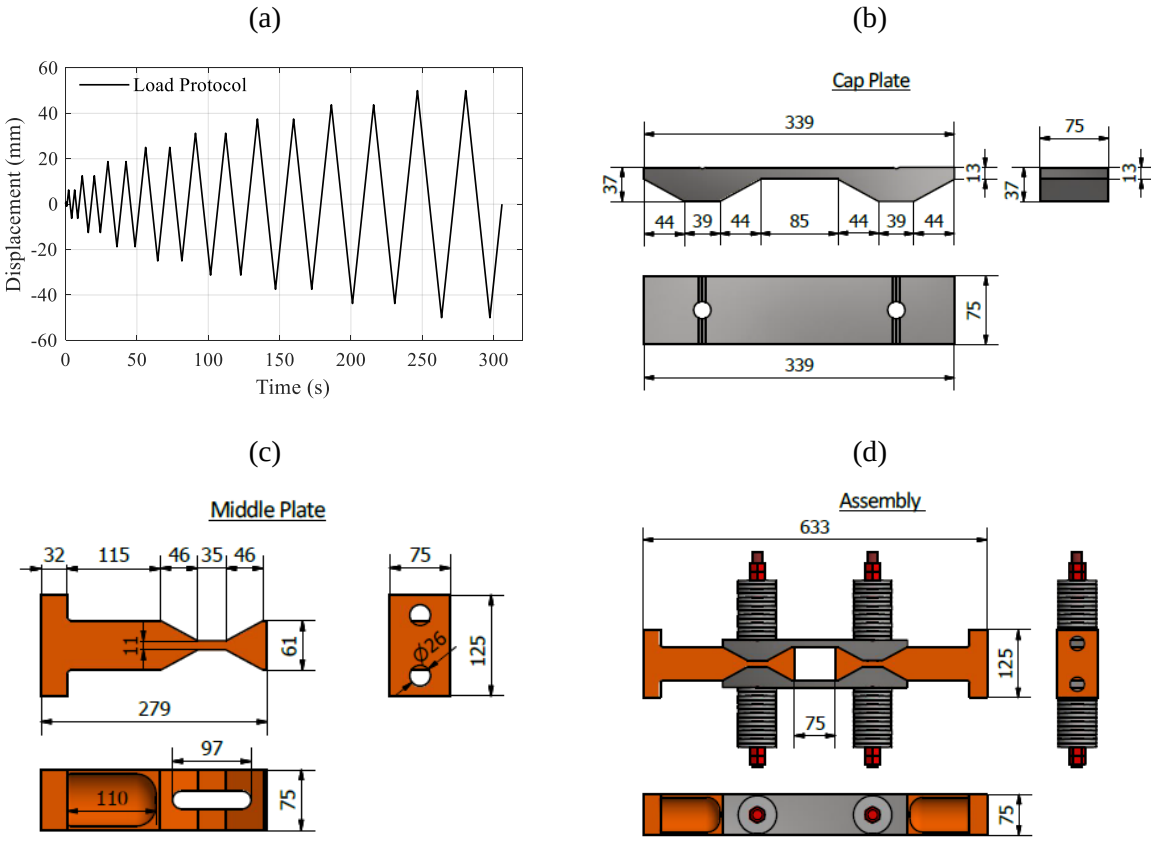

Figure 4.13: (a) Load protocols applied to two RSFJs dampers, (b) Cap plate, (c) Middle plate and (d) Assembly of RSFJ

4.5.1. *Design and fabrication of the brace specimen*

The specimen was borrowed from a real under-construction project in New Zealand. This brace was used in the form of chevron configuration within a frame with 3340 m height and 6750 m width. The brace body was composed of a timber Glue-Lam GL8 grade with an elastic modulus of 8 GPa. The cross-section of the specimen was square-shaped with 270 mm width. The ABT was composed of two circular hollow sections (shown in Figure 4.12.b). Two RSFJs (shown in Figure 4.13.d or Figure 4.14.a) were attached to the end of the brace to provide energy-dissipation and self-centering characteristics. Besides, all the connections were designed with respect to the brace capacity.

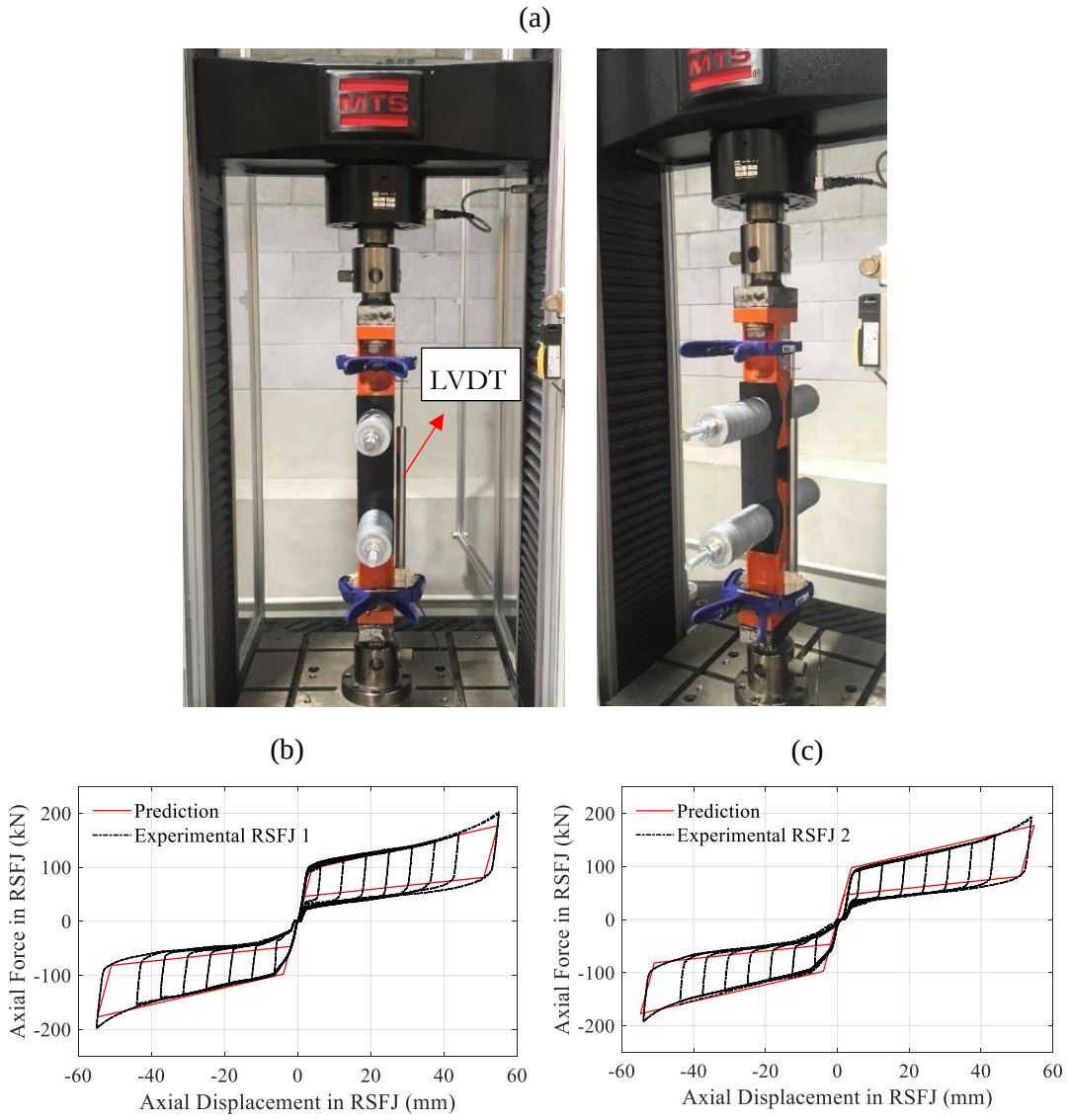

Figure 4.14: (a) setup for the joint component test, (b) results of RSFJ 1, (c) results of RSFJ 2

Regarding the design of ABT, it should be noted that the process explained in section 4.3.1 was followed to quantify the buckling load but Eq 4.18 is replaced by the following equation assuming that the ABT is working in parallel to RSFJ resulting in summation of the damper tangent stiffness with rotational stiffness of the ABT as:

$$\beta = \frac{[K_{tan} + K_{ABT}].L}{EI_{body}} \quad 4.23$$

The rotational stiffness of the ABT can be calculated from the well-known virtual work method (will be discussed in the next chapter – more info and the relevant equations have been provided in appendix B). The proper ABT was designed in a way that the new elastic buckling load was higher than the force demand. If no ABT was used, the buckling load of the brace would have been extremely low (19.5 kN); however, when the ABT was used, the buckling load improved to 1353 kN (force demand was 400 kN).

4.5.2. *Component RSFJ test*

The RSFJ dampers for the large-scale test were designed with respect to force and deflection demand in the brace, which was considered to be 400 kN and 2.5% drift ratio of the frame or 50 mm in the joints. As two dampers were working in parallel, each of them was designed for 200 kN force. The dampers were made using mild steel with a minimum yield strength of 340 MPa. The clamping rods were 8.8 grade with an ultimate strength of 800 MPa. The design parameters of the dampers are listed in Table 4.2, and the components' drawings are provided in Figure 4.13.

Table 4.2: Design parameters for RSFJs

Parameters	Definition	Value
n_d	Number of disc springs per bolt	20
n_b	Number of bolts per side	1
θ_g	Angle of grooves	28.6
F_{pr}	Prestressing load of the disc springs' stack	65 kN
F_u	Flat load of disc springs' stack	120 kN
F_{slip}	Slip force	97.5 kN
F_{res}	Residual force	46.3 kN
F_{ult}	Ultimate force	177.1 kN
$F_{restoring}$	Restoring force	84.2 kN

According to current literature, it is suggested that the AISC 341 load protocol for Buckling Restrained Braces (BRBs) can be employed for the purpose of the quasi-static test (Erochko et al. 2014a). This protocol necessitates that the brace should possess twice the ductility capacity of the design story drift together with an accumulative inelastic axial ductility capacity ratio of 200. As such, the quasi-static loading protocol, shown in Figure 4.13.a in accordance with this standard is used for the component RSFJ testing. The design story drift was assumed to be 1.4% or 45 mm, which was equivalent to 25 mm displacement in the dampers. The maximum displacement of the dampers was assumed to be 50 mm, which is equivalent to 80 mm frame drift or 1.8 times of design drift. The tested RSFJ components and the assembly are illustrated in Figure 4.14.b and Figure 4.14.c.

The experimental test on joints was performed according to mentioned loading protocol using MTS 300kN UTM (Universal Testing Machine) shown in Figure 4.14.a during which the displacement was recorded using a LVDT attached to the right side of the joint. The experimental result of the tests is shown in Figure 4.14.b and Figure 4.14.c in which they are compared to analytical results. As it can be seen, the results are in good agreement with what was predicted analytically.

4.5.3. *Fabrication of the test setup*

Figure 4.15 illustrates the test setup that was used for the demonstration of the brace. The steel vertical column was composed of two channels (PFC 180) attached in a back to back configuration with a 41 mm gap using batten plates. It should be mentioned that there were two lateral supports to limit the out-of-plane displacement of the column and stabilize the specimen in cyclic loading (shown in Figure 4.15.d). The setup was designed in a way that the brace can experience the target force and displacement (400 kN at 50mm displacement). The loading process was performed via a 250 kN MTS actuator with ±125 mm stroke capacity, which was positioned at the height of 4250 mm from the strong floor. For the purpose of data acquisition, one LVDT and one drew wire was used to measure the joint and brace response, respectively during the test. The instrumentation system is depicted in Figure 4.15.d.

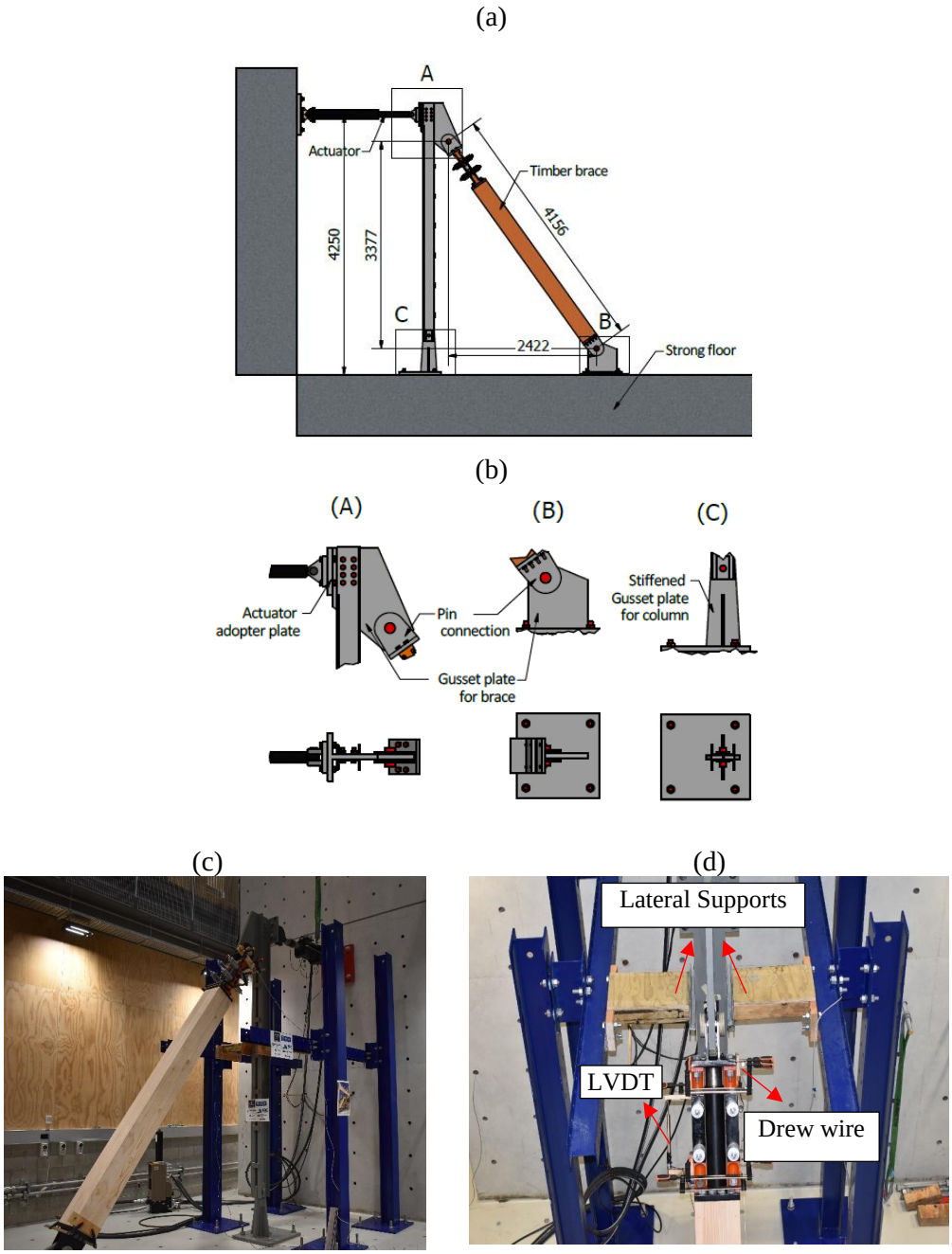

Figure 4.15: Test set up: (a) side view, (b) top view, (c) front view and (d) setup in reality

4.5.4. *Full-scale test results*

The full-scale timber brace was designed and tested under reversed cyclic loading to investigate the efficiency of the ABT, for which the loading protocol in Figure 4.16 was employed. Note that the loading protocol used here is different from what was applied to the tested joints, yet it was

still designed to meet the AISC 341 requirements. The loading rate used for the test was 0.3 mm per second, similar to what was used for the component testing.

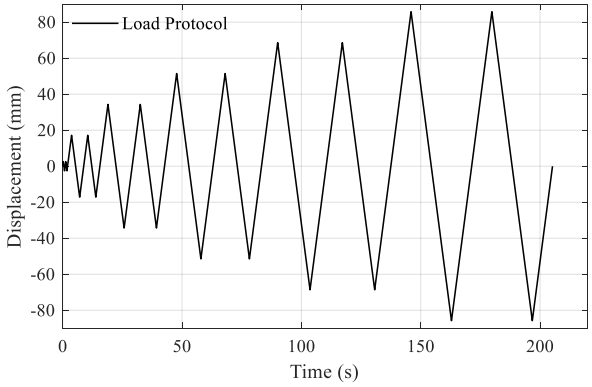

Figure 4.16: Load protocol applied to the brace via actuator

The brace performance subjected to mentioned loading protocol is illuminated in Figure 4.17 where the drew wire readings are shown in Figure 4.17.a and indicative of the cumulative deformation of all components including the internal deflections of the brace body, the deformation of the embedded epoxied rods and end gusset connections. The readings of the LVDT are shown in Figure 4.17.b which only included the displacement of the damper. As can be vividly observed, no instability in the compression was witnessed and the flag-shaped response was symmetrical, demonstrating the effectiveness of the ABT. It should be also noted that if no ABT was used in the system, the buckling load of the brace was extremely low (19.5 kN) because of the long span of the brace and high number of disc springs utilized for the damper. Furthermore, as it can be observed, the initial stiffness of the brace in the compression zone softened faster than the tension part that was a consequence of the extra moment on the brace due to the second-order effect. The secondary order effect appeared unavoidably due to the presence of the clearance in the connections, out-of-plumpness of the brace and the accidental actuator eccentricity. Furthermore, there is an ongoing research program about the effects of the secondary order forces (moment and shear) that appears and applies additionally in the compression zone on the brace components. The possible extreme consequences of the secondary order effect can be the formation of a plastic hinge in either the brace body or ABT and finally instability of the brace. This is investigated in greater detail in the next chapter.

4.1 Summary and conclusion

This paper introduces a new self-centring timber brace that utilizes a damage-free self-centring joint (RSFJ). Furthermore, it has been shown by a small-scale test that the brace is prone to lateral instability mainly because of the rotational flexibility that will arrive with the installation of the damper. The buckling was damage-free, managed to restore at end of unloading and provided

passive damping; however, it was preferred to be avoided as it may bring complexity and unpredictability to the brace performance. Apart from that, it was shown that the middle of the brace was the worst location to install the damper while the end area adjacent to the pin supports was the best position for the instalment. Both approximate and exact formulas have been provided to predict the buckling load and were validated using a small-scale test, which can be used for design purposes. In order to address the buckling, a telescopic configuration using two sliding tubes has been suggested for which the stiffness requirement was also provided and tested using a full-scale quasi-static test. The results demonstrated symmetrical flag-shape behaviour for the brace validating the effectiveness of the anti-buckling concept.

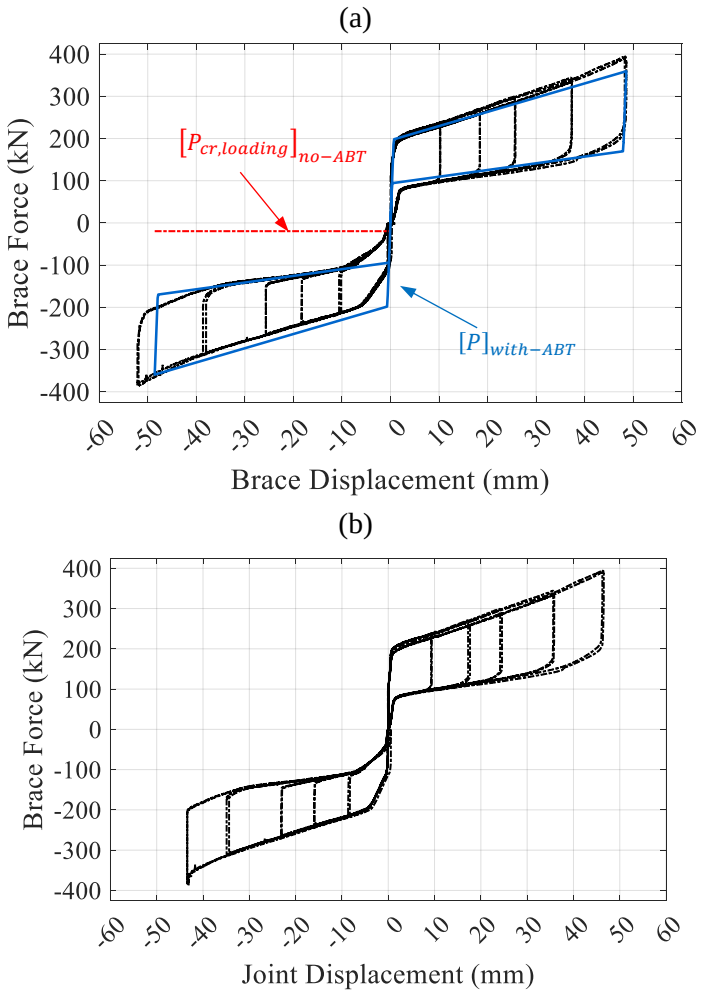

Figure 4.17: Brace Performance (a) Brace force VS Brace displacement, (b) Brace force VS RSFJ displacement

5 Manuscript.3 - Global Inelastic Buckling of the RSFJ-Brace

Based on the article Submitted to peer-reviewed "Journal of Constructional Steel Research",

5.1 Abstract

The self-centring RSFJ brace is a relatively new system providing high stiffness, damping and self-centring for a structure. Past studies have shown that the unstrengthened RSFJ brace capacity in compression might be too low because of the damper rotational flexibility leading to a premature elastic buckling of the brace. A concept of telescopic tubes was introduced to be put in parallel to the damper(s) whereby the elastic buckling of the brace was successfully postponed to a certain calculated limit. However, the failure load, collapse mode and mechanism were not investigated. In this sense, herein a framework, entitled a Simplified Collapse Mechanism Approach (SCMA), is proposed to quantify the collapse load of the brace at the ultimate limit state so that a designer is able to design the brace knowing the ultimate load and collapse mode. The process tends to be more complex than the conventional Concentrically Braced Frames (CBFs) because of the non-continuity that appears as a result of the installation of the dampers. Hence, the plastic hinge may form in different locations rather than in the mid-span. To validate the proposal and performance of the brace, static, dynamic, and destructive experimental tests have been conducted on the steel self-centring brace.

5.2 Introduction

In an attempt to increase the disaster-resiliency of the structures against seismic hazards, self-centring low-damage structures have been developed with the main intention of providing damage-avoidant and/or replaceable seismic fuses [17]. Priestley et al [51] started to study the performance of these systems in the late nineteenth century through the program entitled "Pre-cast Seismic Structural Systems or PRESSS". In this program, the post-tensioned cables were used with dampers to bring the flag-shape hysteresis performance. Christopoulos et al. [77] extended the technique to the braced frame structures and developed a new self-centring energy dissipative brace using two hollow steel box sections, post-tensioned tendons and friction dampers. Several researchers have also developed similar concepts but with different mechanisms and sources of damping [81, 83, 85, 86, 90, 177-180].

The Resilient slip friction joint (RSFJ) is relatively a new self-centring friction damper that dissipates the input energy through a passive damping and a slip-friction mechanism [137], which can be applied in different lateral load resisting systems. Among different applications, it can be referred to the self-centring tension-compression braces [54, 98, 165], self-centring tension-only braces [158, 181], rocking timber or concrete shear walls [159, 160], rocking steel braced frames with shear links [161], Moment Resisting Frames (MRFs) [162] and rotational links [173].

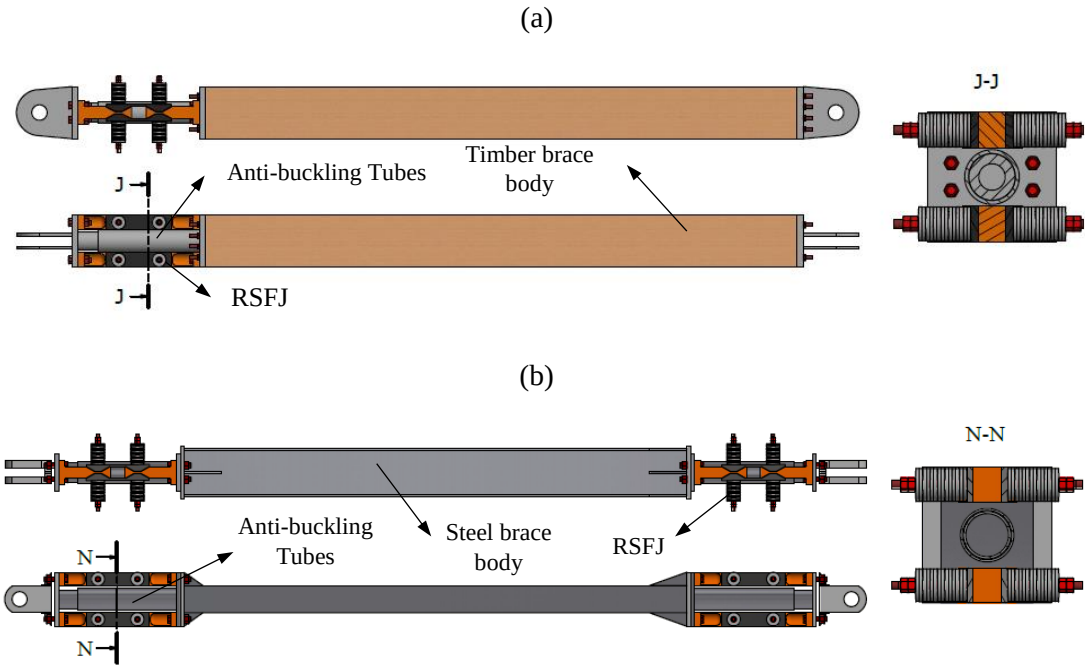

Figure 5.1: (a) RSFJ brace with one damper and timber brace body [165], (b) RSFJ brace with two dampers and steel body

RSFJ brace assembly is a self-centring brace that is composed of three main elements as depicted in Figure 5.1. The first element is the damper, which depending on the displacement demand can be installed in either one or two locations along with the brace (Figure 5.1.a or Figure 5.1.b). The second element is the brace body, which depending on the architectural or structural considerations can be made up of either timber or steel. The last but not the least element is the telescopic steel tubes entitled "Anti-Buckling Tubes or ABT", which are responsible to strengthen the brace where dampers are located, thereby increasing the compressive elastic buckling capacity of the brace. Previous studies [98, 164, 165] demonstrated that if the RSFJ brace is not equipped with the ABT, the compression capacity of the brace would be very low because of the rotational flexibility of RSFJ. To further strengthen the brace against premature instability, the telescopic ABT was installed in parallel to the damper(s) to increase their rotational stiffness [165]. The closed-form equation to calculate the elastic buckling of the strengthened brace with ABT was proposed in the previous study for the case of a brace with one non-continuity (Figure 5.1.a) [165].

In this regard, it was shown that even if the elastic buckling capacity of the brace is improved with ABTs, this load cannot be a reliable indicator for the design as the ultimate load can be lower than the elastic buckling [182]. In fact, the ultimate capacity of the brace in compression might be lower than that improved elastic buckling capacity due to the arrival of the second-order actions. Furthermore, the failure mode of the brace was still unclear. This paper first deals with establishing a proper framework for the design of the RSFJ brace for ultimate strength in compression, then validate it with experimental tests. In this process, the failure mode of the brace will be also discussed.

5.3 Concept of Simplified Collapse Mechanism Analysis (SCMA)

The behaviour of almost any steel column when subjected to a compressive load is shown in Figure 5.2. with the black continuous line. The lateral deflection will increase as the axial load grows due to the second-order effects ($p-\delta$), and the rate of this increase will accelerate as the axial load approaches the Euler (elastic) buckling load asymptotically. During this travel, a plastic hinge will form at the midspan of the column due to the combined effect of axial force and second-order moment. If the column is stocky (relatively small slenderness ratio $\lambda = L/r$), the plastic hinge will form sooner than the axial load gets close to the elastic buckling load with a small portion of lateral displacement (Figure 5.2.a). On the contrary, if the column is slender, the plastic hinge will form at relatively large lateral displacement and at a load very close to the elastic buckling (Figure 5.2.b). This load at which the column becomes mechanism and unstable can be regarded as the ultimate strength of the column and can be well approximated using "elastic perfectly plastic analysis" (see chapter 8 of Bažant, Z.P. and L. Cedolin [127]), which is referred to as SCMA here. The basis of this method lies in intersecting two curves namely: (i) stiffness deterioration (shown with ascending blue dash-dot line in Figure 5.2) and (ii) strength deterioration (shown with the descending red dash-dot line in Figure 5.2). The first curve shows the behaviour of an imperfect column with an inherent initial out-of-straightness and tends to converge to the Euler load asymptotically. The latter curve shows the strength of the member in the presence of axial load. It should be noted that if the member is determinant, the strength deterioration curve is governed by the section strength mainly because the formation of one plastic hinge is enough to make the system a mechanism. However, if the member is indeterminate, the strength deterioration curve should be derived from the plastic analysis. This is out of the scope of the current chapter and is further discussed in appendix B for interested readers. In case of a pin-pin column (determinant system), the strength deterioration curve is, in fact, the moment-axial load interaction curve. This method is introduced and employed in the

literature as an alternative method for approximating the ultimate strength of the compressive members like columns and BRB braces [31, 32, 127].

The stiffness deterioration curve can be well approximated using Eq.5.1 [127] – proof has been provided in Appendix B, which, in fact, illustrates the impact of second-order actions ($P-\delta$) on the axial performance of the column:

$$P(\delta) = P_{cr}\frac{\delta}{\delta + \delta_0} \tag{5.1}$$

where P_{cr} is the elastic or Euler buckling load, δ is the lateral deflection at midspan measured from the straight line (the undeflected midspan of the column) (Figure 5.2.b), and δ_0 is the initial-imperfection of the column at midspan, normally assumed to be ($L/1000$) assuming no erecting tolerance. The strength deterioration curve can be approximated conservatively as Eq.5.2 for determinant system ignoring the variation for different structural shapes [183, 184]:

$$\frac{P}{P_n} + \frac{P\delta}{M_p} = 1 \tag{5.2}$$

where P_n is the squash load and equals the yield stress of the steel multiplied by the gross cross-section area ($A_g F_y$). M_p is the plastic flexural strength of the section (ZF_y) assuming that the section is compact enough to develop a perfect plastic behaviour without any prior local instability. If Eq.5.2 is rearranged with respect to the axial load, the strength deterioration curve, as a function of the lateral displacement of the column, would yield as below:

$$P(\delta) = \frac{M_p}{\frac{M_p}{P_n} + \delta} \tag{5.3}$$

From intersecting the mentioned two curves (Eq.5.1 and Eq.5.3) and some mathematical simplification, the lateral deflection at which the plastic mechanism would form (δ_{int}) will be derived as:

$$\delta_{int} = 0.5M_p\left[\frac{1}{P_{cr}} - \frac{1}{P_n} + \sqrt{\left(\frac{1}{P_{cr}} - \frac{1}{P_n}\right)^2 + \frac{4\delta_0}{M_p P_{cr}}}\right] \tag{5.4}$$

Finally, the ultimate (collapse) load of the column can be calculated if the intersection point is input to either of the stiffness or strength deterioration curves as:

$$P_{ult} = P_{cr}\frac{\delta_{int}}{\delta_{int} + \delta_0} \quad 5.5$$

Or

$$P_{ult} = \frac{M_p}{\frac{M_p}{P_n} + \delta_{int}} \quad 5.6$$

(a)

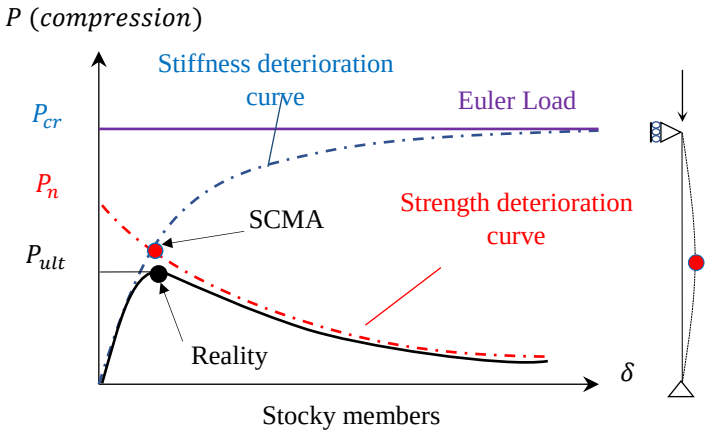

(b)

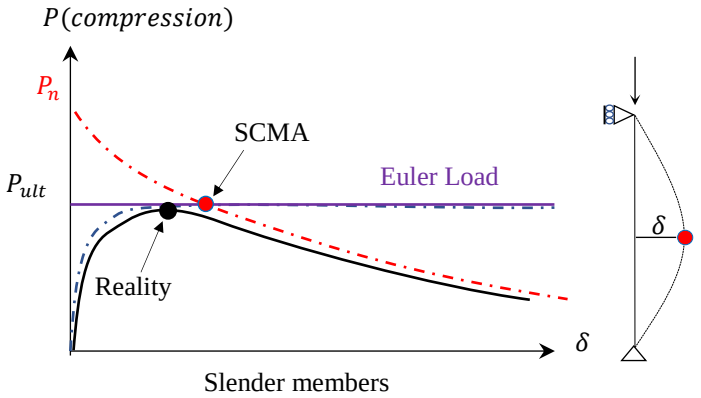

Figure 5.2: Performance of the column subjected to compression force (a) stocky members and (b) slender members [127]

5.3.1. *Validation with codes prescription for the conventional braces*

5.3.1.1. Steel Columns according to NZS 3404 and AISC 360

Though a large number of efforts in the twentieth century on the calculation of the ultimate strength of the column [121], most of the international building codes now use the empirical curves to calculate the ultimate strength of a column in the interest of simplicity and accuracy. In this section, the proposed SCMA method is compared with both AISC 360 and NZS 3404 prescriptions just to validate the methodology. In this manner, three steel section types namely, SHS (Square Hollow Section), UC (Universal Column or IPB) and UB (Universal Beam or IPE) were opted. The slenderness ratio (λ) of the hypothetical column was assumed to vary between zero and 300 while the end condition was assumed to be the ideal pin–pin. The steel material was assumed to be mild steel with a yield stress of 340 MPa and an elastic modulus of 200 GPa. The resultant ultimate forces calculated from Eq.5.5 or Eq.5.6 based on SCMA for all structural sections were calibrated with the cross-section area and are plotted in Figure 5.3 for different slenderness ratios.

As evident in Figure 5.3, for the slender columns, the result of SCMA is completely matching the codes. However, for the stocky columns, SCMA slightly overestimates the ultimate load. The reason can be attributed to two phenomena. The first reason is that the effect of residual stress is not included in the SCMA, which partially resulted in the overestimation. The second and more important reason is that SCMA always gives the upper bound of the result. Given Figure 5.2, it can be seen that the intersection point (red dot) is always higher than the real value (black dot) of ultimate capacity, which will result in overestimating the capacity. This overestimation can be compensated with a calibration factor based on slenderness [165].

5.3.1.1. Timber Columns according to NZS 3603 and Eurocode 5

In case of timber braces (columns), the cross-section does not have the capability to develop a fully inelastic behaviour, contrary to the steel members with compact section, mainly because the extreme fiber in tension due to second-order bending would experience a tension fracture as a result of its limited capacity of inelastic deformation (brittle). In other words, and as shown in Figure 5.4, a timber column's performance is different from a steel one in terms of post-inelastic strength and ductility. A timber column would experience a dramatic and sudden strength deterioration as soon as it reaches its ultimate capacity [185] due to progressive tension fracture.

(a)

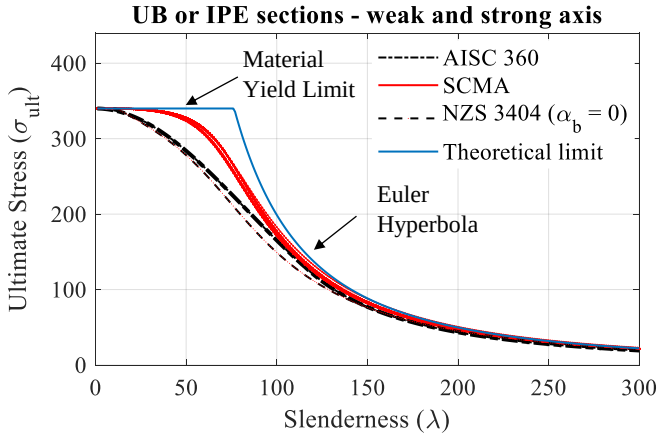

(b)

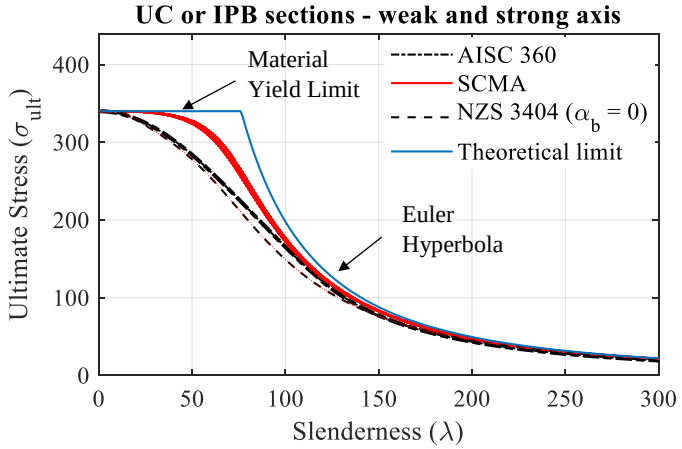

(c)

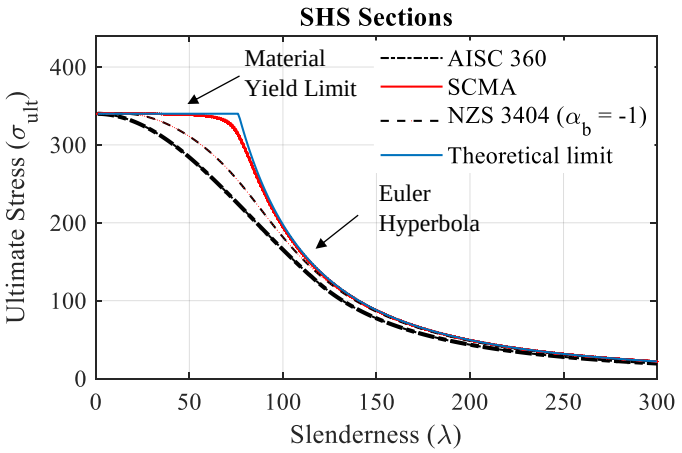

Figure 5.3: Comparison among SCMA, AISC 360 and NZS3404 (a) UB section, (b) UC section and (c) SHS section

Therefore, to predict the ultimate load, the elastic section capacity should be considered for the combined action while respecting that at what stage the tension stress would reach the characteristic tension stress. More specifically, Eq.5.2 should be modified as Eq.5.7 [186-188], simplified combined action formulation, in which the squash load is replaced by $(P_n = A_g f_c)$ and the plastic flexural strength of the section is replaced by the elastic capacity ($M_e = Sf_b$). Parameters f_c, f_b and S are the characteristic compressive, bending stress and elastic modulus of the section, respectively. In this manner, the intersection point between stiffness and strength deterioration curves should be modified accordingly as shown in Eq.5.7:

$$\frac{P^*}{A_g f_c} + \frac{M^*}{Sf_b} = 1 \qquad 5.7$$

$$(\delta_{int})_{body} = 0.5 Sf_b \left[\frac{1}{P_{cr}} - \frac{1}{A_g f_c} + \sqrt{\left(\frac{1}{P_{cr}} - \frac{1}{A_g f_c} \right)^2 + \frac{4\delta_0}{Sf_b P_{cr}}} \right] \qquad 5.8$$

It is extremely important to note that the interaction curve shown in Eq.5.7 is effective at the section level. The interaction formulation that most of the building codes (NZS 3404 [189] and Eurocode 5 [190]) have adopted today is only valid when the member strength is intended to be quantified and not the section strength. If the code interaction formula is envisioned, two noticeable differences can be detected compared with Eq.5.7. The first is that in the denominator of the first term in Eq.5.7, the term in the code-format equation is, indeed, the member axial strength rather than the squash load. The second difference is that in the code-format equation, the applied moment in the numerator of the second term is amplified by a factor greater than one to account for the second-order effect, which is absent in Eq.5.7.

Here, in this study, an alternative way has been proposed to quantify the member strength because the code procedure is not applicable to be used for the proposed self-centring brace due to the installation of the dampers and non-continuity(ies) in the length of the brace (refer to section 1.4). However, the procedure has been validated using prismatic continuous columns against the code results and then generalized to self-centring brace applications.

Similar to the previous section and as evident in Figure 5.4, the resultant of the SCMA method for the different timber products - Glued Laminated Timber (Glulam) and Laminated Veneer Lumber (LVL) - is very close to both New Zealand code (NZS 3603) [186, 189] and Eurocode 5 [190]. The point that should be highlighted here is that the SCMA provides a closed-form unique equation matching the code results for different timber products Glulam and LVL with different slenderness ratios. The material properties of the different LVL and Glulam used herein is provided in Table 5.1.

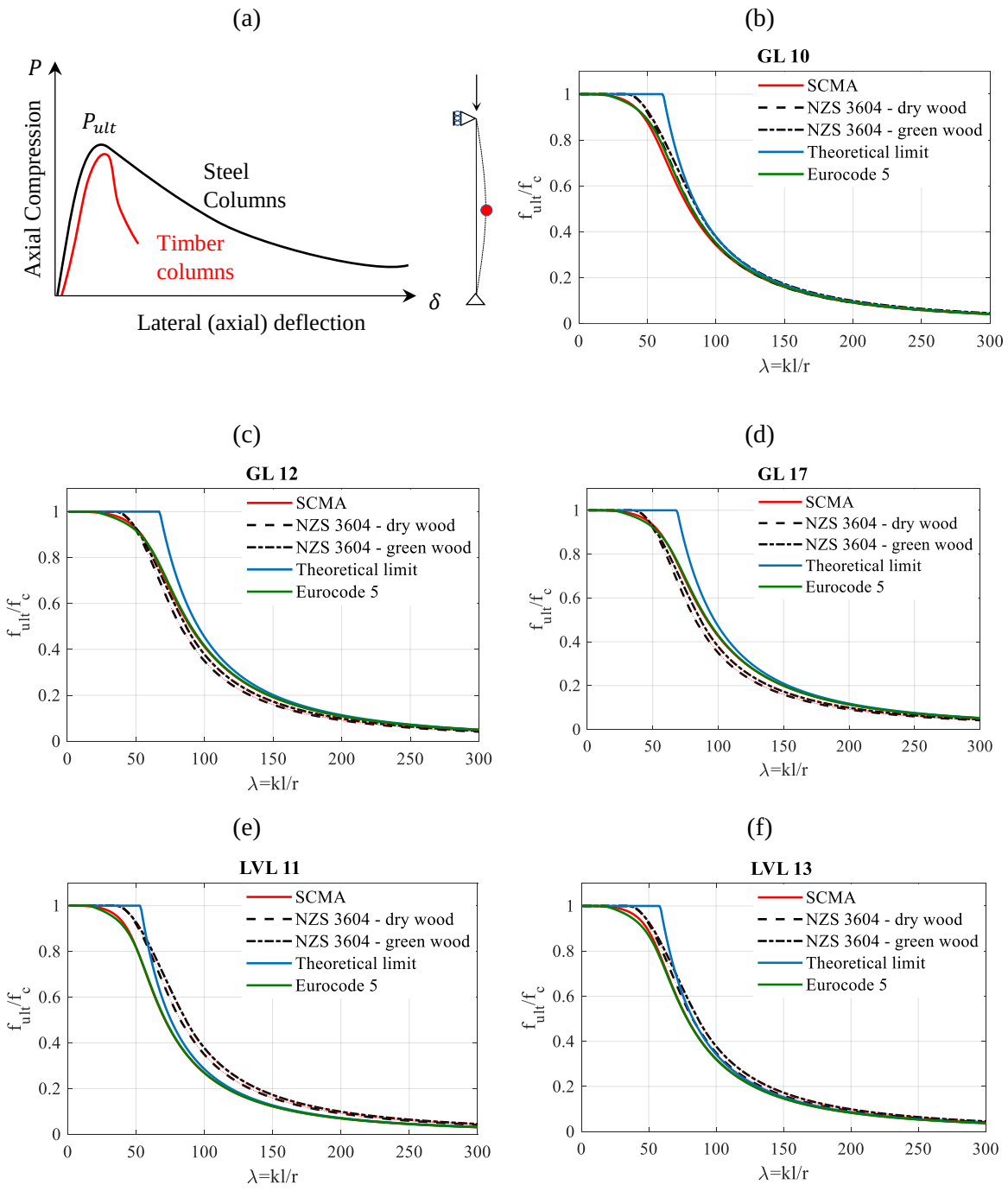

Figure 5.4: Comparison among SCMA, NZS 3604 and Eurocode 5 (a) Timber column performance Vs Steel Column, (b) GL10 Column, (c) GL12 Column, (d) GL17 Column, (e) LVL 11 Column and (f) LVL 13 Column.

Table 5.1: Characteristics of the different timber products to be used as timber body (from local timber manufacturer)

Type	f_c (MPa)	f_b (MPa)	E (parallel to grain) (MPa)
GL10 (Techlam)	26	22	10000
GL12 (Techlam)	29	25	11500
GL17 (Techlam)	35	42	16700
LVL11 (NelsonPine)	38	38	11000
LVL13 (NelsonPine)	38	48	13200

5.1 Generalization of SCMA to Self-centring RSFJ Brace Assembly

SCMA method has two main steps. The first and foremost step is to approximate the elastic buckling load of the system from which the stiffness deterioration path (Eq.5.1) will be discovered. The elastic buckling load of the system can be estimated by any of the closed-form, iterative or finite element methods alternatively. In this study, the closed-form formulation is developed and presented. The second step is to calculate the ultimate strength curve of the system as a function of lateral displacement. The intersection between the two diagrams will bring the approximate ultimate strength of the system. Accordingly, this section firstly deals with calculating the elastic buckling of the self-centring brace and then deals with calculating the ultimate strength function.

5.1.1. *Self-centring RSFJ brace*

The self-centring brace in this study is composed of three components namely: (a) self-centring friction damper (RSFJ), (b) brace body, which can be made of timber [165] or steel [99] and (c) Anti-buckling tubes, which are used to strengthen the system [165]. In order to increase the displacement capacity of the brace, two locations, preferably close to the end supports [99, 165], were considered for installation of the dampers in series (Figure 5.1.b). The damper used in this study is the Resilient Slip Friction Joint (RSFJ), which is a friction damper yet with inherent self-centring characteristics. The performance of this damper is shown in Figure 5.5 [54, 158, 191-193].

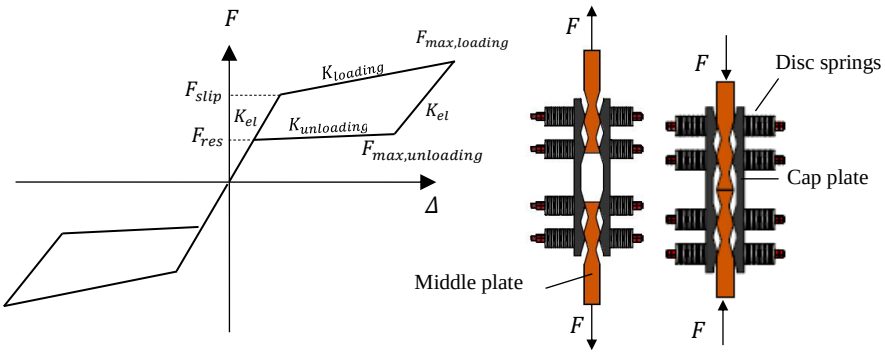

Figure 5.5: **Performance and deflected shape of RSFJ damper in tension and compression**

5.1.2. *Stiffness deterioration curve*

As shown in the first part of the paper, the elastic buckling of a pin-pin column with a uniform section was $\pi^2 EI/L^2$. However, this is not necessarily valid for the self-centring brace along with which one or two non-continuities appear. In this regard, the stability model that has been developed for the RSFJ brace assembly with one non-continuity [165] has been extended to be used for a system with two non-continuities. The proof is provided in the appendix.1. The elastic buckling load can be calculated using Eq.5.9:

$$P_{cr} = \alpha \frac{EI}{L^2} \tag{5.9}$$

Where L is the total length of the brace, EI is the flexural rigidity of the body and parameter α is the minimum real positive root of Eq.5.10 and is expected to be less than π^2 if the first mode of buckling is considered. Eq.5.10 is entitled as the characteristic equation (For proof, it can be referred to Appendix B):

$$\begin{aligned} f(\delta_1, \beta) = {} & 2\alpha \sin\left(\sqrt{\alpha}(2\delta_1 - 1)\right) - \alpha \sin\left(\sqrt{\alpha}(4\delta_1 - 1)\right) + \alpha \sin\left(\sqrt{\alpha}\right) \\ & - 4\beta^2 \sin\left(\sqrt{\alpha}\right) + 4\sqrt{\alpha}\beta \cos\left(\sqrt{\alpha}(2\delta_1 - 1)\right) - 4\sqrt{\alpha}\beta \cos\left(\sqrt{\alpha}\right) \end{aligned} \tag{5.10}$$

in which δ_1 and β are the relative location and relative rotational stiffness of the non-continuity region (ignoring the contribution from the damper – see Eq.4.18), respectively and can be calculated using Eq.5.11 and Eq.5.12 (Figure 5.6)

$$\delta_1 = \frac{0.5L_{RSFJ} + L_{con}}{L} \tag{5.11}$$

$$\beta = \frac{K_{ABT} L}{EI} \tag{5.12}$$

in which L_{con} is the distance between pin and beginning of the damper as shown in Figure 5.6, L_{RSFJ} is the length of damper and $(K_{rot})_{ABT}$ is the rotational stiffness of the non-continuity region, which is assumed to be only coming from ABT. This parameter can be simply derived using the method of virtual work [194]. The rotational stiffness of the ABT is illustrated in Eq.5.13 as:

$$K_{ABT} = \frac{2m.EI_{ABT}}{\delta_2 L} \tag{5.13}$$

in which

$$m = \frac{\delta_2}{[2(\delta_2 - \delta_1) + \beta_b(1 - 2\delta_2)]} \tag{5.14}$$

In the two above mentioned equations, parameters β_b and δ_2 are the relative rigidity and relative length of ABT:

$$\delta_2 = \frac{L_{RSFJ} + L_{con}}{L} = \frac{L_{ABT} + L_{con}}{L} \tag{5.15}$$

$$\beta_b = \frac{(EI)_{ABT}}{(EI)_{body}} \tag{5.16}$$

when the elastic buckling load is known, the stiffness deterioration curve can be approximated using Eq.5.1 in which the initial imperfection is:

$$\delta_0 = \frac{L}{1000} + \frac{L}{500} + \delta_{clearance} \tag{5.17}$$

in which the initial imperfection of the body is ($L/1000$), erection tolerance is $L/500$ and $\delta_{clearance}$ is the clearance in the gusset and ABTs.

5.1.3. *Strength deterioration curve*

Figure 5.6 shows the different possible failure mechanisms of the brace. Generally, there are two possible places for a plastic hinge to form: (a) mid-span of the brace within the brace body (mode 1) because the second-order moment might be at the highest level at this section, (b) end of the brace body within the female section of the ABT (mode 2) because the male part of ABT is not extended till the end of female. It is worth noting that the first collapse mode is desired in case of RSFJ brace mainly because in mode 2, the damper would be damaged due to deformation

compatibility between ABT and damper. In this regard, the experimental destructive tests were mainly focused on the first mode.

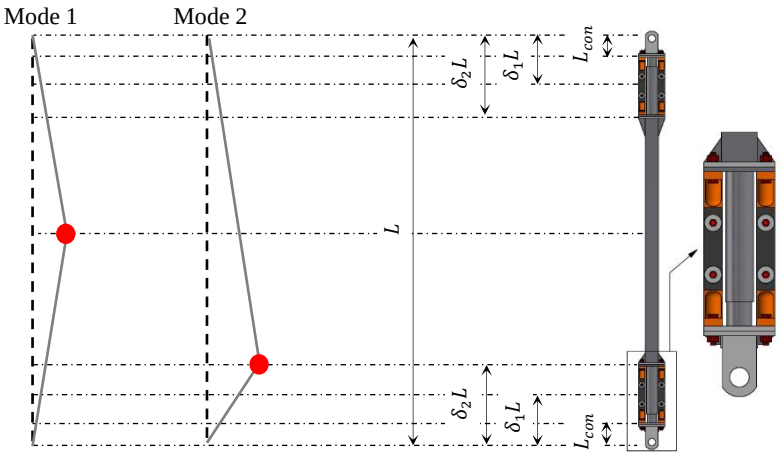

Figure 5.6: **Different failure (mechanism) modes of the brace**

In case of both modes of collapse (Figure 5.6), the plastic strain energy stored in the plastic hinge is:

$$U = \left(M_p\right)' \times 2\theta \tag{5.18}$$

In which 2θ is the rotation in the plastic hinge, $\left(M_p\right)'$ is the reduced plastic capacity of the section if there is any axial load. The work carried out as a result of axial deformation can be calculated as [127]:

$$T = PL(1 - cos\,\theta) \tag{5.19}$$

By satisfying the balance of energy, the strict minimum of the potential energy [31, 32, 127], the ultimate load can be derived:

$$\frac{d(U-T)}{d\theta} = 2\left(M_p\right)' - PL\theta = 0 \tag{5.20}$$

If the axial loads (P) is brought in the left side of the equation, the *axial strength* can be calculated as a function of lateral displacement:

$$P = \frac{\left(M_p\right)'}{\delta} \tag{5.21}$$

Eq.5.21 will lead to Eq.5.2 if mode 1 is considered but will lead to Eq.5.22 if mode 2 is considered:

$$P = \frac{\left(M_p\right)_{female}}{\delta} \tag{5.22}$$

in which $(M_p)_{female}$ is the plastic capacity of the female section of the ABT without any reduction because no axial load is transferred by the ABT (telescopic configuration). Accordingly, the intersection point between the stiffness and strength deterioration curves when mode 2 is considered can be estimated as:

$$\delta_{int\,female} = 0.5(M_p)_{female}\left[\frac{1}{P_{cr}} + \sqrt{\left(\frac{1}{P_{cr}}\right)^2 + \frac{4\delta_0}{(M_p)_{female}.P_{cr}}}\right] \quad 5.23$$

Note that the intersection point for mode 1 was illustrated already in Eq.5.4 for steel brace or column application) and Eq.5.8 for timber brace or column application. By having two sets of intersection points (Eq.5.4 (Steel body) or Eq.5.8 (Timber Body) and Eq.5.21 (Steel ABT)) from two failure modes, the ultimate strength of the RSFJ brace can be approximated using Eq.5.5 or Eq.5.6.

5.2 Experimental Validation

5.2.1. *Test setup*

To validate the suggested SCMA method for quantifying the ultimate load of the self-centring brace, a full-scale experimental test was performed at the Auckland University of Technology laboratory for which the test set up is shown in Figure 5.7. A total of 3 specimens (tabulated in Table 5.2) were employed and the drawings are provided in Figure 5.8. Each specimen had a 4466 mm length and was installed at an angle of 49.2 degree with respect to the horizontal floor. Both brace bodies and the ABTs were manufactured using mild steel with a nominal yield strength of 340 MPa and an elastic modulus of 200 GPa. Two locations along with the brace were considered for the dampers' installation in each of which two dampers were located. For the purpose of testing, a 250 kN MTS actuator with ±125 mm stroke capacity was used. For the purpose of data acquisition, two drew wires and two LVDTs (Linear Variable Differential Transformer) were used, which LVDTs were responsible to record the dampers axial movement at two locations, and drew wires were responsible to record the brace axial and lateral deformations, respectively.

5.2.2. *Component Testing of RSFJs*

The RSFJ damper in this study was already tested experimentally and explained in [165]. However, in this study, the number of disc springs and prestressing of the disc have been changed to get different flag-shapes to suit the test and reach the desired level of load at the desired level of

displacement. There were four RSFJs in total for each brace specimen all of which had the same characteristics in terms of flag-shape performance as reported in Table 5.3. All of the four RSFJs were tested according to the prescribed load protocol of AISC 341 for BRBs [157, 165] shown in Figure 5.9.a. The experimental results of the component testing are shown in Figure 5.9.b

Figure 5.7: **Test set for steel RSFJ brace: (a) isometric view, (b) front view, (c) side view-joint and (d) side view-brace**

(a)

SCB1:

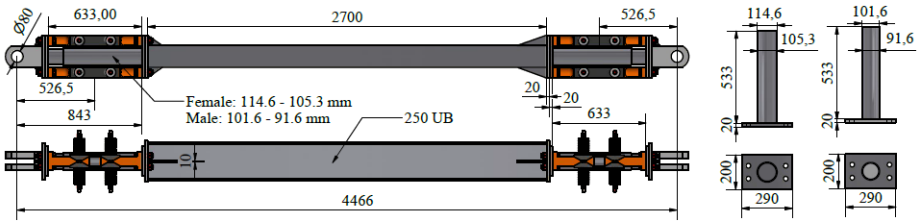

(b)

SCB2:

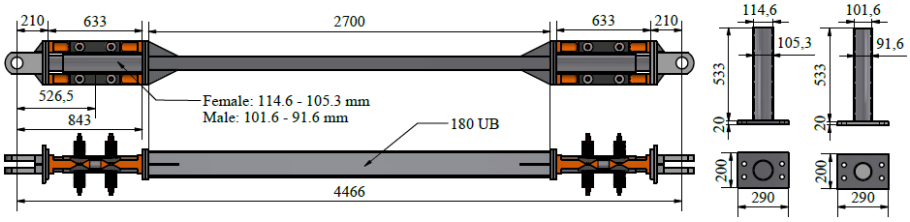

(c)

SCB3:

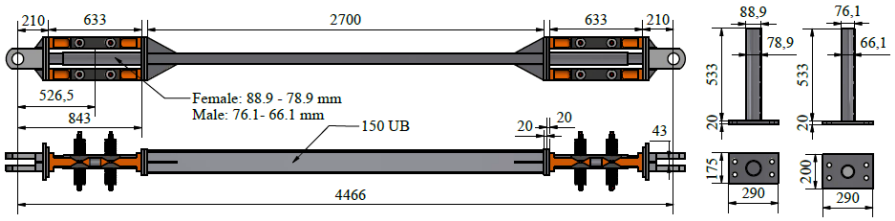

(d)

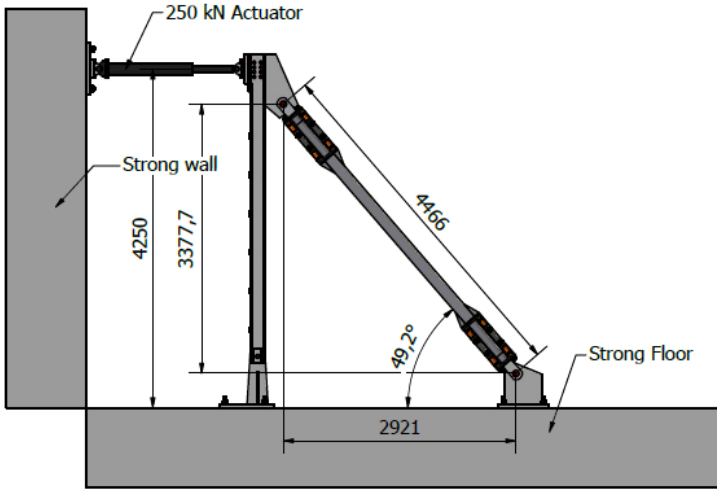

Figure 5.8: **Specimens and set up dimensions: (a) SCB1, (b) SCB2, (c) SCB3, (d) Test set up dimensions**

Table 5.2: Testing Plan and Specimens' information

Specimen	Brace body	Anti-buckling Tube				L_{RSFJ} mm	L mm	δ_1L mm	δ_2L mm	Failure
		Female		Male						
		Outer diameter (mm)	Inner diameter (mm)	Outer diameter (mm)	Inner diameter (mm)					
SCB1	250 UB	114	105.3	101.6	91.6					Undamaged
SCB2	180 UB	114	105.3	101.6	91.6	633	4466	526.5	843	Brace Body
SCB3	150UB	88.9	78.9	76.1	66.1					Brace Body

Table 5.3: Damper characteristics for different specimens

Specimens	n_d	F_{pr} (kN)	F_{slip} (kN)	$F_{residual}$ (kN)	$F_{max,loading}$ (kN)	$F_{max,unloading}$ (kN)
SCB1						
SCB2	14	36	56.7	24.7	146.6	63.8
SCB3						

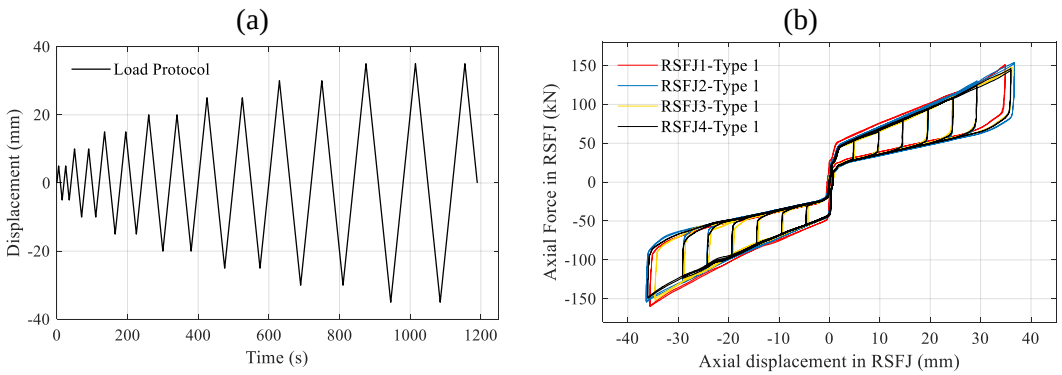

Figure 5.9: Experimental results of the component testing of the dampers: (a) displacement load protocol, (b) Hysteric performance of RSFJs subjected to the load protocol

5.2.3. *Full-scale Testing*

This section discusses the results of three brace specimens. In the first part of this section, the result of specimen SCB1 is discussed, which was designed to be undamaged during the testing

program, and therefore, the main emphasis in this section is placed on the evaluation of the brace performance when it is subjected to a static and dynamic loading regime. In the second part of this section, the results of destructive tests on the specimens SCB2 and SCB3 are discussed where failure mode 1 was intended to be observed. The failure of the brace according to mode 2 when ABT is installed in parallel to the dampers was not investigated in this study mainly because it may contribute to yielding the damper due to deformation compatibility. However, it should be also pointed that the failure according to mode 2 in an elastic manner was studied [165] but with the difference that the brace was not strengthened with ABT and there was one weakened location for the damper installation along with the brace.

5.2.3.1. Reversed Cyclic Static and Dynamic test on SCB1

A full-scale reversed cyclic test in both static and dynamic manner was performed on the brace SCB1, which was specifically designed in a way that it stays undamaged for the maximum capacity of the actuator (250 kN) or equivalent force in the brace (400 kN). Validation with the dynamic type of test with the frequency of the building after activation of the dampers and the displacement amplitude at Maximum Considerable Earthquake (MCE) is a requirement for certifying any damper according to ASCE 7 [195]. Based on the literature [78, 79, 157, 165], evaluation of a self-centring brace performance against combined load protocol of AISC 341 for Buckling-Restrained Frame [196] and dynamic load protocol for dampers of ASCE 7 [195] would suffice to approve the brace performance [78, 157, 165]. For this purpose, the brace SCB1 was firstly subjected to a reversed static cyclic loading protocol up to 2.5% drift with 10 mm step of the displacement and repetition of two for each amplitude as shown in Figure 5.10.a. The result of the reversed cyclic test is shown in Figure 5.10.b.

After performing the static test, the specimen was subjected to two sinusoidal shape dynamic load protocols (Figure 5.10.c and Figure 5.10.e) up to 2% drift with 0.25 Hz and 0.4 Hz frequency in which the last cycle (40 mm), which was assumed to be MCE displacement, was repeated five times as per the requirement of ASCE 7 [195]. The results of these two tests are shown in Figure 5.10.d and Figure 5.10.f. As can be seen, the brace performance in all three experiments was in accordance with the analytical predictions [165] and more importantly, its behaviour was unaffected due to the dynamic loading regime.

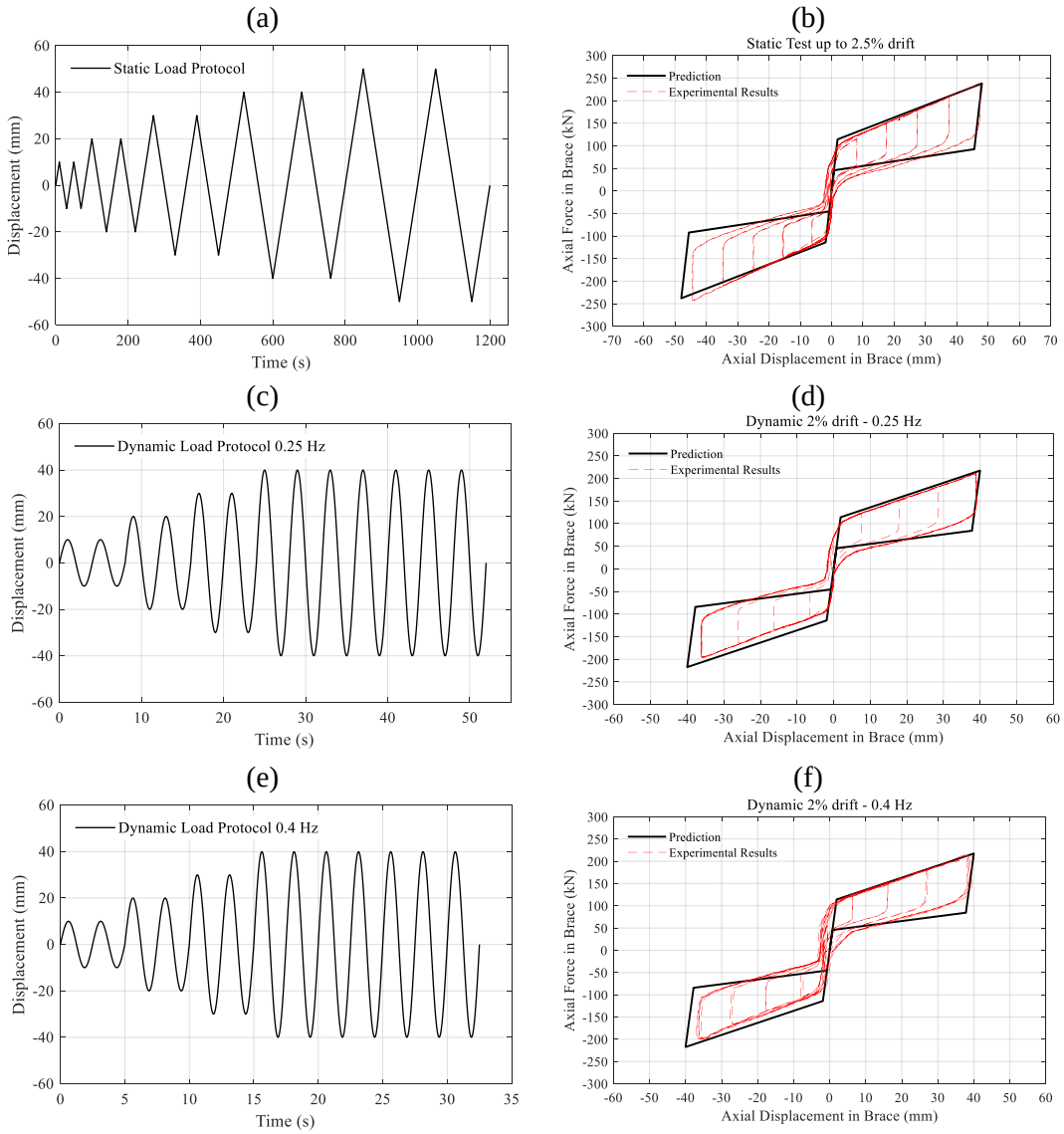

Figure 5.10: **Experimental results of the specimen SCB1- (a, b) Load protocol and hysteresis response for the static test, (c, d) Load protocol and hysteresis response for the dynamic test 0.25 Hz, (e, f) Load protocol and hysteresis response for the dynamic test 0.4 Hz**

5.2.3.2. Destructive Monotonic test on Specimen SCB2 and SCB3

Both specimens SCB2 and SCB3 were subjected to a single cycle monotonic loading with an amplitude of 50 mm (equivalent to 2.5 % drift). Both of them experienced a premature failure before reaching the 2.5 % target displacement. In case of the SCB2, the failure occurred after activation of the dampers (after-slip) while in case of the SCB3, the failure occurred before activation of the dampers. Both of these scenarios highlight the importance of a proper design of the brace in compression.

Figure 5.11.a and Figure 5.11.b show the result of the experimental test on specimen SCB2 in which the brace body was 180 UB 22. The elastic buckling of this specimen according to the procedure explained in section.3.2 was calculated to be 104.3 kN, which is depicted in Figure 5.11.a with the green line. According to Figure 5.11.a, it can be observed that the predicted ultimate strength of the brace should have been around 100 kN based on SCMA, which was the intersection between the green and purple curves. However, the ultimate strength was observed to be 200 kN based on experimental data. After further investigation, it was discovered that lateral support interrupted the test. In fact, the specimen was tightly gripped between two lateral supports as shown in Figure 5.11.c, which resulted in having an unintentional intermediate constraint and as a result, a shorter effective length for buckling. The lateral supports were originally used with the main intention of limiting the out-of-plane displacement of the setup. As for further supports, they were also tightly buttressed using the blue props shown in Figure 5.11.c. Having this situation contributed to having a frictional resistance between the specimen and lateral supports, though minimal (around 2kN) in the in-plane direction. Even such small force (larger than 0.004 member strength = 0.004 *100 kN = 0.4 kN) is enough to resist the second-order action and act as an intermediate constraint as per AISC 360 ([123]). Another evidence for having an intermediate constraint was that the plastic hinge formed in the brace body but with an offset from the midspan (shown in Figure 5.11.d). In order to modify the calculation, the effective length of the brace was replaced with the distance between the end pin and the intermediate constraint. The modified buckling load was approximated to be 192 kN (shown with blue line), which resulted in the predicted ultimate strength of 184 kN (the intersection between blue and purple curves), which is closer to the experimental observation of 200 kN as the ultimate strength. Figure 5.11.b shows the axial load in the brace against the axial displacement. As can be seen, the dash-dotted line is the ideal flag-shape performance of the brace, which was not accomplished by the specimen due to the inelastic buckling of the brace. In other words, the brace experienced a premature failure before reaching the load that it was supposed to resist. In this specimen, the failure occurred in the after-slip phase, but in the next specimen SCB3, the inelastic buckling occurred in the before-slip phase.

The problem of additional intermediate constraint was solved for the test on specimen SCB3 by loosening the props and providing a gap between the specimen and lateral supports so that there was no contact in between. The ultimate strength of the brace was observed to be nearly 71.5 kN. The elastic buckling of this specimen according to the procedure explained in section.3.2 was calculated to be 57.3 kN, which is depicted with the blue line in Figure 5.12.a. According to Figure 5.12.a, the ultimate strength of the brace was 55.7 kN from the intersection between blue and purple curves. As shown in Figure 5.12.b, the specimen SCB3 experienced a premature failure and buckled inelastically even before the slippage of the dampers in the brace.

(a)

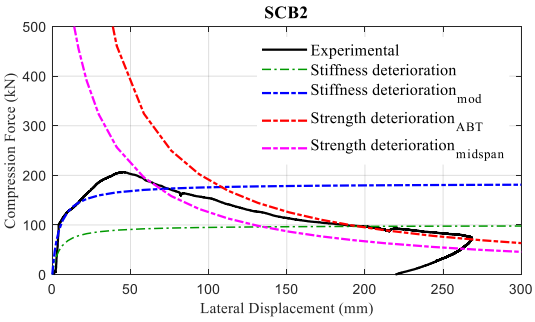

(b)

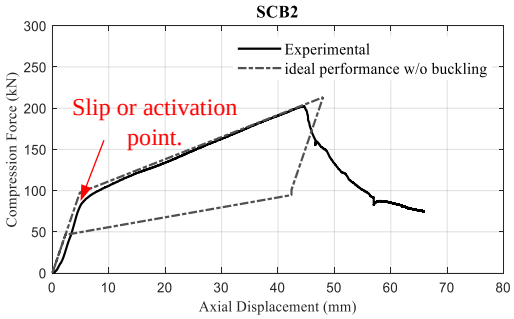

(c)

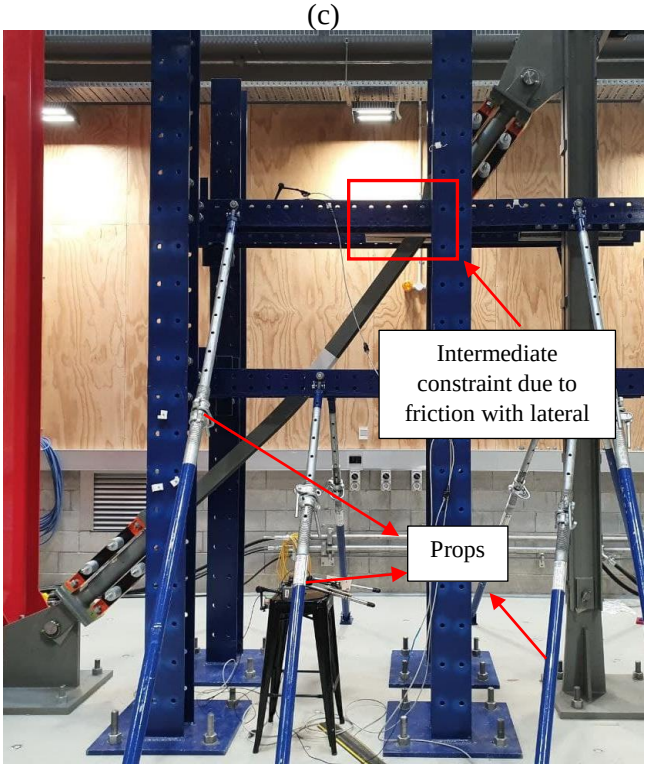

(d)

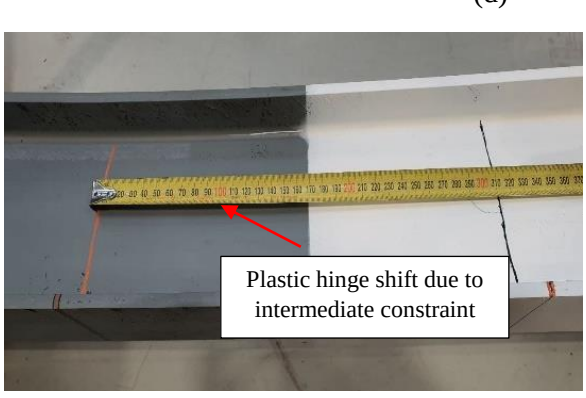

Figure 5.11: Experimental results of specimen SCB2: (a) axial load Vs lateral deflection, (b) axial load Vs axial displacement, (c) deformed shape of tested brace and (d) plastic hinge formation

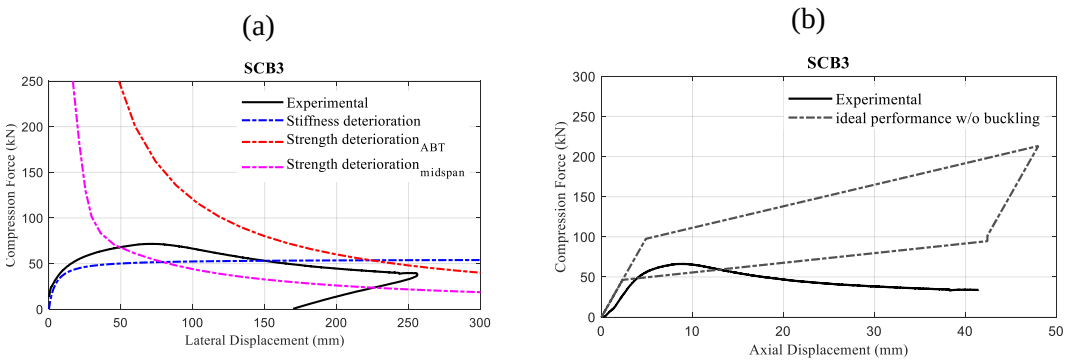

Figure 5.12: Experimental results of specimen SCB3: (a) axial load Vs lateral deflection and (b) axial load Vs axial displacement

5.3 Further Discussions

5.3.1. *Desirable mode*

As discussed in the paper, two possible scenarios may exist for the self-centring brace to fail. The first scenario is that the plastic hinge forms at the mid-span of the brace and within the brace body. This is more probable when the relative stiffness (β_b) is considerable. The second one is that the plastic hinge forms within the damper location and in the female part of the ABT. This scenario is more probable when the relative rigidity (β_b) of the ABT to brace body is small. The first case seems to be desirable and recommended to be governed in the design process mainly because if the plastic hinge forms within the ABT, it indicates that the damper would be damaged, and the brace may not resist any further inelastic load cycles either in the main event or aftershocks. Moreover, if the brace body is assembled with the bolted connections to the damper, like the braces used in this paper, it can be easily replaced in case of being damaged during a seismic event beyond the design level. Therefore, until sufficient study is done on mode 2, mode 1 is recommended to be governing.

5.3.2. *Additional shear*

Normally shear force in the braces is negligible since originating from the second-order actions ($P-\Delta$), but they can be critical in some cases (designing connections, welding and so on) and discussed here accordingly. Assuming that the plastic hinge is formed at the mid-span of the brace (desirable mode), the deflected shape at the ultimate limit state would be:

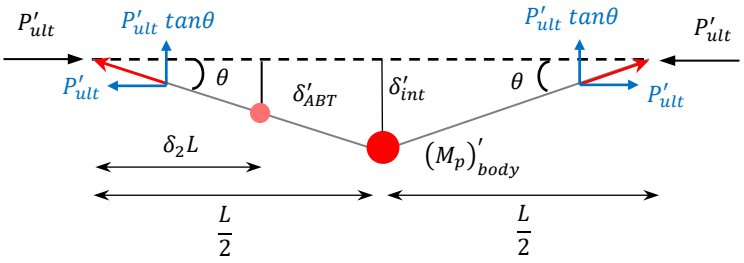

Figure 5.13: Deformed shape of the brace at the time of mechanism formation

According to Figure 5.13 and assuming that the deformations are of small magnitude ($sin\theta \sim tan\theta \sim \theta$ & $cos\theta \sim 1$), the shear force due to $P-\Delta$ can be approximated with the vertical component of the ultimate load as "$P'_{ult}\ tan\theta$ or $P'_{ult}\ \theta$". It should be pointed out that the "P'_{ult}" and "δ'_{int}" are the modified ultimate load and intersection point with respect to the material overstrength. In other words, the strength deterioration curve should be multiplied by the material overstrength factor $R_y(M_p)'$, and then the ultimate load and intersection point should be recalculated and relocated. The stiffness deterioration curve does not need to be modified as it is independent of the material yielding limit. This modification originates from the well-known capacity design concept. If the initial imperfection ($L/1000$) of the body, erection tolerance ($L/500$) and clearance in the connection is also considered, the additional shear force due to second-order and plastic hinge formation can be calculated using Eq.5.24:

$$V_{ult} = P'_{ult}\left(\frac{2\delta'_{int}}{L} + \frac{1}{1000} + \frac{1}{500} + \theta_{clearance}\right) \geq 0.004P'_{ult} \qquad 5.24$$

where $\theta_{clearance}$ is the additional initial rotation due to possible clearance in the connections (gusset plate and ABT). The value of the shear force is also recommended to be more than $0.004P'_{ult}$, suggested by the AISC 360 [123] – Appendix 6 (requirement for column bracing). In this regard, all elements of the brace – connections, bolts, welding and etc – should be checked to be able to resist this shear.

5.3.3. *End plate*

Another point that should be considered in the seismic design of RSFJ brace is the design of end plates of ABT and RSFJ as shown in Figure 5.14. This plate should possess sufficient strength so that the performance of the brace is not disrupted because of the local yielding of the plate. In

the case that the governing failure mode is mode 2 and the plastic hinge forms within the ABT, then the endplate should be designed in a way to be capable of accommodating the factored plastic capacity of the ABT (plastic capacity including the material overstrength). However, if the governing failure mode is mode 1 and the plastic hinge forms within the brace body, then the endplate can be designed for the applied moment at the location of ABT and at the onset of plastic hinge formation (ultimate limit state) as shown in Eq.5.25 and Figure 5.13, which is less demanding compared to the first case:

$$\left(M_{ep}\right)^{*} = P'_{ult}\delta'_{ABT} \sim 2\,P'_{ult}(\delta_2\delta'_{int}) \qquad 5.25$$

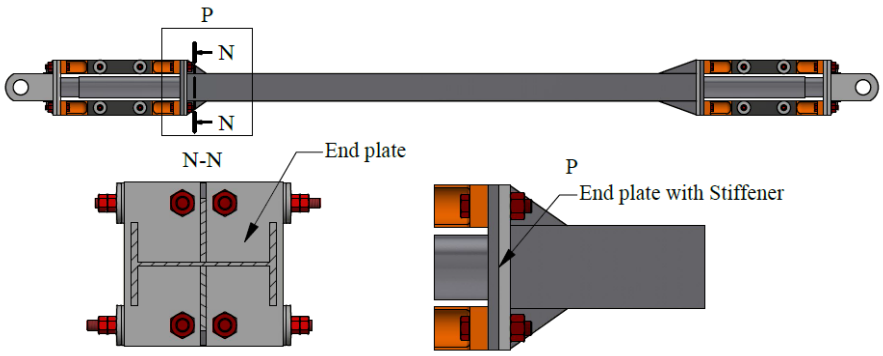

Figure 5.14: End plate

5.3.4. *Design flowchart*

Figure 5.15 summarizes the whole process of RSFJ brace design (for compression) in six consecutive steps. The process initiates with calculating the elastic buckling load of the system (P_{cr}). Though a procedure was developed in this study (section 3.2) to calculate the elastic buckling load, any other well-known methods or simulation techniques with the finite element software can be recruited at step 1 to determine the elastic buckling load. At step 2, the pure axial capacity (squash strength) P_n is determined, which along with the critical load P_{cr} will be input in the intersection formulations to figure out at what lateral deflection, the plastic hinges form based on two modes of collapse. The process continues in step 4 with calculating the ultimate loads associated with each failure mode where the minimum of them will be entitled as the final ultimate load, and the associated mode is called the governing failure mode. While in this step, it should be also made sure that the failure mode is the first mode; otherwise, a stronger ABT should be selected, and the previous steps should be repeated. In step 5, the brace demand would be checked

against the ultimate load to be less with a safe margin. The process ends with the capacity design of connections and adjacent members.

Step 1: Calculate the elastic buckling load P_{cr} using Eq.5.7 – Eq.5.15, any other well-known methods, or numerical techniques.

Step 2: Calculate the section axial strength using $P_n = A_g F_y$

Step 3: Calculate the intersection points using Eq.5.4 and Eq.5.21

Step 4: Calculate the associated ultimate load using Eq.5.5 or Eq.5.6. Call the minimum as the ultimate strength and the failure mode. (If the failure mode is not mode one, the ABT should be changed to a stronger section and go back to *step 1*)

Step 5: Check that the force demand be less than the ultimate strength with a safe margin.

Step 6: Check the seismic design of connections and capacity design of adjacent members using Eq.5.22 and Eq.5.23

Figure 5.15: **Design steps**

5.4 Summary and Concluding Remarks

Previous studies on the RSFJ steel brace demonstrated that the compression capacity of the brace might be very low due to the rotational flexibility of the damper for which a telescopic mechanism was suggested to be put in parallel to dampers to increase their rotational stiffness. Doing that successfully increased the elastic buckling load of the system, yet the ultimate strength and collapse mode of this system was not studied. In this manner, there was a lack of a process to accurately predict the failure load and collapse mechanism of the RSFJ brace in compression.

As for any member subjected to compression, the strength in compression would be adversely affected by the arrival of the second-order actions. In an ideal elastic system, the lateral displacement will increase due to $P - \Delta$ effect as the axial load approaches the elastic buckling load while the rate of this increase will grow in the vicinity of the elastic buckling load. However, in elasto-plastic system where the material has a limited strength, the weakest section may fail during this increase of lateral deflection, and depending on the geometry, the strength can be less or equal to the elastic buckling load. This study presented an analytical closed-form framework for quantification of the ultimate compressive strength of a self-centring brace, which is based on

intersecting two curves namely: stiffness degradation curve and strength degradation curve. Employment of this method not only will result in illustrating where the weakest section is but also lead to quantifying the load at which system becomes mechanism. The first part of the paper deals with illustrating how two curves are determined and intersect with each other. In the second part, experimental validations were provided for the possible failure mode to validate the method. In the final part of the paper, seismic design considerations are discussed and a step-by-step concise procedure for the design of RSFJ brace in compression is provided.

6 Finite Element Study on the Elastic and Inelastic Buckling Capacities of the RSFJ Brace

6.1 Abstract

In the previous sections, a closed-form analytical approach entitled SCMA (Simplified Collapse Mechanism Analysis) was proposed in order to calculate the ultimate capacity of the RSFJ brace in either case of a brace with one or two dampers. The main benefit of this closed-form approach was the simplicity and being easy to employ which would make the design more intelligible to an engineer when compared to detailed numerical modelling and complex differential equations. In this section, though experimental validations were provided, the accuracy and effectiveness of this approach will be further examined to make sure that the proposed method has sufficient precision in the range of different design parameters. For this purpose, a parametric finite element study is performed on the timber and steel braces with one- and two-damper configurations. Furthermore, two types of analyses were involved. The first one is the elastic buckling analysis that was used to evaluate whether the proposed approach is able to successfully predict the elastic buckling load or not. The second analysis is the inelastic buckling analysis which was used to approximate the accuracy of the method in predicting the ultimate capacity. Each of these processes was executed separately in the ABAQUS software environment (Version 2019). The finite element study shows that under specific limits, the proposed procedure is both reliable and accurate and can successfully predict the failure mode as well as the elastic and inelastic capacities of the brace.

6.2 Introduction and motivation

As was described in chapter 5, the exact solution for predicting the elastic buckling load (Euler load) of the RSFJ-brace assembly is very difficult to derive mainly because of the complex boundary conditions of the damper and anti-buckling tubes. More specifically, in the RSFJ-brace assembly, the axial load is being transferred by the RSFJ to the brace body while the ABT is resisting the second-order effects without transferring any axial load (because they are installed in a telescopic configuration). This means that the load path for the axial and flexural strength and stiffness are decoupled in the zone where the RSFJ(s) are installed. However, this phenomenon

is not seen in the analytical model, which simply assumes an equivalent rotational stiffness parallel to the RSFJs. Although this simplification will considerably reduce the computational efforts and complexity of the problem, it may come with a cost of possible limited inaccuracy. Accordingly, the main aim of this section accordingly is placed on the evaluation of the circumstances under which the model is working correctly. More specifically, it is aimed to provide a number of geometrical and structural recommendations so as to guarantee the efficiency of the method.

6.3 Finite Element Study on elastic and inelastic capacities of RSFJ brace

This section has two parts in which two configurations of the RSFJ brace assembly are discussed. Each of them consisted of three main sections discussing: (i) the elastic buckling, (ii) the inelastic buckling and (iii) the calibration factor. The elastic buckling load of the RSFJ brace assembly for the cases of one and two weakened locations for damper installation was described in sections 4.3.1 and 5.1.2, respectively. The method for inelastic buckling quantification – SCMA method – was. Described in great detail in chapter 5.

6.3.1. *Part 1 - Brace with one weakened zone*

For the purpose of finite element analysis, eleven types of telescopic circular hollow sections (CHS) were employed in the role of ABT. These sections were assumed to be made up of mild steel with the elastic modulus of 200 GPa, yield strength of 340 MPa and ultimate strain of 0.2. The specification of these sections are tabulated in Table 6.2. Furthermore, two types of brace body – steel and timber – were considered to figure out if the geometry of the brace bodies has any effect. The brace bodies were employed in a way that they both have the same flexural rigidity (EI) so that the effect of body geometry can be simply traced. The timber body was square-shaped with 270 mm dimension, the net area of 72900 mm^2 and the moment of inertia of 4.43e8 mm^4. Furthermore, it was assumed that it is made up of Glulam timber with an elastic modulus of 8 GPa and a flexural characteristic strength of 25 MPa. The steel body was of SHS (square hollow section) type with an outer diameter of 152.5 mm and a thickness of 9.5 mm, the net area of 5434 mm^2 and moment of inertia of 1.86 e7 mm^4. The overall length of the brace "L" was assumed to be 4156 mm. In order to further investigate the effect of the damper length, three scenarios were considered for the length of the damper to be 10%, 20% and 25% of the brace length. The

end bracket length ($\delta_e . L$) was also assumed to be 202 mm. The parameters used and the schematic overview of the braces are depicted in Table 6.2 and Table 6.1.

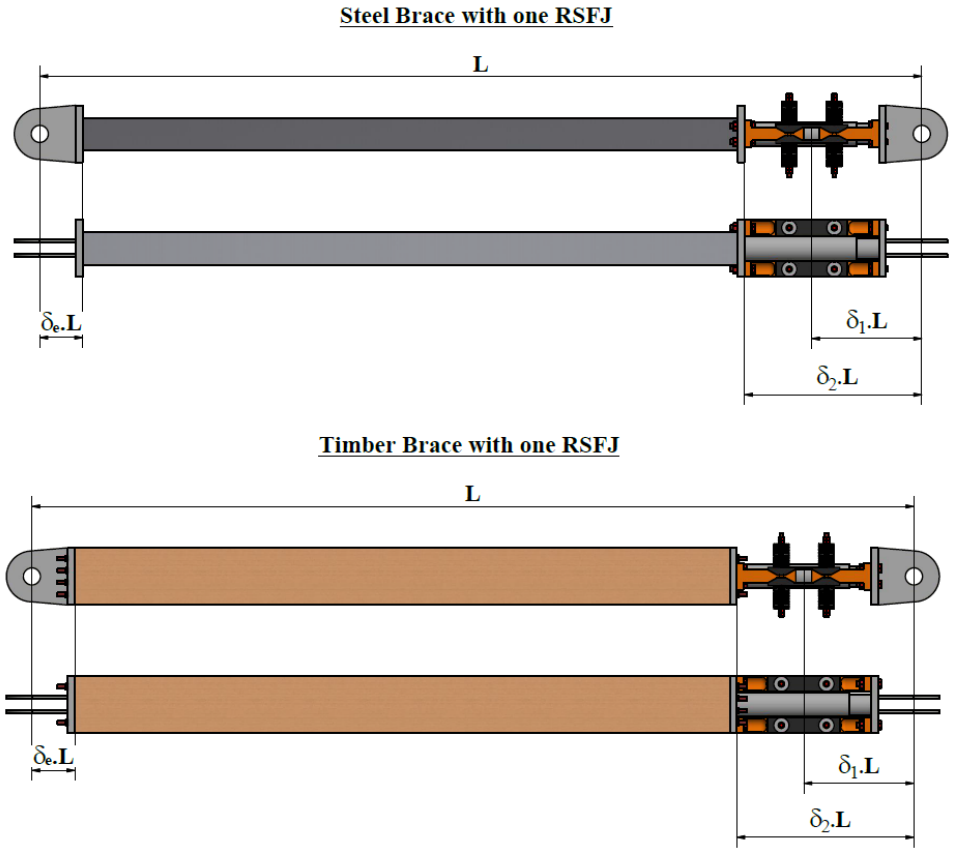

Figure 6.1: RSFJ-brace Assembly for Finite Element Study Part 1

Table 6.1: Scenarios of the damper length for Finite Element Study Part 1

Scenario	$\delta_2 L$ (mm)	$\delta_1 L$ (mm)	L_{RSFJ} (mm)	L (mm)	$\delta_e . L$ (mm)	Analysis	
						Elastic	Inelastic
1	835	518.5	633	4156	202	✓	✓
2	1250	720	1060			✓	----
3	400	295	210			✓	✓
4	1035	585	900		190	----	✓

Table 6.2: Telescopic Sections for Finite Element Study Part 1

Section	$(D_{out})_f$ (mm)	$(D_{in})_f$ (mm)	$(D_{out})_m$ (mm)	$(D_{in})_m$ (mm)	E (GPa)	F_y (MPa)	ε_u
ABT1	50.3	39.5	38.3	27.5			
ABT2	60.3	49.5	48.3	37.5			
ABT3	70.30	59.50	58.30	47.50			
ABT4	80.30	69.50	68.30	57.50			
ABT5	90.30	79.50	78.30	67.50			
ABT6	100.30	89.50	88.30	77.50	200	340	0.2
ABT7	110.30	99.50	98.30	87.50			
ABT8	120.30	109.50	108.30	97.50			
ABT9	130.30	119.50	118.30	107.50			
ABT10	140.30	129.50	128.30	117.50			
ABT11	160.30	149.50	148.30	137.50			

6.3.1.1. Elastic buckling

The elastic buckling analysis was performed in the ABAQUS program environment using the "Buckle" analysis engine and the subspace method. The problem is viewed as an eigenvalue analysis where the solver engine calculates the singular values for the stiffness matrix considering the second-order effect from an axial compressive load. These singularities (eigenvalues) are, in fact, the buckling loads of the system with respect to different mode shapes (eigenvectors). Figure 6.2 shows the model in the ABAQUS environment where the RSFJs were idealized with two rectangular plates attached together using a rotational hinge link. The rotational behaviour of the RSFJ was ignored as it is negligible compared to that of ABT. For the modelling of the different parts of the brace, the 20-node 3D quadratic brick element (Higher-order element with varying

stress and strain within the element) was used so that the errors of analysis are minimized. Different parts of the model were attached using the "Tie" constraint. The male and female steel parts of the ABT were attached using a link with the released axial degree of freedom and restrained rotational degree-of-freedom so that the telescopic motion is properly simulated.

(a)

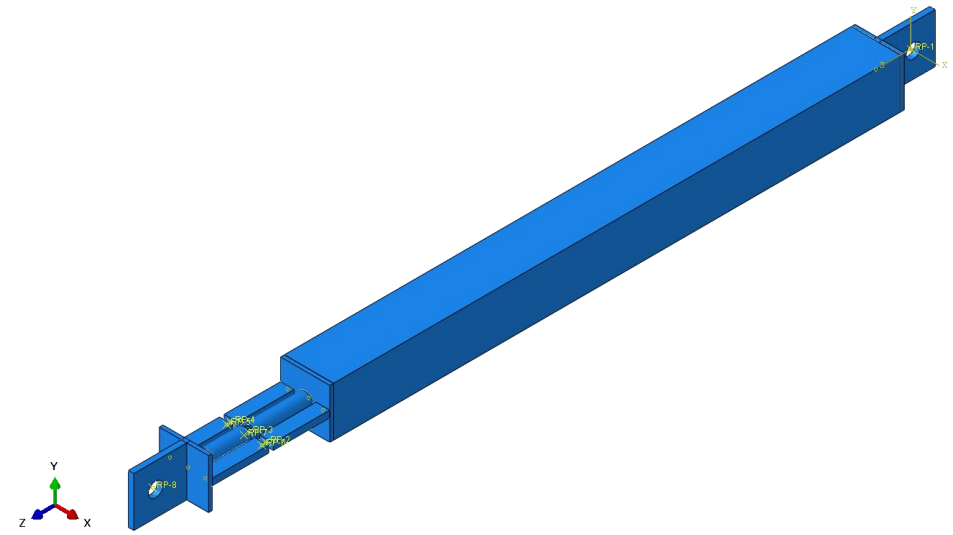

(b)

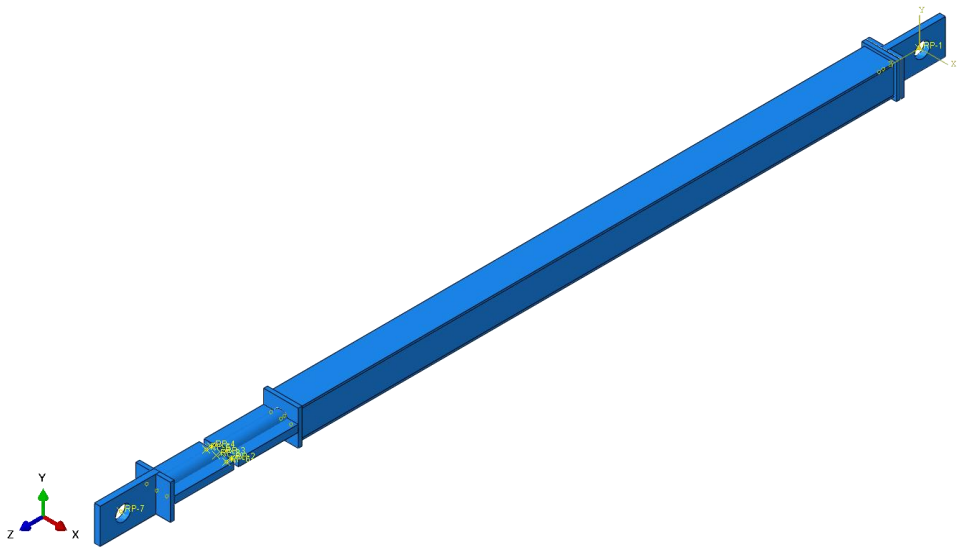

Figure 6.2: Finite element model (a) RSFJ *timber* brace assembly with one damper and (b) RSFJ *steel* brace assembly with one damper

(a)

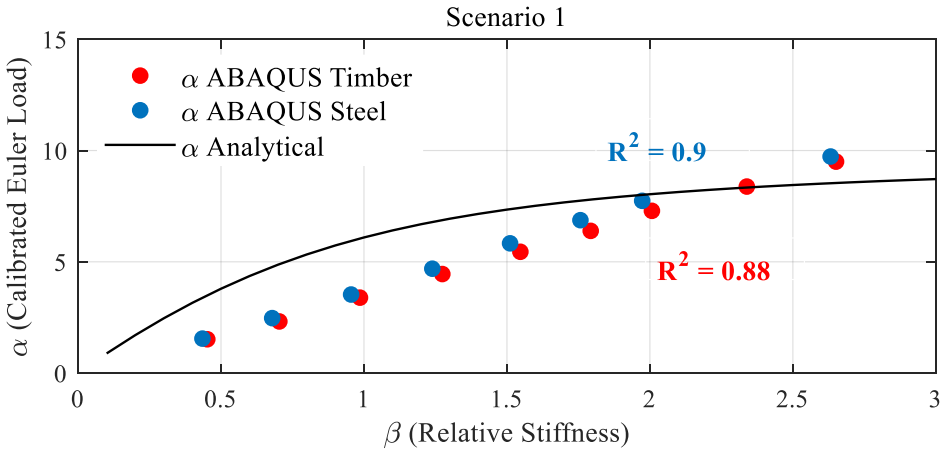

(b)

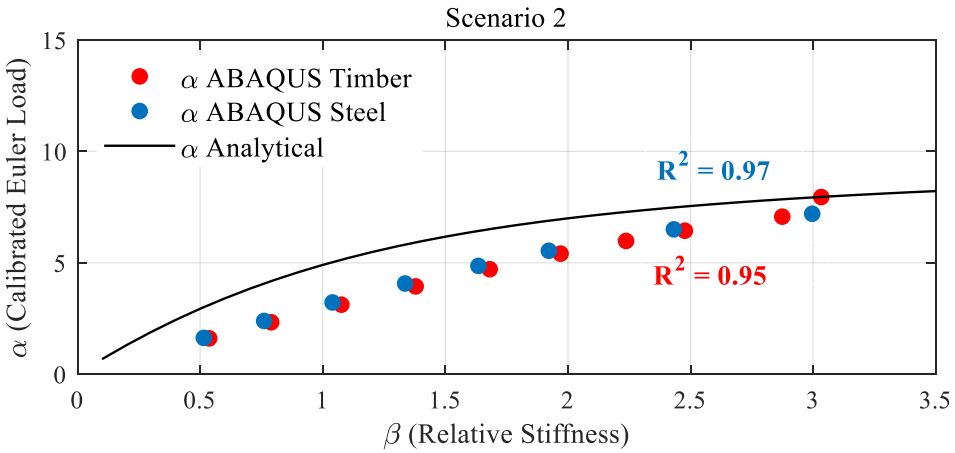

(c)

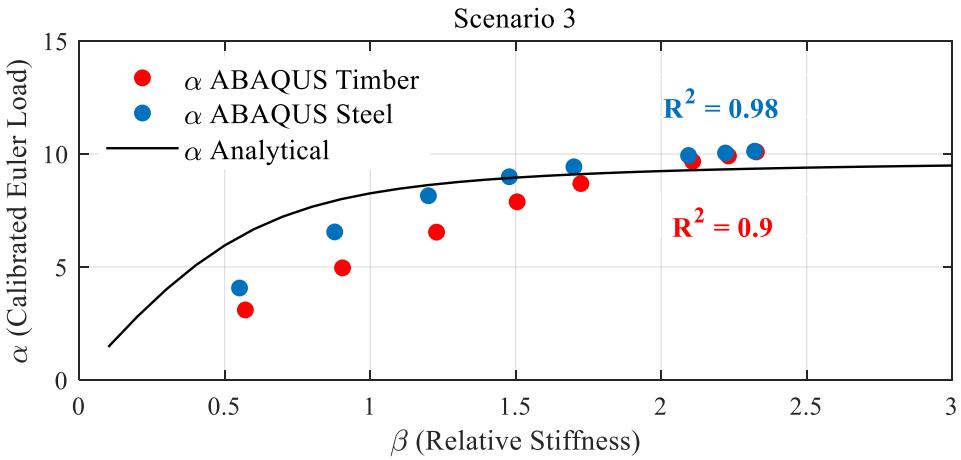

Figure 6.3: Numerical results Vs analytical predictions FE (part 1): (a) scenario 1, (b) scenario 2 and (c) scenario 3

(a)

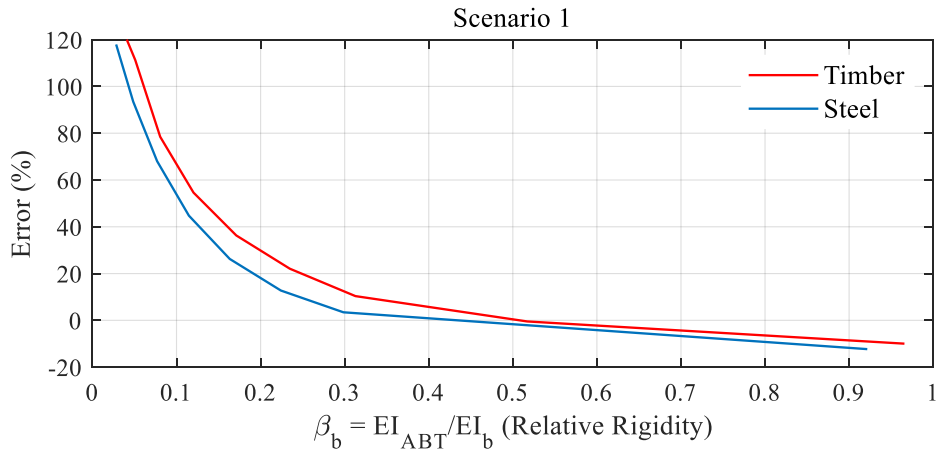

(b)

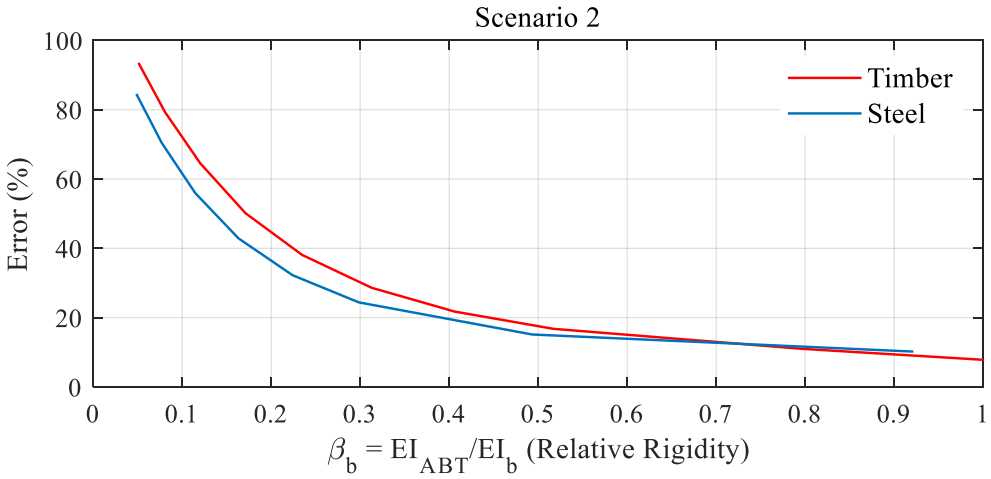

(c)

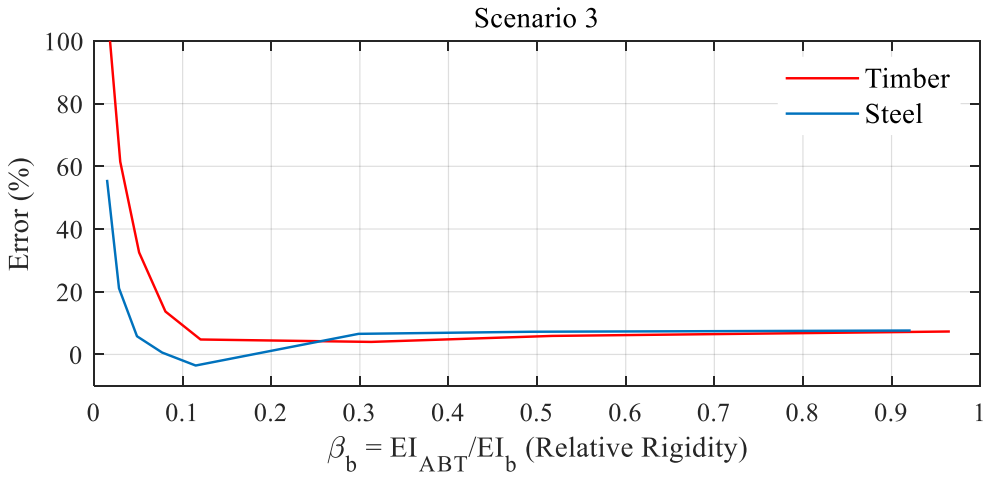

Figure 6.4: Error of the analytical approach versus relative rigidity for elastic buckling (part 1): (a) scenario 1, (b) scenario 2 and (c) scenario 3

Figure 6.3 shows the results of finite element analysis for the RSFJ braces with one intermediate weakened location with the timber and steel bodies. The horizontal axis is the relative rotational stiffness of the ABT to the brace body (β as per E 5.12), and the vertical axis is the calibrated elastic buckling with EI/L^2 , shown as $\alpha = (P_{cr})_{Abaqus}L^2/EI$. As it can be seen, as the β (relative rotational stiffness defined as per Eq 5.12) increases, the α tends to converge to π^2, which is indicative of the Euler buckling load. From the analytical predictions, it can be deduced that the predictions are in good agreement with the numerical results by comparing the dotted data versus the black solid line. It should be also pointed out that the blue dots, representative of the numerical results of the steel brace, are not that much different from the red dots, the numerical results for the timber brace. Therefore, the shape or geometry of the body will not affect the results. To further support this, it can be referred to the correlation coefficients "R^2" in the figure, which are more than 0.9 for all the scenarios for the steel and timber bodies.

Figure 6.4 shows the error (defined as the difference between analytical and ABAQUS results divided by ABAQUS results = $(F_{analytical} - F_{ABAQUS})/ F_{ABAQUS}$) of the analytical approach versus the relative rigidity of the ABT to that of the brace body (β_b). For scenarios one and two, this error converges to almost zero when the relative rigidity is higher than 0.25 - 0.3, while for scenario three, this value is 0.1. It should be also pointed out that this range of relative rigidity is desirable for design purposes as normally it falls between 0.1 and 0.5 for an optimum design with commonly available sections. Having an ABT with a smaller size and dimensions than the brace body is also desired because the footprint of the damper and ABT are best to be less than that of the brace body to respect the architectural considerations.

6.3.1.2. Inelastic buckling

The inelastic buckling was similarly analysed with the ABAQUS software using the *Arc Length method* or the *modified Riks* analysis [197], which its self, uses the mode shape of the elastic buckling analysis as the initial imperfection. In the finite element analysis, the equilibrium equations are normally solved using Newton's law in the context of matrix analysis. By applying the boundary conditions and the external loads, the variables, which are the deflection and/or rotation of each degree-of-freedom will be determined. When the stiffness matrix is nearly singular (determinant is near zero) due to the second-order, this method is not a good choice for satisfying the equilibrium, and the concept of the stationary potential energy approach is a better choice [197]. According to the Lagrange-Dirichlet theorem [127], the strict minimum for the potential energy will bring the critical loads for the system of interest. The arch length method, or so-called "modified Riks method", is a powerful and incremental numerical technique to satisfy the energy method.

As it was mentioned in the previous section, the inelastic buckling or the collapse load of a system is a load at which the member becomes a mechanism and is not able to resist any further load. This load is almost identical to the Euler (elastic) buckling load for the slender members while it is less than the Euler load for stocky members. More specifically, as the axial load in the brace increases, the lateral deflection will increase as well because of the second-order ($p-\Delta$) actions. The rate of this increase will rise as the axial load approaches the Euler buckling load (shown in Figure 6.5.a and Figure 6.6.a in blue line). This curve can be entitled the "stiffness deterioration" diagram mainly because the lateral and axial stiffness is being deteriorated resulting in progressive lateral and axial deflections. Depending on the strength of the different parts of the brace, (shown in Figure 6.5.a and Figure 6.6.a in red and green lines), a plastic hinge can form elsewhere within the *stiffness deterioration* curve (see section 5.1.2). This point can be approximated and quantified by plotting the *strength deterioration* curves (see section 5.1.3) and finding the intersection between stiffness and strength decay curves. For slender members, columns or braces, this intersection will be most probably close to the Euler buckling load while for stocky members, it can be much less than the Euler buckling load. In the RSFJ brace assembly, it is ABT that determines at what load and location, the plastic hinge may form.

Figure 6.5.a and Figure 6.6.a describe the analytical prediction of the collapse curve for scenario 3 for the RSFJ brace with the ABT 3 and ABT 7 configurations, which is resulted from intersecting the strength and stiffness curves. Furthermore, the inelastic behaviour of the brace is also illustrated in the black dashed line based on which it can be seen that the collapse load using analytical prediction is fairly close to that derived from the ABAQUS model. Apart from that, the analytical framework had successfully detected the failure mode which was the ABT failure (mode 2) for the first case (Figure 6.5) and brace body failure (mode 1) for the second case (Figure 6.6). The inelastic buckling mode shape (mode of collapse) is depicted in Figure 6.5.b and Figure 6.6.b. As shown in the first case, the plastic hinge formed in the ABT while it formed in the brace body for the second case. Figure 6.7 shows the difference between the finite element results and the analytical predictions for the different scenarios as per Table 6.1. As it can be observed, as the length of the damper (plus the end connection) increases (δ_2), the error in the results will increase. In this regard, the relative length of the damper was assumed to be limited to 0.25 of the brace length for the inelastic buckling study. Furthermore, it should be mentioned that the error is almost identical between timber and steel brace assemblies in all of the scenarios and will reduce and approach to zero as the relative rigidity increases (β_b). As can be seen in Figure 6.7, for scenarios 1, 2 and 3 ($\delta_2 = 0.2, 0.1\ and\ 0.25$), it is after ($\beta_b = 0.2, 0.05\ and\ 0.3$) that the amount of error is almost less than 15-20%.

(a)

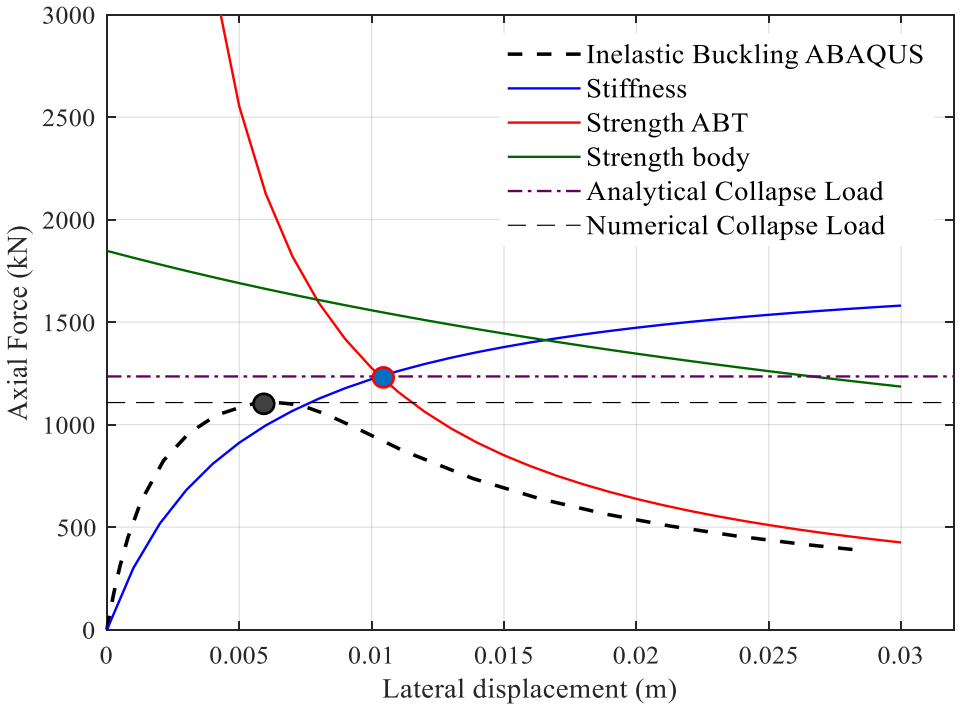

(b)

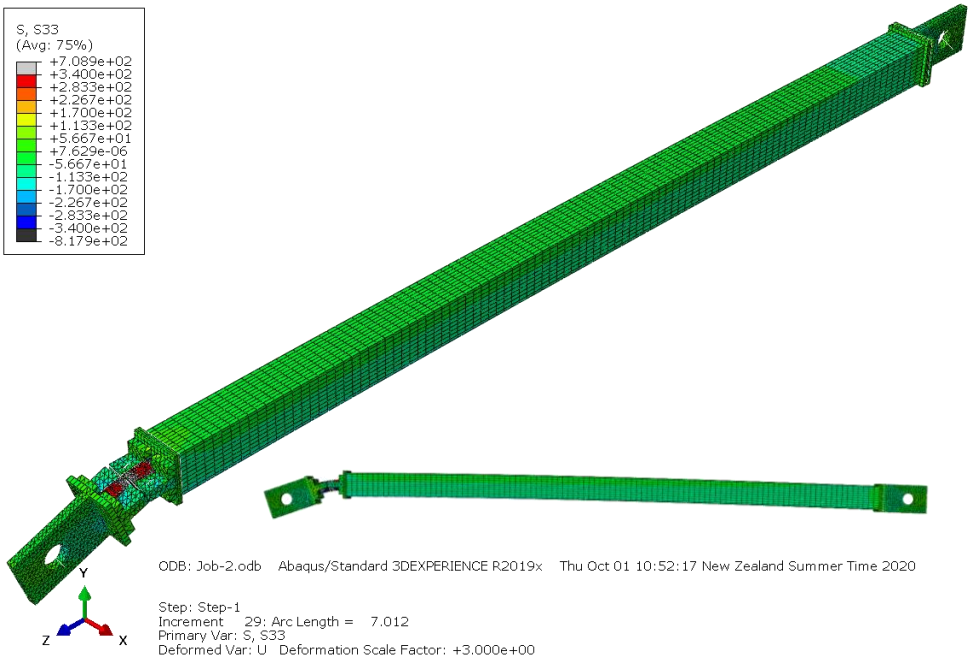

Figure 6.5: Inelastic Buckling of Steel brace scenario 3 with ABT 3: (a) Performance curves and analytical predictions, (b) Inelastic mode shape in ABAQUS

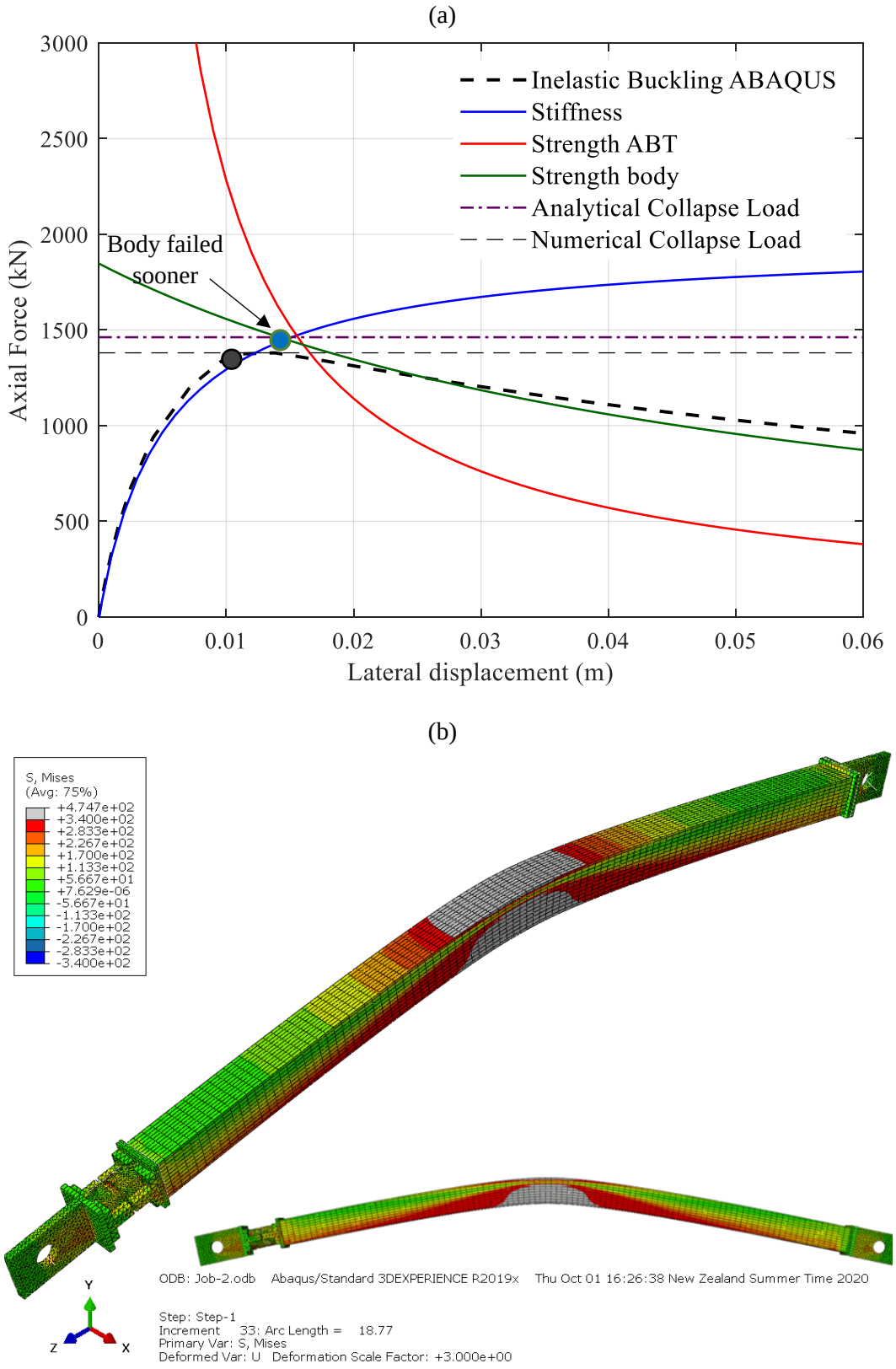

Figure 6.6: Inelastic Buckling of Steel brace scenario 3 with ABT 7: (a) Performance curves and analytical predictions, (b) Inelastic mode shape in ABAQUS

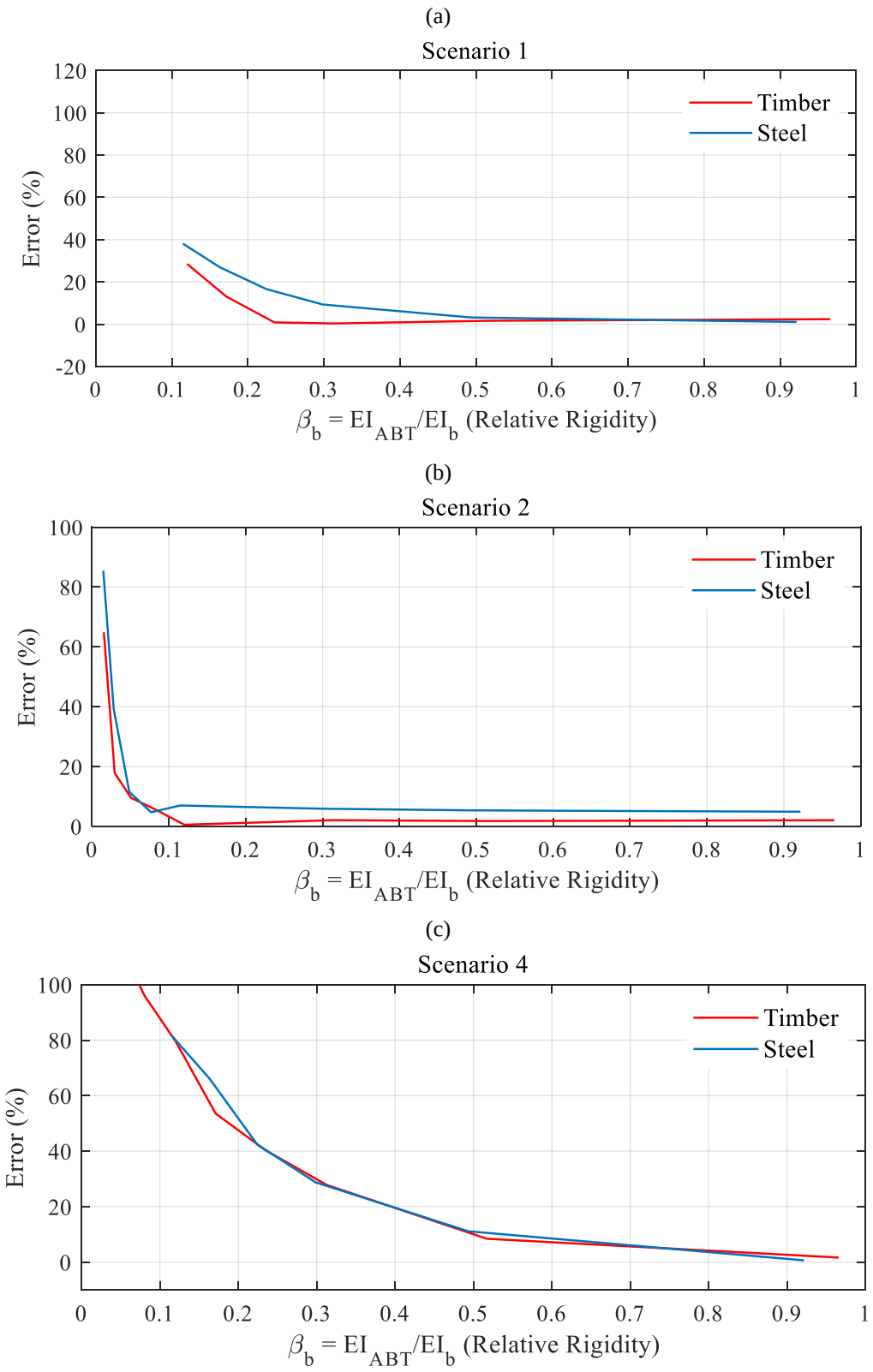

Figure 6.7: Error of the analytical approach versus relative rigidity for inelastic buckling: (a) scenario 1, (b) scenario 2 and (c) scenario 4

Figure 6.8 shows the comparison between the analytical prediction and numerical results for the inelastic buckling (collapse) load for the scenarios mentioned in Table 6.1. In this diagram, both x- and y-axis are the collapse loads where the vertical axis is associated with the analytical predictions and the horizontal axis is concerning the ABAQUS results. If data falls on the bisector line, it implies that the predictions and ABAQUS results are completely equal. In other words, the more data that are scattered along with the bisector line, the more agreement there is between the analytical framework and ABAQUS results. The results shown in this figure are divided into two zones: (a) the results within 15% accuracy and (b) the result within 25% accuracy. Those data that are outside of these zones had a very low ratio of β_b and can be classified as non-practical for the brace application. This is further discussed in the next section.

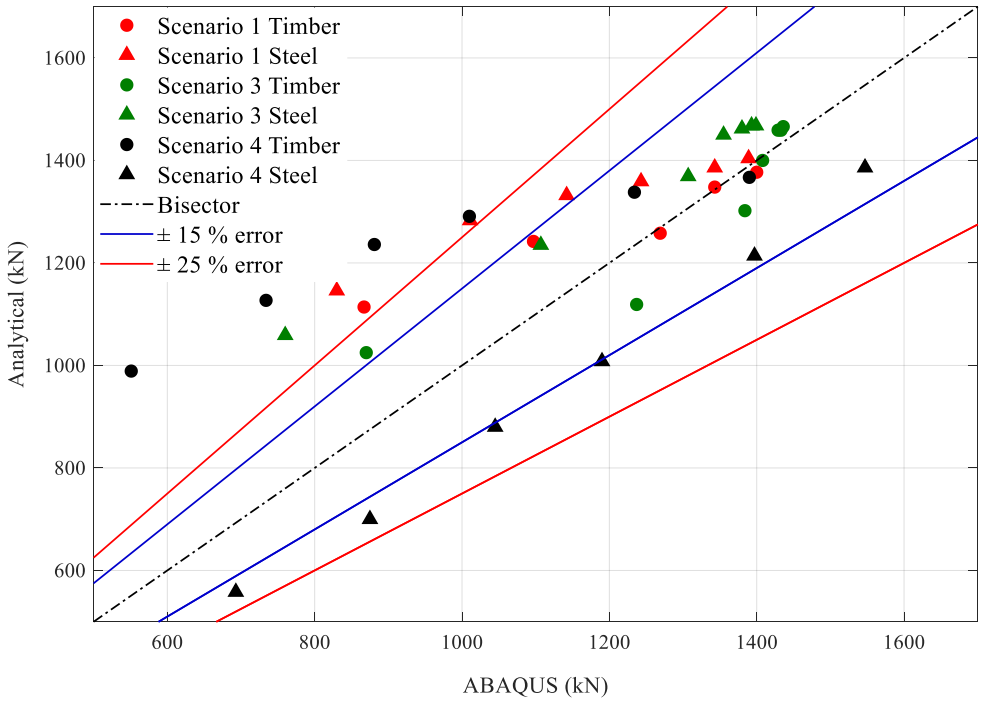

Figure 6.8: Analytical predictions for inelastic buckling versus numerical results from FE (part 1)

6.3.1.3. Calibration coefficient

The root cause of the mentioned difference is shown in Figure 6.9 and lies in the fact that the real ultimate load of the brace falls below the intersection point. More specifically, the intersection point would always yield an upper limit for the ultimate load. Accordingly, a calibration factor is introduced here based on the finite element study to compensate for that effect.

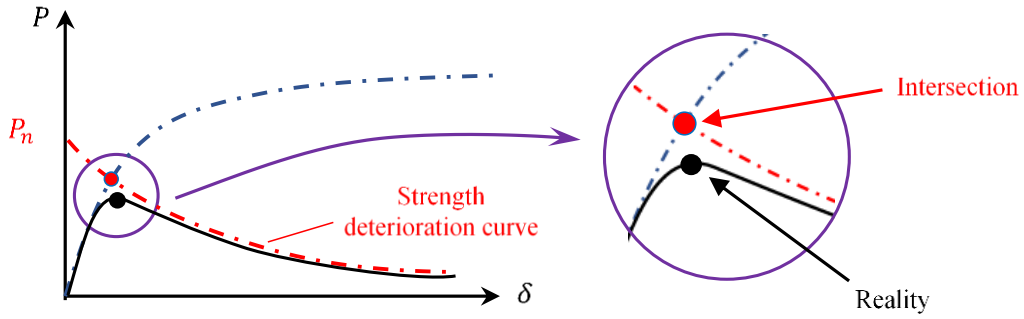

Figure 6.9: Real ultimate load Vs upper limit as the intersection point

Figure 6.10.a shows the result of the finite element study and the value of the calibration factor. A calibration factor of one implies that the result of the analytical approach matches the numerical one. It can be observed that for all three scenarios, the calibration factor approaches one as the relative rigidity β_b increases. It can be also deduced that the shorter the damper is, the faster the calibration factor hits the value of one. In the interest of being conservative and bringing simplicity to the design, a unified calibration factor can be assumed for the different zones. For example, for the blue and the green zones, a calibration factor of 0.85 and 0.75 can be assumed, respectively. Because the grey zone involves a large portion of inaccuracy and also tends not to be practical for the design (small amount of β_b), no calibration factor is considered for this zone. If any design falls in this zone, further numerical and/or experimental validation is required for the brace performance as the simplified closed-form equations will not provide the required accuracy.

If the results of the finite element study are categorized based on the calibration factor (γ_c) (Eq.6.1), relative rigidity and length, Figure 6.10.b could be visualized. As mentioned before, this diagram has been divided into three zones. These zones are formulated as a piece-wise function shown in Eq.6.2.

$$P_{ult,mod} = \gamma_c P_{ult} = \gamma_c \, P_{cr} \frac{\delta_{int}}{\delta_{int} + \delta_0} \tag{6.1}$$

$$\gamma_c = \begin{cases} 0.85 & 0.1 \leq \delta_2 \leq 0.25 \ and \ \beta_b \geq 0.0115e^{14.54\delta_2} \\ 0.75 & 0.1 \leq \delta_2 \leq 0.25 \ and \ \beta_b \geq 0.0083e^{14.54\delta_2} \\ 0.85 & \delta_2 < 0.1 \ and \ \beta_b \geq 0.05 \\ 0.75 & \delta_2 < 0.1 \ and \ \beta_b \geq 0.035 \\ 1 & \beta_b \geq 0.7 \\ Not\ recommended & else \ (\text{Figure } 6.10.b) \end{cases} \tag{6.2}$$

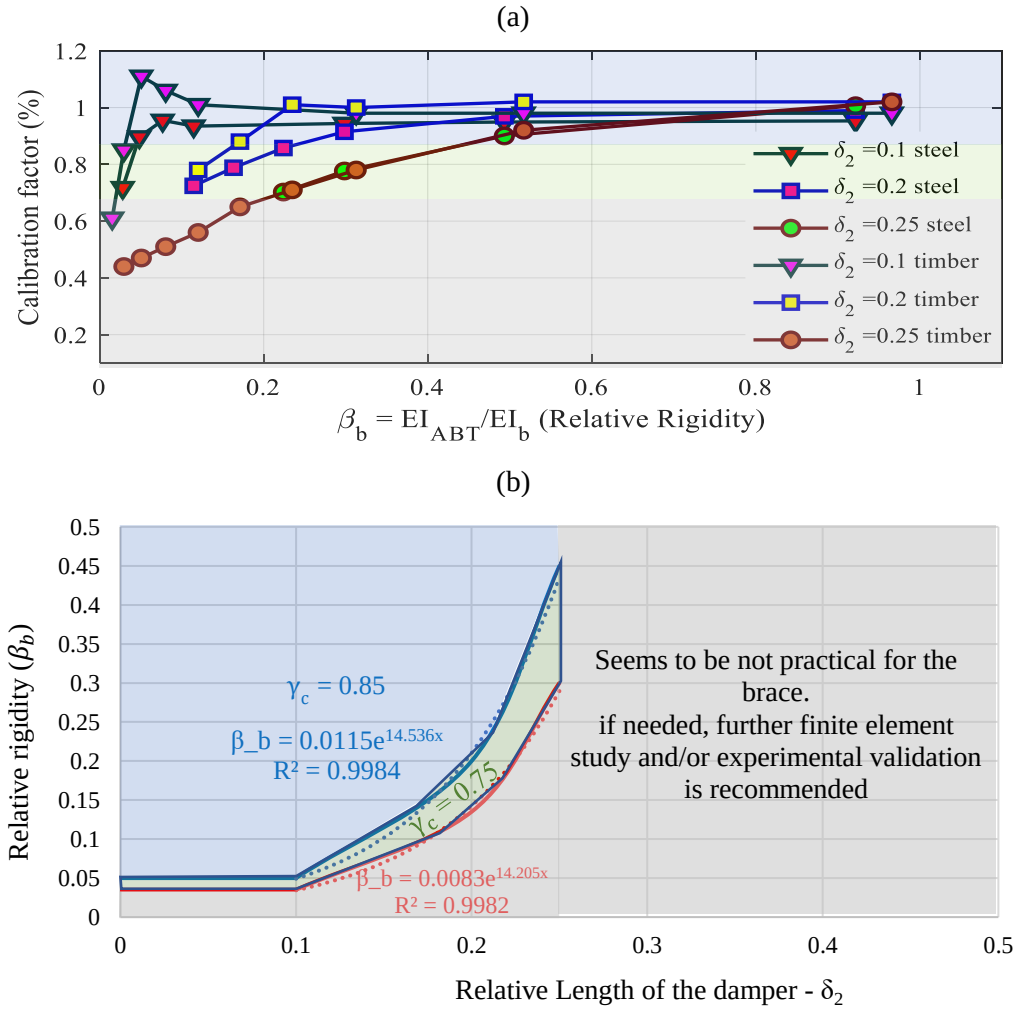

Figure 6.10: Calibration factor for Brace Design with one intermediate weakness: (a) Calibration factor for a brace with different damper lengths and (b) Simplification of the calibration factor for design purposes

6.3.2. *Part 2 -Brace with two weakened zones*

Similar to the previous section, the same study is carried out on the RSFJ brace with two weaknesses along the brace. For the purpose of finite element analysis, eight types of telescopic CHS sections were employed in the role of ABT. These sections had the same characteristics as the ABT in the previous section and tabulated in Table 6.3. Unlike the previous section, the brace body was considered to be only steel as it was observed that the results for timber and steel body were almost identical. The steel body was of SHS (square hollow section) type with an outer diameter of 152.5 mm and a thickness of 9.5 mm. The overall length of the brace "L" was assumed to be 4466 mm. In order to further investigate the effect of the damper length, two scenarios were considered for the length of the damper to be 10 and 20% of the brace length. The end bracket

length ($\delta_e . L$) was also assumed to be 222 mm. The parameters used and the schematic overview of the braces are depicted in Table 6.3 and Table 6.4.

Table 6.3: Telescopic Sections for Finite Element Study Part 2

Section	$(D_{out})_f$ (mm)	$(D_{in})_f$ (mm)	$(D_{out})_m$ (mm)	$(D_{in})_m$ (mm)	E (GPa)	F_y (MPa)	ε_u
ABT1	50.3	39.5	38.3	27.5	200	340	0.2
ABT2	60.3	49.5	48.3	37.5			
ABT3	70.30	59.50	58.30	47.50			
ABT4	80.30	69.50	68.30	57.50			
ABT5	90.30	79.50	78.30	67.50			
ABT6	120.30	109.50	108.30	97.50			
ABT7	140.30	129.50	128.30	117.50			
ABT8	170.30	159.50	158.30	147.50			

Table 6.4: Scenarios of the damper length for Finite Element Study Part 2

Scenario	$\delta_2 L$ (mm)	$\delta_1 L$ (mm)	L_{RSFJ} (mm)	L (mm)	$\delta_e . L$ (mm)	Analysis	
						Elastic	Inelastic
1	500	360	280	4466	222	✓	✓
2	900	560	680			✓	✓

6.3.2.1. Elastic buckling

Figure 6.11 shows the results of finite element analysis for the RSFJ braces with two intermediate weakened locations with steel bodies. The horizontal axis is the relative rotational stiffness of the ABT to the brace body, and the vertical axis is the elastic buckling calibrated load with EI/L^2, shown as $\alpha = (P_{cr})_{Abaqus} L^2 / EI$. As it can be seen, as the β (relative rotational stiffness defined

as per Eq 5.12) increases, the α tends to converge to π^2, which is indicative of the Euler buckling load for a pin-pin column. The analytical predictions (see section 5.1.2 for the case of brace with two weakened locations) can be deduced to be in good agreement with the numerical results by comparing the dotted data versus the black line. However, the accuracy is better for the larger β. To further support this, it can be referred to the correlation coefficients, which all are 0.95 and 0.98 for scenarios one and two, respectively.

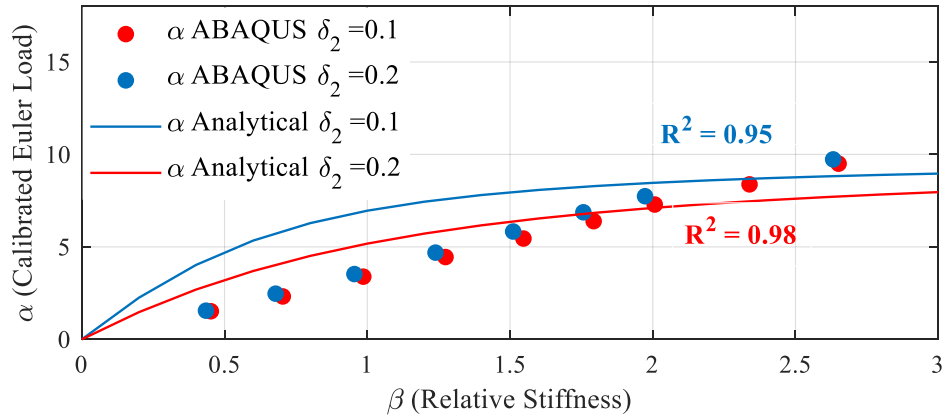

Figure 6.11: Numerical results Vs analytical predictions for elastic buckling FE (part 2) – scenario 1 and 2

Figure 6.12 shows the error of the analytical approach (defined as the difference between analytical and ABAQUS results divided by ABAQUS results = $(F_{analytical} - F_{ABAQUS})/ F_{ABAQUS}$) versus the relative rigidity of the ABT to that of the brace body. For scenarios one and two, this error converges to almost zero when the relative rigidity is higher than 0.08 - 0.1. It should be also pointed out that this range of relative rigidity can be easily met for design purposes as normally it falls between 0.1 and 0.5 for an optimum design with commonly available telescopic sections.

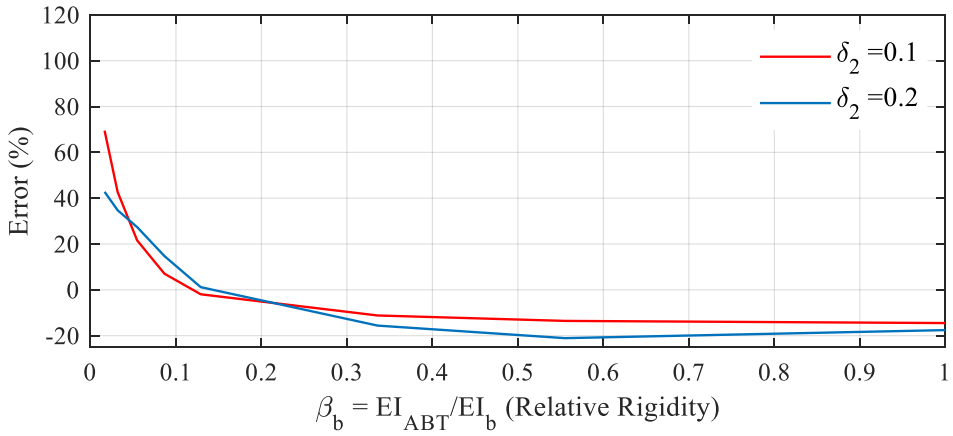

Figure 6.12: Error of the analytical approach versus relative rigidity for elastic buckling (part 2)

6.3.2.2. Inelastic buckling

The procedure of the modelling of the brace in ABAQUS was previously covered in section 6.3.1.2. The same procedure was followed here but with the difference that two locations were considered for the damper installation. Figure 6.13 shows two examples of ultimate load quantification using the SCMA method (simplified collapse mechanism analysis) previously explained in chapter 5. In Figure 6.13.a, it is the ABT that fails before the brace body showing that the failure mode of the brace is according to the 2nd mode. However, in Figure 6.13.b, it is the brace body that fails before the ABT showing that the failure mode of the brace is according to the 1st mode. In both cases, the SCMA method successfully predicted the ultimate load with a marginal difference.

Figure 6.14 shows the comparison between the analytical predictions (SCMA) and numerical results for the inelastic buckling (collapse) load for the scenarios mentioned in Table 6.4 and the ABTs in Table 6.3. In this diagram, both x- and y-axis are the collapse loads where the vertical axis is associated with the SCMA predictions and the horizontal axis is concerning the ABAQUS results. If a dot falls on the bisector line, it implies that the SCMA prediction and ABAQUS result are completely equal. In other words, the more data that are scattered along with the bisector line, the more agreement there is between the analytical framework and ABAQUS results. The results shown in this figure are divided into two zones: (a) the results within 15% accuracy and (b) the result within 25% accuracy. As can be observed most of the data are scattered around the bisector line while a portion of them (collapse load less than 600 kN) are outside the 25% margin. These data outside of the zone had a very low ratio of β_b and can be classified as the non-practical cases for the brace application. If any design falls in this zone, it is recommended that a detailed numerical study and/or an experimental validation be conducted.

(a)

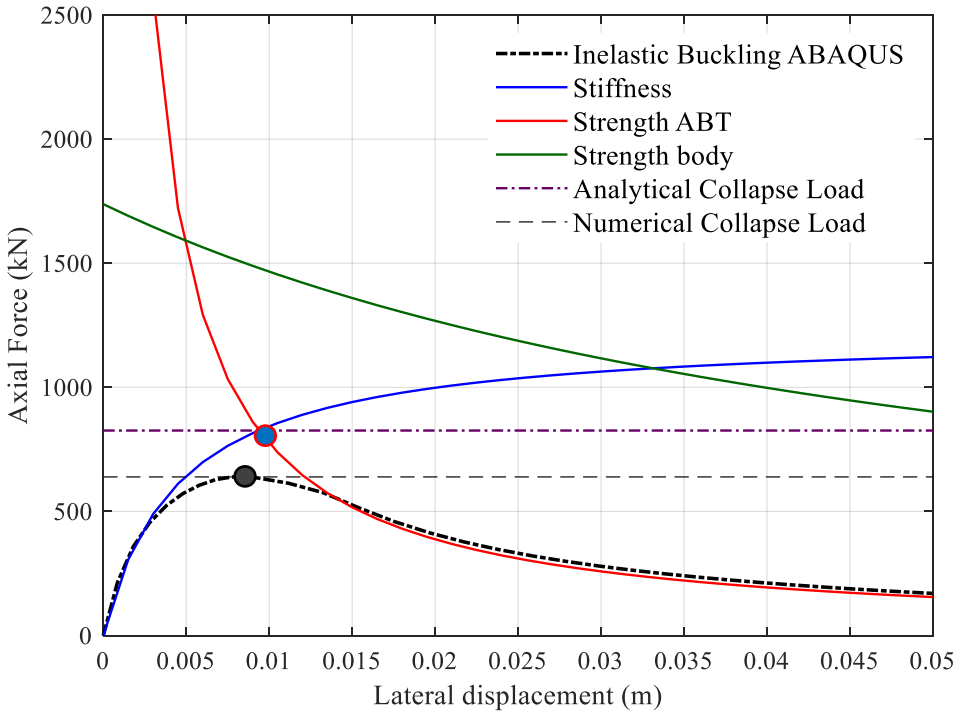

(b)

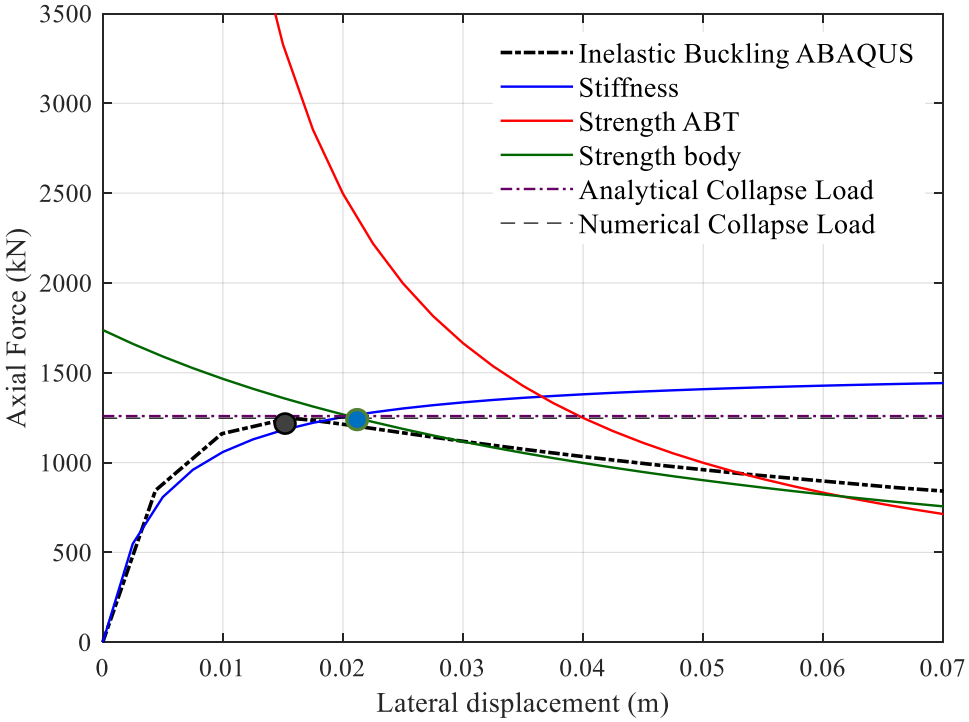

Figure 6.13: Inelastic Buckling of Steel brace scenario1 with (a) ABT 3 and (b) ABT 8

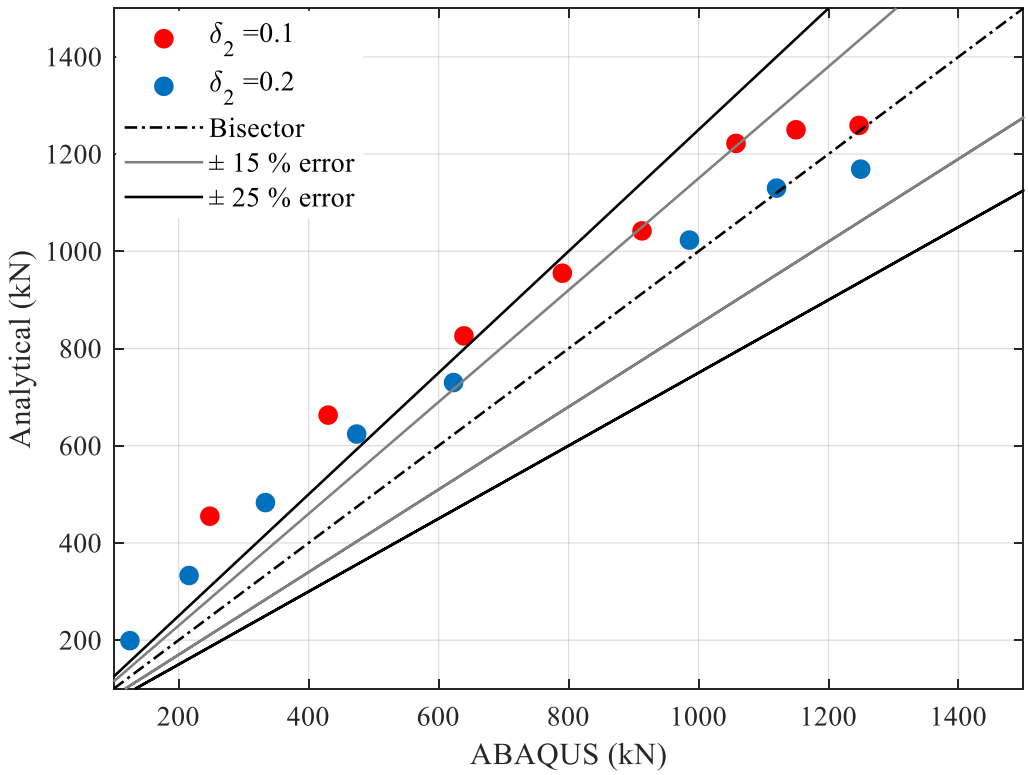

Figure 6.14: Analytical predictions for inelastic buckling versus numerical results from FE part 2

6.3.2.3. Calibration coefficient

Figure 6.15 shows the result of the finite element study and the value of the calibration factor. A calibration factor of one implies that the result of the analytical approach matches the numerical one. It can be observed that for all two scenarios, the calibration factor approaches one as the relative rigidity β_b increases. In the interest of being conservative and bringing simplicity to the design, a unanimous calibration factor can be assumed for different zones. For example, for the blue and the green zone, a calibration factor of 0.85 and 0.75 can be assumed, respectively. The grey zone involves a large portion of inaccuracy and also tends not to be practical for the design (small amount of β_b). Therefore, if any design falls in this zone, it should be either transferred to other zones by using stronger ABTs or experimental study is required. It should be also noted that this factor is different from the strength reduction factors that the building codes normally employ. If the results of the finite element study are sorted out based on the calibration factor (Eq.6.1), the relative rigidity and the length, Figure 6.15 could be envisioned. As mentioned

before, this diagram has been divided into three zones. These zones are formulated as a piece-wise function shown in Eq.6.3.

$$\gamma_c = \begin{cases} 0.85 & \beta_b \geq 0.12 \\ 0.75 & 0.08 \leq \beta_b \leq 0.12 \\ 1 & \beta_b \geq 0.8 \end{cases} \quad 6.3$$

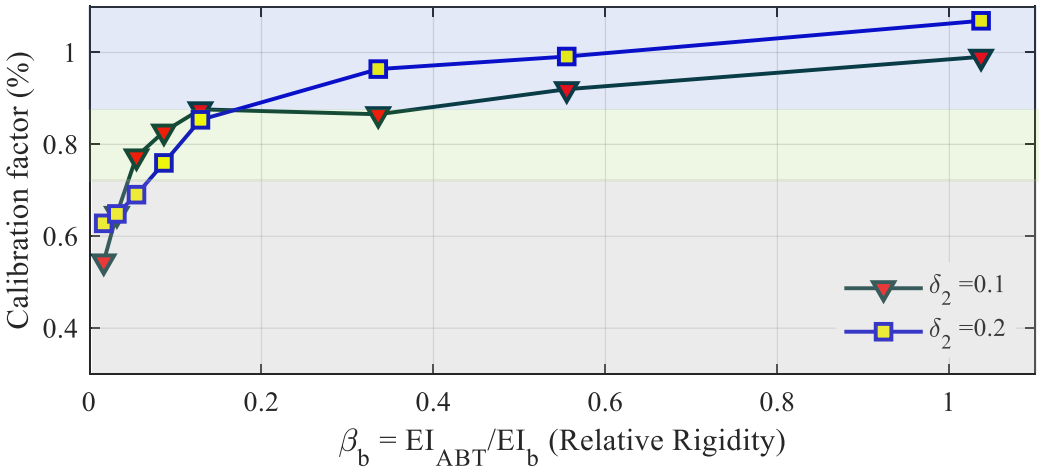

Figure 6.15: Calibration factor for Brace Design with two intermediate weaknesses

6.4 Conclusion

In this chapter, a parametric finite element study (with 98 models) was performed so that the accuracy of the proposed method is evaluated. For this purpose, both the elastic and inelastic buckling analyses were carried out within the ABAQUS software environment where in the 1st part of the study, 11 ABT sections, two brace body types (steel and timber) and three different dampers lengths were considered while in the 2nd part, 8 ABT sections and two scenarios for the damper's length were considered. Overall, it was observed that the proposed model could successfully predict both the elastic and inelastic capacities of the RSFJ brace with an acceptable accuracy while it was also capable of predicting the location of the plastic hinge and the failure mode. The failure mode prediction is highly important when the seismic design considerations are taken into account. This topic was further discussed in chapter 5.

In terms of inelastic strength prediction using the proposed SCMA method, because the method was developed based on intersecting the stiffness and strength deterioration curves, it always brought the upper limit of the ultimate strength of the brace while in reality, this force may be slightly less. In order to compensate for this, a calibration factor, less than one, for both cases of

brace with one and two weakened locations was introduced so that it decreases the load. This factor was dependent on the relative length of the damper and also the relative rigidity of the ABTs to the brace bodies.

7 Design Examples

7.1 Motivation

In this section, three examples of RSFJ brace design are provided to assist the engineers in better understanding the design process. In the provided examples, it is attempted to consider as many variations as possible so that the engineer is exposed to the possible scenarios in real practice. For instance, the examples includes both steel or timber body options, installation of dampers in one or two positions within the brace, single or parallel employment of ABTs, and Circular or Square Hollow Sections (CHS and SHS) for ABTs. In this respect, the first example is considered to represent a *steel* brace with *one* weakened location for the damper installation strengthened with *multiple* parallel ABTs, the second example is considered to represent a *steel* brace with *two* weakened locations for damper placement strengthened with a *single* ABT, and finally, the third example is considered to represent a *timber* brace with *one* weakened location for damper installation strengthened with *multiple* parallel ABTs. In terms of anti-buckling tubes, two are designed with telescopic SHS section and one is designed with telescopic CHS section. It should be noted that most of the practical cases fall in the category of the brace with one weakened location for damper mainly because the displacement demand in the bracing system would not be that high to necessitate two locations for dampers in series. The detailed connection design and capacity-desing of other elements of the brace is also provided in the first example.

7.2 Summary of the design process

As for any member subjected to compression, the strength in compression would be adversely affected by the arrival of the second-order actions. In an ideal *elastic system*, the lateral displacement will increase due to $p-\Delta$ effect as the axial load increases and approaches the elastic buckling load while the rate of this surge will grow in the vicinity of the elastic buckling load. However, in *elasto-plastic system* where the material has a limited strength, the weakest section may fail during this increase of lateral deflection, and depending on the geometry, the strength can be less or equal to the elastic buckling load. The analytical closed-form framework for quantification of the ultimate compressive strength of the self-centring brace was discussed in great detail in chapter 5 and chapter 6. As mentioned, the method – SCMA – is based on intersecting two curves namely:

stiffness degradation curve and strength degradation curve. Employment of this method not only will result in illustrating where the weakest section is but also lead to quantifying the load at which the system becomes a mechanism and unstable (with negative stiffness). Further on in chapter 6, it was discussed that SCMA might have a marginal overestimation (see section 6.3.1.3 and section 6.3.2.3) for which to compensate, a calibration factor was introduced accordingly. Critical to note is that this calibration is not the strength reduction ($\emptyset$) factor as prescribed in the building codes. Thus, when designing a self-centring brace in the engineering offices, that strength reduction factor should be additionally added and considered in the design process. This is not pursued in this chapter.

Figure 7.1 shows the summary and big picture of the design in form of a flowchart in six consecutive steps. The process initiates with calculating the force demand in the brace, which is the output from 3D modelling of the structures or any other well-known methods. Then, the engineer would decide on the brace body section/material given the force demand. In this stage, the number of dampers in parallel and series would be determined with respect to the force and displacement demand. The procedure continues with the prediction of the elastic buckling load of the system (P_{cr}) given the size and number of ABTs employed. At step 3, the pure axial capacity (squash strength) P_n is determined, which along with the critical load P_{cr} will be input in the intersection formulations to figure out at what lateral deflection, the plastic hinges would form based on two modes of collapse. Here, it should be noted the intersection point - considering mode 1 - for steel braces should be calculated based on Eq.5.4 while for timber braces, it should be according to Eq.5.8. The intersection point for mode 2 (plastic hinge in ABT) is identical (Eq.5.23) for both applications. Step 3 would end with the calculation of the ultimate and modified ultimate capacity of the brace. It should be noted the calibration factors developed in chapter 6 to modify the ultimate capacity are only applicable if the stiffness deterioration curves are calculated based on the proposed procedure. If any finite element study or any other well-known methods is used, the calibration factor is not applicable and not recommended to be used. In the final step, it should be also made sure that the failure mode is the first mode; otherwise, a stronger ABT should be selected, and the previous steps should be repeated. While in this step, the force demand should be checked against the capacity. It is suggested that the code strength reduction factor and load amplification be used in design office cases to increase the safety margin of the design. The process ends with the capacity design of the connections and the adjacent members.

In the interest of convenience for readers and office engineers, the mentioned process is formulated in consecutive steps after the flowchart diagram.

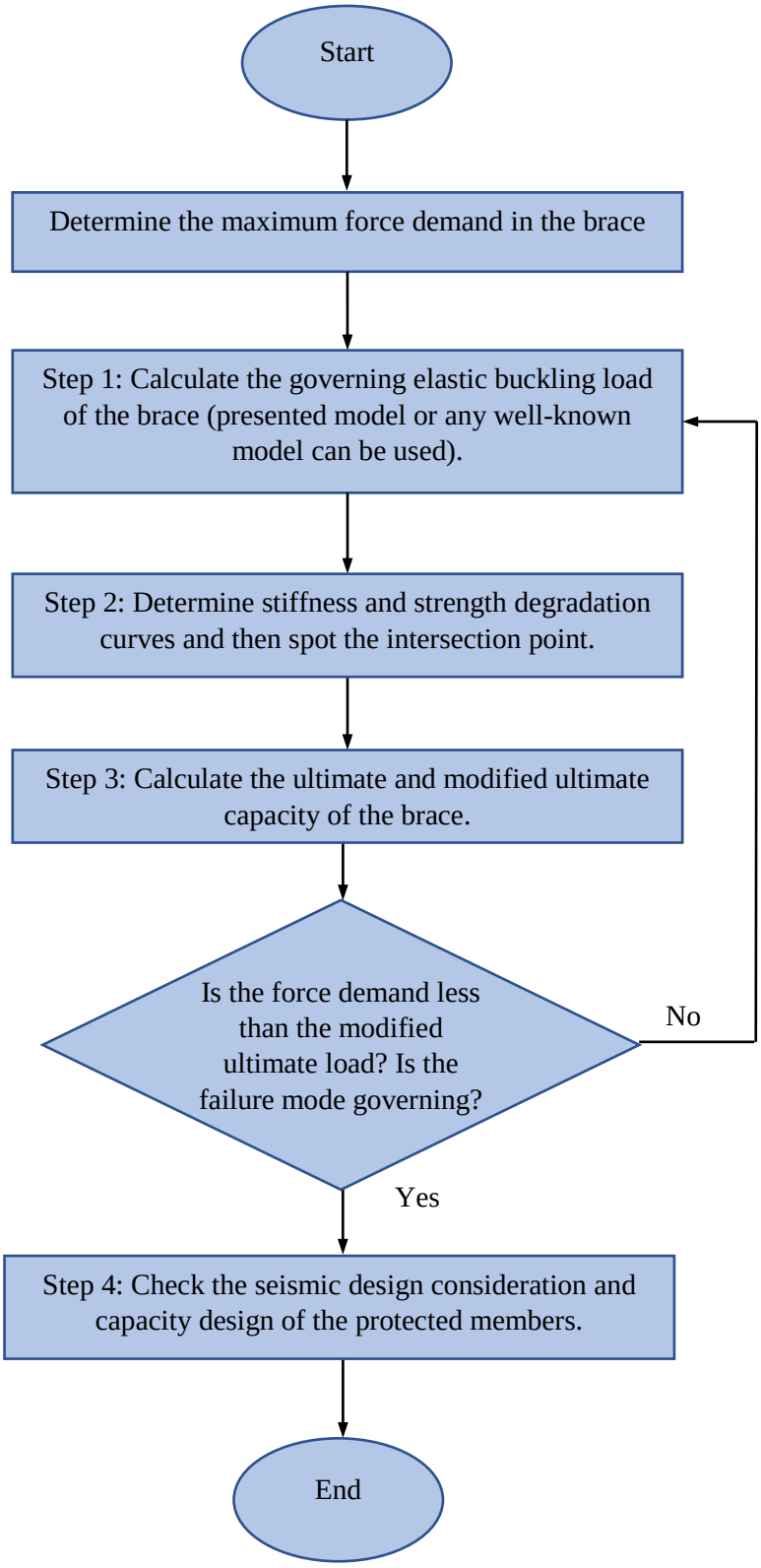

Figure 7.1: Design flowchart for RSFJ brace

- **Brace with one weakened location for damper installation:**

Step 1:

1. $\delta_1 = \frac{L_1}{L}$
2. $\delta_2 = \frac{L_{RSFJ} + L_{con}}{L} = \frac{L_{ABT} + L_{con}}{L}$
3. $\beta_b = \frac{(EI)_{ABT}}{(EI)_{body}}$
4. $m = \frac{\delta_2}{[2(\delta_2 - \delta_1) - (\delta_2)^2 + \beta_b(1-\delta_2)^2]}$
5. $K_{ABT} = \frac{2m.EI_{ABT}}{\delta_2 L}$
6. $\beta = \frac{K_{ABT}L}{EI}$
7. $Solve\ the\ following\ to\ determine\ \alpha$:

$$f(\delta_1, \beta) = 2\alpha\, sin\left(\sqrt{\alpha}(2\delta_1 - 1)\right) - \alpha\, sin\left(\sqrt{\alpha}(4\delta_1 - 1)\right) + \alpha\, sin(\sqrt{\alpha}) - 4\beta^2\, sin(\sqrt{\alpha}) + 4\sqrt{\alpha}\beta\, cos\left(\sqrt{\alpha}(2\delta_1 - 1)\right)$$

8. $P_{cr} = \alpha \frac{EI}{L^2}$
9. $\delta_0 = \frac{L}{1000} + \frac{L}{500} + \delta_{clearance}$

Step 2:

10. $(\delta_{int})_{ABT} = 0.5(M_p)_{female}\left[\frac{1}{P_{cr}} + \sqrt{\left(\frac{1}{P_{cr}}\right)^2 + \frac{4\delta_0}{(M_p)_{female}.P_{cr}}}\right]$

Steel Brace body:

11. $(\delta_{int})_{body} = 0.5(M_p)_{body}\left[\frac{1}{P_{cr}} - \frac{1}{P_n} + \sqrt{\left(\frac{1}{P_{cr}} - \frac{1}{P_n}\right)^2 + \frac{4\delta_0}{(M_p)_{female}.P_{cr}}}\right]$

Timber brace body:

11. $(\delta_{int})_{body} = 0.5Sf_b\left[\frac{1}{P_{cr}} - \frac{1}{A_g f_c} + \sqrt{\left(\frac{1}{P_{cr}} - \frac{1}{A_g f_c}\right)^2 + \frac{4\delta_0}{Sf_b P_{cr}}}\right]$

Step 3:

12. $P_{ult} = \min\left[P_{cr} * \frac{(\delta_{int})_{ABT}}{(\delta_{int})_{ABT} + \delta_0},\ \ P_{cr} * \frac{(\delta_{int})_{body}}{(\delta_{int})_{body} + \delta_0}\right]$
13. $P_{ult,mod} = \gamma_c P_{ult}$

Step 4:

14. Check that the demand is less than capacity: $P^* \leq \varphi.P_{ult,mod}$ and the governing failure mode is brace body failure
15. Design the connections and adjacent members according to the capacity design principle

- **Brace with two weakened locations for damper installation:**

Step 1:

1. $\delta_1 = \frac{L_1}{L}$
2. $\delta_2 = \frac{L_{RSFJ} + L_{con}}{L} = \frac{L_{ABT} + L_{con}}{L}$
3. $\beta_b = \frac{(EI)_{ABT}}{(EI)_{body}}$
4. $m = \frac{\delta_2}{[2(\delta_2 - \delta_1) + \beta_b(1 - 2\delta_2)]}$
5. $K_{ABT} = \frac{2m.EI_{ABT}}{\delta_2 L}$
6. $\beta = \frac{K_{ABT}L}{EI}$
7. $Solve\ the\ following\ to\ determine\ \alpha$:

$$f(\delta_1, \beta) = 2\alpha\, sin\left(\sqrt{\alpha}(2\delta_1 - 1)\right) - \alpha\, sin\left(\sqrt{\alpha}(4\delta_1 - 1)\right) + \alpha\, sin\left(\sqrt{\alpha}\right) - 4\beta^2\, sin\left(\sqrt{\alpha}\right) + 4\sqrt{\alpha}\beta\, cos\left(\sqrt{\alpha}(2\delta_1 - 1)\right)$$

8. $P_{cr} = \alpha \frac{EI}{L^2}$
9. $\delta_0 = \frac{L}{1000} + \frac{L}{500} + \delta_{clearance}$

Step 2:

10. $(\delta_{int})_{ABT} = 0.5(M_p)_{female}\left[\frac{1}{P_{cr}} + \sqrt{\left(\frac{1}{P_{cr}}\right)^2 + \frac{4\delta_0}{(M_p)_{female}.P_{cr}}}\right]$

Steel Brace body:

11. $(\delta_{int})_{body} = 0.5(M_p)_{body}\left[\frac{1}{P_{cr}} - \frac{1}{P_n} + \sqrt{\left(\frac{1}{P_{cr}} - \frac{1}{P_n}\right)^2 + \frac{4\delta_0}{(M_p)_{female}.P_{cr}}}\right]$

Timber brace body:

11. $(\delta_{int})_{body} = 0.5Sf_b\left[\frac{1}{P_{cr}} - \frac{1}{A_g f_c} + \sqrt{\left(\frac{1}{P_{cr}} - \frac{1}{A_g f_c}\right)^2 + \frac{4\delta_0}{Sf_b P_{cr}}}\right]$

Step 3:

12. $P_{ult} = \min\left[P_{cr} * \frac{(\delta_{int})_{ABT}}{(\delta_{int})_{ABT} + \delta_0},\ P_{cr} * \frac{(\delta_{int})_{body}}{(\delta_{int})_{body} + \delta_0}\right]$
13. $P_{ult,mod} = \gamma_c P_{ult}$

Step 4:

14. Check that the demand is less than capacity: $P^* \leq \varphi.P_{ult,mod}$ and the governing failure mode is brace body failure
15. Design the connections and adjacent members according to the capacity design principle

- **Geometrical controls:**

After that the design of the brace is finished and all of the sections for the brace body and ABTs are determined, the next major step is to decide on the overlap length of the ABTs. As can be observed in Figure 7.2, the sliding tubes must have a minimum overlap as well as a minimum gap to avoid clash during the earthquake. The minimum gap is as per suggestion by the American standards ASCE 7 [195] and ASCE 41[198]. It is worth mentioning that the author thinks the rationale behind this suggestion seems to be that the collapse point of the structure must fall beyond the MCE (Maximum Considerable Earthquake) demand and it appears that the 30% safety margin is a good measure.

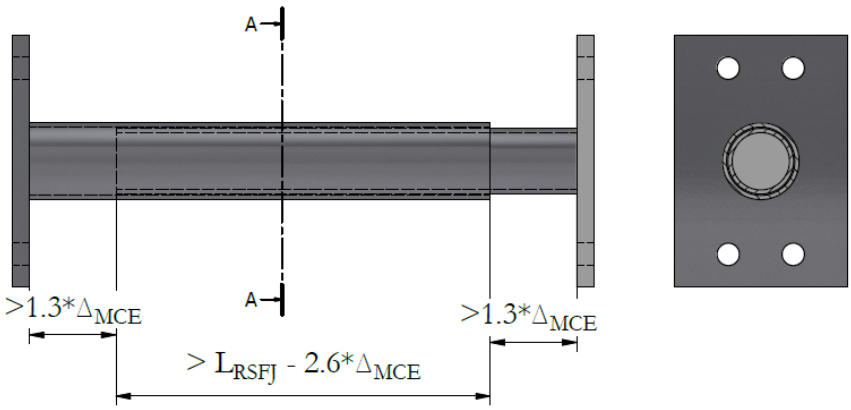

Figure 7.2: ABTs geometry control

7.3 Design example 1: Steel brace with one weakened location for damper

The objective in this section is to design a brace for 1300 kN capacity in which all of the members are made up of mild steel with an elastic modulus of 200 Gpa and yield stress of 340 Mpa. The total length of the brace is 8460 mm while the damper length is 1310 mm and the distance between pin and damper is 200 mm. The following parameters are assumed as the input: Overstrength factor (o/s) = 1.35, which is concerning the performance of RSFJ after lockage, referred to as secondary-fuse [158]. The overstrength must account for both possible higher yield stress (expected yield stress) and possible strain-hardening. This makes the force demand factored up to P = 1.35 * 1300 = 1755 kN (Factored Force Demand). The brace section was of CHS (Circular Hollow Section) CHS 323.9 x 9.5 with a moment of inertia of 11600 e4 mm^4. The relative length

of the ABT and RSFJ given that L_{RSFJ} = 1310 mm can be calculated from Eq.5.11 and Eq.5.15 as following:

$$\delta_1 = \frac{835}{8460} \sim 0.1$$

$$\delta_2 = \frac{1510}{8460} \sim 0.18$$

The ABTs were assumed to be composed of two telescopic SHS (Square Hollow Section) with dimensions 125 mm and 107 mm for the female section and 105 mm and 87 mm for the male part, respectively. The moment of inertia for the female and male sections were 9.433 e6 and 5.366 e6 mm^4. For this design, three ABTs have been provided with two RSFJs on either side of the ABTs:

The parameter "β_b" – relative rigidity – should be calculated for both weak and strong axis (here same for CHS section) from Eq.5.16:

$$(\beta_b)_{weak} = \frac{200{,}000 * 3(9.433 + 5.366) * 10^6}{200{,}000 * 11600 * 10^4} = 0.38$$

$$(\beta_b)_{strong} = \frac{200{,}000 * 3(9.433 + 5.366) * 10^6}{200{,}000 * 11600 * 10^4} = 0.38$$

The parameter "m" should be calculated for both weak and strong axis from Eq.5.14:

$$(m)_{weak} = 0.469$$

$$(m)_{storng} = 0.469$$

The rotational stiffness of ABT "K_{ABT}" should be calculated for both weak and strong axis from Eq.5.13:

$(K_{ABT})_{weak}$ = 5.5 e9 N.mm

$(K_{ABT})_{storng}$ = 5.5 e9 N.mm

The parameter "β" – relative stiffness – should be calculated for both weak and strong axis from Eq.5.12:

$$(\beta)_{weak} = 2.007$$

$$(\beta)_{storng} = 2.007$$

The parameter "α" should be calculated by solving the characteristic equation (Eq.5.10) for both weak and strong axis for the finite minimum non-zero real roots:

$$(\alpha)_{weak} = 8.606$$

$(\alpha)_{storng} = 8.606$

Finally, the Euler load (elastic buckling load) "P_{cr}" should be calculated for both weak and strong axis from Eq.5.9:

$(P_{cr})_{weak} = 2789.76\ kN$

$(P_{cr})_{storng} = 2789.76\ kN$

As it is was mentioned before, this elastic buckling load is not an indicator of the system capacity in compression.

Calculation of the possible clearances and imperfections:

$L/500$ for the total out-of-straightness of the brace and erection error

Clearance between male and female telescopic tubes:

$$\delta_0 = \frac{8460}{500} + 2 = 18.9\ mm$$

Strength curves associated with ABT (female) and the brace body can be derived from Eq.5.22 and Eq.5.4, respectively:

$$P_{ABT}(\delta) = \frac{(M_p)_f}{\delta}$$

$$P_{body}(\delta) = \frac{(M_p)_{body}\left(1 - \frac{P_{body}}{P_n}\right)}{\delta} \ \ or \ \ P_{body} = \frac{(M_p)_{body}}{\frac{(M_p)_{body}}{P_n} + \delta}$$

Note that the strength of the brace body is modified with the combined action formula given it is carrying axial load and bending moment at the same time. However, the ABT does not need modification as it is not carrying any axial load.

Plastic modulus of the female part of ABT

= number of ABT $\times \left(\frac{bh^2}{4} - (b - 2t)(\frac{h}{2} - t)^2\right)$

S_{ABT} = 1.82 e5 mm^3

Plastic moment capacity of ABT and brace body

$(M_p)_{female} = S_{female} \times F_y =$ 185.66 kNm

$(M_p)_{body} = S_{body} \times F_y =$ 319.26 kNm

The nominal axial capacity of brace body = $P_n = A_g F_y =$ 3189.20 kN

The intersection points can be approximated using the following equations and shown in Figure 7.3:

$$(\delta_{int})_{ABT} = 0.5(M_p)_{female}\left[\frac{1}{P_{cr}} + \sqrt{\left(\frac{1}{P_{cr}}\right)^2 + \frac{4\delta_0}{(M_p)_{female}.P_{cr}}}\right] = 82\ mm$$

$$(\delta_{int})_{body} = 0.5(M_p)_{body}\left[\frac{1}{P_{cr}} - \frac{1}{P_n} + \sqrt{\left(\frac{1}{P_{cr}} - \frac{1}{P_n}\right)^2 + \frac{4\delta_0}{(M_p)_{female}.P_{cr}}}\right] = 54\ mm$$

Finally, the ultimate load capacity of the brace can be derived from Eq.5.5 if the intersection point is assumed as the input (Figure 7.3).

$$P_{ult} = min\left[P_{cr} * \frac{(\delta_{int})_{ABT}}{(\delta_{int})_{ABT} + \delta_0},\ P_{cr} * \frac{(\delta_{int})_{body}}{(\delta_{int})_{body} + \delta_0}\right] = min\ [2266,\ 2116\ ]$$

$$P_{ult} = 2116\ kN$$

Given that $\delta_2 = 0.18$ and $\beta_b = 0.38$, the calibration coefficient is 0.85 (Eq.6.2). The modified capacity of the brace can be derived from Eq.6.1 as:

$$P_{ult,mod} = \gamma_c P_{ult} = 0.85 * 2116 = 1798.6\ \text{kN}$$

As it can be observed, the governing failure mode is the plastic hinge in the brace body, which was discussed to be the desired mode of failure. The next step would be the design of the endplate of the ABT, which is similar to the design of base plates. Since the governing failure mode is the plastic hinge in the brace body, the endplate can be designed for the bending demand at the end of ABT at the time of plastic hinge formation (Eq.5.25)

7.3.1.1. End plate design

Bending moment and axial force demands for endplate would be:

$$(M_p)_{body_{int}} = 2P'_{ult}\delta_2\delta'_{int} = 54\ kNm$$

$$P_{ult,mod} = 1798.6\ kN$$

Dimension of circular end plate: B = D = 580 mm

Yield stress of the plate $F_y = 340\ Mpa$ (Yielding stress of mild steel)

Check for eccentricity of the axial load: If the eccentricity is high (e > B/6), the bearing stress should be coming from strain compatibility due to partial separation.

$$e = \frac{(M_p)_{body_{int}}}{P} = \frac{5.4\ e7}{1798\ e3} = 30.8\ mm < \frac{B}{6}\ (96\ mm)$$

Bearing stress for circular plate:

$$\sigma_{bearing} = \frac{P}{A} \pm \frac{M}{Z}$$

$$\sigma_{bearing\_max} = 9.5\ MPa$$

$\sigma_{bearing\_min}$ = 3.8 MPa

$\sigma_{bearing\_avg}$ = 6.6 MPa

The moment in the plate is considered for the maximum outstanding free length from the end of RSFJ base support. Considering no stiffener action from the ABTs.

Free length = 235.3 mm (shown in Figure 7.4)

$$M^*_{endplate} = \frac{\sigma_{bearing\_avg} \cdot L^2}{2} = 188224\ Nmm$$

The thickness of end plate = $t_{endplate} = \sqrt{\frac{4 \cdot M^*_{endplate}}{0.9 \cdot F_y}}$ = 49.6 mm so it is suggested to provide a 60mm end plate.

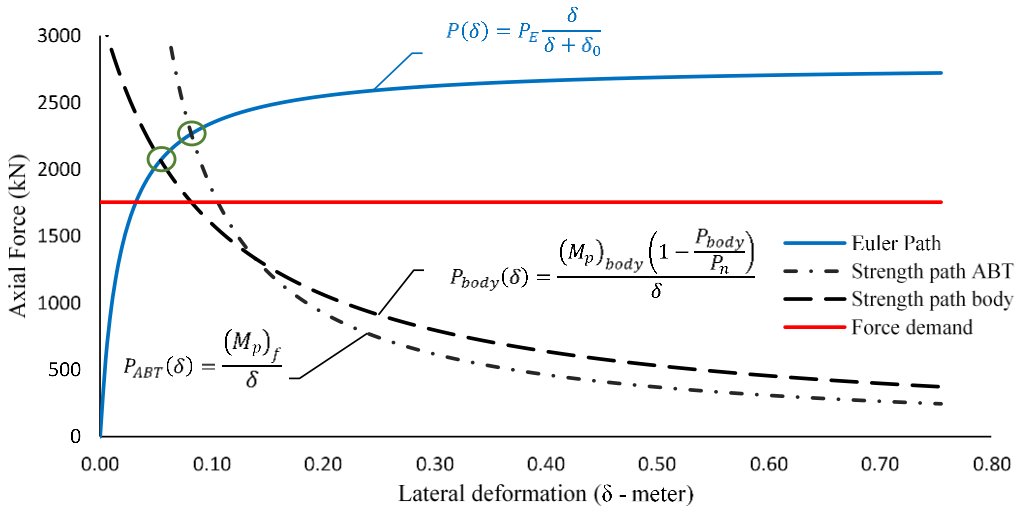

Figure 7.3: Spotting the ultimate capacity by intersecting the stiffness and strength deterioration curves – example 1.

7.3.1.2. Design of the welding for attaching the ABTs to the end-plate

The ultimate stress of weld shall be higher than the material strength F_y = 340Mpa. Therefore, the welding metal was assumed to have a tensile strength of F_u = 690 MPa.

The maximum fillet weld thickness shall be governed by the minimum plate or the ABT section size thickness which in this case shall be 9mm. In this case, the fillet weld is assumed to be 8mm.

The area for weld shall be taken for the outside perimeter of the smaller male tube. As in this case, the force being higher small stiffener plates has been added for additional weld length.

The weld shall be checked for combined action of the shear force from Eq.5.24, which is almost 2.5% of axial force due to the second-order effect, and the plastic moment capacity of the ABT section (female section).

V* = 2.5%P = 4.4 e4 N

M* = 2.5 e8 N.mm

Tensile stress due to moment and shear:

$$\sigma_t = \frac{M * c}{Iw} + \frac{\mathrm{V}}{\mathrm{Aw}} = 100.79 \text{ Mpa}$$

Nominal capacity of weld = 0.6*F_u = 0.6*690 = 414 MPa

Resisting capacity = 0.8*nominal capacity = 0.8*414 = 331.2 MPa

Tensile stress/resisting capacity = 100.79/331.2 = 0.3 "OK"

7.3.1.3. Design of the welding for attaching the ABTs to the end-plate

Applied shear on the vertical weld on ABT shall be from the bearing stress on the end plate.

V* = Area of plate * $\sigma_{bending\_avg}$ = 1.76 e6 N

A_w = 13776 mm2 (5.6 mm being effective thickness of 8mm weld)

σ_v = V*/A_w = 246.5 MPa

Nominal capacity of weld = 0.6*F_u = 0.6*690 = 414 MPa

Resisting capacity = 0.8*nominal capacity = 0.8*414 = 331.2 MPa

Tensile stress/resisting capacity = 331.2/246.5 = 0.74 "OK"

The drawings and dimensions of the anti-buckling tubes can be found in Figure 7.4.

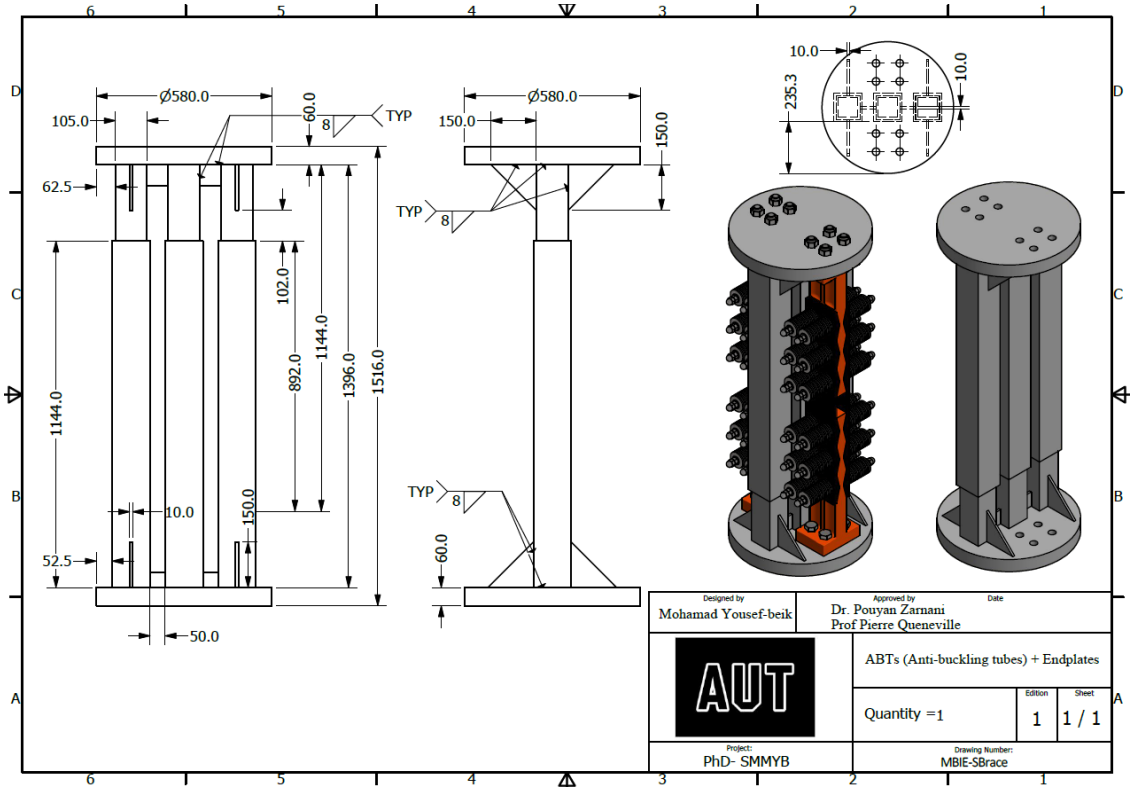

Figure 7.4: drawings and dimensions of Anti-buckling tubes with their end plates

7.4 Design example 2: Steel brace with two weakened locations for damper

The objective in this section is to design a brace for 220 kN capacity in which all of the members are made up of mild steel with an elastic modulus of 200 Gpa and yield stress of 340 Mpa. The total length of the brace is 4460 mm while the damper length is 633 mm and the distance between pin and damper is 200 mm. The following parameters have been assumed as the input: Overstrength factor (o/s) = 1.35, which is concerning the performance of RSFJ after lockage, referred to as secondary-fuse [158]. The overstrength must account for both possible higher yield stress (expected yield stress) and possible strain-hardening. This makes the force demand factored to P = 1.35 * 220 = 297 kN (Factored Force Demand). The brace section is of "I" section – 250 UB 37 with a moment of inertia of 5.57 e4 mm^4 and 5.66 e4 mm^4 in storng and weak axis, respectively. The relative length of the ABT and RSFJ given that L_{RSFJ} = 633 mm can be calculated from Eq.5.11 and Eq.5.15 as follows:

$$\delta_1 = \frac{526.5}{4460} \sim 0.12$$

$$\delta_2 = \frac{843}{4460} \sim 0.19$$

The anti-buckling tubes were assumed to be composed of two telescopic CHS (Circular Hollow Section) with dimensions 114.6 mm and 105.3 mm for the female section and 101.6 mm and 91.6 mm for the male part, respectively. The moments of inertia for the female and male sections were 2.43 e6 and 1.77 e6 mm^4. For this design, one ABTs has been provided with RSFJ on either side of it:

The parameter "β_b" – relative rigidity – should be calculated for both weak and strong axis (here same for CHS section) from Eq.5.14:

$$(\beta_b)_{weak} = \frac{200{,}000 * 3(9.433 + 5.366) * 10^6}{200{,}000 * 11600 * 10^4} = 0.74$$

$$(\beta_b)_{storng} = \frac{200{,}000 * 3(9.433 + 5.366) * 10^6}{200{,}000 * 11600 * 10^4} = 0.075$$

The parameter "m" should be calculated for both weak and strong axis from Eq.5.14:

$(m)_{weak}$ = 3.31

$(m)_{storng}$ = 10.6

The rotational stiffness of ABT "K_{ABT}" should be calculated for both weak and strong axis from Eq.5.13:

$(K_{ABT})_{weak}$ = 6.23 e8 N.mm

$(K_{ABT})_{storng}$ = 2.0 e9 N.mm

The parameter "β" – relative stiffness – should be calculated for both weak and strong axis from Eq.5.12:

$(\beta)_{weak} = 2.46$

$(\beta)_{storng} = 0.8$

The parameter "α" should be calculated by solving the characteristic equation (Eq.5.10) for both weak and strong axis for the finite minimum non-zero real roots:

$(\alpha)_{weak} = 7.75$

$(\alpha)_{storng} = 4.72$

Finally, the Euler load (elastic buckling load) "P_E" should be calculated for both weak and strong axis from Eq.5.9:

$(P_{cr})_{weak} = 440$ kN

$(P_{cr})_{storng} = 2636$ kN

As it is was mentioned before, this elastic buckling load is not an indicator of the system capacity in compression.

Calculation of the possible clearances and imperfections:

$L/500$ for the total out-of-straightness of the brace and erection error

Clearance between male and female telescopic tubes:

$$\delta_0 = \frac{4460}{1000} + 7.4 = 12\ mm$$

Strength curves associated with ABT (female) and the brace body can be derived from Eq.5.22 and Eq.5.4, respectively:

$$P_{ABT}(\delta) = \frac{(M_p)_f}{\delta}$$

$$P_{body}(\delta) = \frac{(M_p)_{body}\left(1 - \frac{P_{body}}{P_n}\right)}{\delta} \quad or \quad P_{body} = \frac{(M_p)_{body}}{\frac{(M_p)_{body}}{P_n} + \delta}$$

Note that the strength of the brace body is modified with the combined action formula given it is carrying axial load and bending moment at the same time. However, the ABT does not need modification as it is not carrying any axial load.

Plastic modulus of the female part of ABT

$= \text{number of ABT} \times \left(\frac{bh^2}{4} - (b-2t)(\frac{h}{2}-t)^2\right)$

$S_{ABT} = 5.62$ e4 mm^3

Plastic moment capacity of ABT and brace body

$(M_p)_{female} = S_{female} \times F_y = 19.12$ kN.m

$(M_p)_{body} = S_{body} \times F_y = 40.46$ kN.m

The nominal axial capacity of brace body = $P_n = A_g F_y = 1615$ kN

The intersection points can be approximated using the following equations (Eq.5.4 and Eq.5.23) and shown in Figure 7.5:

$$(\delta_{int})_{ABT} = 0.5(M_p)_{female}\left[\frac{1}{P_{cr}} + \sqrt{\left(\frac{1}{P_{cr}}\right)^2 + \frac{4\delta_0}{(M_p)_{female}.P_{cr}}}\right] = 53\ mm$$

$$(\delta_{int})_{body} = 0.5(M_p)_{body}\left[\frac{1}{P_{cr}} - \frac{1}{P_n} + \sqrt{\left(\frac{1}{P_{cr}} - \frac{1}{P_n}\right)^2 + \frac{4\delta_0}{(M_p)_{female}.P_{cr}}}\right] = 81\ mm$$

Finally, the ultimate load capacity of the brace can be derived from Eq.5.5 if the intersection point is assumed as the input (Figure 7.5).

$$P_{ult} = \min\left[P_{cr} * \frac{(\delta_{int})_{ABT}}{(\delta_{int})_{ABT} + \delta_0},\ \ P_{cr} * \frac{(\delta_{int})_{body}}{(\delta_{int})_{body} + \delta_0}\right] = \min\left[359,\ 382.8\ kN\right]$$

$$P_{ult} = 359\ kN$$

Given that $\delta_2 = 0.19$ and $\beta_b = 0.74$, the calibration coefficient is 0.85. The modified capacity of the brace can be derived from Eq.5.3 as:

$$P_{ult,mod} = \gamma_c P_{ult} = 0.85 * 359 = 305\ \text{kN}$$

As it can be observed from calculations and in Figure 7.5, the governing failure mode is the plastic hinge in the ABT, which was discussed to be not the desired mode of failure. The next step would be choosing stronger ABT or changing the section to SHS. The rest of the procedure is similar to the previous example. The drawings for this design was provided in Figure 5.8.a.

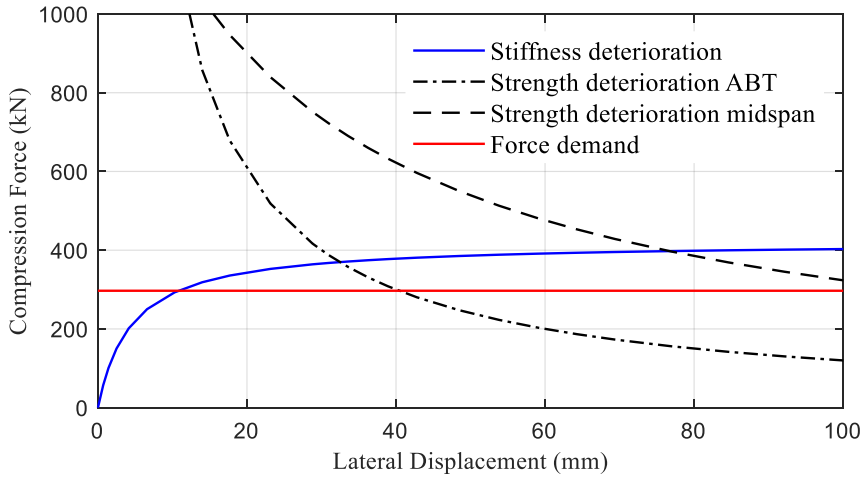

Figure 7.5: Spotting the ultimate capacity by intersecting the stiffness and strength deterioration curves – example 2.

7.5 Design example 3: Timber brace with one weakened location for damper

The objective in this section is to design a timber brace for 1100 kN capacity in which all of the steel parts are made up of mild steel with an elastic modulus of 200 Gpa and yield stress of 340 MPa while the timber parts are made up of Glulam GL12 with an elastic modulus of 9700 MPa while having the bending and compressive characteristic stress of 9.8 and 25.2 Mpa, respectively. The total length of the brace is 8500 mm while the damper length is 1224 mm and the distance between pin and damper is 200 mm. The following parameters have been assumed as the input: Overstrength factor (o/s) = 1.35, which is concerning the performance of RSFJ after lockage, referred to as secondary-fuse [158]. This makes the force demand factored up to P = 1.35 * 1100 = 1485 kN (Factored Force Demand). The brace section is of rectangular section with 430 and 450 mm dimensions resulting in the strong- and weak-axis moment of inertia of 3.27 e9 mm^4 and 2.98 e9 mm^4. The relative length of the ABT and RSFJ given that L_{RSFJ} = 1224 mm can be calculated from Eq.5.11 and Eq.5.15 as following:

$$\delta_1 = \frac{812}{8500} \sim 0.095$$

$$\delta_2 = \frac{1424}{8500} \sim 0.168$$

The anti-buckling tubes were assumed to be composed of three telescopic SHS (Square Hollow Section) with dimensions 105 mm and 89 mm for the female section and 87 mm and 71 mm for the male part, respectively. The moment of inertia for the female and male sections were 1.47 e7 and 7.58 e6 mm^4. For this design, three ABTs have been provided with two RSFJ on either side of it:

The parameter "β_b" – relative rigidity – should be calculated for both weak and strong axis (here same for CHS section) from Eq.5.16:

$$(\beta_b)_{weak} = \frac{200{,}000 * 3(9.433 + 5.366) * 10^6}{200{,}000 * 11600 * 10^4} = 0.16$$

$$(\beta_b)_{storng} = \frac{200{,}000 * 3(9.433 + 5.366) * 10^6}{200{,}000 * 11600 * 10^4} = 0.14$$

The parameter "m" should be calculated for both weak and strong axis from Eq.5.14:

$(m)_{weak}$ = 0.746

$(m)_{storng}$ = 0.779

The rotational stiffness of ABT "K_{ABT}" should be calculated for both weak and strong axis from Eq.5.13:

$(K_{ABT})_{weak}$ = 4.75 e9 N.mm

$(K_{ABT})_{storng}$ = 4.96 e9 N.mm

The parameter "β" – relative stiffness – should be calculated for both weak and strong axis from Eq.5.12:

$$(\beta)_{weak} = 1.396$$

$$(\beta)_{storng} = 1.331$$

The parameter "α" should be calculated by solving the characteristic equation (Eq.5.10) for both weak and strong axis for the finite minimum non-zero real roots:

$$(\alpha)_{weak} = 8.08$$

$$(\alpha)_{storng} = 7.97$$

Finally, the Euler load (elastic buckling load) "P_E" should be calculated for both weak and strong axis from Eq.5.9:

$$(P_{cr})_{weak} = 3233 \text{ kN}$$

$$(P_{cr})_{storng} = 3492 \text{ kN}$$

As it is was mentioned before, this elastic buckling load is not an indicator of the system capacity in compression.

Calculation of the possible clearances and imperfections:

$L/500$ for the total out-of-straightness of the brace and erection error

Clearance between male and female telescopic tubes:

$$\delta_0 = \frac{8500}{1000} + 4 = 12.5\ mm$$

Strength curves associated with ABT (female) and the brace body can be derived from the following equations. Note that the strength curve for ABT in this application is similar to steel brace while for the timber brace body is different. For timber brace application, the strength curve of the brace is based on the elastic capacity of the timber mainly because it does not have the capability to reach its fully plastic capacity due to tension failure of the fibres at the tension side. Accordingly, the strength curves are:

$$P_{ABT}(\delta) = \frac{(M_p)_f}{\delta}$$

$$P_{body} = \frac{(Sf_b)_{body}}{\frac{(Sf_b)_{body}}{A_g f_c} + \delta}$$

Plastic modulus of female part of ABT = number of ABT $\times \left(\frac{bh^2}{4} - (b-2t)(\frac{h}{2}-t)^2\right)$

S_{ABT} = 1.13 e5 mm^3

Plastic moment capacity of ABT (three ABT combined) and Elastic moment capacity of the brace body is:

$(M_p)_{female} = S_{female} \times F_y =$ 92.34 kN.m

$(M_p)_{body} = Z_{body} \times F_b = 136$ kN.m (assuming same capacity for weak and strong given that section is almost square)

The nominal elastic axial capacity of brace body = $P_n = A_g F_c =$ 4876 kN

The intersection points can be approximated using the following equations and shown in Figure 7.5:

$$(\delta_{int})_{ABT} = 0.5(M_p)_{female}\left[\frac{1}{P_{cr}} + \sqrt{\left(\frac{1}{P_{cr}}\right)^2 + \frac{4\delta_0}{(M_p)_{female}.P_{cr}}}\right] = 42\ mm$$

$$(\delta_{int})_{body} = 0.5Sf_b\left[\frac{1}{P_{cr}} - \frac{1}{A_g f_c} + \sqrt{\left(\frac{1}{P_{cr}} - \frac{1}{A_g f_c}\right)^2 + \frac{4\delta_0}{Sf_b P_{cr}}}\right] = 36\ mm$$

Finally, the ultimate load capacity of the brace can be derived from Eq.5.5 if the intersection point is assumed as the input (Figure 7.6).

$$P_{ult} = \min\left[P_{cr} * \frac{(\delta_{int})_{ABT}}{(\delta_{int})_{ABT} + \delta_0},\ \ P_{cr} * \frac{(\delta_{int})_{body}}{(\delta_{int})_{body} + \delta_0}\right] = \min\left[2219\ kN\ ,\ 2120\ kN\right]$$

$$P_{ult} = 2219\ kN$$

Given that $\delta_2 = 0.168$ and $\beta_b = 0.14$, the calibration coefficient is 0.85 (Eq.6.2). The modified capacity of the brace can be derived from Eq.6.1 as:

$$P_{ult,mod} = \gamma_c P_{ult} = 0.85 * 2219 = 1886 \text{ kN}$$

The demand to capacity ratio is 0.7 in this example. As it can be observed from calculations and in Figure 7.5, the governing failure mode is the plastic hinge in the ABT, which was discussed to

be not the desired mode of failure. This might be a dubious case as the failure load for both failure modes are very close. The next step would be choosing stronger ABT or changing the brace body section to be smaller. In this manner, both demands to capacity ratio might get more economical while the governing failure mode might change to brace body, which had been discussed to be the desired mode of failure at Maximum Considerable Earthquake. The rest of the procedure is similar to the previous example in terms of the capacity design of connections and adjacent members. The drawings for this design is provided in Figure 7.6.

(a)

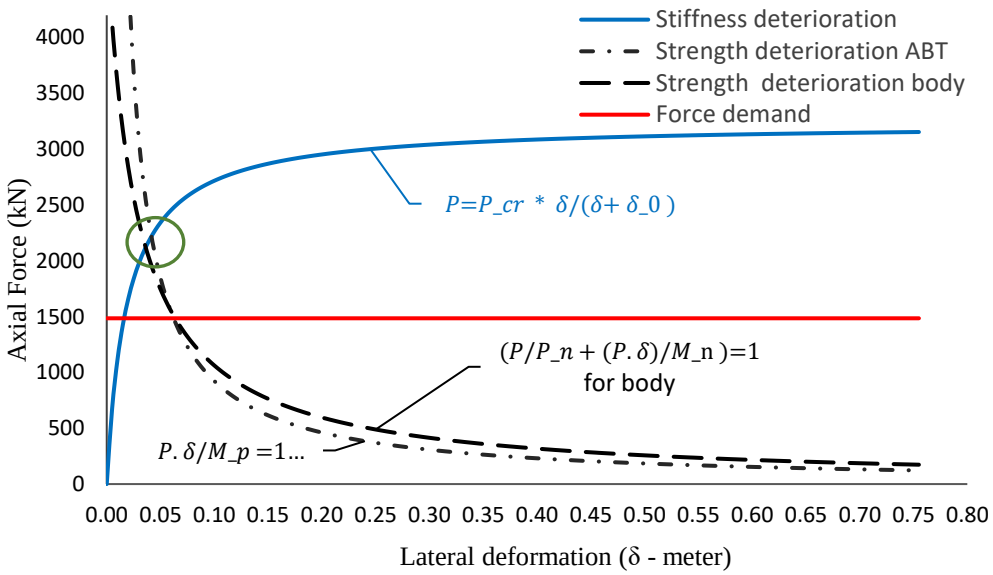

(b)

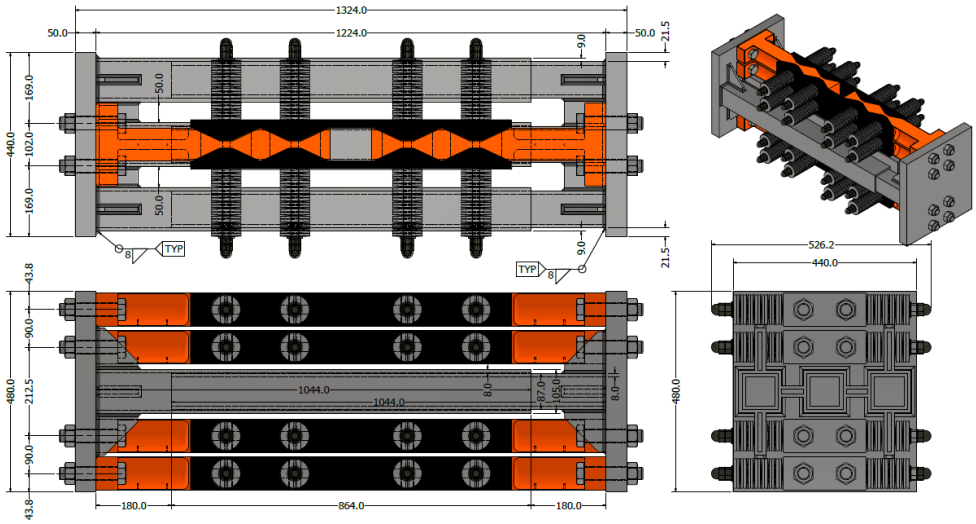

Figure 7.6: (a) Spotting the ultimate capacity by intersecting the stiffness and strength deterioration curves – example 3, (b) drawings and dimensions of Anti-buckling tubes with their end plates.

7.6 Conclusion

Explaining the detailed procedure of RSFJ brace design for compression in the previous chapters, there was a need for proper and holistic examples to further illustrate the method to quantify the capacity of the brace in compression. This chapter presented three design examples in which both configurations of RSFJ brace – Steel and Timber – were considered. Moreover, in the examples, the seismic design considerations, capacity design, endplate design and other design challenges were also illustrated.

One important point to be highlighted here is associated with the weight comparison of the brace in examples one and three. As can be found, their force demands and length were almost in the same range (example 1: 1300 kN with 8460 mm length and example 2: 1100 kN with 8500 mm length). The cross-section used for their brace bodies were CHS 323.9 x 9.5 and rectangular section 430 x 450 mm, respectively. Given the density of both materials, which for timber is around 450-550 kg/m^3 and for steel is around 7850 kg/m^3, it can be observed that the weight of both braces is in the same range.

8 Manuscript.5 - Seismic Performance Improvement of Conventional Timber Brace Using Re-Centring Friction Connection

Based on the article published on 2020/8/1 by peer-reviewed "Journal of Structures", Volume 26, page 958-968

8.1 Abstract:

The Conventional Timber Brace (CTB) is a simple and economical lateral load resisting system capable of providing a suitable elastic (initial) stiffness, thanks to the stiff behaviour of the timber in parallel to the grain direction. However, their inelastic behaviour, appearing in case of major seismic events, is a matter of concern mainly because of the degradation of both ultimate strength and elastic stiffness. This issue is normally cited as the pinching effect in the literature and originates from the arrival of timber crushing in the end connections. The main focus of this paper is accordingly placed on introducing a new timber brace with alleviated end connection performance. More specifically, the aim is achieved by replacing the conventional connection with a new damage-free self-centring connection, named Resilient Slip Friction Joint (RSFJ) to form a new self-centring timber brace (SC-TB). To evaluate the efficiency of the proposed system, an experimental testing program was considered where a number of scaled specimens were experimentally tested. At the final stage of this study, a comparative study is presented in which the seismic performance of a 4-storey archetype building using SC-TB is compared with that of a building with CTB. According to the results, the performance of the building with the proposed SC-TB outperformed the CTB one in terms of the base shear, not having a pinched response and possessing a reusable damping resource.

8.2 Introduction and background:

Conventional Timber Brace (CTB)[199] is common, economical and easy to construct Lateral Load Resisting System (LLRS), which can deliver suitable elastic (initial) stiffness in case of low and moderate seismic events, relying on the stiff behaviour of the timber when being loaded parallel to the grain. However, the application of timber braces or timber structures in regions with high seismic activity is of concern as the ductility and energy dissipation capacity for these buildings should be provided only by steel connections and not the timber due to its brittle

behaviour [199, 200]. Taking that responsibility by the steel connectors results in irreversible timber crushing where the steel connectors are embedded in the timber and arrive as the pinching and slackness in the system cyclic response. Consequently, most of the current building codes such as ASCE 7 [201] normally assumes relatively lower force reduction factors for timber structures as compared to either steel or concrete structures, and normally do not permit their construction in regions with high-seismic activity. An indication of such concern regarding the seismic performance of the timber structures can also be found in the post-earthquake construction in Christchurch, New Zealand where nearly just 5% of the newly built buildings possess timber LLRS after the Christchurch earthquake in 2011[8], which is concerning for timber industry.

In general, based on the type of end connection used for a CTB (riveted [200, 202], bolted [200, 203]or nailed [204], the behaviour and ductility of the system may change. Popovski et al. [200, 202] studied and tested CTB with timber riveted and bolted connections. A total of 48 brace specimens composed of 4 various timber types namely Laminated Strand Lumber (LSL), Laminated Veneer Lumber (LVL), Spruce-Pine (SP) and Parallel Strand Lumber (PSL) were included in their research. They also observed that the short length rivets and short diameter bolts exhibited the best performance in terms of ductility capacity and energy dissipation. Xiong and Liu [203] studied Glulam timber braces in different configurations. They studied the X-type, K-type and Knee-type bracing and concluded that the timber bracing system provided a good elastic stiffness, yet brittle failure mode in timber was also observed, which might be due to not designing the connections for ductile failure.

According to the above-mentioned studies, the following concerns can be raised for CTBs:

i. The first is that the cyclic behaviour of the timber braces (hysteric curve) is severely pinched. As it was indicated earlier, the pinching effect is a common phenomenon in timber connections and lies in irreversible timber crushing. The pinched hysteresis curve can adversely affect the acceleration and displacement response of the structure up to varying degrees depending on the fundamental period of the structure [205-207].

ii. The second is that the hysteric response of the CTB experienced both strength and stiffness degradation. The low stiffness and strength will be problematic when the serviceability limit states, aftershocks vulnerability, wind loading, and other post-event hazards are taken into consideration [208, 209].

iii. The last concern is related to the possible premature brittle failure of the timber brace body before connection, which was observed in [203] and it is not desirable. In this regard, a proper framework is needed for predicting the failure modes (ductile, mixed or brittle) and the ultimate load capacity of the timber brace application. Such a framework is provided and discussed in section.4.

To compensate for those afore-mentioned concerns for a CTB, some new bracing systems and connections have been suggested and studied to be used in timber structures. Chan et al [210] proposed and studied a new tension-only pinching-free connection that is able to achieve a complete load-plateau behaviour in the first and third quadrants of the hysteresis curve while eliminating the pinching. Gilbert and Erochko [211] proposed a new hybrid steel-timber braced frame for heavy timber frame applications with Glued-in end connections and employed a steel brace with friction connection as LLRS. They also validated the system for cyclic and wind loading protocols. Blomgren et al [212] proposed a new Buckling-Restrained Brace (BRB) with timber sleeves for the application of timber structures. In the present study, the conventional connection of the CTB (might be bolted, riveted, nailed or glued-in) is replaced with the Resilient Slip Friction Joints "RSFJs" [137] to form a new self-centring timber brace to be used for a low damage LLRS [213, 214]. This connection is an elevated version of the previous friction spring dampers [135, 136] while possessing more flexibility in terms of capacity and geometry. Generally, there are three main objectives to be met when a structure is designed in accordance with the low-damage concept [215]. The first one is that the system should not allow any damage to the gravity system. The second one is that there should be some re-centring capability so that the structure would be realigned and ready to be re-occupied after experiencing a major earthquake. Such re-centring capability can be provided by a secondary elastic structure [216] or by a self-centring mechanism [18]. Last but not the least objective is to possess a repeatable, reliable and reusable damping mechanism. Although engineers may argue that many conventional lateral load resisting systems may fall into this category such as elastic systems, Eccentrically-Braced Frame (EBF) with replaceable links [10, 11], Buckling Restrained Brace (BRB) [12], base isolation technologies, frictional and viscous dampers [153, 172, 217, 218] and so on, most of the international efforts today have been placed on developing new lateral load resisting systems. Among many low-damage technologies, it can be referred to a number of systems popular in New Zealand namely: Sliding Hinge Joints [13], Grip 'n' Grab [14], Pres-Lam system [15], Resilient Slip Friction Joint (RSFJ) [137], Pinching-Free Connection - PFC[16] and Self-centring Structural Connector – SSC and branded as RSFD [219, 220]

In this regard, the proposed self-centring timber brace (SC-TB) system is expected to meet all of the above-mentioned criteria for a low-damage system while importantly, it does not have concerns regarding the CTB – pinching, strength and stiffness deterioration. In this regard, the first part of this paper deals with experimental and numerical validation of the SC-TB whilst the second part describes a comparative study on an archetype four-storey framed building equipped with different lateral load resisting systems including the SC-TB, BRB and CTB with the intention of depicting the seismic performance of the new proposed brace. Regarding the recent development of RSFJ connection and its applications, it can be referred to [139] in which this connection was used as the hold-downs for CLT shear walls. Bagheri et al. [157, 160, 192] developed a new tension-only brace system using this damper. Yousef-beik et al [99, 156] developed a general stability model in order for stability investigation of the self-centring dampers and compressive members, and moreover, studied the feasibility of using this damper in the tension-compression brace. The application in the braces was further extended to a new re-centring brace that had a zero post-slip stiffness [54]. Darani et al. [159] utilized this damper as the hold-downs for concrete shear walls coupled with unboned steel rebar to control the tension cracking of the wall during the rocking.

8.3 Resilient Slip Friction Joint (RSFJ) Performance

In this paper, the conventional timber connection is replaced with RSFJ connection to improve the seismic performance of the brace. Figure 8.1 shows a typical RSFJ connection with its main components: high strength bolts and pre-stressed disc springs clamping the cap and middle plates. The axial performance of RSFJ is of flag-shape type and depicted in Figure 8.2 [99]. The basis of the RSFJ performance is rooted in the frictional sliding between two middle and cap plates that are clamped together using bolts and pre-compressed disc springs. When an axial load is applied to the joint, it will not slip until a certain limit which is referred to as slip. The slippage phase can continue until the disc springs get flat due to the vertical movement of the cap plate. When the axial load is removed in the unloading phase, it will not slip until certain a limit, which is referred to as reversed-slip. Then, the friction force will act in the opposite direction in the unloading phase resulting in providing the passive damping resource. For further information on the performance characteristics of RSFJ, it can be referred to [99, 165].

For an arbitrary axial displacement "$\Delta \leq \Delta_{max}$", the associated axial loads in loading and unloading phases are formulated in Eq.8.1 and Eq.8.2, respectively:

$$F_{loading} = 2n_b\left(F_{pr} + \frac{k_{st}\Delta \tan\theta_g}{2}\right)\left(\frac{sin\theta_g + \mu cos\theta_g}{cos\,\theta_g - \mu sin\theta_g}\right) \quad 8.1$$

$$F_{unloading} = 2n_b\left(F_{pr} + \frac{k_{st}\Delta \tan\theta_g}{2}\right)\left(\frac{sin\theta_g - \mu cos\theta_g}{cos\,\theta_g + \mu sin\theta_g}\right) \quad 8.2$$

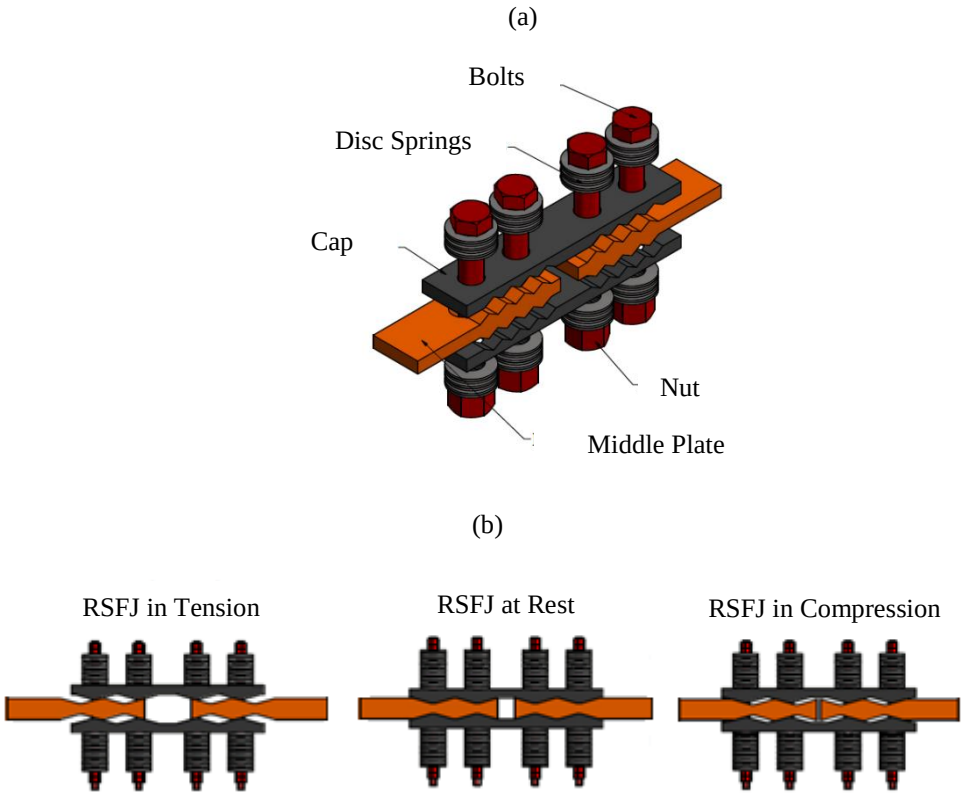

Figure 8.1: (a) RSF joint assembly, components and (b) displaced shape in the different stages

where the minimum of them ($\Delta = 0$) yields the slip (F_{slip}) and residual force (F_{res}); respectively, while their maximum ($\Delta = \Delta_{max}$) gives the maximum load in loading ($F_{max,loading}$) and unloading ($F_{max,unloading}$) phase. In the mentioned equations, "θ_g" indicates the grooves angle; "μ" denotes the friction coefficient, "k_{st}" represents the stack of disc springs stiffness. Parameter "n_b" stands for the number of bolts on each middle plate (Figure 8.1, $n_b = 2$), and "F_{pr}" shows the prestressing force in the disk springs. The maximum axial displacement (Δ_{max}) that a RSFJ can experience during the slip can be calculated from the remaining deflection of the pre-stressed disk springs to get fully flattened and is formulated as:

$$\Delta_{max} = n_j n_d \frac{\Delta_{s,max}}{tan(\theta_g)}(1-\gamma) \quad 8.3$$

where "n_j" is the number of joints in series arrangement (for instance, in the joint illustrated in Figure 8.1, "n_j" equals to 2 as a double-acting). Parameter "n_d" is the number of disk springs per side of a bolt and "$\Delta_{s,max}$" is the listed deflection of a disk spring. The parameter "$\gamma = F_{pr}/F_{u,s}$" is indicative of prestressing percentage and "$F_{u,s}$" is the flat load of a disc spring.

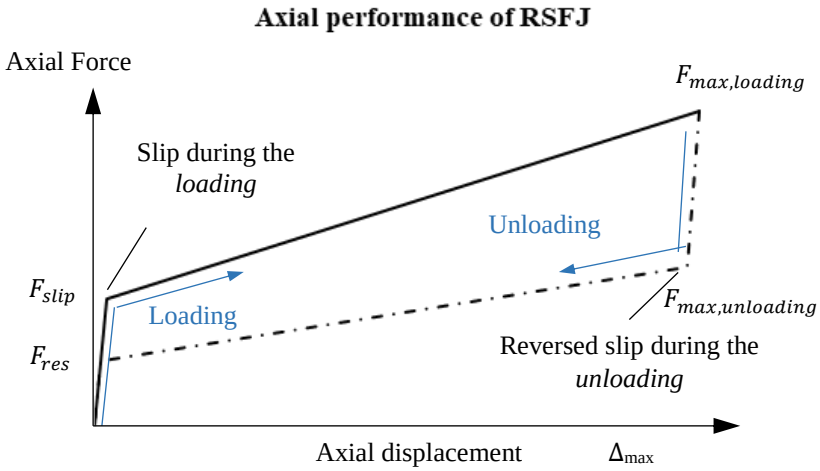

Figure 8.2: Passive self-centring hysteretic axial response of RSF joint (flag-shaped hysteresis)

8.3.1. *Experimental test on disc springs*

In order that the re-centring connection response is accurately predicted, the approximate initial stiffness of the disc springs and their ultimate (flat) load is required. Accordingly, a number of incremental cyclic tests were performed on the stack of disc springs up to the flat position to quantify the characteristics of the springs. As it can be seen in Figure 8.3, a nonlinear behaviour was observed when the disc springs were subjected to the cyclic loading especially when they were close to getting flat. However, with good accuracy, their initial linear stiffness was used in the analytical models. According to the experimental results, the initial stiffness associated with the stacks with 5, 6, 8 and 11-disc springs were approximated to be 7.686 kN/mm, 6.405 kN/mm, 4.292 kN/mm and 4.73 kN/mm, respectively and the flat load ($F_{u,s}$) was observed to be 38.8 kN.

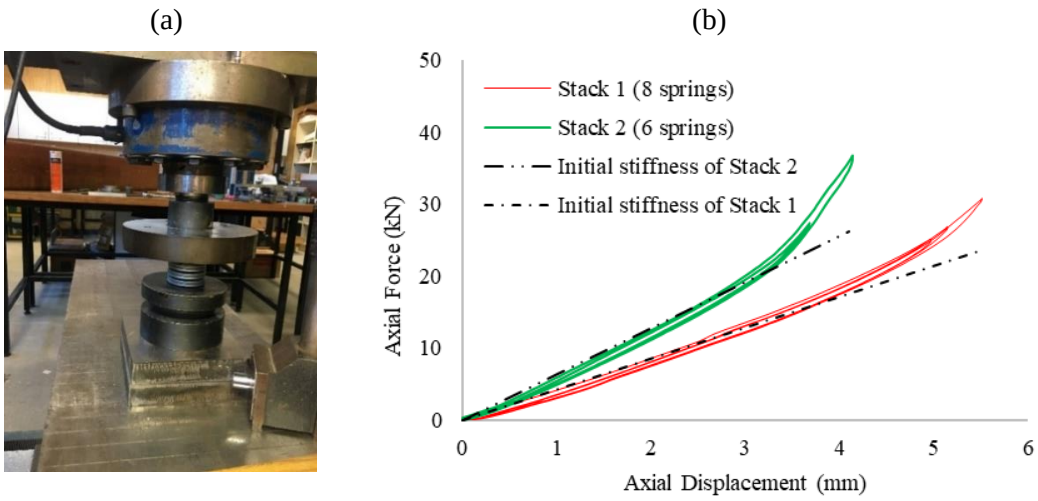

Figure 8.3: Experimental Test on the stacks of disc springs (6 springs in the figure): a: Experimental test setup, b: Experimental Results for Stacks with 6- and 8-disc springs

8.3.2. *Reversed Cyclic Test on scaled SC-TB Behaviour with Tests:*

A one third scaled timber brace was designed and constructed with a 1699 mm length and was composed of a timber body, a RSFJ and steel end connections for attaching the RSFJ to timber. The timber part was composed of an LVL grade 11 with an elastic modulus of E = 11 GPa and a density of $\rho = 620$ Kg/m^3. Besides, it had a cross-section of square shape with 150 mm width. The timber body part had a nominal tension and compression capacity of 740 kN and 910 kN, respectively in parallel to the grain direction. There were two gusset plates at both ends of the brace with a thickness of 20 mm with a hole in them to provide the real pin ended situation for the brace (shown in Figure 8.4) and were welded to two bearing plates at both ends of the timber body. These plates were then screwed to the timber with 180 mm long screws of 7 mm diameter. Furthermore, this connection was capacity designed with a factor of 2 with respect to the capacity of the RSFJ. The RSFJ, itself, had 340 mm in length and 50 mm in width. The angle of the grooves was designed to be 30 degrees. More details can be found in Figure 8.4.d in terms of the RSFJ geometry. The cyclic test was performed using an actuator of 300 kN force capacity. Further information on the dimensions of the test set-up can be found in Figure 8.4. Regarding the data acquisition system, axial and lateral deformations of the specimens were recorded using two displacement gauges and two LVDTs (Linear variable differential transformer).

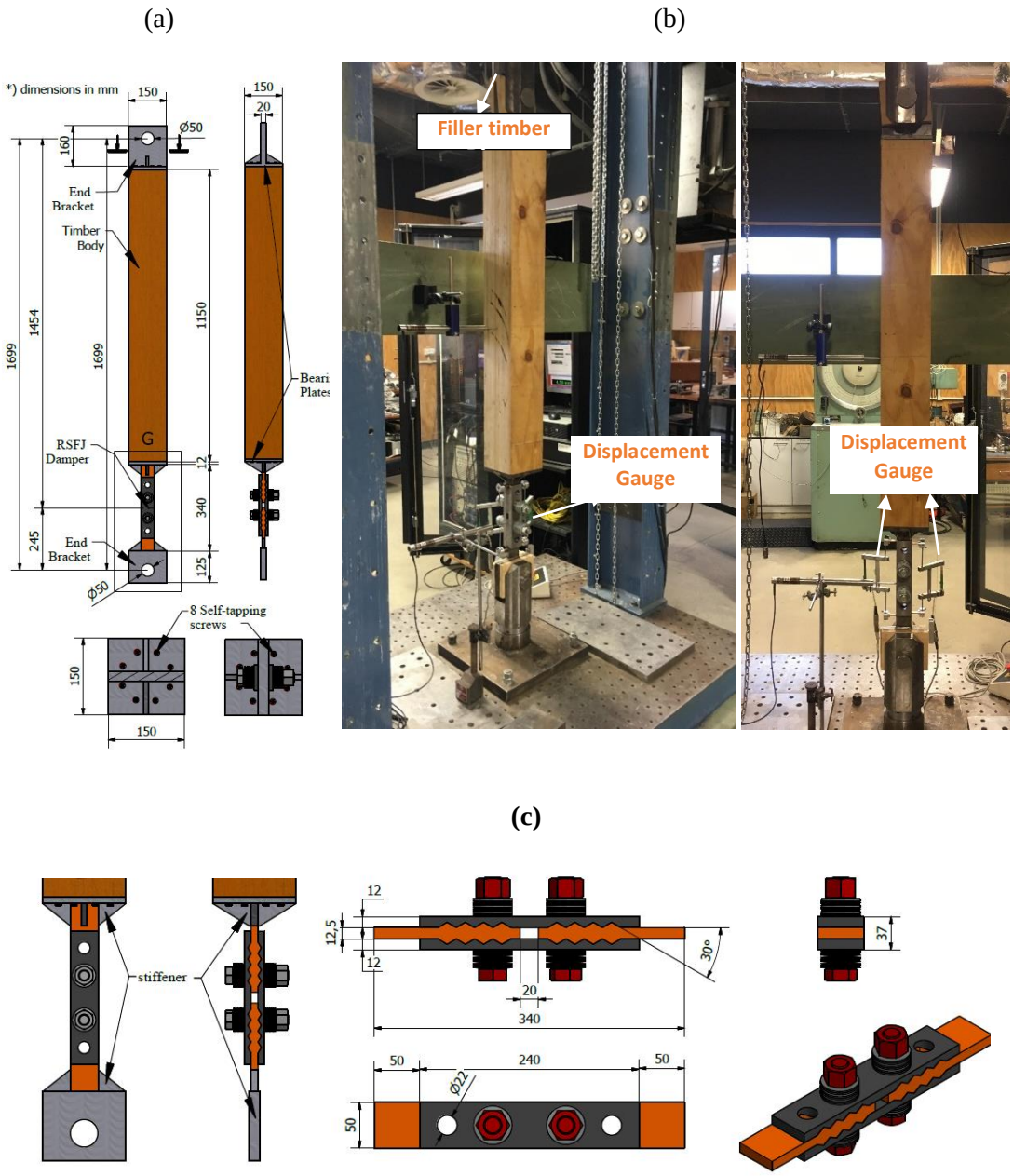

Figure 8.4: (a) Side views of the test specimen for the in-plane testing (dimensions in mm), (b) Experimental test setup and data acquisition apparatus and (c) utilized RSFJ (dimensions in mm)

Different specimens equipped with 4 different stacks of disc springs and pre-stressing force were used for the testing program. Employed specimens and their related flag-shape characteristics are tabulated in Table 8.1: Testing specimens. The maximum load the RSFJ connection was able to resist was calculated to be 64.3 kN based on the experimental tests on the disc spring.

Table 8.1: Testing specimens

Specimen	n_b	n_d	θ_g (degree)	K_{st} (kN/mm)	γ (%)	F_{slip} (kN)	$F_{residual}$ (kN)	$F_{loading}$ (kN)	$F_{unloading}$ (kN)	$F_{max,loading}$ (kN)
1	1	5	30	7.7	18	11.3	4.1	38.9	17.4	64.3
2	1	6	30	6.4	13	7.9	3.8	30.9	15	
3	1	8	30	4.3	13	7.9	3.8	23.7	11.5	
4	1	11	30	4.7	40	24.3	11.8	40.7	19.8	

The reversed cyclic loading protocol is shown in Figure 8.6 - according to AISC 341 [196] suggestion for BRB braces – and was used for this testing program. The accumulative displacement of this loading protocol exceeded 200 times of slip displacement, which is analogous to what AISC 341 [196] necessitates for BRB. The reason for this lies in the fact that a SC-TB can be used in a structure as the main LLRS, and it should be able to dissipate the energy similar to what BRB is expected to do in a braced frame.

The experimental results of the tested SC-TB are illustrated in Figure 8.6. As it can be observed, the analytical envelope curves (red dotted lines) calculated from analytical formulas (equations 8.1 – 8.3) were in good agreement with the experimental results of the reversed cyclic test. Besides, one of the test results (specimen 3) was also compared with numerical simulation done in ABAQUS [221] software (will be explained in the following section). According to Figure 8.6.a, a limited nonlinearity was observed at the end of the loading phase which is indicative of the fact that disc springs were about to get flattened. It is worth noting that in order to avoid any lateral movement of the brace, two extra bolts were put inside the empty bolt holes (shown in Figure 8.6.e) of the RSFJ so that the relative rotation of the middle and cap plates are restricted [156, 222]. This solution was an initial attempt to rule out the possibility of the elastic buckling and as it can be seen, it was effective because no performance interruption has appeared in the compression zone [156, 222]. More information about the elastic buckling of the RSFJ brace can be found in [165].

8.1 Finite element study on brace performance

As discussed previously, the brace sample was made up of two main sections. One timber body and one RSFJ. The timber body was made up of an LVL grade 11 with an elastic modulus of E = 11 GPa and a density of $\rho = 620$ Kg/m^3. The cap plates and middle plates of the RSFJ were made up of high strength steel with a yield stress of 690 MPa and an elastic modulus of 200 GPa. A numerical model representative of the SC-TB was constructed using the ABAQUS software package and compared with experimental and analytical results in order for demonstration of the brace behaviour.

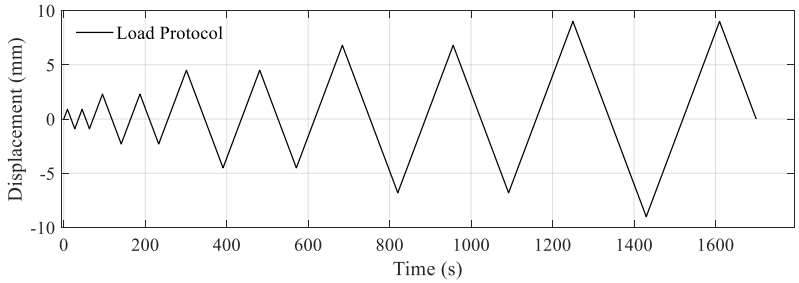

Figure 8.5: The loading protocol

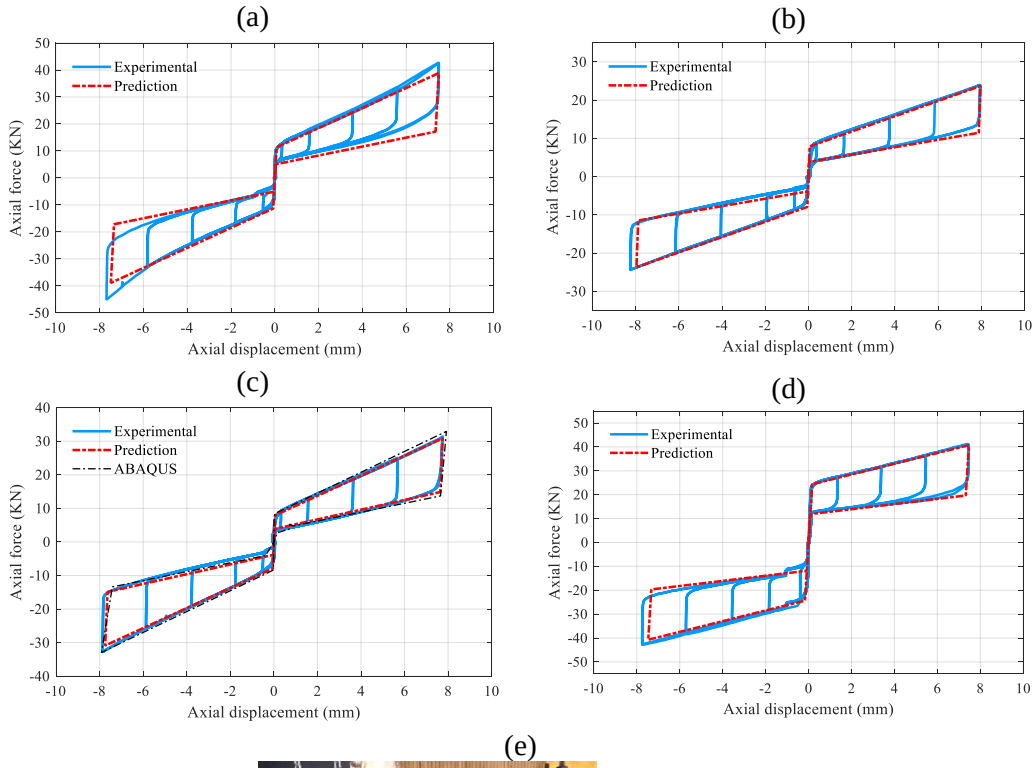

Figure 8.6: (a) flag-shape response of specimen 1, (b) flag-shape response of specimen 2, (c) flag-shape response of specimen verified with ABAQUS, (d) flag-shape response of specimen 4 and (e) Proposed Anti-buckling Tubes.

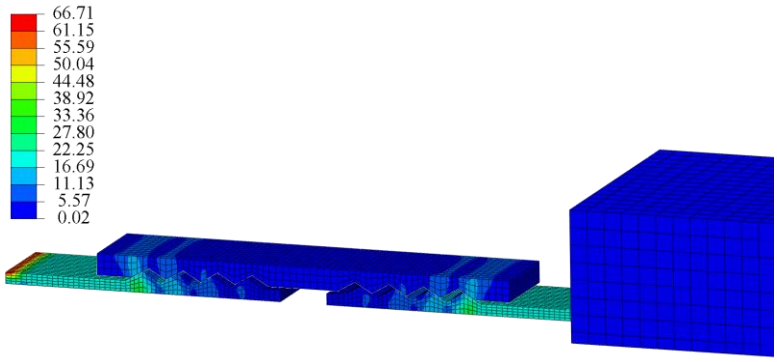

Figure 8.7: Von Mises Stress (MPa) at the ultimate condition

The numerical model is illustrated in Figure 8.7 while the characteristics of specimen 3 (refer to Table 8.1) was assumed. The load-deformation diagram resulting from ABAQUS is depicted in Figure 8.6 with a black dashed line and compared with analytical and experimental results. As can be seen, there is a good agreement between the analytical, numerical and experimental results. To check whether the materials were elastic, the Von Mises stress is plotted in Figure 8.7 based on which it can be observed that the maximum stress in RSFJ connection was less than the steel yield point (High strength steel $F_y = 690$ MPa), and in the timber part was less than both compressive and the tensile strength of Timber (LVL 11, $f_c = 45$ MPa and $f_t = 33$ MPa).

8.2 Prototype Building with BRB, SC-TB and CTB

A four-storey frame (shown in Figure 8.9.a) [223], was used as a reference benchmark model to demonstrate the performance of the SC-TB brace system in comparison with two other buildings using BRB and CTB. For further information regarding the member sizes and BRB sections, readers are referred to [223].

Regarding the building with CTB, all of the braces were composed of LVL grade 11 with elastic moduli of 11 GPa and density of 620 Kg/m^3 and were equipped with riveted end connections (rivet length = 65 mm) and designed to have a ductile failure mode according to the stiffness-based model developed by Zarnani et al [224-227]. The key point to achieving a connection with a ductile failure mode is that the ultimate capacity of the rivets should be less than the elastic capacity of wood (block tear-out). According to this model, there are three types of failure modes for a riveted connection namely (Figure 8.8): (1) brittle mode which is due to the timber failure prior to rivets yielding (block tear out), 2) ductile mode which is due to reaching the ultimate capacity of rivets prior to the elastic capacity of wood and 3) mixed mode which the combination of rivets yielding and wood failure. The governing failure mode is determined by comparing the capacity of wood

and rivets in a connection and can be found in the new version of New Zealand Code for Timber building (NZS 3603), which uses this stiffness model developed by the authors [224-227]. Given that all rivet connections for CTB were designed to fail in a ductile manner (ultimate capacity of rivets is less than the elastic capacity of wood), the following capacity curve can be presumed for a connection with a ductility ($\mu = \Delta_u/\Delta_y$) of 16 [228]:

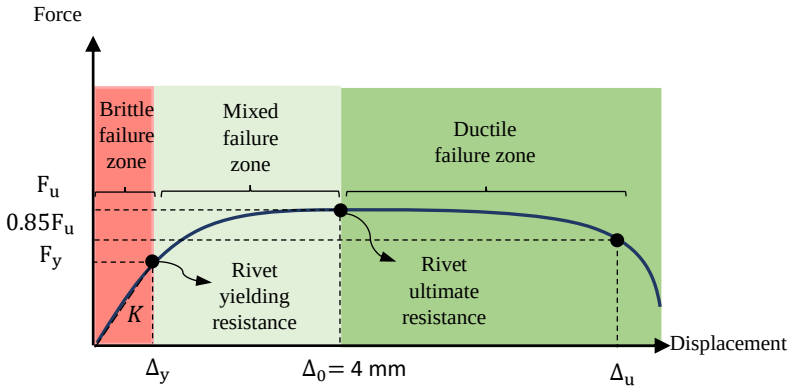

Figure 8.8: Capacity curve for a rivet connection [224, 225, 227, 229].

Based on the ductile failure mode design philosophy, the ultimate and yielding resistance of a riveted connection and the yielding and ultimate deformation of the connection for CTBs can be calculated using Eq.8.4 - Eq.8.7:

$$F_y = n_p n_R n_C P_{ry} \quad 8.4$$

$$F_u = n_p n_R n_C P_{ru} \quad 8.5$$

$$\Delta_y = 4\text{mm} * \left(1 - \sqrt{1 - \frac{F_y}{F_u}}\right) \quad 8.6$$

$$\Delta_u = \mu \Delta_y \quad 8.7$$

where "n_R" is the number of rows, "n_c" is the number of columns, "n_c" is the number of side-plate, "a_1" and "a_2" are the spacing along and across the grain and "t_p" is the side plate thickness. These parameters and the capacity of each connection are reported in Table 8.2 and illustrated in Figure 8.9.b. Parameters "P_{ry}" and "P_{ru}" are the yield and ultimate resistance of a single rivet embedded in a connection and are the minimum of two failure modes, both of which are functions of withdrawal and bending resistance of a rivet. According to [224, 225], they can be calculated with respect to Eq.8.8 and Eq.8.9 for 65 mm long rivets:

$$P_{ry} = min\begin{cases} 0.93\left[0.8f_{hy,0}L_p d_l\left(\sqrt{2+\frac{4M_{ry,l}}{f_{hy,0}d_l L_P^2}}-1\right)+\frac{L_p f_{ax}}{5.33}\right]10^{-3} \\ 0.93\left[2J_p\left(\sqrt{M_{ry,l}f_{hy,0}d_l}\right)+\frac{L_p f_{ax}}{5.33}\right]10^{-3} \end{cases} \quad 8.8$$

$$P_{ru} = min\begin{cases} 0.93\left[0.8f_{hu,0}L_p d_l\left(\sqrt{2+\frac{4M_{ru,l}}{f_{hu,0}d_l L_P^2}}-1\right)+\frac{L_p f_{ax}}{5.33}\right]10^{-3} \\ 0.93\left[2J_p\left(\sqrt{M_{ru,l}f_{hu,0}d_l}\right)+\frac{L_p f_{ax}}{5.33}\right]10^{-3} \end{cases} \quad 8.9$$

where "t_p" is the thickness of the side plate, "J_p" is the side plate factor and can be assumed one for plates with thickness more than 6mm, "d_l" is the rivet cross-section dimension bearing on the wood parallel to the grain, which is 3.2 mm, "$L_p = 65 - t_p - d_l$" is the penetration length of a 65 mm rivet. "$f_{hy,0}$" and "$f_{hu,0}$" are the yielding and ultimate embedment strength of a rivet parallel to grain (MPa) and can be estimated as 46 and 55.4 MPa, respectively. Parameters "$M_{ry,l}$" and "$M_{ru,l}$" are the yielding and ultimate moment capacity of a rivet parallel to grain and are 24.9 and 30 N.m, respectively. The parameter "$f_{a,x}$" is the withdrawal resistance per millimetre of penetration and can be estimated as 61.6 N/mm based on experimental results [224, 225, 227, 229]. Based on this assumption, the initial stiffness of the brace can be calculated from Eq.8.10 based on the premise that the brace body and end connections act in series.

$$K_b = \frac{K_r \times K_b}{2K_b + K_r} \quad 8.10$$

where "K_r" is the initial stiffness of the rivet connection and was assumed to be the ratio of yield strength to yield displacement (Eq.8.4 and Eq.8.6), and "K_b" is the elastic axial stiffness of the brace body.

In order to draw a fair comparison, the SC-TB and CTB braces for each story were designed in a way to encourage all of the three buildings to have a similar fundamental period and activation strength. Doing so will guaranty that all of the three buildings have similar possible maximum inelastic base shear while having the same structural sections with respect to the capacity design concept. The details for RSFJ connection for each story are provided in Table 8.3 and the concise information on SC-TB, CTB and BRB for each story is reported in Table 8.4.

Table 8.2: Design of end rivet connections for CTB

Story	a_1 (mm)	a_2 (mm)	Thickness h (mm)	Depth b (mm)	End distance (mm)	t_P (mm)	n_R	n_c	n_p	P_{ry} (kN)	P_{ru} (kN)	Δ_y (mm)	Δ_u (mm)
1	25	15	500	500	200	10	19	4	4	3.7	4.7	2.16	34.6
2			450	450	200		16	4					
3			400	400	200		15	3					
4			350	350	150		12	3					

Table 8.3: Design of RSFJ connection for SC-CTB

Story	Prestressing force in disc springs F_{pr} (kN)	Number of bolts n_b	Number of springs n_d	Angle of groove θ_g	Stiffness of a disc spring (kN/mm)
1	60.5	11	21	16	71
2	65	9	23		
3	65	7	23		
4	65	5	23		

Table 8.4: Summary of design for BRB, SC-TB and CTB

Story	BRB				SC-TB			CTB			
	Elastic Stiffness	F_y	F_u	Δ_u	F_{slip}	F_{unload}	F_{res}	Initial Stiffness	F_y	F_u	Δ_u
1	133.8	848	1165.5	101	639	269	148	137.5	902	1143	72.1
2	112.7	714	981.7	101	561	220.4	130	112.3	760	963	72.2
3	84.5	535	736	101	436	171.4	101	84.9	534	677	71.8
4	63.2	401.7	552	101	311	122.5	72	66.6	427	542	72

*) Units are in kN and mm.

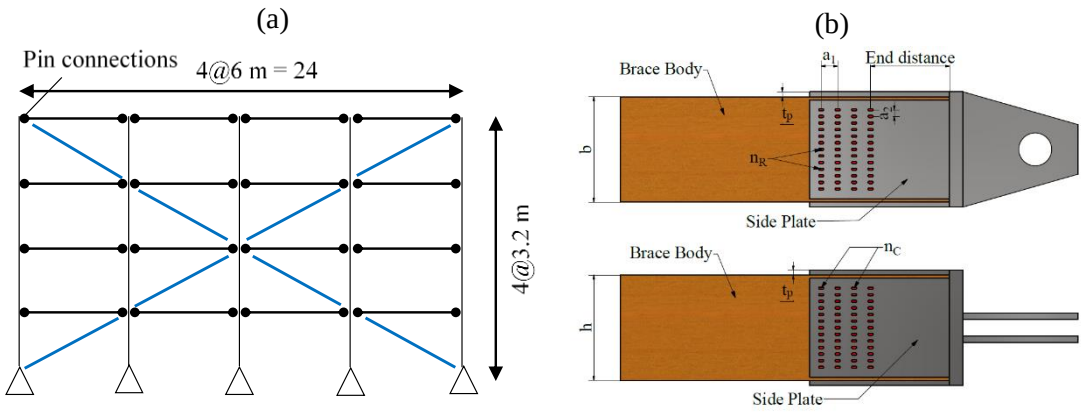

Figure 8.9: (a) The Prototype four-story Structure, (b) Timber brace with rivet connection

8.2.1. *Nonlinear Dynamic Time History Analysis of the prototype buildings*

Nonlinear Time History (NTH) simulation was implemented using SAP2000 software in which plastic (Wen) hysteresis model was used to model the BRB brace behaviour, pivot hysteresis model was used to simulate the performance of CTB and the friction-spring link was used to model the SC-TB. So that the accuracy of modelling is guaranteed, a component BRB brace was modelled in SAP2000 software and calibrated with the test [230]. The same procedure was followed using experimental results of a CTB with the rivet connection provided by Popovski [228]. Figure 8.10 shows the test data and simulated component in SAP2000 where can be seen a good agreement between the calibrated numerical and experimental results.

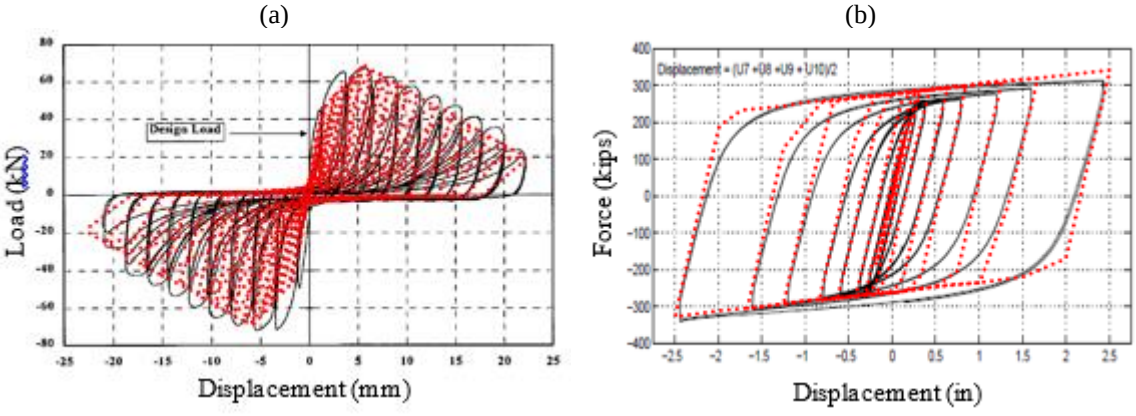

Figure 8.10: (a, b) Calibrated CTB and BRB in SAP2000 with experimental results [228, 230]

An ensemble of ten earthquake records (Table 8.5), scaled to Ultimate Limit State (ULS) and MCE design spectra (10% and 2% probability of exceedance in 50 years, respectively) according

to New Zealand code (NZS 1170.5) were selected for nonlinear time history analysis. The reason why ten records were used was that according to Shome and Cornell, 1999 [231], it has been observed that a selection of 10 to 20 records is generally sufficient for mid-rise buildings to provide reasonable accuracy of seismic demand. The ULS and MCE spectra are shown in Figure 8.11[54].

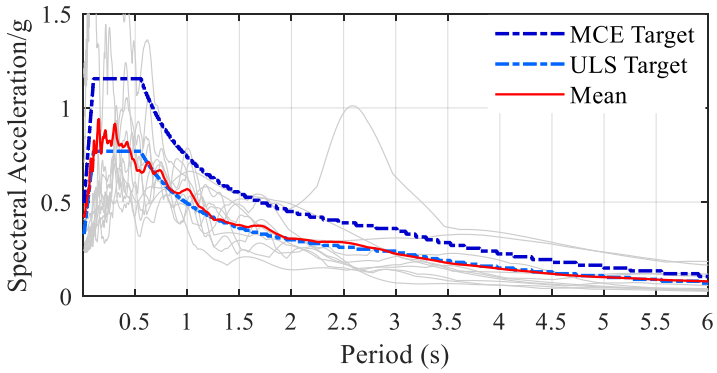

Figure 8.11: Utilized ground motions

Table 8.5: Earthquake records for NTH

No.	Name	Location	Date	M_w	Year	Scale Factor	Target Spectrum
1	Chi Chi	Taiwan	20/09/1999	7.62	1999	0.6	ULS
2	Christchurch	New Zealand	21/02/2011	6.3	2011	1.65	ULS
3	Duzce	Turkey	12/11/1999	7.2	1999	0.67	ULS
4	Hokkaido	Japan	26/09/2003	8.3	2003	0.89	ULS
5	Kaikoura	New Zealand	13/11/2016	7.8	2016	1	MCE
6	Kobe	Japan	16/01/1995	6.9	1995	0.85	ULS
7	Landers	USA	28/06/1992	7.28	1992	0.98	ULS
8	LomaPrieta	USA	18/10/1989	6.93	1989	0.93	ULS
9	Northridge	USA	17/01/1994	6.69	1994	0.61	ULS
10	Kocaeli	Turkey	17/08/1999	7.5	1999	0.78	ULS

Apart from modelling the component BRB and CTB accurately, the precise modelling of the building was another parameter that was taken into consideration. In this respect, the first three periods of the three modelled structures in SAP2000 were compared to those of the original work [223] and the differences were less than 1.5%. This demonstrates that the buildings were correctly modelled in SAP2000 software in terms of mass, stiffness and geometry.

8.2.2. *Results and discussion*

Figure 8.12.a shows that all the maximum inter-storey drifts were within the code limitation (less than 2.5%). The mean storey drifts associated with the two upper floors (3rd and 4th floor) were almost equal for the three buildings while the SC-TB building showed the highest inter-story drift for the first two floors. Generally, it was observed that the story-drift was inversely correlated with yield force (slip force in case of SC-TB) and energy dissipation capability. SC-TB had the slip force lower than those yielding forces of BRB and CTB (see Table 8.4) as well as the smaller area enclosed in a hysteresis loop, which resulted in the fact that it tended to have larger story displacements.

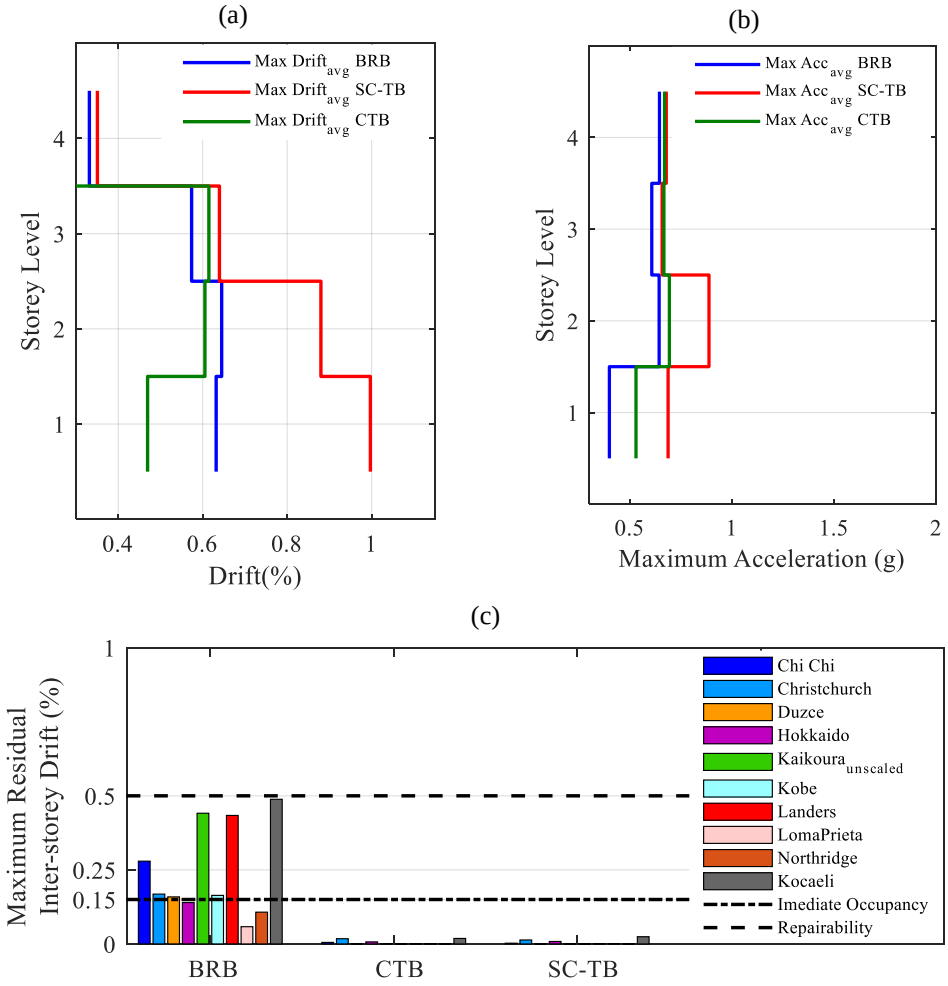

Figure 8.12: (a) Maximum inter-storey drift for the three buildings, (b) Maximum story-acceleration for the three buildings, (c) Maximum residual inter-storey drift.

Figure 8.12.b expresses the mean story-acceleration. It was observed that the differences among the three buildings in terms of story- accelerations were less than that of story-drifts. This indicates

that the acceleration response of each story was less sensitive to energy-dissipation capability. This confirms previous findings [65] that the maximum storey-acceleration is much sensitive to transition zones in hysteretic loops.

Maximum residual inter-storey drifts are depicted in Figure 8.12.c. Three thresholds [54] are assumed here to cite a building as the low-damage (ready for re-occupancy), repairable and should-be-demolished. In case that the residual drift is larger than 0.5%, the building should be demolished [34, 55, 232]. In another case, if the residual drift is less than a limit (normally between 0.1 – 0.2 % [55, 56, 232] herein is assumed to be 0.15 %), the building can be re-occupied and classified as low-damage. Lastly, the permanent drift between 0.15 and 0.5% indicates that the building has undergone repairable damage, yet careful attention should be placed on the repair time and cost. In this respect, the building with SC-TB experienced a near-zero residual for all records, so it can be seen as a low-damage system.

Ironically, the same happened for the building with CTB and it was nearly re-centred for all of the seismic events; however, it could not be classified as a low-damage system as the timber connection experienced permanent damage and crushing, and there was not any reusable damping resource. The reason for recentring lies in the hysteresis response of CTB brace and lies in the fact that it normally experiences considerable stiffness and strength deterioration when subjected to a number of inelastic cycles. Consequently, a limited restoring force, such as those provided by elastic columns, can re-centre the whole structure. The recentring phenomenon for building with CTB, indeed, were in agreement with the shake table results for single and double story building with CTB provided by Popovski [228].

Regarding the building with BRB, it was in the vicinity of being non-repairable for three events as the permanent drift ratio was close to 0.5 %, repairable for five events, and ready for immediate re-occupancy for the rest. Previous researches [55, 209, 216] also shows the same results, stating that the residual drifts of buildings with BRB might be concerning.

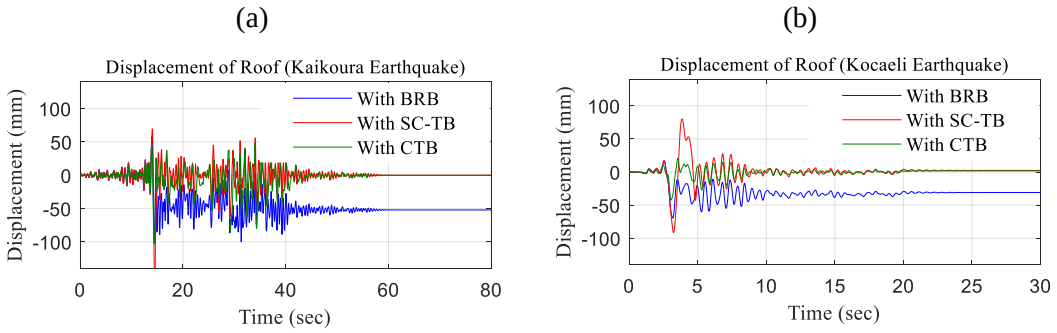

Figure 8.13: (a, b) roof displacement time history for Kaikoura and Kocaeli earthquakes

Figure 8.13.a and Figure 8.13.b depicts the displacement time history and provides further clarification about the residual displacement of the roof during the two events (Kaikoura and Kocaeli). As clear, considerable residual displacements could be found at the end of Kaikoura and Kocaeli events for BRB while there were almost zero residual displacements at the end of both events for SC-TB and CTB.

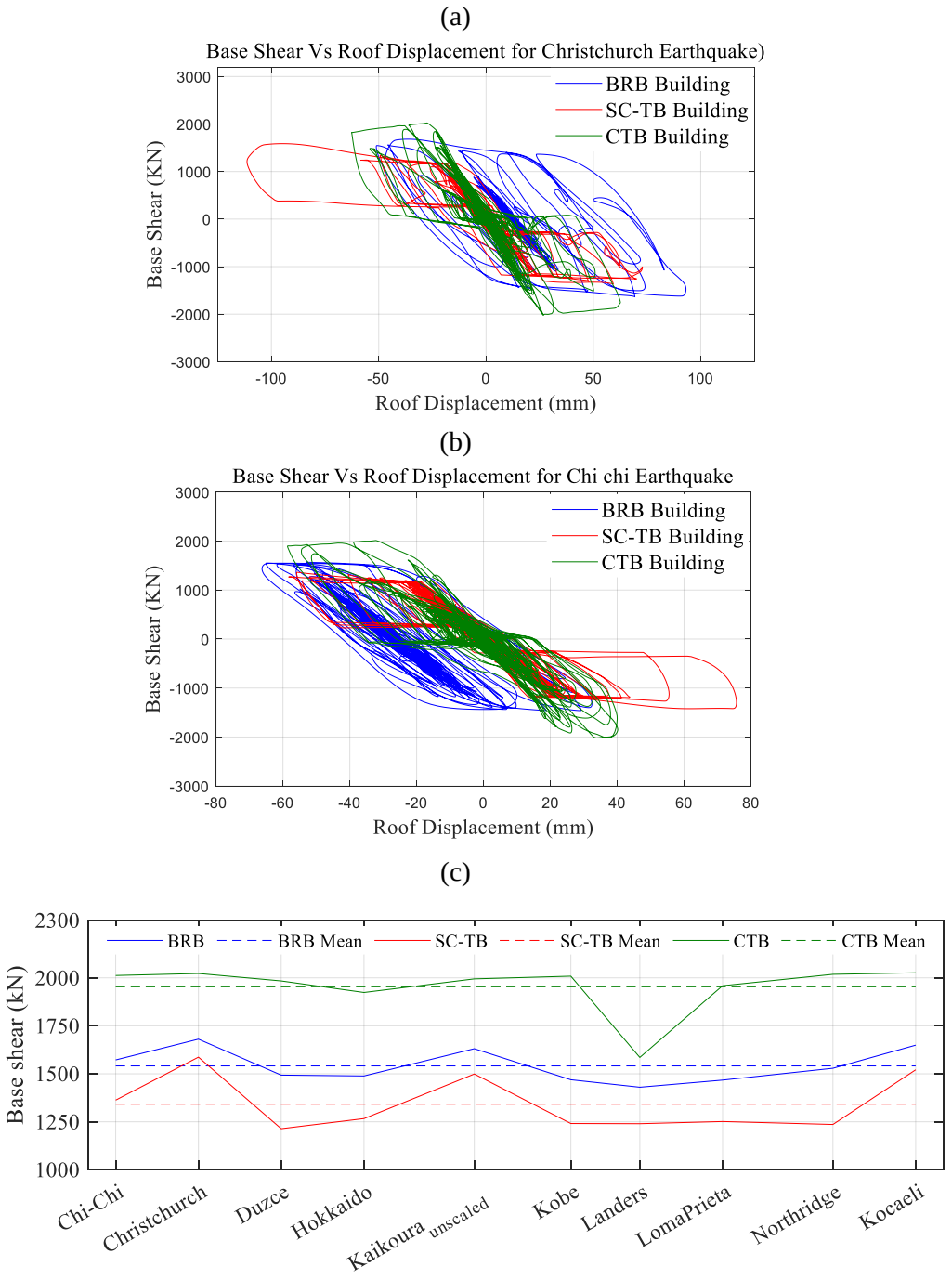

Figure 8.14: (a, b) Base shear versus roof displacement for three studied buildings, (c) Maximum base shear for the three buildings

The base shear versus roof displacement plot is provided in Figure 8.14.a and Figure 8.14.b for three structures subjected to Christchurch and Chi-Chi earthquake. Figure 8.14.c depicts the maximum base shear of the buildings for each event. As can be seen, if it assumed that all the three buildings had equal initial stiffness and ultimate strength, the following results can be carried out based on mean data. Building with SC-TB had the lowest amount of base shear, while CTB building experienced almost 40% more base shear and BRB experienced 15% more base shear compared to SC-TB. Further studies for building with higher fundamental periods are required as the results discussed here was limited to a relatively short-period structure. However, it should be noted that structures with higher periods are expected to be much less sensitive to the amount of hysteresis damping, stiffness and strength degradation, pinching and yielding point of structures [233].

8.3 Summary and Conclusion:

This study presented a new damage-free (Self-centring Timber Brace) SC-TB by which it is attempted to alleviate the drawbacks of (Conventional Timber Brace) CTB, including pinching, timber crushing, strength and stiffness deterioration, by employing a SC connection (RSFJ). In the first part of this paper, an analytical model was developed to predict the response of SC-TB equipped with RSFJ connection. In the second part of this study, a total number of four different brace specimens composed of RSFJ connections with different characteristics were experimentally tested and compared to analytical predictions based on which a satisfactory accuracy was observed. Furthermore, the performance of one of the specimens was validated using Finite Element software ABAQUS. In summary, the results of numerical, analytical and experimental studies were in good agreement.

In the last part of this study, firstly a framework was discussed illustrating how to design the CTB for ductile failure. Furthermore, a comparative study was conducted on the seismic performance of a building with SC-TB as the main lateral load resisting system as compared to a reference building with BRB and a ductile CTB. In the design procedure, all of the three buildings were designed in a way that they, all, have an identical fundamental period and ultimate strength to draw a fair comparison. According to these assumptions in the design, zero-residual drift was observed for the buildings with SC-TB and CTB while relatively considerable residual drift was observed for the building with BRB. The relatively higher maximum inter-storey response was observed for the structure equipped with SC-TB, which can be attributed to both having a lower activation force (slip force in case of the building with SC-TB comparable to yield force in case of the building with CTB and BRB) and less hysteresis damping. It is expected that this can be

further improved by adjusting the activation strength. For instance, by increasing the activation strength, the inter-storey response is expected to decrease. It was also observed that the design base shear was 15% less for SC-TB building as compared to BRB. Regarding the difference in inter-storey drifts, it should be noted that the building with SC-TB had the highest inter-storey drift while the difference among the three buildings got smaller as the floor increased. This difference was almost 50% for the first floor while it was 5% for level 4. This would have been further adjusted with different activation strength, yet not considered in the study.

Finally, in the building with SC-TB, as the employment of the SC-TB contributed to reducing the maximum base shear, it is expected that the cost of forced-controlled elements (non-ductile) decreases to some extent, yet probably more should be spent on the brace elements. Therefore, it cannot simply judge whether the final cost of this building exceeds the building with CTB or not. Detailed design and optimization are needed with respect to the project.

9 Manuscript.6 - A New Self-Centring Brace with Zero Secondary Stiffness Using Elastic Buckling

Based on the article published on 2020/6/1 by peer-reviewed "Journal of Constructional Steel Research", Volume 169, pp 106035

9.1 Abstract

It has been shown that having a low post-elastic (secondary) stiffness for conventional structures can be beneficial in terms of putting a limit on the base shear of the structure although it could result in having a residual and permanent drift. A well-recognized example can be Buckling-Restrained Braced Frames (BRBFs) offering stable, repeatable and reliable damping while suffering from residual displacements owing to low secondary stiffness. This paper introduces a new type of self-centring brace with a flag-shape behaviour possessing a zero post-elastic (secondary) stiffness, Self-Centring Zero-Stiffness Brace (SC-ZSB), bringing the benefit of systems with minimal secondary stiffness without their deficiency. Basically, the elastic damage-free buckling of the brace is combined with the friction damping to form the intended flag-shape behaviour with zero post-elastic stiffness. The introduced bracing system will recover and re-centre at the end of buckling without any inelastic deformation, strength and stiffness degradation while providing passive damping. The proposed SC-ZSB is experimentally validated using a scaled self-centring brace. Besides, a comparative study is performed using OpenSeeS software to illustrate the seismic performance of the SC-ZSB in comparison with a BRB Frame. The results demonstrate that SC-ZSB system efficiently limits the base shear of the structure with an almost similar inter-story drift of the BRB frame, while it can eliminate any residual drifts as well.

9.2 Introduction

One of the major benefits of having a positive secondary stiffness in the load-displacement response of structural systems is the reduction of the residual drift after seismic events [234]. MacRae [234] showed that the residual displacement is directly correlated with the secondary stiffness of structures. It has been shown that buildings with zero or negative secondary stiffness will experience a larger residual drift compared to those with positive secondary stiffness. Accordingly, some techniques have been suggested to increase the secondary stiffness such as by the employment of an elastic secondary system, either stiff or flexible, which is regarded to be one

of the most efficient ways [235-238]. In fact, controlling the residual displacement could be a critical seismic design parameter when the economic losses such as the cost for realignment and repair are taken into account. In this regard, Pampanin and Christopoulos [239, 240] have proposed a performance-based design method considering the residual drift requirements allowing an engineer to achieve a desirable performance for the target building. A well-recognized example of a system with negligible post-yield stiffness is the Buckling-Restrained Braces (BRBs), which has been reported to have strain-hardening ratio of about 0.005 ~ 0.020 [55, 209, 241-243]. Another problem induced by the residual drift could be the building vulnerability to aftershocks given the collapse probability of the structure increases. A recent study [209] showed that those buildings constructed with BRBs could be 15% more probable to collapse if the aftershock events are considered given the residual drift experienced in the mainshock. As such, researchers and practitioners have been focusing on finding efficient ways to reduce the residual drift as a significant structural response parameter by increasing the secondary stiffness.

Apart from increasing the secondary stiffness, the application of a re-centering mechanism was shown to be highly effective in decreasing the residual displacement [51]. Such re-centering mechanism can be achieved by using post-tensioned tendons [51] or pre-pressed springs [135] coupled with a damping source (friction [153], yielding [244] or viscous [217]. Utilization of the SMA material has been also studied to provide the self-centering response [245, 246]. It is worth noting that some recent techniques have been used with the main intention of reducing the residual displacement. As an example for BRBs, it can be referred to [85, 247, 248] where SMA (Shape Memory Alloy) rods were used to assist the recentring of the brace. Guo et al studied the application of friction damping and pre-pressed disc spring to form a new tension-only brace [249]. Numerous novel self-centring LLRS systems have been suggested and experimentally verified in the literature, and readers are referred to [17, 246, 250] to see a comprehensive review. Other researchers also studied the application of bare friction dampers to be applied in structures as a low-damage system [13, 26, 153, 169] without any need for a secondary system for recentring.

Resilient Slip Friction Joint (RSFJ) was developed by Zarnani and Quenneville [137] with inherent self-centring and damping and have been used in different damage-free LLRSs including rocking shear walls, tension-only and tension-compression brace [99, 139, 156, 192, 222, 251, 252]. This study introduces a new SC bracing system with zero secondary stiffness (SC-ZSB) using RSFJ as the friction damper. It should be noted that nearly most of the current SC braces have a positive secondary stiffness while the proposed SC brace possesses zero secondary stiffness owing to taking a controlled damage-free elastic buckling as a means to zero the post-elastic stiffness. It should be noted that this self-centring brace with zero post-elastic stiffness could be utilized in some practical situations where there are limitations on both base shear capacity and residual drift of the structure. Furthermore, experimental tests were performed on three scaled specimens to

further illuminate the concept. At the final stage of this study, a comparative study is conducted through which the performance of a building with proposed braces is compared to that of a building using Buckling-restrained Braces (BRBs).

9.3 Concept of Self-centring Zero-stiffness Brace

It is a well-known fact that the combination of a nonlinear elastic spring (such as post-tensioned cables or pre-pressed springs) and a damping mechanism (friction, yielding or viscous) can form a flag-shape response [51, 135] as shown in Figure 9.1. However, if it is intended to attain a flag-shape response with zero secondary stiffness ($\alpha_1 = 0$), the conventional ways seem to be ineffective.

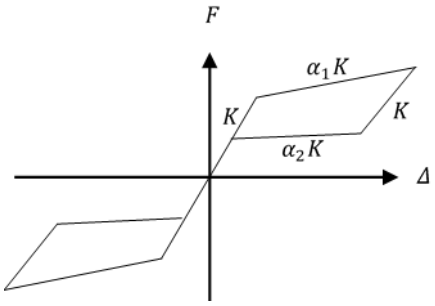

Figure 9.1: Conventional flag-shape behaviour ($\alpha_1 \neq 0$)

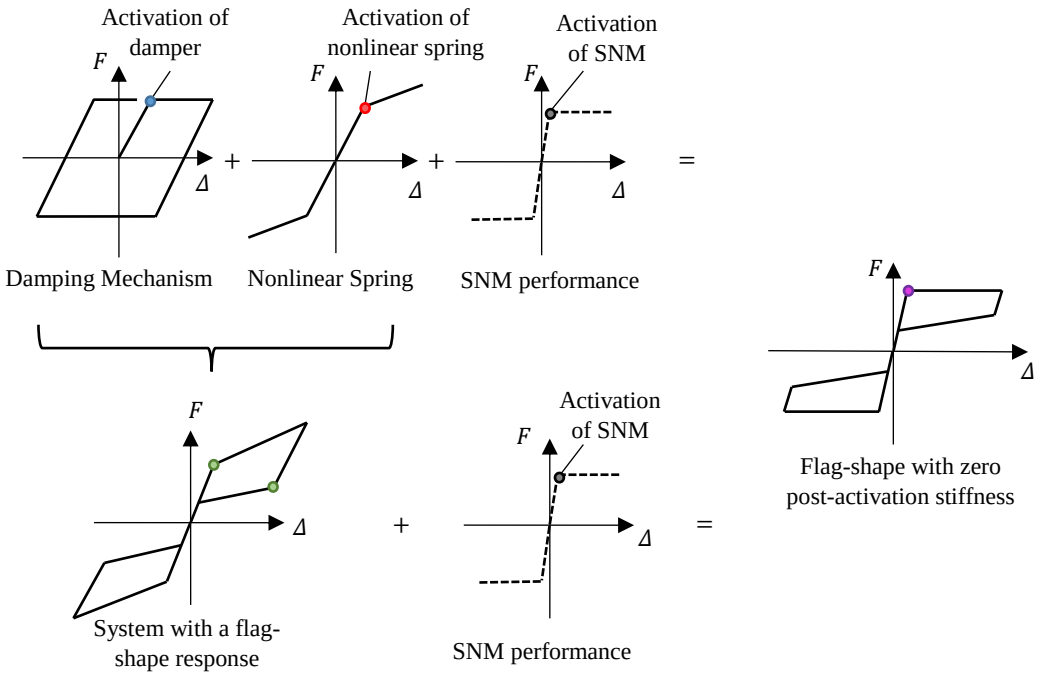

Figure 9.2: Schematic way to achieve a SC behaviour with zero secondary stiffness

The way through which the new zero-stiffness flag-shape response could be created is described in Figure 9.2. Firstly, the friction damping (possessing perfectly elastoplastic behaviour) is combined with pre-pressed springs (possessing nonlinear elastic behaviour) resulting in the well-known conventional flag-shape response (RSFJ axial performance). Following this combination, an additional Stiffness Neutralizer Mechanism (SNM), which is the controlled damage-free elastic buckling (possessing bilinear behaviour), is used to zero the secondary stiffness. The necessary condition to be considered is that the SNM activation point should coincide with or be after the activation of the damper and the nonlinear spring (in the loading phase). It should be also noted that due to the involvement of the buckling in the performance of the brace, its deformation mechanism is different from the RSFJ brace that was studied in previous chapters (Chapter 4 and chapter 5). The deformation mechanism and shape of the brace when buckling in compression can be found in Figure 9.14. In this paper, the SC mechanism is generated by the use of the RSFJ damper [137] while the SNM is provided by the controlled damage-free elastic buckling of the brace. It should be noted that the mentioned technique for achieving an SC system with zero secondary stiffness is may be generalized to other SC systems though it may require further studies and research. The proper framework to achieve the target flag-shape and buckling load will be illustrated in section 9.4 and section 9.5.

9.4 Analytical model for axial and rotational performance of RSFJ damper

As it was mentioned, the RSFJ damper in this study has two main roles. Firstly, to provide an SC response when the brace is loaded axially. Secondly and more importantly, to provide the SNM with the intention of inducing a controlled damage-free elastic buckling soon after RSFJ activation. To meet those aims, the axial and rotational performance of this damper is studied and discussed in the following sections.

9.4.1. *Axial Performance*

As it is depicted in Figure 9.3, the RSFJ consists of two types of grooved steel plates namely: cap plates (grey plates) and middle plates (orange plates), clamped together using high strength bolts and prestressed disc springs. It has been shown that the axial behaviour of this damper is of flag-shape (Figure 9.4). The slip force of RSFJ can be determined by the equilibrium of forces in the free body diagram as per Eq.9.1 [138].

$$F_{slip} = 2n_b F_{pr}\left(\frac{sin\theta_g + \mu cos\theta_g}{cos\theta_g - \mu sin\theta_g}\right) \quad 9.1$$

Where θ_g denotes the angle of grooves; "μ" is the coefficient of friction. F_{pr} indicates the pre-stressing force of disc springs; and n_b is the number of bolts on each splice (for instance, in Figure 9.1, n_b= 6). Similarly, the residual force at the end of the unloading can be calculated by Eq.9.2 using the frictional resistance, however with the opposite direction.

$$F_{res} = 2n_b F_{pr}\left(\frac{sin\theta_g - \mu cos\theta_g}{cos\theta_g + \mu sin\theta_g}\right) \quad 9.2$$

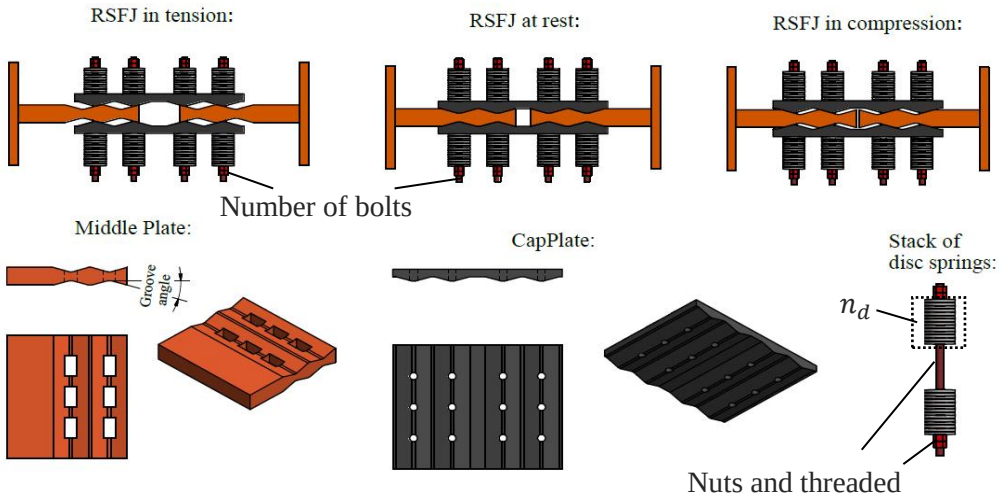

Figure 9.3: RSFJ assembly and components

The ultimate and the restoring axial loads that an RSFJ damper can experience (F_{ult} and $F_{restoring}$) can be computed by replacing F_{pr} by F_u– which is the maximum force of the disc spring stack in its fully flat position –in the F_{slip} and F_{res} equations, respectively. It is worth noting that the RSFJ damper in the SC-ZSB application will not see the ultimate load – P_{ult} – because it is designed to buckle within the brace right after the slip force. In other words, the axial performance of RSFJ would be limited to the vicinity of the slip force, yet its rotational performance comes into play when the buckling triggers.

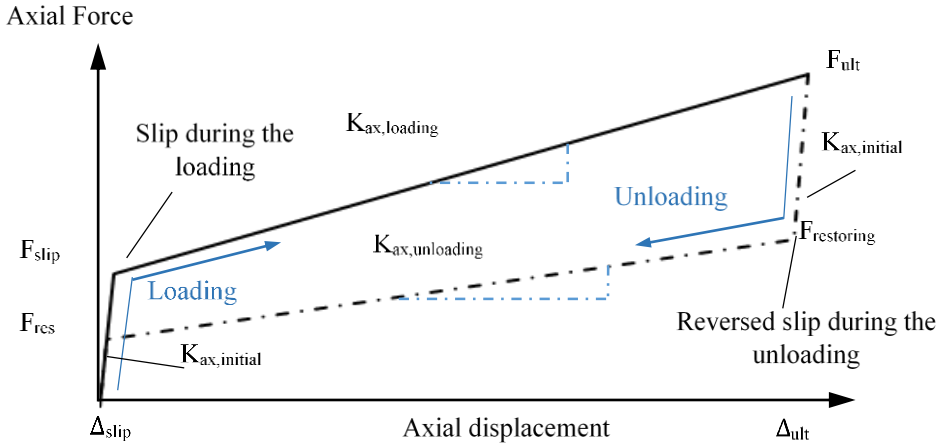

Figure 9.4: Self-centring hysteretic axial response of RSFJ (flag-shaped behaviour)

9.4.2. *Rotational Performance*

Comparable to the axial performance, RSFJ damper has also a flag-shape response (shown in Figure 9.5 and Figure 9.6) if it is subjected to an in-plane moment ($M_{in,\theta}$) [164]. In fact, this behaviour will appear as a nonlinear rotational spring along the brace and perform as the main key to encourage the brace to buckle at the desired load.

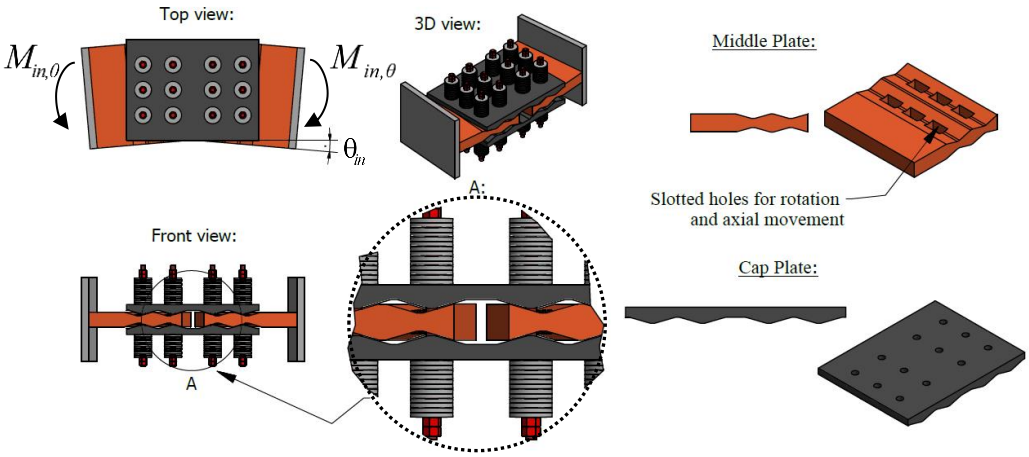

Figure 9.5: In-plane rotation of the RSFJ

The slip moment of the RSFJ - due to symmetric rotations at both ends - can be calculated using Eq.9.3:

$$M_{in,slip} = n_b F_{pr} b \frac{(sin\theta_g + \mu\, cos\theta_g)}{(cos\theta_g - \mu sin\theta_g)} \quad 9.3$$

Where b is the width of joint or cap plates. Other parameters are as defined previously. Similarly, the residual in-plane moment ($M_{in,res}$) at the end of the unloading phase can be calculated with friction in the opposite direction as per Eq.9.4:

$$M_{in,res} = n_b F_{pr} b \frac{(sin\theta_g - \mu cos\theta_g)}{(cos\theta_g + \mu sin\theta_g)} \quad 9.4$$

By replacing F_{pr} by F_u (which is the flat load of disc springs) in $M_{in,slip}$ and $M_{in,res}$ equations, the ultimate and restoring moments can be calculated via Eq.9.5 and Eq.9.6, respectively. The PE slope of the rotational flag-shape hysteresis corresponding to the loading and unloading phase can be determined by [156, 222]:

$$K_{in,sec,loading} = \frac{K_{st} n_b b^2}{2} tan\theta_g \frac{(sin\theta_g + \mu\, cos\theta_g)}{(cos\theta_g - \mu\, sin\theta_g)} \quad 9.5$$

$$K_{in,sec,unloading} = \frac{K_{st} n_b b^2}{2} tan\theta_g \frac{(sin\theta_g - \mu\, cos\theta_g)}{(cos\theta_g + \mu\, sin\theta_g)} \quad 9.6$$

From Eq.9.5 and Eq.9.6, it can be concluded that the after-slip rotational stiffnesses are only functions of characteristics of the stack of disc springs ($K_{st} = K_s/n_d$), the angle of grooves, the coefficient of friction and the width of the plates.

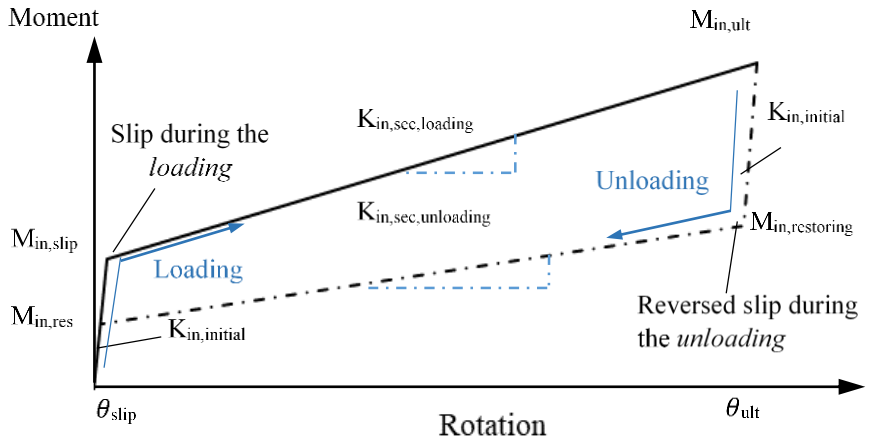

Figure 9.6: Self-centring hysteretic rotational response of RSFJ (flag-shaped behaviour)

9.4.3. *Anti-locking mechanism*

There is a possibility that the displacement demand for the RSFJ exceeds the displacement capacity due to a major seismic event beyond the design level and the disc spring becomes flat. If this happens, the joint may become locked and the axial or rotational stiffness may increase rapidly. A mechanism has been put forth entitled "Anti-locking mechanism or secondary fuse" [99, 253] in which the prestressing bolts (or rods) will start to yield when disc springs become flat and the plastic deformation of the rods will provide more displacement capacity for the joint. There is still an ongoing program at the University of Auckland and Auckland University of Technology to further investigate this solution.

9.5 Quantification of buckling load

An SC-ZSB can be mathematically modelled with a single-degree-of-freedom (SDOF) system as shown in Figure 9.7 based on the premise that the axial movement of RSFJ is negligible. This assumption tends to be valid as the slip force of the RSFJ should be marginally less than the buckling load as was discussed in section 9.3. This implies that the axial degree of freedom can be ignored for the sake of simplicity. The SDOF model is composed of a nonlinear spring and two rigid beam elements. The nonlinear spring is representative of the rotational behaviour of the damper while the rigid elements resemble the brace bodies. Here, the brace is considered to be made of timber, yet it can be steel or any other material as it is supposed to stay elastic. As it was mentioned earlier, the key point to attain the target flag-shape is that the SNM activation force should be higher than that of the damper. To achieve this, a framework is needed to quantify the buckling load. In this section, a simplified analytical model is introduced to predict the buckling load of the SC-ZSB.

Based on the premise that the energy stored in the system is path-independent and the stored energy in the beam elements is relatively negligible (rigid) compared to the energy stored in the damper, the potential energy of the SDOF system during the loading phase is:

$$\Pi(\theta) = U(\theta) - W(\theta) = \int_0^{\theta<\theta_{ult}} M(\theta)\, d\theta - PL_1 cos(\theta_1) - PL_2 cos(\theta_2) \qquad 9.7$$

Using stability analysis and the Lagrange-Dirichlet theorem, stating that the strict minimum of potential energy brings the critical state [127, 254], the critical load can be calculated as:

$$\frac{d\pi}{d\theta} = 0 \rightarrow P_{cr,loading} = \frac{L\frac{d}{d\theta}\left(\int_0^{\theta<\theta_{ult}} M(\theta)\right)}{L_1 L_2} \quad 9.8$$

where L, L_1 and L_2 are defined in Figure 9.7. According to Eq.9.8, it can be concluded that the buckling load of the system is a function of tangent rotational stiffness " $\frac{d}{d\theta}\int_0^{\theta\leq\theta_{ult}} M(\theta)$". Therefore, if the tangent stiffness of the rotational spring (RSFJ damper) is assumed to be $\frac{d}{d\theta}\int_0^{\theta\leq\theta_{ult}} M(\theta) = K_{in,sec,loading}$, the buckling load can be calculated as:

$$P_{cr,loading} = \frac{K_{in,sec,loading} L}{L_1 L_2} \quad 9.9$$

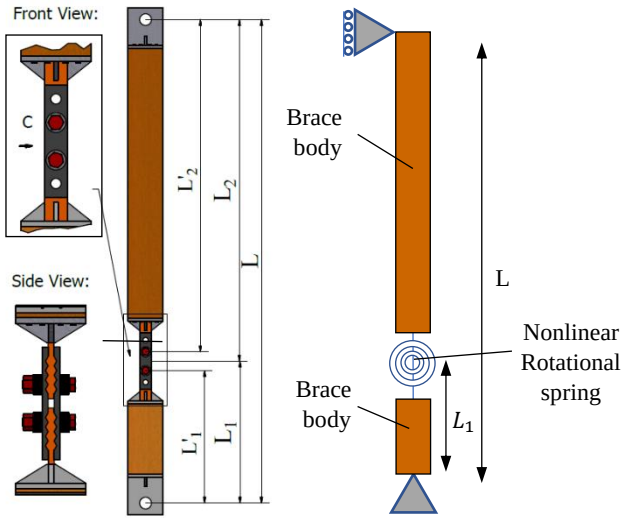

Figure 9.7: Proposed model for SC-ZSB

Eq.9.9 can be re-arranged with respect to Eq.9.5, considering that the damper is activated:

$$P_{cr,loading} = \frac{n_b b^2 L K_{stack}}{2L_1 L_2}\left(\frac{2sin^2\theta_g + \mu\, sin2\theta_g}{2cos^2\theta_g - \mu\, sin2\theta_g}\right) \quad 9.10$$

The restoring force can be calculated if the friction acts in the opposite direction:

$$P_{restoring} = \frac{n_b b^2 L K_{stack}}{2L_1 L_2}\left(\frac{2sin^2\theta_g - \mu\, sin2\theta_g}{2cos^2\theta_g + \mu\, sin2\theta_g}\right) \quad 9.11$$

For the design purposes, based on geometry shown in Figure 9.8, the following equation can be considered to determine the lateral displacement of the cap plate as a function of axial

displacement in which L'_1 and L'_2 are shown in Figure 9.7. This equation is based on the assumption that the brace bodies are relatively rigid with respect to RSFJ rotation. Finally, in the real applications, the parameters, number of bolts (n_b), stiffness and number of disc springs ($K_{st} = K_s/n_d$), pre-stressing force (F_{pr}) and angle of grooves (θ_g) should be selected in a repetitive trial and error process so that the buckling load in the loading phase occur immediately after the slip point and is equal to the intended force demand.

$$\Delta_{lat} = \sqrt{2\Delta_{max}\frac{L'_1 L'_2}{L}} \qquad 9.12$$

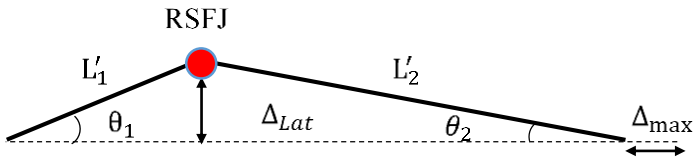

Figure 9.8: Lateral displacement as a result of axial displacement and rotation

9.6 Hysteretic behaviour of SC-ZSB

In order to predict the response of a structure using SC-ZSB, a reliable and precise hysteresis model representative of the real behaviour of the system is required. In this regard, this section discusses the behaviour of the brace during different phases of loading and unloading. It should be noted that SC-ZSB is only effective in compression. Therefore, the symmetric flag-shape shown in Figure 9.9.b can be achieved when two braces are recruited in each story in a way that both are working in cyclic loading. Such configuration can be an X-type, chevron or converted chevron brace.

The hysteretic response of the SC-ZSB in compression is depicted in Figure 9.9.a. According to this figure, when SC-ZSB is loaded in compression, it does not move until the imposed axial load overcomes the frictional resistance between the grooved plates of RSFJ damper (activation of the damper or slippage). This point is referred to as the slip point and shown with P_{slip}. Following this point, the curve is smoothly approaching the buckling load in a nonlinear manner as far as it hits a plateau. During this phase, the brace is following a zero-stiffness path and is exhibiting lateral displacement as it is buckling whilst no increase is observed in the axial force. Once the unloading begins, the direction of frictional resistance changes. The SC-ZSB does not slip in unloading till the frictional resistance reduces to a certain load. At this point, the reversed activation (reversed slip) takes place $F_{restoring}$. The slip in unloading continues to residual force F_{res}.

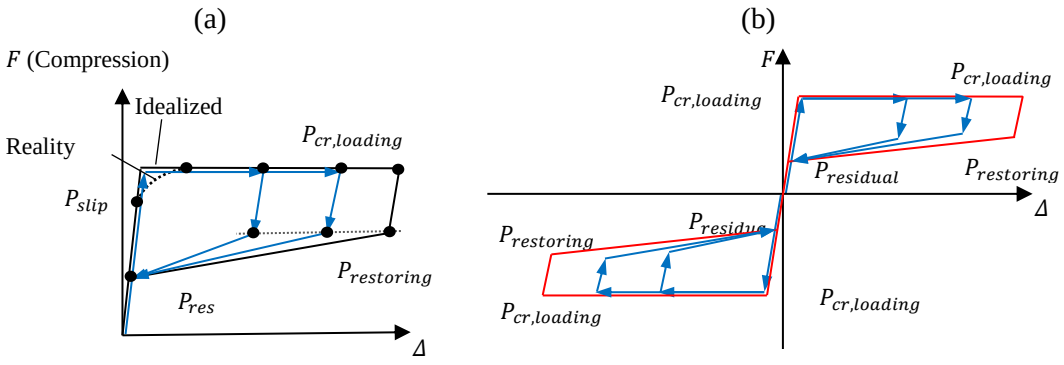

Figure 9.9: Cyclic performance: (a) single SC-ZSB, (b) double SC-ZSB in X or chevron configuration

9.6.1. *Experimental Validation*

The performance of the SC-ZSB was experimentally examined via a timber brace, which was designed and tested under cyclic loading. The test specimen was made of LVL (Laminated Veneer Lumber) timber material with an elastic modulus of 11 GPa as for brace body and it had a square cross-section with 150 mm width. Note that the timber can be replaced by steel or any other material as it is supposed to remain elastic. The timber section had 600 kN capacity in tension and 810 kN capacity in compression parallel to the grain, according to the timber specifications. An RSFJ (portrayed in Figure 9.10) was connected to the end of the brace to provide the intended behaviour. This RSFJ had 340 mm length, 50 mm width and a groove angle of 30 degrees. The overall length of the brace – pin to pin distance – together with the RSFJ was 1699 mm. Two end bracket plates with a thickness of 20 mm, one was directly welded to RSFJ and the other was welded to a bearing plate performed as the gusset plates of the brace which had 50 mm holes for insertion of pins. Eight self-tapping screws with 180 mm length and 7 mm diameter were used to connect the bearing plates to the timber brace. An actuator with 300 kN capacity and 100 mm stroke was utilized for the test. The schematic drawings of the test setup and the RSFJ used are illustrated in Figure 9.10. Two displacement gauges were used at both sides of the RSFJ to measure the axial deformation of the specimen. Furthermore, two Linear Variable Differential Transformers (LVDTs) were employed along with the height of the brace in order to record the lateral displacement of the cap plates (Figure 9.10). Different configurations including two different stacks with the different number of springs and pre-stressing forces were considered for the tests, as per details in Table 9.1. The number of bolts n_b, number of disc springs n_d and the prestressing force F_{pr} are shown in Table 9.1. The important point in the procedure of design of the specimens where the pre-stressing force of the disc springs. The pre-stressing force should be quantified in a trial-and-error process so that the slip force of the brace is slightly less than the critical load ($P_{cr,loading} > F_{slip}$).

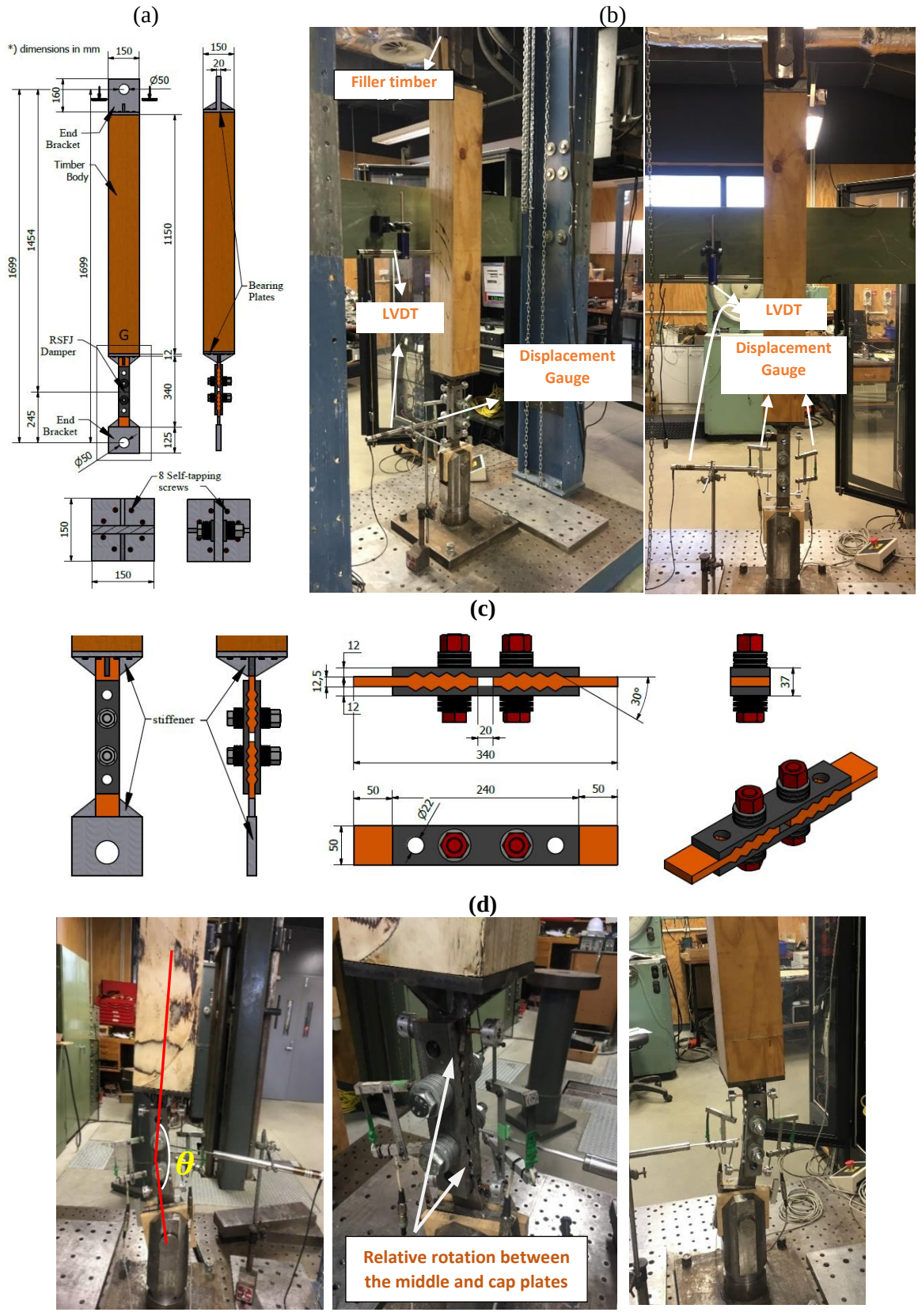

Figure 9.10: In-plane testing of the SC-ZSB: (a) test specimen dimensions (in mm), (b) specimen in the testing apparatus, (c) recruited RSFJ damper (dimensions in mm) and (d) buckled mode shape of SC-ZSB

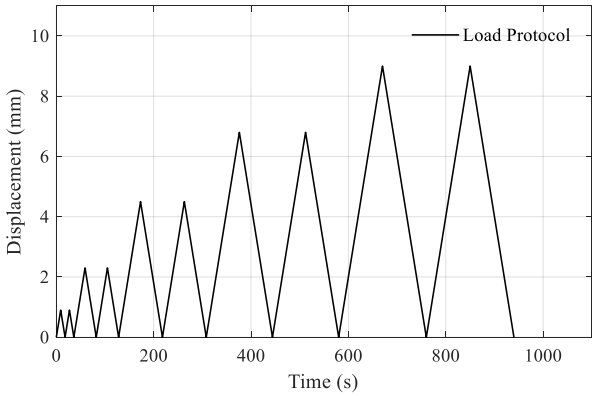

Figure 9.11: Loading protocol

Table 9.1: Testing Matrix

Configuration	n_d	Prestressing force (kN)	F_{slip} (kN)	$F_{residual}$ (kN)	$F_{restoring}$ (kN)	$P_{cr,loading}$ (kN)	$K_{in,sec,unload}$ (kN. m)	$K_{in,sec,load}$ (kN. m)	$\frac{EI_{body}}{L}$ (kN. m)
1	6	3.8	6.5	2.7	9.4	16.4	1.6	2.8	144
2	6	6.8	11.7	4.8	9.4	16.4	1.6	2.8	144
3	8	5	8.5	3.5	6.3	11.0	1.0	1.85	144

Figure 9.11 shows the cyclic loading regime that was used for the testing program where the maximum displacement was 9 mm.

Figure 9.12 illustrates the results of the testing performed on the prototype SC-ZSB. Figure 9.12.a-c and d are associated with a brace using RSFJ with 6 springs per side while Figure 9.12.e and f are associated with a brace using RSFJ damper with 8 springs per side. Figure 9.12.a, c, and e show the axial load of the brace versus the axial displacement while Figure 9.12.b, d, and f depict the axial load versus lateral displacement of cap plates. As can be seen in Table 9.1, all of the slip forces were adjusted to be less than the buckling load but with different margins. As can be deduced from the results, all of the specimens performed as expected. The red line backbone curves are the analytical predictions using Eq.9.1 and Eq.9.10 -12 and the blue dashed lines are what was witnessed during the experimental program. As it can be noted, the brace had high initial axial stiffness before the slippage; however, it started to reduce after the slippage point as the axial force approached the buckling load. During the buckling, the axial stiffness was completely diminished to zero and the SC-ZSB was only exhibiting lateral deflection to the side (shown in Figure 9.12.b, d and f). The buckling mode shape of the SC-ZSB is shown in Figure 9.10.d. According to Eq.9.12, the lateral displacement of the cap plate was estimated to be 47.3 mm, which was in good agreement with the 40 mm that was achieved in the experimental tests. The

most important point to be highlighted is that this buckling was completely damage-free as opposed to the buckling in the conventional bracing systems. More specifically, no strength degradation, no permanent inelastic deformation and no yielding of the material was involved.

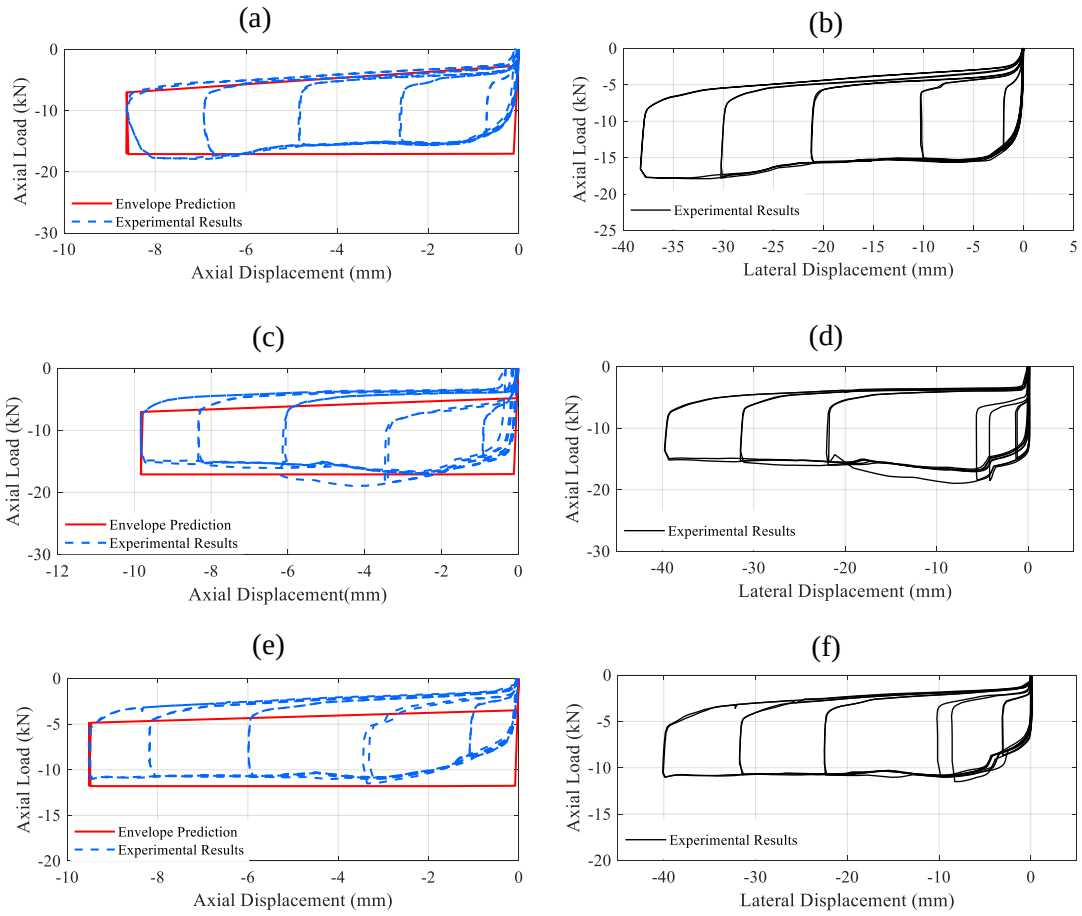

Figure 9.12: Experimental results of the tested SC-ZSB brace, (a, c & e): Axial load versus axial displacement for configuration 1, 2 and 3, respectively (b, d & f): Axial load versus lateral displacement for configuration 1, 2 and 3, respectively

9.7 A comparative study with BRB

9.7.1. *Nonlinear Dynamic Time History Analysis*

A well-recognized example of an alternative system with minimal secondary stiffness that offers both reliable and repeatable damping mechanism is BRBF, taken as the reference model here for comparative study. For this purpose, a four-story benchmark BRB framed building [223] is used here to compare the performance of the proposed SC-ZSB and the BRB. The mega-bracing layout has been utilized for both systems because it helps to better distribute the strength and stiffness among the stories [255]. As the proposed SC-ZSB brace works only in compression, the X-type

configuration of SC-ZSBs (using RSFJ damper) was replaced by the BRBs in the original building (Figure 9.13.a and Figure 9.13.b) in order to offer the symmetric response shown in Figure 9.9.b. It is worth noting that this might affect the cost of construction to a varying degree depending on the target performance, utilized construction material and other parameters. This area was out of the scope of the present study and further studies are required to compare the cost of the two systems. The beams and columns were assumed to be the same for both systems [223]. As for the columns, $W\,14 \times 38$ and $W\,14 \times 26$ were assigned for the first and second two floors, respectively. Beams for the first three stories were assigned to be $W\,12 \times 19$ while for the last floor was $W\,12 \times 16$. The gravity load was composed of 4 kN/m² dead load and 1.5 kN/m² live load for the first three floors. Whereas the values were 4.7 kN/m² and 2 kN/m² for the roof, respectively. The equivalent SC-ZSB using RSFJ damper associated with each story was designed in a way to have relatively an identical initial stiffness and activation strength (as per Table 9.2 and Table 9.3) to encourage two buildings to have similar fundamental periods. Furthermore, this implies that the buckling load of each SC-ZSB was assumed to be identical to the yielding strength of the associated BRB. By having the same activation strength (yielding in case of BRB and buckling load in case of SC-ZSB), a more reasonable conclusion on the effects of secondary stiffness could be drawn. Each SC-ZSB was designed to have a steel body while the RSFJ damper was assumed to be located at the middle of the brace. The grooves for each RSFJ and the steel body for SC-ZSB were designed in a way that they had the ability to experience lateral deflection (Δ_{lat} shown in Table 9.2). An example of such a brace with RSFJ damper is illustrated in Figure 9.14. As it can be seen, there is a steel jacket with slotted holes connected from one side to the brace body via bolts and welded from another side to the end plate of the RSFJ damper. The main purpose of this jacket is to allow the free movement of the brace in tension while transferring the moment between RSFJ and the brace body during the buckling in compression.

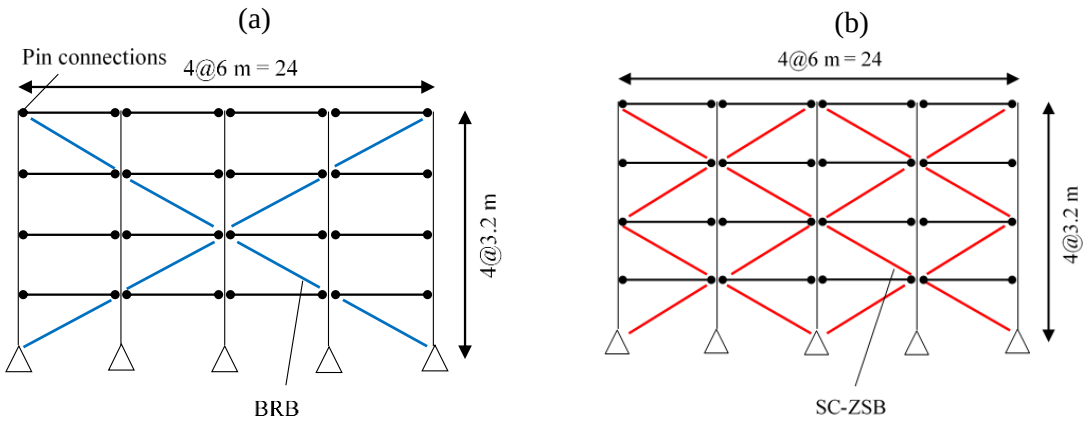

Figure 9.13: (a) 4 story building with BRB and (b) 4 story building with SC-ZSB brace

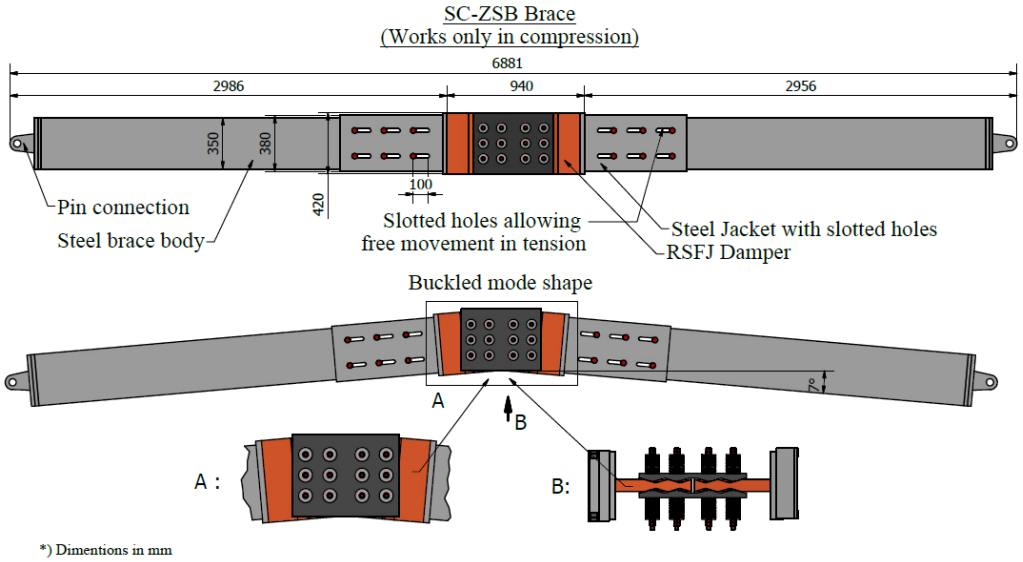

Figure 9.14: An example of SC-ZSB brace

Table 9.2: Details of RSFJ damper for SC-ZSB brace

Story	Width of plates (mm)	Prestressing force in disc springs F_{pr} (kN)	Coefficient of Friction (μ) [99]	Number of bolts n_b	Number of springs n_d	Angle of groove θ_g (degree)	Stiffness of a disc spring (kN/mm)	Δ_{lat} (mm)
1	420	44 (40%)	0.17	10	16	26	70	491
2				9	16	25		515
3				8	13	21		508
4				5	13	23		460.6

Table 9.3: SC-ZSB and BRB design summary for each storey

Story	BRB					SC-ZSB					
	Initial Stiffness (kN/mm)	Core Area (mm2)	F_y (kN)	F_u (kN)	Δ_u (mm)	Initial Stiffness (kN/mm)	F_{slip} (kN)	$P_{cr,loading}$ (kN)	$F_{restoring}$ (kN)	P_{res} (kN)	Δ_{max} (mm)
1	133767	29.23	847.67	1165.5	101	133767	631	850	348	258	71
2	112670	24.62	713.98	981.7	101	112670	547	705	280	217.4	78
3	84479	18.46	535.34	736	101	84479	417	544	184	141	76
4	63251	13.85	401.65	552	101	63251	282	407	150.8	104	62.4

Nonlinear Time History (NTH) analysis was performed using the OpenSees software package in which constitutive SMA material proposed by Fugazza [256] was used to model the flag-shape with zero secondary stiffness brace. Steel02 material with a strain hardening ratio of 0.5% [209] was selected from the OpenSees material library to model the BRB behaviour together with the corotational truss element to consider the nonlinear geometry. Furthermore, MinMax material was utilized to limit the BRBs ductility to 15 [209] in the plastic region. To adequately resemble the hysteresis behaviour of both systems in numerical modelling, calibration was carried out. A BRB brace was simulated and calibrated with the experimental results of specimen 99-1 from PEER Report 2002/8 [230] using far-field load protocol. Similarly, an SC-ZSB was modelled and calibrated using the experimental results provided in this paper. The resulted calibration for both brace components is illustrated in Figure 9.15.

As for modelling of the beams and columns, the nonlinear beam-column with the force-based formulation was used for modelling columns and beams with distributed plasticity. Also, a total number of 60 fibers (20 fibers for each flange and web) was implemented to model each elements cross-section. Here, the midspan imperfection of L/1000 was considered for all the columns to trigger the overall buckling and secondary effects. The Steel01 with strain hardening ratio of 2% was assumed to represent the bilinear hysteresis curve with kinematic hardening.

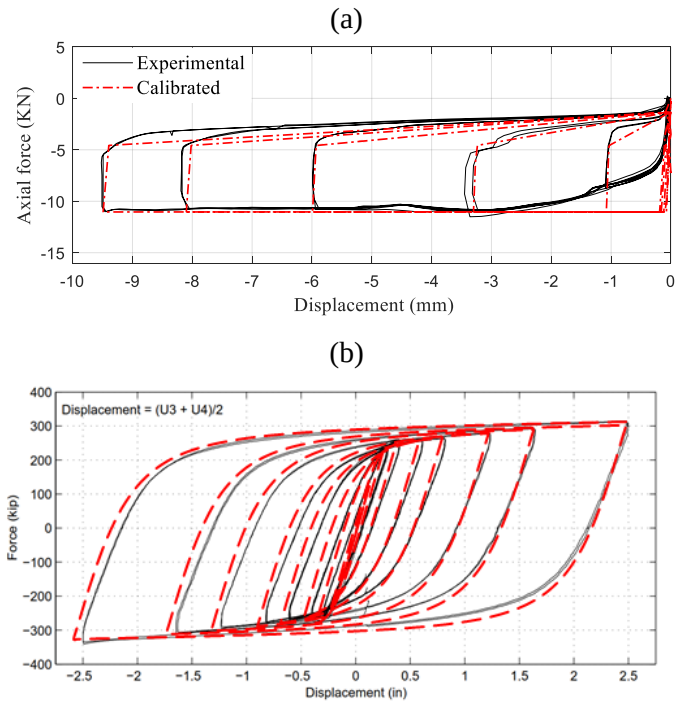

Figure 9.15: Calibration of brace modelling with experimental data (a) SC-ZSB brace, (b) BRB brace using results of [230, 257].

For the purpose of NTH, a suite of 10 ground motions (shown in Table 9.4) were selected and scaled to ULS (Ultimate Limit State) and MCE (Maximum Considerable) earthquake with respect to New Zealand code (NZS 1170.5) for which the associated target and mean spectrums are provided in Figure 9.16. The first three periods of the studied buildings were almost identical and were 0.53 s, 0.24 s and 0.16 s, respectively. These values were close to the modal analysis results of the original frame [223] and show the validity and accuracy of the modelling.

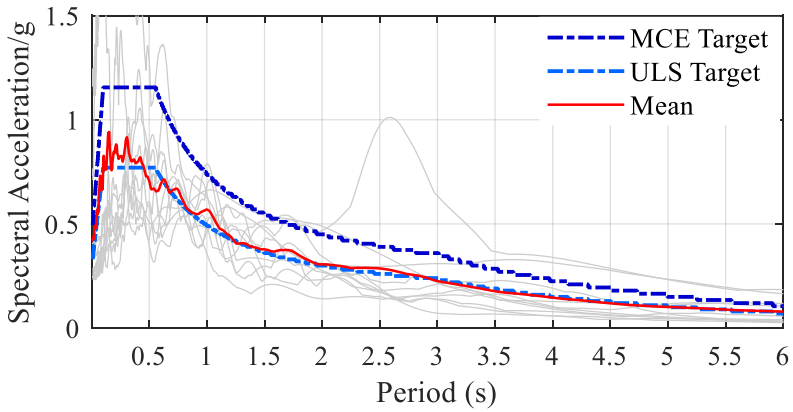

Figure 9.16: Target and mean spectrum of input earthquakes

Table 9.4: Selected ground motions for NTH

No.	Name	Magnitude	Fault Mechanism	Year	Scale Factor	Level
1	Chi Chi	7.62	Reverse Oblique	1999	0.6	ULS
2	Christchurch	6.3	Oblique	2011	1.65	ULS
3	Duzce	7.2	Strike-slip	1999	0.67	ULS
4	Hokkaido	8.3	Subduction	2003	0.89	ULS
5	Kaikoura	7.8	Strike-slip	2016	1	MCE
6	Kobe	6.9	Strike-slip	1995	0.85	ULS
7	Landers	7.28	Strike-slip	1992	0.98	ULS
8	LomaPrieta	6.93	Reverse Oblique	1989	0.93	ULS
9	Northridge	6.69	Reverse	1994	0.61	ULS
10	Kocaeli	7.5	Strike-slip	1999	0.78	ULS

9.7.2. *Results and Discussions*

Figure 9.17 presents the result of the NTH analysis performed in OpenSees. According to Figure 9.17.a and Figure 9.17.b, all the maximum inter-story drifts associated with two buildings were

less than 2.5%, the codified limit for the inter-story drift. Interestingly, it should be also noted that the mean story drifts associated with the building using SC-ZSBs were marginally higher than that of the BRB building. Generally, it was observed that the inter-story drifts were more influenced by the activation forces rather than the energy dissipation capacity (area enclosed in a hysteresis loop). Therefore, as the SC-ZSB braces had activation forces similar to those of BRBs (see Table 9.3), the associated inter-story drifts tended to be roughly the same. The maximum inter-story drifts (shown with green bar) were associated with the unscaled Kaikoura event, which was in fact the MCE event according to New Zealand code. As it can be observed, both buildings survived the MCE event and managed to keep the inter-story drift less than 2%.

Figure 9.17.c depicts the maximum residual inter-story drift for both studied structures. Here, it was presumed that if the residual drift is less than 0.15% after a major seismic event (average of 0.1% and 0.2 %, regarded in the literature [55, 56, 232], the building can stay functional and is considered as a low damage seismic resisting system (if and only if there is a reusable or replaceable damping resource). In the second case, if the residual displacement is limited between 0.15 and 0.5%, the buildings can be cited as repairable; however, the repair time and cost should be taken into consideration. Lastly, if the residual drift exceeds 0.5%, the option of demolishing and rebuilding would be more economical as compared to that of realignment and repair [55, 232]. Thus, for all of the events, the building using SC-ZSB was able to keep the residual drift to the least possible (almost zero). Moreover, as it had a reusable damping mechanism, it could be cited as a damage-free system in terms of the structural system. However, the BRB building was regarded as non-repairable (residual drifts were more than 0.5%) for the MCE event, needed to be repaired for 4 ULS events, and could be reoccupied immediately for 5 ULS events. These results attempt to confirm the previous findings of scholars such as [55] in which the residual drift was reported to be concerning for buildings where BRBs are used.

Figure 9.18.a and Figure 9.18.b describes the base shear versus roof displacement of both structures subjected to Chi-Chi and Christchurch earthquakes. The nonlinear behaviour in the BRB building was coming from the yielding of the steel core while in SC-ZSB building, it was coming from the nonlinear elastic buckling of the brace coupled with friction damping. As it can be noticed, although the SC-ZSB building had considerably less capability (almost half) to damp the earthquake energy (area enclosed in hysteresis loop), the displacement demands were almost the same for the two structures, which can be attributed to having the same activation strength.

(a)

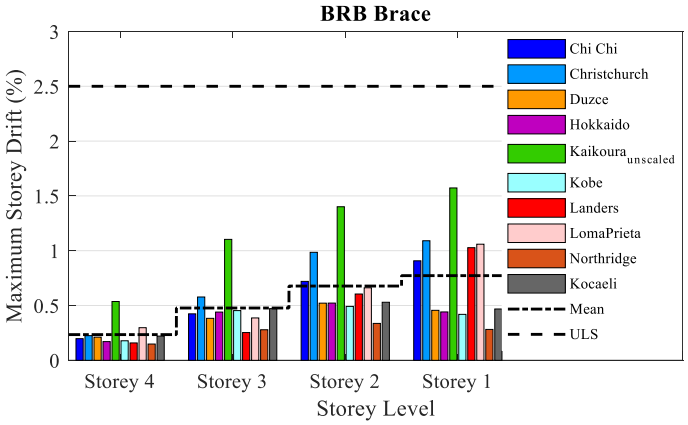

(b)

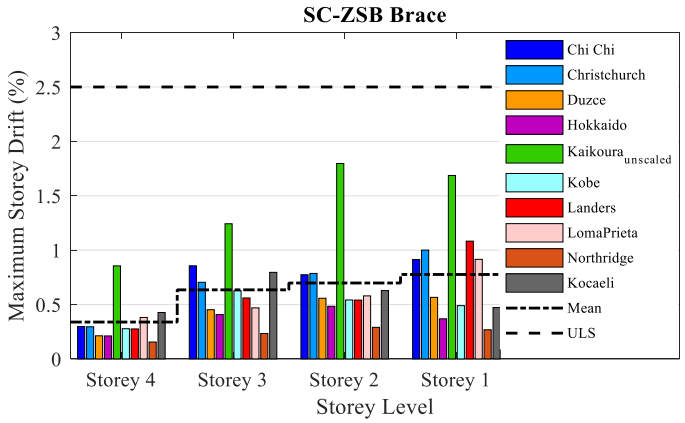

(c)

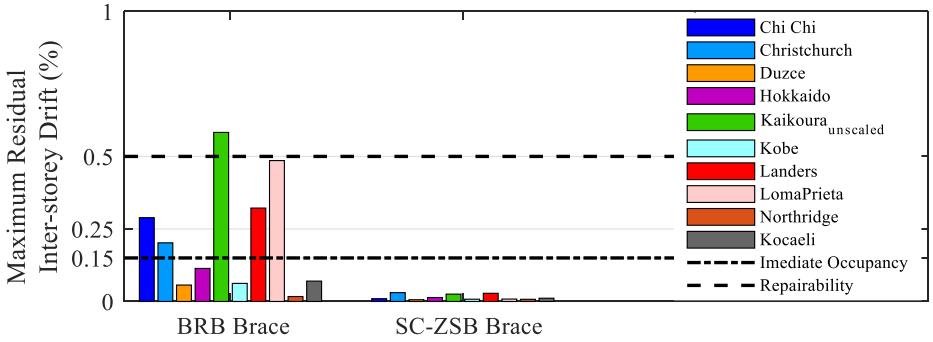

Figure 9.17: Results of NTH analysis: (a) inter-storey drift for BRB building, (b) inter-storey drift for SC-ZSB building, (c) Maximum residual inter-storey drift

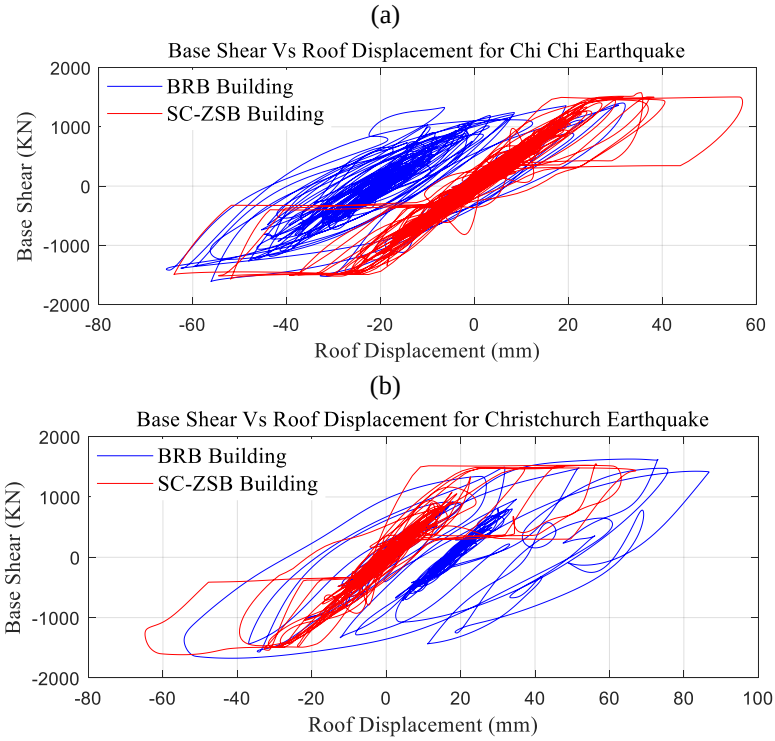

Figure 9.18: Base shear vs roof displacement: (a) Chi-Chi earthquake, (b) Christchurch earthquake

Figure 9.19 shows the maximum base shear that each building experienced during different seismic events. The following results are discussed based on the premise that both buildings had equal initial stiffness and activation force. Building with SC-ZSB brace had lower base shear for nearly all of the events while on average it had the same level of base shear force as compared to that of the one with BRBs. The lower base shear for SC-ZSB, although it was negligible, can be attributed to the absolute zero secondary stiffness, which was around 0.5% for BRB. Less deviation from the average base shear was observed for building with SC-ZSB, which similarly can be attributed to the zero-secondary stiffness. In other words, the building with SC-ZSB was experiencing the same base shear after activation of all SC-ZSB braces regardless of the displacement demand while the building with BRB experienced higher base shear in case of larger displacement demand due to the positive secondary stiffness.

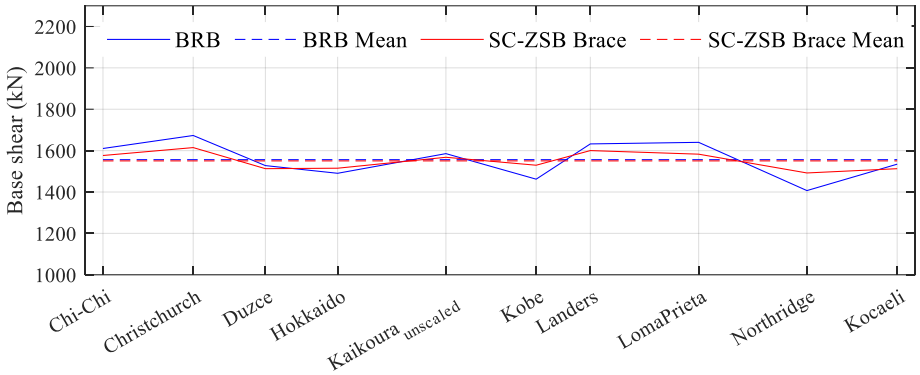

Figure 9.19: Maximum base shear for the two buildings subjected to input seismic events

9.8 Summary and Concluding Remarks

A new self-centring brace with zero post-elastic stiffness was introduced in this paper. The general concept is grounded in the combination of a flag-shape response and an additional stiffness neutralizer mechanism (SNM). Specifically, an SC brace using an RSFJ damper was used to offer the conventional flag-shape while the controlled damage-free elastic buckling was utilized to offer the SNM. The first and foremost privilege of achieving such a system is that the base shear can remain constant after activation of all seismic dampers similar to those LLRS with low secondary stiffness such as BRB. Secondly, as the system possesses flag-shape behaviour, the structure can benefit in terms of having no residual displacement and needing no post-event maintenance. The overall performance of the proposed system is similar to the conventional concentrically braced frames (CBFs), dissipating the earthquake energy through its post-buckling behaviour in compression, yet with the difference that the SC-ZSB brace does not have any strength and stiffness degradation and permanent deformation.

The first part of the paper introduced the axial and rotational performance of the utilized damper for the SC-ZSB brace and it was further discussed how it can be used in an SC-ZSB brace to form the targeted flag-shape with zero secondary stiffness. In the second part of the paper, the experimental program was described, and the performance of the brace was demonstrated through the testing of three configurations of a prototype SC-ZSB brace.

The last part of the paper included a comparative study to further illuminate the seismic performance of a prototype building using the proposed brace in comparison with a reference building using BRB. In the modelling procedure, both buildings were designed in a way to have identical initial stiffness and equal activation strength so that a reasonable debate on the effects of damping and secondary stiffness can be conducted. According to the numerical simulation, relatively identical base shears were observed for both buildings while the frame with the SC-ZSB

brace had the privilege of zero residual drift. Although SC-ZSB brace had both zero secondary stiffness and less damping capacity in comparison to BRB, its average displacement demand was almost identical to BRB frame. Such a system can be useful in practice where base shear and residual drift are not allowed to exceed a certain limit.

10 Conclusion

10.1 Abstract

This chapter delivers an overview of the materials that were discussed in previous chapters. Section 10.2 summarizes the main motivations and aims for the work as well as the methods used to achieve those aims. Moreover, it reviews the conclusions from each chapter in a way to show how it assisted to attain the overall objectives of the study. Based on the assumptions and variations that were presumed to meet the objectives of the study, section 10.3 provides key areas that need to be studied and investigated in future works on the topic.

10.2 Summary and concluding remarks

The main aim of the study was to investigate the feasibility of using the RSFJ dampers in concentrically braced frame structures. More specifically, it was intended to detect and discover the possible challenges in the common practice and design of this type of self-centring brace, thereby proposing a proper design guide for design engineers. In this regard, chapter 1 justified and illustrated the employment of low-damage construction, to which the RSFJ brace system belongs, and also discussed the different performance objectives that a low-damage system should meet. It was discussed that a low-damage design should address the whole structure rather than only the lateral load resisting system because a building with an intact lateral load resisting system but with a damaged gravity system or destroyed non-skeletal elements would be a complete economic loss for the owner given the high recovery costs associated. Section 1.3 and section 1.4 gave a literature review on the subject with the main focus on low-damage and self-centring braces and inelastic buckling load quantification, respectively. In the initial part of the chapter, some main characteristics of the seismic response of these systems were reviewed including the ductility demand, peak displacement, residual drift and peak floor acceleration. It was concluded that these low-damage systems normally tend to have the same seismic performance compared to the conventional systems though with less capability of damping. Then, the different types of self-centring braces and the different techniques that can be employed to make a brace re-centred were introduced and discussed. For example, a combination of pre-tensioned cables with different types of damping mechanisms (friction, viscous or yielding) can bring a flag-shape response. In

chapters 2 to 7, the behaviour of the RSFJ brace and its components were investigated while in chapters 8 and 9, the main focus was placed on the investigation of seismic performance of this new type of low-damage brace.

Chapter 2 introduced the RSFJ damper and illustrated its axial and rotational performances assuming that there is no interaction between them. Furthermore, it depicted an overview of how it would be employed in the brace application and what would be the possible failure modes. The failure modes for the RSFJ brace were discussed to be the local damper buckling and the global brace buckling. In this manner, chapter 3 discussed the buckling of the damper in in-plane and out-of-plane directions with respect to different boundary conditions. It was further discussed that the pin-pin end condition for the RSFJ damper is the worst case in terms of being vulnerable to second-order action and having a deteriorated performance in compression. Furthermore, it was concluded that the RSFJ must be installed with a fix-fix end condition for brace applications and pin-fix or fix-fix for any other applications that may be affected by second-order actions. The global elastic buckling of the brace was investigated in chapter 4. It was shown that the global buckling of the RSFJ might be of the elastic type with a very low magnitude of compressive force when there is no ABT to resist against the $p-\Delta$ effect. This was rooted in the rotational flexibility of the RSFJ damper. As for the solution to tackle this problem, a telescopic configuration called Anti-buckling tubes (ABTs) were recommended and tested. Chapter 5 presented the method – simplified collapse mechanism or SCMA – through which the inelastic buckling (ultimate strength) of the RSFJ self-centring brace could be quantified. This load was, in fact, the maximum theoretical design load. In this chapter, a closed-form formulation combined with experimental validation were also provided based on which the failure mode of the brace could be also detected. Two parametric finite element studies were performed in chapter 6 based on which design recommendations were made regarding the possible modification on the ultimate strength based on the relative rigidity of ABTs to brace body. Three practical numerical examples concerning the design of RSFJ braces were provided in chapter 7 in which the design of different components of the brace is also discussed with different types of RSFJ brace configurations (brace with either one or two weakened locations for damper installation).

The seismic performance of a prototype four-story building equipped with RSFJ timber braces was studied in chapter 8 as compared to that of the same building equipped with either Buckling-Restrained Brace (BRB) or conventional timber brace with rivet connections. Based on the finding of the study, it was concluded that the building with RSFJ could have less base shear because the dampers could be activated sooner than the yielding point of the BRBs. Furthermore, because of having a recentring ability, there was no residual drift at the end of seismic events while there were considerable residual drifts in the buildings with BRBs. In the study, it was shown that the conventional timber brace did not have residual drift concern because of the pinching behaviour

while it was severely affected in terms of stiffness and strength degradation. The main demerit of these buildings was the lack of strength and stiffness at the end of seismic events.

A new type of flag-shape resulting from a new type of mechanism was introduced and discussed in chapter 9. In this chapter, the elastic buckling of a brace was employed in combination with conventional friction damping and pre-pressed disc springs so as to form a flag-shape behaviour that has zero tangent stiffness after activation. The observed performance was similar to the conventional bilinear elasto-plastic behaviour with the major difference that it re-centred after the unloading. The seismic performance of a building equipped with such a self-centring brace was also studied in this chapter.

10.3 Future works

The present study validates a new type of self-centring brace, which can be used in timber, steel and concrete structures. The main focus was put on detecting the different potential failure modes of the brace in compression. As a part of the proposed design guide, a closed-form formulation was suggested to predict the elastic and inelastic capacities of the brace for which experimental tests have been performed. In this process, a series of assumptions have been made and some variations have been ignored. The potential open areas for further investigation for future studies are as follows:

- The rotational performance of the RSFJ in in-plane and out-of-plane was investigated numerically and analytically in chapter 2. Experimental validation is recommended to confirm the performance with respect to different end conditions.
- The torsional performance related to the torsional degree of freedom and torsional buckling of the RSFJ was ignored in the study. Though to the best knowledge of the author, it was not observed in any of the testing programs so far, it is highly recommended to be investigated in future studies.
- In chapter 3, it was discussed that a minimum imperfection is needed so that the RSFJ with pin-pin end condition to be adversely affected by the second-order actions (SOE). This was qualitatively studied for one type of joint and it was concluded that the in-plane direction is more prone to SOE. An extensive experimental program and finite element validation are recommended to quantify this imperfection and the limitation on the use of RSFJ with pin-pin ends.

- In chapters 4 and 5, a model composed of a nonlinear rotational spring(s) was proposed for the braces with one or two weakened locations by which the elastic buckling load of the system would be approximated. The method involved solving a nonlinear trigonometric equation and might be troublesome for office engineers. It is recommended for future studies to come up with an accurate model but with less computational effort.

- In chapters 4 and 5, it was assumed that the end condition of the brace is a real pin in-plane while in reality, it might be installed with bolted or welded connection as well. These connections cannot be assumed as the real pin either in- or out-of-plane mainly because they have the ability to transfer moment. This will not only increase the elastic buckling capacity of the brace but also bring the strength curve of the system up, thereby increasing the ultimate strength. This effect was conservatively ignored in the study and needs to be further investigated and properly quantified.

- In chapter 4 and 5, the effect of the gusset plate on the performance of the system was ignored. The main difference between the design of the gusset plate in the proposed system and the conventional concentrically braced frame is that the gusset plate here should be designed for the factored ultimate load while it is usually designed for the reduced load (by response modification factor or ductility) in the conventional systems. In another word, in the conventional systems, the gusset is supposed to buckle inelastically in the out-of-plane and assist the brace to provide the required damping. However, in the presented system, the gusset plate should remain elastic until reaching the factored strength. Therefore, the possible effect of the extra stiffness of the gusset plate in the out-of-plane direction is recommended to be studied.

In this respect, another open area in terms of the interaction of the brace performance with the gusset plate is the drift in the out-of-plane. The out-of-plane drift of the frame may transfer a moment action through the brace and decrease the strength of the system. Although it can be discussed that the maximum out-of-plane drift may not occur at the maximum in-plane drift, the performance of the brace in different amounts of out-of-plane drifts is recommended to be investigated (bi-directional loading of the brace similar to).

- In chapters 4 and 5, the steel and timber brace were tested in the absence of the embracing frame. For future studies, it is recommended to test the whole frame subassembly so that the effect of frame connection and gusset in-plane stiffness are all included especially in large lateral drifts.

- In chapter 5, the destructive testing was designed in a way that the failure mode is based on mode 1 because the dampers were not supposed to be sacrificed in the testing program. It is recommended for future studies to do a number of experimental studies in which mode 2 is governing.
- In chapter 6, the brace body and RSFJ section were assumed not to be changed during the modelling. It is recommended to extend this study to include different brace bodies (different slenderness) so that the effect of brace body slenderness if exists, to be further investigated.
- One of the main topics that should be covered in future studies is the quantification of the seismic response modification factors based on FEMA P695 [258]. By having the right response modification factor, an engineer can design the structure without a need to perform nonlinear time history analysis, thereby speeding up the process of design.
- In chapters 8 and 9, the seismic performance of the structure was investigated only for a 4-story prototype building and in a way that the damper is installed in all storey braces. Firstly, it is recommended for the study to be extended to include 8- and 12- and 16-story cases and the effectiveness of the system to be examined for buildings with different fundamental periods. Secondly, it is recommended that the optimized places for damper installation (in terms of defining which stories) and the least number of dampers be identified.
- Given the results shown in chapter 8, a feasibility study and experimental program are recommended to be done in terms of retrofitting a building having conventional timber braces with self-centring timber braces. More specifically, the conventional timber braces can be cut at the end conditions and then the damper can be installed and attached to the brace in-situ. The same study is recommended to be performed for the conventional steel braces especially the ones with X-configuration mainly because they are the most frequently used in the industry. [17, 258].
- In chapter 9, a new self-centring flag-shape performance was developed that had zero post-activation stiffness. This behaviour was developed for a self-centring bracing lateral load resisting system. For future works, it is recommended that a similar concept be developed for rocking shear walls where the damper itself can buckle and show a zero-stiffness flag-shape. Such performance was observed for the RSFJ damper in section 3.1.1 (Figure 3.9).

11 References

1. Bruneau, M., S.E. Chang, R.T. Eguchi, G.C. Lee, T.D. O'Rourke, A.M. Reinhorn, M. Shinozuka, K. Tierney, W.A. Wallace, and D. Von Winterfeldt, A framework to quantitatively assess and enhance the seismic resilience of communities. Earthquake spectra, 2003. 19(4): p. 733-752.

2. Wachtendorf, T., K.J. Tierney, K. Kompanik, and R. Connell, Disaster Resistant Communities Initiative: Assessment Of The Pilot Phase-Year 3. 2002.

3. Riad, J.K., T. Wachtendorf, K.J. Tierney, and J.M. Nigg, Disaster Resistant Communities Initiative: Evaluation Of The Pilot Phase. Year 2. 2000.

4. Blume, J.A., N.M. Newmark, and L.H. Corning, Design of multistory reinforced concrete buildings for earthquake motions. Vol. 4. 1961: Portland Cement Association Chicago.

5. Fardis, M.N., Capacity design: early history. Earthquake Engineering & Structural Dynamics, 2018. 47(14): p. 2887-2896.

6. Pauly, T., Deterministic design procedures for earthquake resisting ductile reinforced concrete buildings. Journal of Building Structures, 1983. 4(4): p. 12-23.

7. Commission, C.E.R., Final Report-Volume 3-Low-Damage Building Technologies. Christchurch, New Zealand, 2012.

8. Bruneau, M. and G. MacRae, Building Structural Systems in Christchurch's Post-Earthquake Reconstruction. Earthquake Spectra, 2019. 35(4): p. 1953-1978.

9. MacRae, G.A., G.C. Clifton, and M. Bruneau. New Zealand research applications of, and developments in, low damage technology for steel structures. in Key Engineering Materials. 2018. Trans Tech Publ.

10. Mansour, N., C. Christopoulos, and R. Tremblay, Experimental validation of replaceable shear links for eccentrically braced steel frames. Journal of Structural Engineering, 2011. 137(10): p. 1141-1152.

11. Volynkin-Ewens, D., G.C. Clifton, and P. Dusicka. Experimental Testing and Design of High Performance Shear Links for Eccentrically Braced Frames. in Key Engineering Materials. 2018. Trans Tech Publ.

12. Miller, D.J., L.A. Fahnestock, and M.R. Eatherton, Development and experimental validation of a nickel–titanium shape memory alloy self-centering buckling-restrained brace. Engineering Structures, 2012. 40: p. 288-298.

13. Ramhormozian, S., G.C. Clifton, G.A. MacRae, and H.H. Khoo. The Sliding Hinge Joint: Final Steps towards an Optimum Low Damage Seismic-Resistant Steel System. in Key Engineering Materials. 2018. Trans Tech Publ.

14. Cook, J., G.W. Rodgers, and G.A. MacRae, Design and Testing of Ratcheting, Tension-Only Devices for Seismic Energy Dissipation Systems. Journal of Earthquake Engineering, 2020. 24(2): p. 328-349.

15. Buchanan, A., A. Iqbal, A. Palermo, and S. Pampanin. Improved seismic performance of LVL post-tensioned walls coupled with UFP devices. in Proceedings of the 8th Pacific Conference on Earthquake Engineering. 2007.

16. Chan, N., A. Hashemi, P. Zarnani, and P. Quenneville, Pinching-Free Connector for Timber Structures. Journal of Structural Engineering, 2021. 147(5): p. 04021036.

17. Chancellor, N.B., M.R. Eatherton, D.A. Roke, and T. Akbaş, Self-centering seismic lateral force resisting systems: High performance structures for the city of tomorrow. Buildings, 2014. 4(3): p. 520-548.

18. Granello, G., A. Palermo, S. Pampanin, S. Pei, and J. Van De Lindt, Pres-lam buildings: state-of-the-art. Journal of Structural Engineering, 2020. 146(6): p. 04020085.

19. Zhong, C. and C. Christopoulos, Self-centering seismic-resistant structures: Historical overview and state-of-the-art. Earthquake Spectra, 2021: p. 87552930211057581.

20. Mander, J.B., Beyond ductility. Bulletin of the New Zealand Society for Earthquake Engineering, 2004. 37(1): p. 35-44.

21. Li, L., J.B. Mander, and R.P. Dhakal, Bidirectional cyclic loading experiment on a 3D beam–column joint designed for damage avoidance. Journal of Structural Engineering, 2008. 134(11): p. 1733-1742.

22. Uang, C.-M. and M. Bruneau, Closure to "State-of-the-Art Review on Seismic Design of Steel Structures" by Chia-Ming Uang and Michel Bruneau. Journal of Structural Engineering, 2019. 145(5): p. 07019002.

23. Mander, J.B. and C.-T. Cheng, Seismic resistance of bridge piers based on damage avoidance design, in Seismic resistance of bridge piers based on damage avoidance design. 1997. p. 109-109.

24. Bradley, B.A., R.P. Dhakal, J.B. Mander, and L. Li, Experimental multi-level seismic performance assessment of 3D RC frame designed for damage avoidance. Earthquake Engineering & Structural Dynamics, 2008. 37(1): p. 1-20.

25. Mander, T.J., G.W. Rodgers, J.G. Chase, J.B. Mander, G.A. MacRae, and R.P. Dhakal, Damage avoidance design steel beam-column moment connection using high-force-to-volume dissipators. Journal of structural engineering, 2009. 135(11): p. 1390-1397.

26. Borzouie, J., G. MacRae, J. Chase, G. Rodgers, and G. Clifton, Experimental studies on cyclic performance of column base strong axis–aligned asymmetric friction connections. Journal of Structural Engineering, 2016. 142(1): p. 04015078.

27. Hare, J., S. Oliver, and B. Galloway. Performance objectives for low damage seismic design of buildings. in NZSEE conference, Christchurch. 2012.

28. Wiebe, L., Design and construction of controlled rocking steel braced frames in New Zealand, in Improving the Seismic Performance of Existing Buildings and Other Structures 2015, R. Leon, Editor. 2015. p. 810-821.

29. Steele, T.C. and L.D. Wiebe, Large-scale experimental testing and numerical modeling of floor-to-frame connections for controlled rocking steel braced frames. Journal of Structural Engineering, 2020. 146(8): p. 04020163.

30. Zaboli, B., G. Clifton, and K. Cowie, Out-of-plane stability of gusset plates using a simplified notional load yield line method, in NZSEE Annual Technical Conference. 2017: Wellington, New Zealand.

31. Takeuchi, T., H. Ozaki, R. Matsui, and F. Sutcu, Out-of-plane stability of buckling-restrained braces including moment transfer capacity. Earthquake Engineering & Structural Dynamics, 2014. 43(6): p. 851-869.

32. Takeuchi, T., R. Matsui, and S. Mihara, Out-of-plane stability assessment of buckling-restrained braces including connections with chevron configuration. Earthquake Engineering & Structural Dynamics, 2016. 45(12): p. 1895-1917.

33. Ramirez, C.M. and E. Miranda, Significance of residual drifts in building earthquake loss estimation. Earthquake Engineering & Structural Dynamics, 2012. 41(11): p. 1477-1493.

34. McCormick, J., H. Aburano, M. Ikenaga, and M. Nakashima. Permissible residual deformation levels for building structures considering both safety and human elements. in Proceedings of the 14th world conference on earthquake engineering. 2008. Wcee.

35. Eatherton, M.R. and J.F. Hajjar, Residual drifts of self-centering systems including effects of ambient building resistance. Earthquake Spectra, 2011. 27(3): p. 719-744.

36. Kazantzi, A., D. Vamvatsikos, and E. Miranda, The effect of damping on floor spectral accelerations as inferred from instrumented buildings. Bulletin of Earthquake Engineering, 2020. 18(5): p. 2149-2164.

37. Miranda, E. and S. Taghavi, Approximate floor acceleration demands in multistory buildings. I: Formulation. Journal of structural engineering, 2005. 131(2): p. 203-211.

38. Taghavi, S. and E. Miranda, Approximate floor acceleration demands in multistory buildings. II: Applications. Journal of Structural Engineering, 2005. 131(2): p. 212-220.

39. Dhakal, R.P., Damage to non-structural components and contents in 2010 Darfield earthquake. Bulletin of the New Zealand Society for Earthquake Engineering, 2010. 43(4): p. 404-411.

40. Dhakal, R.P., G.A. MacRae, and K. Hogg, Performance of ceilings in the February 2011 Christchurch earthquake. 2011.

41. Yan, Z., G. MacRae, R. Dhakal, H. Bagheri, C. Clifton, P. Quenneville, S. Ramhormozian, X. Zhao, L. Jia, and P. Xiang, Shaking table test of a near full scale low damage structural steel building: structural aspects. 2019.

42. Vu, K.A.T. and M.G. Stewart, Structural reliability of concrete bridges including improved chloride-induced corrosion models. Structural safety, 2000. 22(4): p. 313-333.

43. Stewart, M.G. and D.V. Rosowsky, Time-dependent reliability of deteriorating reinforced concrete bridge decks. Structural safety, 1998. 20(1): p. 91-109.

44. Peng, L. and M.G. Stewart, Climate change and corrosion damage risks for reinforced concrete infrastructure in China. Structure and Infrastructure Engineering, 2016. 12(4): p. 499-516.

45. Granello, G., C. Leyder, A. Palermo, A. Frangi, and S. Pampanin, Design approach to predict post-tensioning losses in post-tensioned timber frames. Journal of Structural Engineering, 2018. 144(8): p. 04018115.

46. Ataei, H. and K. Kalbasi Anaraki, A proposed structural design method considering fluid viscous damper degradations. The Structural Design of Tall and Special Buildings, 2018. 27(15): p. e1512.

47. Dyanati, M., Q. Huang, and D. Roke, Cost-benefit evaluation of self-centring concentrically braced frames considering uncertainties. Structure and Infrastructure Engineering, 2017. 13(5): p. 537-553.

48. Priestley, M.N. and J.R. Tao, Seismic response of precast prestressed concrete frames with partially debonded tendons. PCI journal, 1993. 38(1): p. 58-69.

49. Priestley, M.N., Overview of PRESSS research program. PCI journal, 1991. 36(4): p. 50-57.

50. Priestley, M.N. and G.A. MacRae, Seismic tests of precast beam-to-column joint subassemblages with unbonded tendons. PCI journal, 1996. 41(1): p. 64-81.

51. Priestley, M.N., S. Sritharan, J.R. Conley, and S. Pampanin, Preliminary results and conclusions from the PRESSS five-story precast concrete test building. PCI journal, 1999. 44(6): p. 42-67.

52. Christopoulos, C., A. Filiatrault, and B. Folz, Seismic response of self-centring hysteretic SDOF systems. Earthquake engineering & structural dynamics, 2002. 31(5).

53. Seo, C.-Y. and R. Sause, Ductility demands on self-centering systems under earthquake loading. ACI Structural Journal, 2005. 102(2): p. 275.

54. Yousef-beik, S.M.M., S. Veismoradi, P. Zarnani, and P. Quenneville, A new self-centering brace with zero secondary stiffness using elastic buckling. Journal of Constructional Steel Research, 2020. 169: p. 106035.

55. Erochko, J., C. Christopoulos, R. Tremblay, and H. Choi, Residual drift response of SMRFs and BRB frames in steel buildings designed according to ASCE 7-05. Journal of Structural Engineering, 2010. 137(5): p. 589-599.

56. Clifton, G., M. Bruneau, G. MacRae, R. Leon, and A. Fussell, Multistorey steel framed building damage from the Christchurch earthquake series of 2010/2011. Behaviour of Steel Structures in Seismic Areas: STESSA 2012, 2012: p. 15.

57. Rad, A.A., G.A. MacRae, T.Z. Yeow, and D.K. Bull, Seismic behavior of steel buildings with out-of-plumb. Earthquake Engineering & Structural Dynamics, 2015. 44(14): p. 2575-2588.

58. Miranda, E., A. Kazantzi, and D. Vamvatsikos. New approach to the design of acceleration-sensitive non-structural elements in buildings. in 16th European Conference on Earthquake Engineering. 2018.

59. Rodriguez, M.E., J.I. Restrepo, and J.J. Blandón, Seismic design forces for rigid floor diaphragms in precast concrete building structures. Journal of structural engineering, 2007. 133(11): p. 1604-1615.

60. Tremblay, R., M. Lacerte, and C. Christopoulos, Seismic response of multistory buildings with self-centering energy dissipative steel braces. Journal of structural engineering, 2008. 134(1): p. 108-120.

61. Wiebe, L. and C. Christopoulos, Mitigation of higher mode effects in base-rocking systems by using multiple rocking sections. Journal of Earthquake Engineering, 2009. 13(S1): p. 83-108.

62. Wiebe, L., C. Christopoulos, R. Tremblay, and M. Leclerc, Mechanisms to limit higher mode effects in a controlled rocking steel frame. 1: Concept, modelling, and low-amplitude shake table testing. Earthquake Engineering & Structural Dynamics, 2013. 42(7): p. 1053-1068.

63. Erochko, J., C. Christopoulos, R. Tremblay, and H.J. Kim, Shake table testing and numerical simulation of a self-centering energy dissipative braced frame. Earthquake engineering & structural dynamics, 2013. 42(11): p. 1617-1635.

64. Wiebe, L. and C. Christopoulos, Characterizing acceleration spikes due to stiffness changes in nonlinear systems. Earthquake engineering & structural dynamics, 2010. 39(14): p. 1653-1670.

65. Wiebe, L. and C. Christopoulos, Using Bézier curves to model gradual stiffness transitions in nonlinear elements: Application to self-centering systems. Earthquake Engineering & Structural Dynamics, 2011. 40(14): p. 1535-1552.

66. Eatherton, M.R., Large-scale cyclic and hybrid simulation testing and development of a controlled-rocking steel building system with replaceable fuses. 2010: University of Illinois at Urbana-Champaign.

67. Tremblay, R., L. Poirier, N. Bouaanani, M. Leclerc, V. Rene, L. Fronteddu, and S. Rivest. Innovative viscously damped rocking braced steel frames. in Proceedings of the 14th world conference on earthquake engineering, Beijing, China. 2008.

68. Wiebe, L. and C. Christopoulos, Performance-based seismic design of controlled rocking steel braced frames. I: Methodological framework and design of base rocking joint. Journal of Structural Engineering, 2015. 141(9): p. 04014226.

69. Eatherton, M., J. Hajjar, G. Deierlein, H. Krawinkler, S. Billington, and X. Ma. Controlled rocking of steel-framed buildings with replaceable energy-dissipating fuses. in Proceedings of the 14th world conference on earthquake engineering. 2008.

70. Deierlein, G., H. Krawinkler, X. Ma, M. Eatherton, J. Hajjar, T. Takeuchi, K. Kasai, and M. Midorikawa, Earthquake resilient steel braced frames with controlled rocking and energy dissipating fuses. Steel Construction, 2011. 4(3): p. 171-175.

71. Wiebe, L. and C. Christopoulos, Performance-based seismic design of controlled rocking steel braced frames. II: Design of capacity-protected elements. Journal of Structural Engineering, 2015. 141(9): p. 04014227.

72. Martin, A., G.G. Deierlein, and X. Ma, Capacity design procedure for rocking braced frames using modified modal superposition method. Journal of Structural Engineering, 2019. 145(6): p. 04019041.

73. Steele, T.C. and L.D. Wiebe, Dynamic and equivalent static procedures for capacity design of controlled rocking steel braced frames. Earthquake Engineering & Structural Dynamics, 2016. 45(14): p. 2349-2369.

74. Rahgozar, N. and N. Rahgozar, Extension of direct displacement-based design for quantifying higher mode effects on controlled rocking steel cores. The Structural Design of Tall and Special Buildings, 2020. 29(16): p. e1800.

75. Kibriya, L., C. Málaga-Chuquitaype, and M. Kashani, Buckling-enabled composite bracing for damage-avoidance rocking structures. International Journal of Mechanical Sciences, 2020. 170: p. 105359.

76. Yim, C.S., A.K. Chopra, and J. Penzien, Rocking response of rigid blocks to earthquakes. Earthquake Engineering & Structural Dynamics, 1980. 8(6): p. 565-587.

77. Christopoulos, C., R. Tremblay, H.-J. Kim, and M. Lacerte, Self-centering energy dissipative bracing system for the seismic resistance of structures: development and validation. Journal of structural engineering, 2008. 134(1): p. 96-107.

78. Erochko, J., C. Christopoulos, and R. Tremblay, Design and testing of an enhanced-elongation telescoping self-centering energy-dissipative brace. Journal of Structural Engineering, 2014. 141(6): p. 04014163.

79. Erochko, J., C. Christopoulos, and R. Tremblay, Design, testing, and detailed component modeling of a high-capacity self-centering energy-dissipative brace. Journal of Structural Engineering, 2014. 141(8): p. 04014193.

80. Ping, Y., C. Fang, Y. Chen, and M.C. Yam, Seismic robustness of self-centering braced frames suffering tendon failure. Earthquake Engineering & Structural Dynamics, 2021.

81. Erochko, J., C. Christopoulos, and R. Tremblay, Design and testing of an enhanced-elongation telescoping self-centering energy-dissipative brace. Journal of Structural Engineering, 2015. 141(6): p. 04014163.

82. Baker, J.W., Quantitative classification of near-fault ground motions using wavelet analysis. Bulletin of the Seismological Society of America, 2007. 97(5): p. 1486-1501.

83. Qing, Y., C.-L. Wang, Z. Zhou, and B. Zeng, Seismic responses of multistory buildings with self-centering buckling-restrained braces: Influence of the pretension force. Engineering Structures, 2021. 238: p. 112249.

84. Somerville, P.G., Development of ground motion time histories for phase 2 of the FEMA/SAC steel project. 1997: SAC Joint Venture.

85. Eatherton, M.R., L.A. Fahnestock, and D.J. Miller, Computational study of self-centering buckling-restrained braced frame seismic performance. Earthquake engineering & structural dynamics, 2014. 43(13): p. 1897-1914.

86. McCormick, J., R. DesRoches, D. Fugazza, and F. Auricchio, Seismic assessment of concentrically braced steel frames with shape memory alloy braces. Journal of Structural Engineering, 2007. 133(6): p. 862-870.

87. Sabelli, R., Research on improving the design and analysis of earthquake-resistant steel-braced frames. 2001: EERI Oakland.

88. Zhu, S. and Y. Zhang, Seismic analysis of concentrically braced frame systems with self-centering friction damping braces. Journal of Structural Engineering, 2008. 134(1): p. 121-131.

89. Zhu, S. and Y. Zhang, Seismic behaviour of self-centring braced frame buildings with reusable hysteretic damping brace. Earthquake engineering & structural dynamics, 2007. 36(10): p. 1329-1346.

90. Qiu, C. and X. Du, Seismic performance of multistory CBFs with novel recentering energy dissipative braces. Journal of Constructional Steel Research, 2019: p. 105864.

91. Qiu, C., H. Wang, J. Liu, J. Qi, and Y. Wang, Experimental tests and finite element simulations of a new SMA-steel damper. Smart Materials and Structures, 2020. 29(3): p. 035016.

92. Huang, H., F. Zhang, W. Zhang, M. Guo, S. Urushadze, and G. Wu, Numerical analysis of self-centering energy dissipation brace with arc steel plate for seismic resistance. Soil Dynamics and Earthquake Engineering, 2019. 125: p. 105751.

93. Xu, L., S. Yao, and Y. Sun, Development and validation tests of an assembly self-centering energy dissipation brace. Soil Dynamics and Earthquake Engineering, 2019. 116: p. 120-129.

94. Xu, L.-H., X.-S. Xie, S.-Q. Yao, and Z.-X. Li, Hysteretic behavior and failure mechanism of an assembled self-centering brace. Bulletin of Earthquake Engineering, 2019. 17(6): p. 3573-3592.

95. Xu, L., X. Fan, and Z. Li, Experimental behavior and analysis of self-centering steel brace with pre-pressed disc springs. Journal of Constructional Steel Research, 2017. 139: p. 363-373.

96. Issa, A.S. and M.S. Alam, Experimental and numerical study on the seismic performance of a self-centering bracing system using closed-loop dynamic (CLD) testing. Engineering Structures, 2019. 195: p. 144-158.

97. Wang, W., C. Fang, Y. Zhao, R. Sause, S. Hu, and J. Ricles, Self-centering friction spring dampers for seismic resilience. Earthquake Engineering & Structural Dynamics, 2019. 48(9): p. 1045-1065.

98. Yousef-beik, S.M.M., H. Bagheri, S. Veismoradi, P. Zarnani, A. Hashemi, and P. Quenneville, Seismic performance improvement of conventional timber brace using re-centring friction connection. Structures, 2020. 26: p. 958-968.

99. Hashemi, A., S.M.M. Yousef-Beik, F.M. Darani, G.C. Clifton, P. Zarnani, and P. Quenneville, Seismic performance of a damage avoidance self-centring brace with collapse prevention mechanism. Journal of Constructional Steel Research, 2019. 155: p. 273-285.

100. Issa, A.S. and M.S. Alam, Seismic performance of a novel single and double spring-based piston bracing. Journal of Structural Engineering, 2019. 145(2): p. 04018261.

101. Hu, S., W. Wang, and B. Qu, Self-centering companion spines with friction spring dampers: Validation test and direct displacement-based design. Engineering Structures, 2021. 238: p. 112191.

102. Hu, S., W. Wang, B. Qu, and M.S. Alam, Self-centering energy-absorbing rocking core system with friction spring damper: Experiments, modeling and design. Engineering Structures, 2020. 225: p. 111338.

103. Hu, S., W. Wang, and B. Qu, Seismic evaluation of low-rise steel building frames with self-centering energy-absorbing rigid cores designed using a force-based approach. Engineering Structures, 2020. 204: p. 110038.

104. Hu, S., W. Wang, B. Qu, and M.S. Alam, Development and validation test of a novel Self-centering Energy-absorbing Dual Rocking Core (SEDRC) system for seismic resilience. Engineering Structures, 2020. 211: p. 110424.

105. Stevens, D. and L. Wiebe, Experimental testing of a replaceable brace module for seismically designed concentrically braced steel frames. Journal of Structural Engineering, 2019. 145(4): p. 04019012.

106. Tsai, C.-Y., K.-C. Tsai, P.-C. Lin, W.-H. Ao, C.W. Roeder, S.A. Mahin, C.-H. Lin, Y.-J. Yu, K.-J. Wang, and A.-C. Wu, Seismic design and hybrid tests of a full-scale three-story concentrically braced frame using in-plane buckling braces. Earthquake Spectra, 2013. 29(3): p. 1043-1067.

107. Roeder, C.W. and E.P. Popov, Eccentrically braced steel frames for earthquakes. Journal of the Structural Division, 1978. 104(3): p. 391-412.

108. ACI, A.C.I., Spall repair of horizontal concrete surfaces. 2005.

109. Leung, H.K., G.C. Clifton, H.H. Khoo, and G.A. MacRae. Experimental studies of eccentrically braced frame with rotational bolted active links. in 8th international conference on behavior of steel structures in seismic areas, Shanghai, China. 2015.

110. Ashikov, A., G. Clifton, and B. Belev. Finite element analysis of eccentrically braced frames with a new type of bolted replaceable active link. in New Zealand Society for Earthquake Engineering 2016 Conference. 2016.

111. Mago, N., K. Cowie, and G.C. Clifton. Finite Element Analysis of eccentrically braced frames with removable link. in Key Engineering Materials. 2018. Trans Tech Publ.

112. Grigorian, C.E., T.-S. Yang, and E.P. Popov, Slotted bolted connection energy dissipators. Earthquake Spectra, 1993. 9(3): p. 491-504.

113. Tremblay, R., Seismic behavior and design of friction concentrically braced frames for steel buildings. 1993, University of British Columbia.

114. Butterworth, J.W. Seismic response of moment-resisting steel frames containing dual-level friction dissipating joints. in Technical Conference, NZ Society for Earthquake Engineering. 1999.

115. Butterworth, J. and G. Clifton. Performance of hierarchical friction dissipating joints in moment resisting steel frames. in Proceedings of 12th World Conference on Earthquake Engineering. 2000.

116. Golondrino, J.C., R. Xie, G. MacRae, G. Chase, G. Rodgers, and C. Clifton. Low damage braces using Asymmetrical Friction Connections (AFC). in New Zealand Society for Earthquake Engineering 2014 Annual Conference. 2014.

117. Golondrino, C., R. Xie, G. MacRae, J. Chase, G. Rodgers, and C. Clifton, Low damage brace using a Symmetrical Friction Connection (SFC) detail. 2015.

118. Qu, B., X. Liu, H. Hou, C. Qiu, and D. Hu, Testing of buckling-restrained braces with replaceable steel angle fuses. Journal of Structural Engineering, 2018. 144(3): p. 04018001.

119. Engesser, F., OBER DIE KNICKFESTIGKEIT GERADER STABE (On the Buckling Strength of Straight Struts) Zeitschrift fur Architektur und Ingenieurwesen. 1889.

120. Galambos, T.V., Guide to stability design criteria for metal structures. 1998: John Wiley & Sons.

121. Ziemian, R.D., Guide to stability design criteria for metal structures. 2010: John Wiley & Sons.

122. Chajes, A., Principles of structural stability theory. 1974: Prentice Hall.

123. 360-16, A., AISC 360-16 Specification for Structural Steel Buildings 2016.

124. NZS 3404, S.S.S., NZS 3404: 1997 Part 1 and 2, in Standards New Zealand, Wellington. 2007.

125. Anderson, J.P. and J.H. Woodward, Calculation of effective lengths and effective slenderness ratios of stepped columns. Engineering Journal, 1972. 9(4): p. 157-66.

126. Timoshenko, S.P. and J.M. Gere, Theory of Elastic Stability, McGraw-Hill Book Company. New York, 1961.

127. Bažant, Z.P. and L. Cedolin, Stability of structures: elastic, inelastic, fracture and damage theories. 2010: World Scientific.

128. MacRae, G. and G. Clifton. NZ research on steel structures in seismic areas. in 8th International Conference on Behavior of Steel Structures in Seismic Areas, STESSA, Shanghai, China. 2015.

129. Lin, P.C., K.C. Tsai, K.J. Wang, Y.J. Yu, C.Y. Wei, A.C. Wu, C.Y. Tsai, C.H. Lin, J.C. Chen, and A.H. Schellenberg, Seismic design and hybrid tests of a full-scale three-story buckling-restrained braced frame using welded end connections and thin profile. Earthquake Engineering & Structural Dynamics, 2012. 41(5): p. 1001-1020.

130. Hikino, T., T. Okazaki, K. Kajiwara, and M. Nakashima, Out-of-plane stability of buckling-restrained braces placed in chevron arrangement. Journal of Structural Engineering, 2012. 139(11): p. 1812-1822.

131. Baktash, P., C. Marsh, and A. Pall, Seismic tests on a model shear wall with friction joints. Canadian Journal of Civil Engineering, 1983. 10(1): p. 52-59.

132. Pall, A.S., C. Marsh, and P. Fazio, Friction joints for seismic control of large panel structures. Journal of Prestressed Concrete Institute, 1980. 25(6): p. 38-61.

133. Popov, E.P., C.E. Grigorian, and T.-S. Yang, Developments in seismic structural analysis and design. Engineering structures, 1995. 17(3): p. 187-197.

134. Clifton, G.C., Semi-rigid joints for moment-resisting steel framed seismic-resisting systems. 2005, ResearchSpace@ Auckland.

135. Nims, D.K., P.J. Richter, and R.E. Bachman, The use of the energy dissipating restraint for seismic hazard mitigation. Earthquake Spectra, 1993. 9(3): p. 467-489.

136. Filiatrault, A., R. Tremblay, and R. Kar, Performance evaluation of friction spring seismic damper. Journal of Structural Engineering, 2000. 126(4): p. 491-499.

137. Zarnani, P. and P. Quenneville, Patent: A Resilient Slip Friction Joint - WO2016185432A1. 2015.

138. Zarnani, P., A. Valadbeigi, and P. Quenneville. Resilient slip friction (RSF) joint: A novel connection system for seismic damage avoidance design og timber structures. in World Conf. on Timber Engineering WCTE2014, Vienna Univ. of Technology, Vienna, Austria. 2016.

139. Hashemi, A., P. Zarnani, R. Masoudnia, and P. Quenneville, Experimental Testing of Rocking Cross-Laminated Timber Walls with Resilient Slip Friction Joints. Journal of Structural Engineering, 2017. 144(1): p. 04017180.

140. Amara, F., M. Bosco, E.M. Marino, and P.P. Rossi, An accurate strength amplification factor for the design of SDOF systems with P–Δ effects. Earthquake engineering & structural dynamics, 2014. 43(4): p. 589-611.

141. MacRae, G.A., P-Δ effects on single-degree-of-freedom structures in earthquakes. Earthquake spectra, 1994. 10(3): p. 539-568.

142. Vian, D., M. Sivaselvan, M. Bruneau, and A. Reinhorn, Analysis, testing and initial recommendations on collapse limit states of frames. Research Progress and Accomplishments (2000–2001) MCEER-01-SP01, 2001.

143. Vian, D. and M. Bruneau, Experimental investigation of P-Delta effects to collapse during earthquakes. 2001: Citeseer.

144. Gupta, A. and H. Krawinkler, Dynamic P-delta effects for flexible inelastic steel structures. Journal of Structural Engineering, 2000. 126(1): p. 145-154.

145. Ma, T. and L. Xu, Effects of column imperfections on capacity of steel frames in variable loading. Journal of Constructional Steel Research, 2020. 165: p. 105819.

146. Hikino, T., T. Okazaki, K. Kajiwara, and M. Nakashima, Out-of-plane stability of buckling-restrained braces placed in chevron arrangement. Journal of Structural Engineering, 2013. 139(11): p. 1812-1822.

147. Piluso, V. and G. Rizzano, Experimental analysis and modelling of bolted T-stubs under cyclic loads. Journal of Constructional Steel Research, 2008. 64(6): p. 655-669.

148. Latour, M., V. Piluso, and G. Rizzano, Experimental analysis of innovative dissipative bolted double split tee beam-to-column connections. Steel Construction, 2011. 4(2): p. 53-64.

149. Latour, M., V. Piluso, and G. Rizzano, Free from damage beam-to-column joints: Testing and design of DST connections with friction pads. Engineering Structures, 2015. 85: p. 219-233.

150. Francavilla, A.B., M. Latour, V. Piluso, and G. Rizzano, Design criteria for beam-to-column connections equipped with friction devices. Journal of Constructional Steel Research, 2020. 172: p. 106240.

151. Latour, M., M. D'Aniello, M. Zimbru, G. Rizzano, V. Piluso, and R. Landolfo, Removable friction dampers for low-damage steel beam-to-column joints. Soil Dynamics and Earthquake Engineering, 2018. 115: p. 66-81.

152. Jaisee, S., F. Yue, and Y.H. Ooi, A state-of-the-art review on passive friction dampers and their applications. Engineering Structures, 2021. 235: p. 112022.

153. Javidan, M.M. and J. Kim, Seismic Retrofit of Soft-First-Story Structures Using Rotational Friction Dampers. journal of structural engineering, 2019. 145(12): p. 04019162.

154. Javidan, M.M. and J. Kim, Experimental and numerical sensitivity assessment of viscoelasticity for polymer composite materials. Scientific reports, 2020. 10(1): p. 1-9.

155. Yousef-Beik, S.M.M., S. Veismoradi, P. Zarnani, P. Quenneville, and A. Hashemi, Self-centring bracing system: avoidance of elastic buckling for braces with one intermediate damper, in New Zealand Society of Earthquake Engineering. 2020: Wellington.

156. Yousef-Beik, S.M.M., P. Zarnani, F.M. Darani, A. Hashemi, and P. Quenneville. New seismic damage avoidant timber brace using innovative resilient slip friction joints for multi-story applications. in WCTE 2018 - World Conference on Timber Engineering. 2018.

157. Bagheri, H., A. Hashemi, S.M.M. Yousef-Beik, P. Zarnani, and P. Quenneville, New Self-Centering Tension-Only Brace Using Resilient Slip-Friction Joint: Experimental Tests and Numerical Analysis. Journal of Structural Engineering, 2020. 146(10): p. 04020219.

158. Bagheri, H., A. Hashemi, P. Zarnani, and P. Quenneville, The resilient slip friction joint tension-only brace beyond its ultimate level. Journal of Constructional Steel Research, 2020. 172: p. 106225.

159. Darani, F., P. Zarnani, E. Haemmerle, A. Hashemi, and P. Quenneville, Application of new resilient slip friction joint for seismic damage avoidance design of rocking concrete shear walls. 2018.

160. Hashemi, A., H. Bagheri, S.M.M. Yousef-Beik, F.M. Darani, A. Valadbeigi, P. Zarnani, and P. Quenneville, Enhanced Seismic Performance of Timber Structures Using

Resilient Connections: Full-Scale Testing and Design Procedure. Journal of Structural Engineering, 2020. 146(9): p. 04020180.

161. Sahami, K., P. Zarnani, and P. Quenneville, Introducing a low damage system incorporating rocking braced frame and resilient slip friction joint as a shear key. 2020.

162. Shabankareh, M., S. Veismoradi, P. Zarnani, and P. Quenneville, Seismic damage avoidance design of moment resisting frames with innovative resilient connection. 2020.

163. Hashemi, A., H. Bagheri, P. Quenneville, A. Van Houtte, M. Kemp, M. Newcombe, S.M.M. Yousef-Beik, and P. Zarnani, Developments and practical case studies for seismic resistant structures using Resilient Slip Friction Joints (RSFJs), in NZSEE. 2020: Auckland.

164. Yousef-beik, S.M.M., P. Zarnani, A. Hashemi, and P. Quenneville, Lateral Instability of Self-centring Braces: Buckling in loading and Unloading, in Pacific Conference on Earthquake Engineering. 2019: Auckland, New Zealand.

165. Yousef-beik, S.M.M., S. Veismoradi, P. Zarnani, A. Hashemi, and P. Quenneville, Experimental Study on Cyclic Performance of a Damage-Free Brace with Self-Centering Connection. Journal of Structural Engineering, 2021. 147(1): p. 04020299.

166. Christopoulos, C., A. Filiatrault, C.-M. Uang, and B. Folz, Posttensioned energy dissipating connections for moment-resisting steel frames. Journal of Structural Engineering, 2002. 128(9): p. 1111-1120.

167. Rojas, P., J. Ricles, and R. Sause, Seismic performance of post-tensioned steel moment resisting frames with friction devices. Journal of Structural Engineering, 2005. 131(4): p. 529-540.

168. Palermo, A., S. Pampanin, A. Buchanan, and M. Newcombe. Seismic design of multi-storey buildings using laminated veneer lumber (LVL). in NZSEE 2005 Conference. 2005. Wairakei, New Zealand.

169. Ramhormozian, S., G.C. Clifton, G.A. MacRae, G.P. Davet, and H.-H. Khoo, Experimental studies on Belleville springs use in the sliding hinge joint connection. Journal of Constructional Steel Research, 2019. 159: p. 81-94.

170. Wu, J. and B.M. Phillips, Passive self-centering hysteretic damping brace based on the elastic buckling mode jump mechanism of a capped column. Engineering Structures, 2017. 134: p. 276-288.

171. Pollino, M., Seismic design for enhanced building performance using rocking steel braced frames. Engineering Structures, 2015. 83: p. 129-139.

172. Javidan, M.M., M.S.E. Nasab, and J. Kim, Full-scale tests of two-story RC frames retrofitted with steel plate multi-slit dampers. Steel and Composite Structures, 2021. 39(5): p. 645-664.

173. Veismoradi, S., P. Zarnani, and P. Quenneville. Development of self-centring Rotational Slip Friction Joint: a novel damage-free damper with large deflections. in Pacific Conference on Earthquake Engineering (PCEE) and New Zealand Society for Earthquake Engineering (NZSEE), Auckland, New Zealand. 2019.

174. Wang, C., C. Wang, and J. Reddy, Exact solutions for buckling of structural members. CRC series in computational mechanics and applied analysis. 2005: CRC Press LLC, Boca Raton, FL.

175. Guide, M.U.s., The mathworks. Inc., Natick, MA, 1998. 5: p. 333.

176. Chen, W.F. and E.M. Lui, Structural stability: theory and implementation. 1987.

177. Zhang, A., Y. Zhang, A. Liu, D. Shao, and Q. Li, Performance study of self-centering steel frame with intermediate columns containing friction dampers. Engineering Structures, 2019. 186: p. 382-398.

178. Issa, A.S. and M.S. Alam, Seismic Performance of a Novel Single and Double Spring-Based Piston Bracing. Journal of Structural Engineering, 2018. 145(2): p. 04018261.

179. Hadad, A.A., B.M. Shahrooz, and P.J. Fortney, Innovative resilient steel braced frame with Belleville disk and shape memory alloy assemblies. Engineering Structures, 2021. 237: p. 112166.

180. Xu, L., X. Xie, and Z. Li, Seismic Behavior and Design Approach of Variable-Damping Self-Centering Braced Frame. Journal of Structural Engineering, 2021. 147(6): p. 05021001.

181. Bagheri, H., A. Hashemi, S.M.M. Yousef-Beik, P. Zarnani, and P. Quenneville, A new self-centering tension-only brace using resilient slip friction joint: experimental tests and numerical analysis. Journal of Structural Engineering, 2020.

182. Yousef-Beik, S.M.M., S. Varier, A. hashemi, P. Zarnani, and P. Quenneville, Design of RSFJ Self-centring Brace for Ultimate Limit State in NZSEE 2021. 2021: Christchurch, New Zealand.

183. Newell, J.D. and C.-M. Uang, Cyclic behavior of steel wide-flange columns subjected to large drift. Journal of structural engineering, 2008. 134(8): p. 1334-1342.

184. Bruneau, M., C.-M. Uang, and S.R. Sabelli, Ductile design of steel structures. 2011: McGraw Hill Professional.

185. Li, H., H. Qiu, Z. Zhao, and Y. Lu, Axial compression behaviour of retrofitted long timber columns. Advances in Structural Engineering, 2018. 21(3): p. 445-459.

186. Buchanan, A.H., Strength model and design methods for bending and axial load interaction in timber members. 1984, University of British Columbia.

187. Zahn, J.J., Design of wood members under combined load. Journal of Structural Engineering, 1986. 112(9): p. 2109-2126.

188. Buchanan, A.H., Combined bending and axial loading in lumber. Journal of Structural Engineering, 1986. 112(12): p. 2592-2609.

189. Standard, N.Z., NZS3603: TIMBER STRUCTURES STANDARD. New Zealand, 1993.

190. EN, C., 1-1. Eurocode 5: Design of timber structures-Part 1-1: General-Common rules and rules for buildings. CEN, Brussels, Belgium, 2004.

191. Yousef-beik, S.M.M., H. Bagheri, P. Zarnani, A. Hashemi, and P. Quenneville, Damage-avoidance timber brace using a self-centring friction damper in Pacific Conference on Eathquake Engineering. 2019: Auckland, New Zealand.

192. Bagheri, H., A. Hashemi, S.M.M. Yousef-beik, P. Zarnani, and P. Quenneville, Experimental test of a new self-centring tension-only brace using the Resilient Slip Friction Joint, in Pacific Conference on Earthquake Engineering. 2019: Auckland, New Zealand.

193. Bagheri, H., A. Hashemi, S.M.M. Yousef-Beik, P. Zarnani, and P. Quenneville. A self-centering tension-only bracing system for seismic resistant structures using the Resilient Slip Friction Joint (RSFJ). in 12th Canadian Conference on Earthquake Engineering. 2019.

194. Hibbeler, R.C. and T. Kiang, Structural analysis. 2015: Pearson Prentice Hall Upper Saddle River.

195. Standard, A., ASCE/SEI, Minimum design loads for buildings and other structures. 2016: American-Society-of-Civil-Engineers

196. AISC:341, AISC 341-10, Seismic Provisions for Structural Steel Buildings. Chicago, IL: American Institute of Steel Construction, 2010.

197. Riks, E., An incremental approach to the solution of snapping and buckling problems. International journal of solids and structures, 1979. 15(7): p. 529-551.

198. Standard, A., ASCE/SEI, Seismic Evaluation and Retrofit of Existing Buildings 2017: American-Society-of-Civil-Engineers

199. Chen, Z. and M. Popovski, Seismic Response of Braced Heavy Timber Frames with Riveted Connections. Journal of Performance of Constructed Facilities, 2021. 35(5): p. 04021051.

200. Popovski, M., H.G. Prion, and E. Karacabeyli, Shake table tests on single-storey braced timber frames. Canadian Journal of Civil Engineering, 2003. 30(6): p. 1089-1100.

201. ASCE. Minimum design loads for buildings and other structures. 2013. American Society of Civil Engineers.

202. Popovski, M. and E. Karacabeyli. Force modification factors and capacity design procedures for braced timber frames. in 14th World Conference on Earthquake Engineering (14WCEE). 2008.

203. Xiong, H. and Y. Liu, Experimental study of the lateral resistance of bolted glulam timber post and beam structural systems. Journal of Structural Engineering, 2016. 142(4): p. E4014002.

204. Lim, H., F. Lam, R.O. Foschi, and M. Li, Modeling load-displacement hysteresis relationship of a single-shear nail connection. Journal of Engineering Mechanics, 2017. 143(6): p. 04017015.

205. Medina, R.A. and H. Krawinkler. Influence of hysteretic behavior on the nonlinear response of frame structures. in 13th World Conference on Earthquake Engineering. 2004.

206. Ibarra, L.F., R.A. Medina, and H. Krawinkler, Hysteretic models that incorporate strength and stiffness deterioration. Earthquake engineering & structural dynamics, 2005. 34(12): p. 1489-1511.

207. Krawinkler, H. and G. Seneviratna, Pros and cons of a pushover analysis of seismic performance evaluation. Engineering structures, 1998. 20(4-6): p. 452-464.

208. Beattie, G., R. Shelton, S. Thurston, and A. Liu, The Performance of Residential Houses in the Darfield Earthquake of 4 September 2010. Proc. 9th PCEE. Auckland, New Zealand, 2011.

209. Veismoradi, S., A. Cheraghi, and E. Darvishan, Probabilistic mainshock-aftershock collapse risk assessment of buckling restrained braced frames. Soil Dynamics and Earthquake Engineering, 2018. 115: p. 205-216.

210. Chan, J., A. Hashemi, P. Zarnani, and P. Quenneville. Pinching-free connector for seismically-resistant timber structures: experimental validation and numerical simulation. in Proc., 2019 Pacific Conf. on Earthquake Engineering. Wellington, New Zealand: New Zealand Society for Earthquake Engineering. 2019.

211. Gilbert, C.F. and J. Erochko, Development and testing of hybrid timber-steel braced frames. Engineering Structures, 2019. 198: p. 109495.

212. Blomgren, H.-E., J. Koppitz, A. Valdes, and E. Ko, The heavy timber buckling-restrained braced frame as a solution for commercial buildings in regions of high seismicity. Vienna, Austria: WCTE, 2016.

213. Rodgers, G.W., J.B. Mander, J.G. Chase, and R.P. Dhakal, Beyond ductility: parametric testing of a jointed rocking beam-column connection designed for damage avoidance. Journal of Structural Engineering, 2015. 142(8): p. C4015006.

214. Bruneau, M. and G. MacRae, Reconstructing Christchurch: A seismic shift in building structural systems. The Quake Centre, University of Canterbury, Christchurch, 2017.

215. Uang, C.-M. and M. Bruneau, State-of-the-art review on seismic design of steel structures. 2018, American Society of Civil Engineers.

216. Pettinga, D., C. Christopoulos, S. Pampanin, and N. Priestley, Effectiveness of simple approaches in mitigating residual deformations in buildings. Earthquake Engineering & Structural Dynamics, 2007. 36(12): p. 1763-1783.

217. Hazaveh, N.K., J.G. Chase, G.W. Rodgers, S. Pampanin, and R. Kordani, Seismic behavior of a self-centering system with 2–4 viscous damper. Journal of Earthquake Engineering, 2020. 24(3): p. 470-484.

218. Javidan, M.M. and J. Kim, Steel hysteretic column dampers for seismic retrofit of soft-first-story structures. Steel Compos. Struct, 2020. 37: p. 259-272.

219. Darani, F.M., P. Zarnani, and P. Quenneville, Development of a New Self-Centring Structural Connector for Seismic Protection of Structures. Journal of Constructional Steel Research, 2022. 189: p. 107064.

220. Sahami, K., P. Zarnani, and P. Quenneville, Earthquake-resilience of storage tanks: using an innovative anchorage system. 2020.

221. ABAQUS, C., Version 6.11, 2011. Hibbitt, Karlsson and Sorenson Inc., Providence, Rhode Island, USA.

222. Hashemi, A., B. Zaboli, S.M.M. Yousef-Beik, P. Zarnani, G.C. Clifton, and P. Quenneville, Seismic performance of resilient slip friction joint (RSFJ) brace with collapse prevention mechanism, in NZSEE 2018: Auckland.

223. Vafaei, D. and R. Eskandari, Seismic response of mega buckling-restrained braces subjected to fling-step and forward-directivity near-fault ground motions. The Structural Design of Tall and Special Buildings, 2015. 24(9): p. 672-686.

224. Zarnani, P. and P. Quenneville, Strength of timber connections under potential failure modes: An improved design procedure. Construction and Building Materials, 2014. 60: p. 81-90.

225. Zarnani, P. and P. Quenneville, Wood block tear-out resistance and failure modes of timber rivet connections: a stiffness-based approach. Journal of Structural Engineering, 2013. 140(2): p. 04013055.

226. Zarnani, P. and P. Quenneville, Splitting strength of small dowel-type timber connections: Rivet joint loaded perpendicular to grain. Journal of Structural Engineering, 2014. 140(10): p. 04014064.

227. Zarnani, P. and P. Quenneville, Group tear-out in small-dowel-type timber connections: brittle and mixed failure modes of multinail joints. Journal of Structural Engineering, 2014. 141(2): p. 04014110.

228. Popovski, M., Seismic performance of braced timber frames. 2000, University of British Columbia.

229. Zarnani, P. and P. Quenneville. Reliable yield model for strength prediction of timber rivet connection under ductile failure. in Proc., 12th World Conference on Timber Eng., Auckland, New Zealand. 2012.

230. Black, C., I.D. Aiken, and N. Makris, Component testing, stability analysis, and characterization of buckling-restrained unbonded braces (TM). 2002: Pacific Earthquake Engineering Research Center.

231. Shome, N., Probabilistic seismic demand analysis of nonlinear structures. 1999.

232. Ghobarah, A., Performance-based design in earthquake engineering: state of development. Engineering structures, 2001. 23(8): p. 878-884.

233. Council, A.T., Effects of Strength and Stiffness Degradation of Seismic Response, FEMA P440A. 2009.

234. MacRae, G.A. and K. Kawashima, Post-earthquake residual displacements of bilinear oscillators. Earthquake engineering & structural dynamics, 1997. 26(7): p. 701-716.

235. Ariyaratana, C. and L.A. Fahnestock, Evaluation of buckling-restrained braced frame seismic performance considering reserve strength. Engineering Structures, 2011. 33(1): p. 77-89.

236. Pettinga, J.D., S. Pampanin, C. Christopoulos, and M. Priestley, Developments in the prediction and mitigation of residual deformations due to seismic demand, including asymmetric structural response. 2007: IUSS Press.

237. Terán-Gilmore, A., J. Ruiz-García, and E. Bojórquez-Mora, Flexible frames as self-centering mechanism for buildings having buckling-restrained braces. Journal of Earthquake Engineering, 2015. 19(6): p. 978-990.

238. Baiguera, M., G. Vasdravellis, and T.L. Karavasilis, Dual seismic-resistant steel frame with high post-yield stiffness energy-dissipative braces for residual drift reduction. Journal of Constructional Steel Research, 2016. 122: p. 198-212.

239. Christopoulos, C., S. Pampanin, and M. Nigel Priestley, Performance-based seismic response of frame structures including residual deformations part I: single-degree of freedom systems. Journal of Earthquake Engineering, 2003. 7(01): p. 97-118.

240. Pampanin, S., C. Christopoulos, and M. Nigel Priestley, Performance-based seismic response of frame structures including residual deformations part II: multi-degree of freedom systems. Journal of Earthquake Engineering, 2003. 7(01): p. 119-147.

241. Jones, P. and F. Zareian, Seismic response of a 40-storey buckling-restrained braced frame designed for the Los Angeles region. The Structural Design of Tall and Special Buildings, 2013. 22(3): p. 291-299.

242. Asgarian, B. and H. Shokrgozar, BRBF response modification factor. Journal of constructional steel research, 2009. 65(2): p. 290-298.

243. Mahmoudi, M. and M. Zaree, Evaluating response modification factors of concentrically braced steel frames. Journal of Constructional Steel Research, 2010. 66(10): p. 1196-1204.

244. Wang, H., X. Nie, and P. Pan, Development of a self-centering buckling restrained brace using cross-anchored pre-stressed steel strands. Journal of Constructional Steel Research, 2017. 138: p. 621-632.

245. Araki, Y., N. Maekawa, K.C. Shrestha, M. Yamakawa, Y. Koetaka, T. Omori, and R. Kainuma, Feasibility of tension braces using Cu–Al–Mn superelastic alloy bars. Structural Control and Health Monitoring, 2014. 21(10): p. 1304-1315.

246. Fang, C. and W. Wang, Self-centring braces with SMA elements, in Shape Memory Alloys for Seismic Resilience. 2020, Springer. p. 147-177.

247. Wang, C.-L., Y. Qing, J. Wang, G. Chen, and B. Zeng, A new buckling-restrained brace with gap-supported tendon protection: Experiment and application. Engineering Structures, 2019. 200: p. 109688.

248. Wang, C.-L., Y. Qing, J. Wu, J. Wang, and Z. Gu, Analytical and experimental studies on buckling-restrained brace with gap-supported tendon protection. Journal of Constructional Steel Research, 2020. 164: p. 105807.

249. Guo, T., J. Wang, Y. Song, W. Xuan, and Y. Chen, Self-centering cable brace with friction devices for enhancing seismic performance of RC frame structures. Engineering Structures, 2020. 207: p. 110187.

250. Ma, H. and M.C. Yam, Modelling of a self-centring damper and its application in structural control. Journal of Constructional Steel Research, 2011. 67(4): p. 656-666.

251. Hashemi, A., P. Zarnani, R. Masoudnia, and P. Quenneville, Seismic resistant rocking coupled walls with innovative Resilient Slip Friction (RSF) joints. Journal of Constructional Steel Research, 2017. 129: p. 215-226.

252. Hashemi, A., P. Zarnani, R. Masoudnia, and P. Quenneville, Seismic resilient lateral load resisting system for timber structures. Construction and Building Materials, 2017. 149: p. 432-443.

253. Darani, F.M., P. Zarnani, S. Veismoradi, S.M.M. Yousef-beik, A. Hashemi, and P. Quenneville. Resilient slip friction joint performance: Component analysis, spring model and anti-locking mechanism. in Structures. 2021. Elsevier.

254. Budiansky, B., Theory of buckling and post-buckling behavior of elastic structures. Advances in applied mechanics., 1974. 14: p. 1-65.

255. Veismoradi, S. and E. Darvishan, Probabilistic seismic assessment of mega buckling-restrained braced frames under near-fault ground motions. Earthquakes and Structures, 2018. 15(5): p. 487-498.

256. Fugazza, D., Shape-memory alloy devices for earthquake engineering: Mechanical properties, constitutive modeling and numerical simulations. Master's Thesis, University of Pavia, Pavia, Italy, 2003.

257. Black, C.J., N. Makris, and I.D. Aiken, Component testing, seismic evaluation and characterization of buckling-restrained braces. Journal of Structural Engineering, 2004. 130(6): p. 880-894.

258. Council, A.T. and U.S.F.E.M. Agency, Quantification of building seismic performance factors - FEMA P695. 2009: US Department of Homeland Security, FEMA.

12 Appendix

12.1 Appendix A: Test set-ups drawings

12.1.1. *Joint buckling (Chapter 3)*

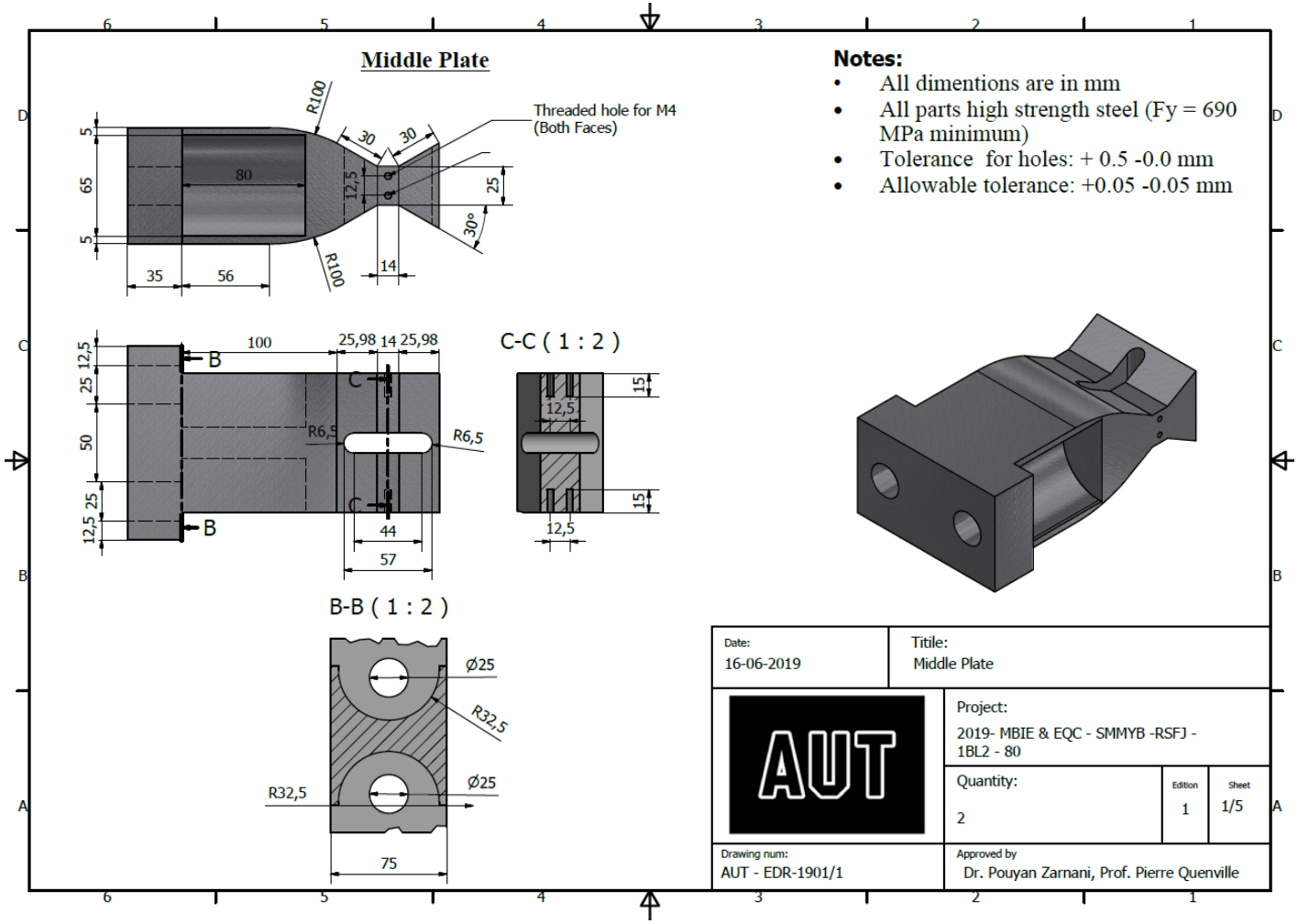

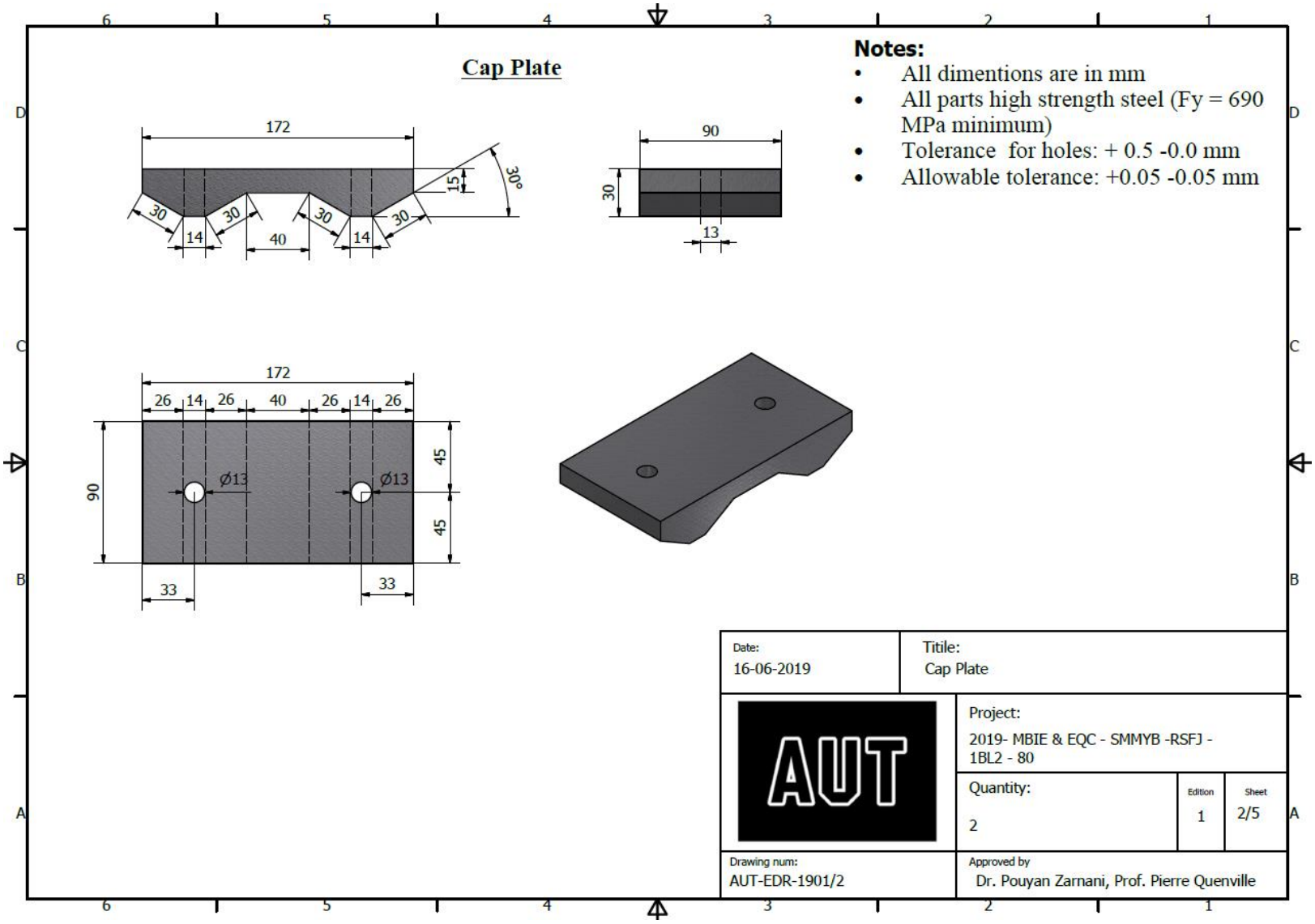
Cap Plate
Notes:
All dimentions are in mm
All parts high strength steel (Fy = 690 MPa minimum)
Tolerance for holes: + 0.5 -0.0 mm
Allowable tolerance: +0.05 -0.05 mm
172
30
14
40
15
30°
90
30
13
26 14 26 40 26 14 26
Ø13
45
33
Date: 16-06-2019
Titile: Cap Plate
AUT
Project: 2019- MBIE & EQC - SMMYB -RSFJ - 1BL2 - 80
Quantity: 2
Edition 1
Sheet 2/5
Drawing num: AUT-EDR-1901/2
Approved by Dr. Pouyan Zarnani, Prof. Pierre Quenville

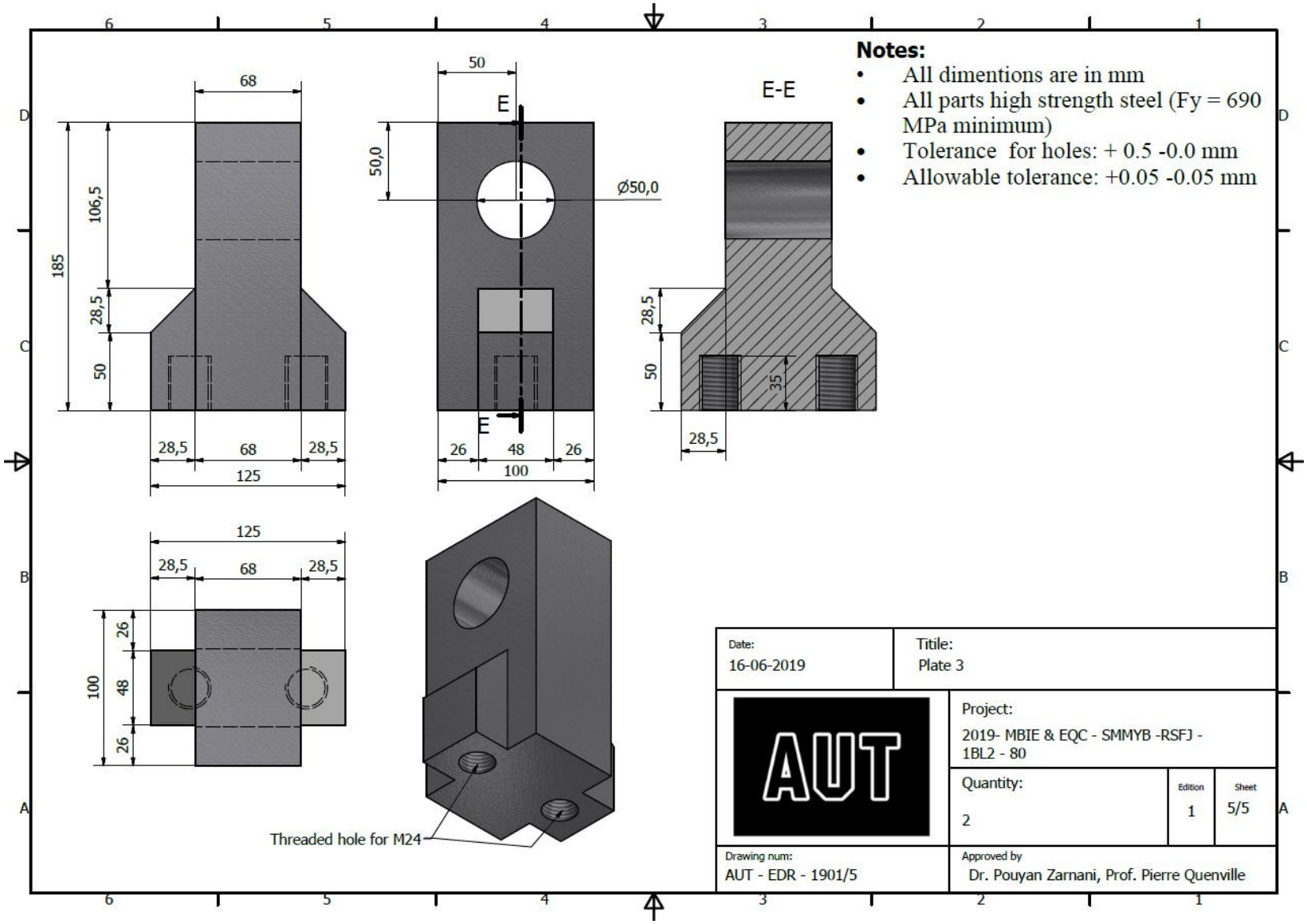
Notes:
All dimentions are in mm
All parts high strength steel (Fy = 690 MPa minimum)
Tolerance for holes: + 0.5 -0.0 mm
Allowable tolerance: +0.05 -0.05 mm
E-E
Threaded hole for M24
Date: 16-06-2019
Titile: Plate 3
AUT
Project: 2019- MBIE & EQC - SMMYB -RSFJ - 1BL2 - 80
Quantity: 2
Edition 1
Sheet 5/5
Drawing num: AUT - EDR - 1901/5
Approved by Dr. Pouyan Zarnani, Prof. Pierre Quenville

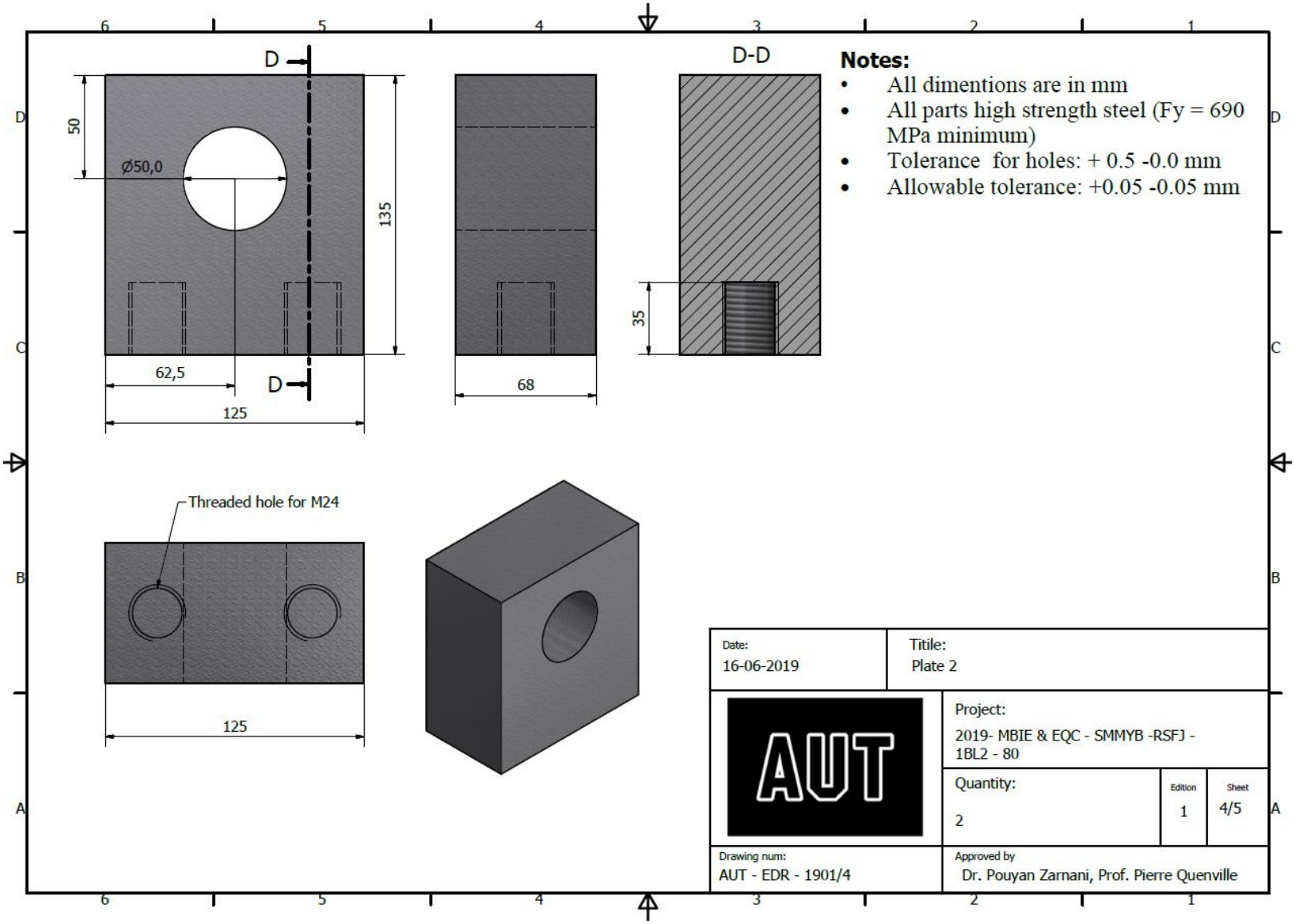
D
D-D
50
Ø50,0
135
62,5
125
68
35
Threaded hole for M24
125
Notes:
All dimentions are in mm
All parts high strength steel (Fy = 690 MPa minimum)
Tolerance for holes: + 0.5 -0.0 mm
Allowable tolerance: +0.05 -0.05 mm
Date: 16-06-2019
Titile: Plate 2
AUT
Project: 2019- MBIE & EQC - SMMYB -RSFJ - 1BL2 - 80
Quantity: 2
Edition 1
Sheet 4/5
Drawing num: AUT - EDR - 1901/4
Approved by Dr. Pouyan Zarnani, Prof. Pierre Quenville

12.1.2. *Assembly of pin-pin damper for the in-plane test (Chapter 3):*

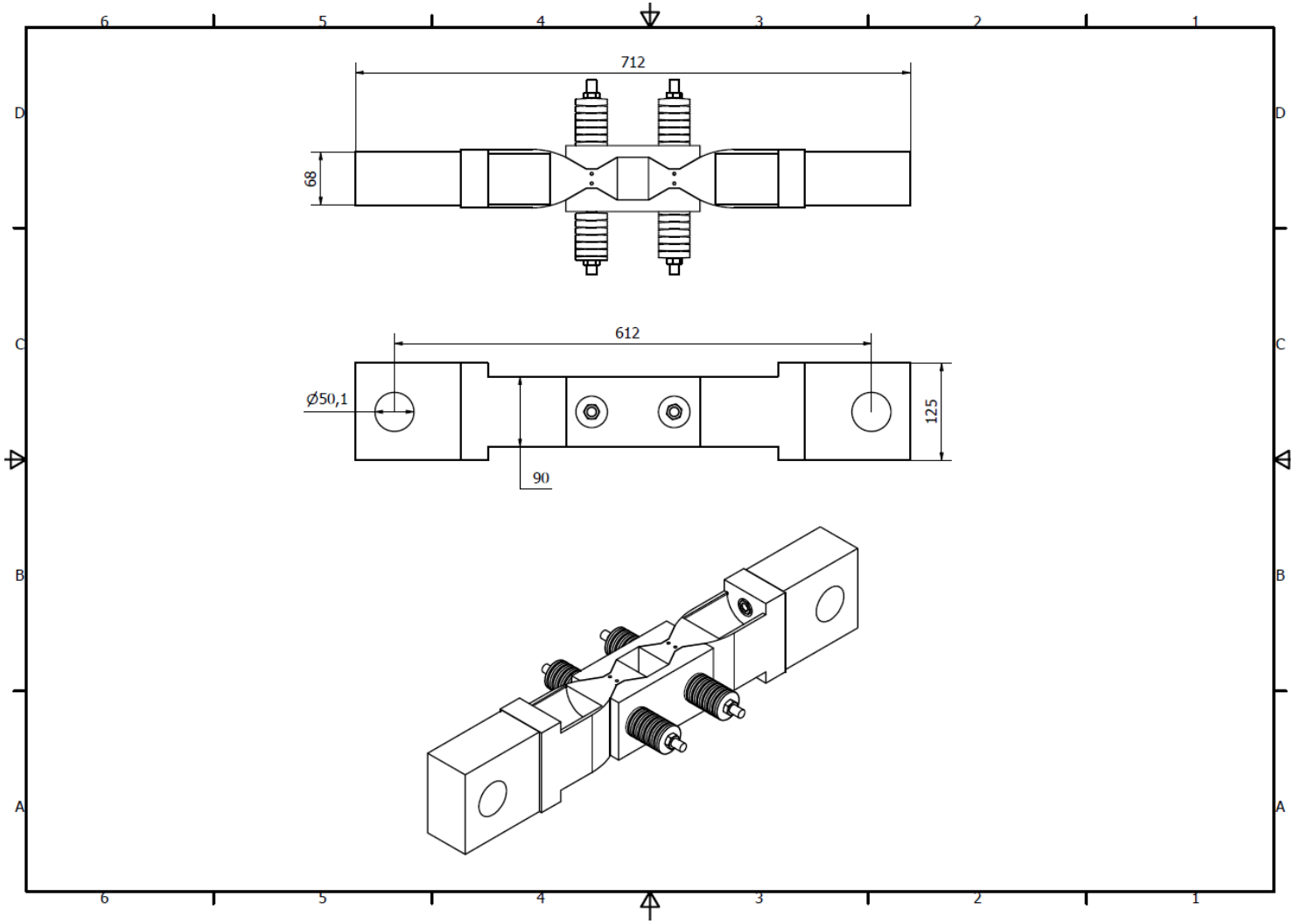

12.1.3. *Assembly of pin-pin damper for the out-of-plane test (Chapter 3):*

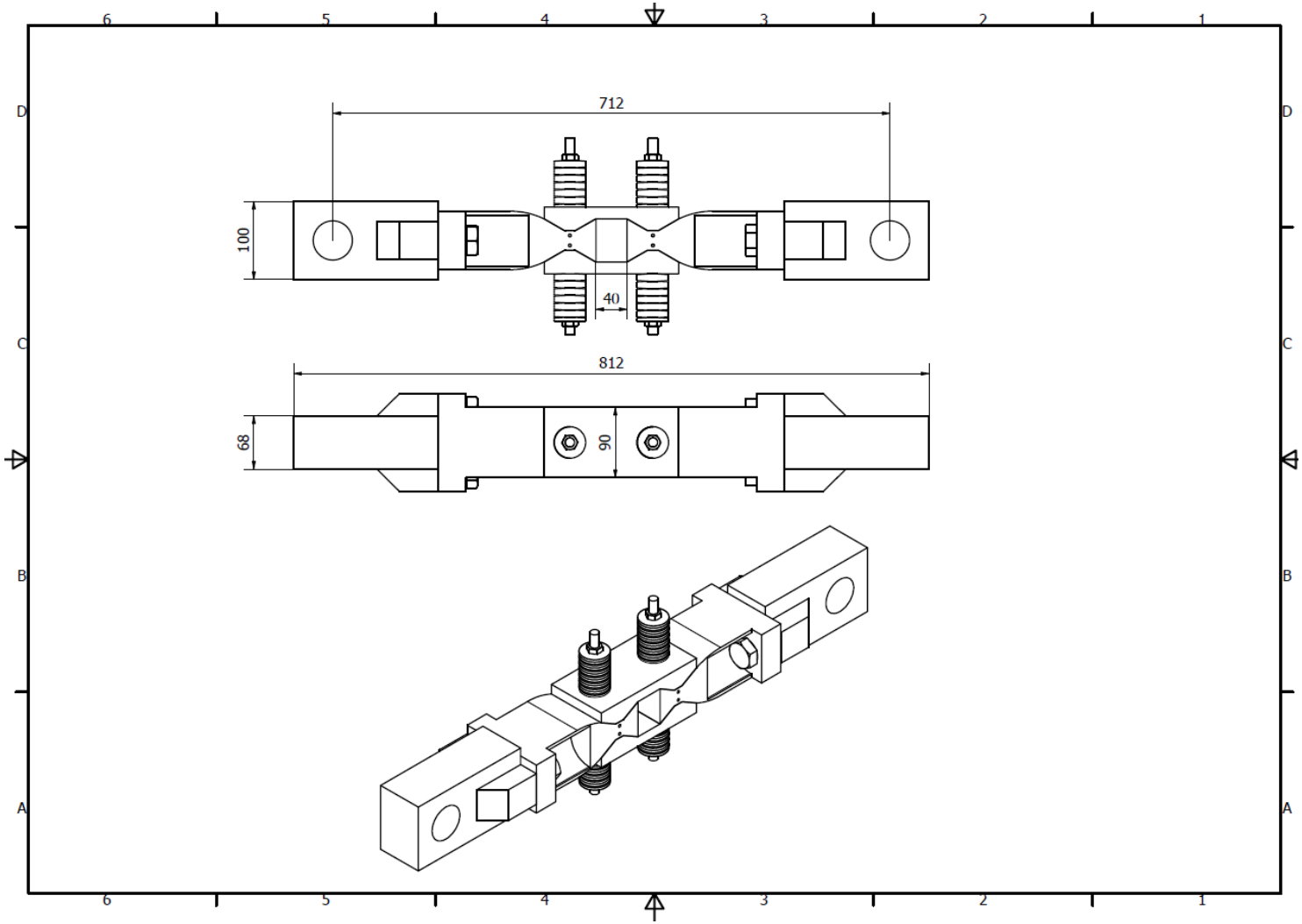

12.1.4. *Assembly of pin-fix damper for the in- and out-of-plane test (Chapter 3):*

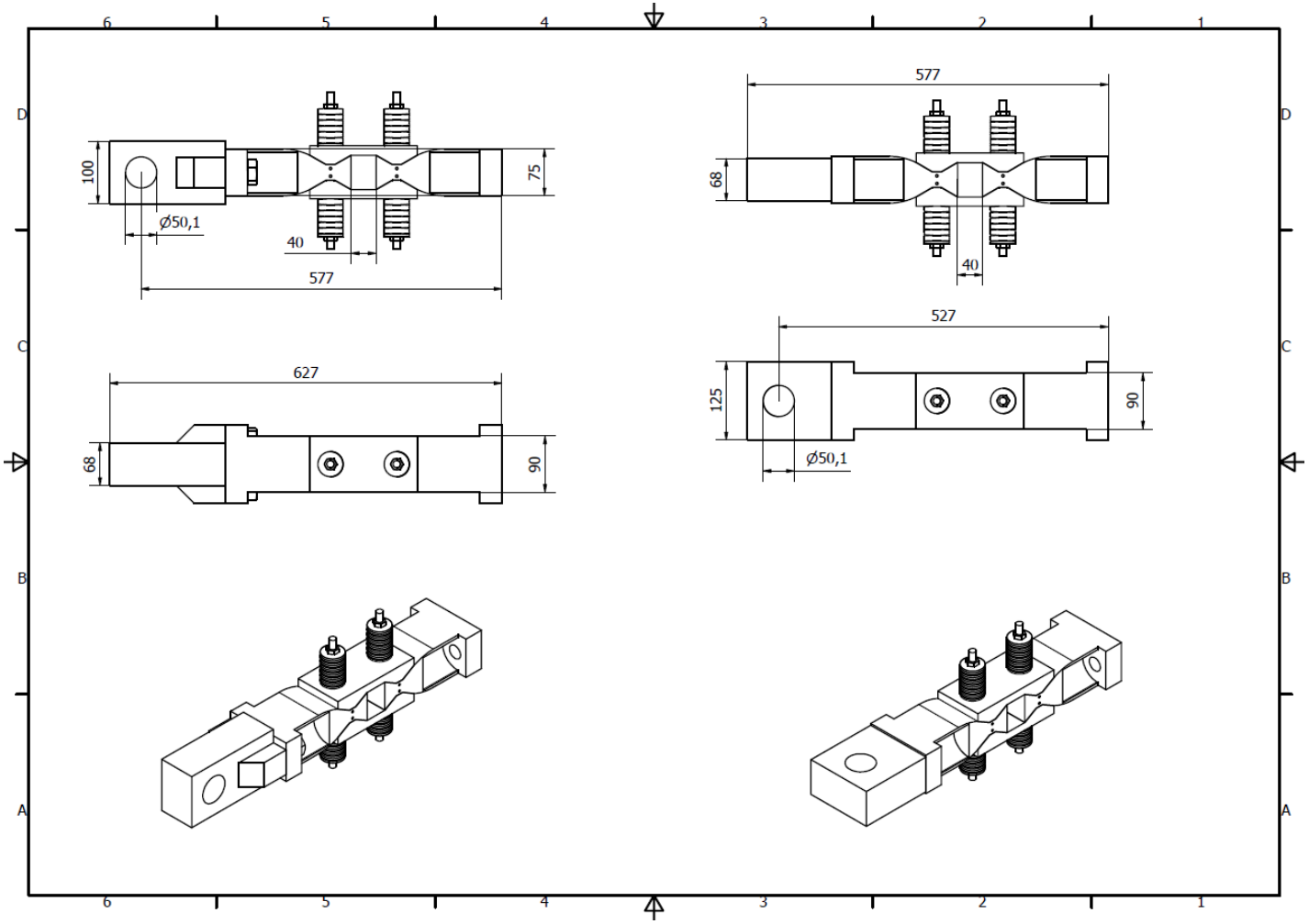

12.1.5. *Small-scale timber brace test (Chapter 4)*

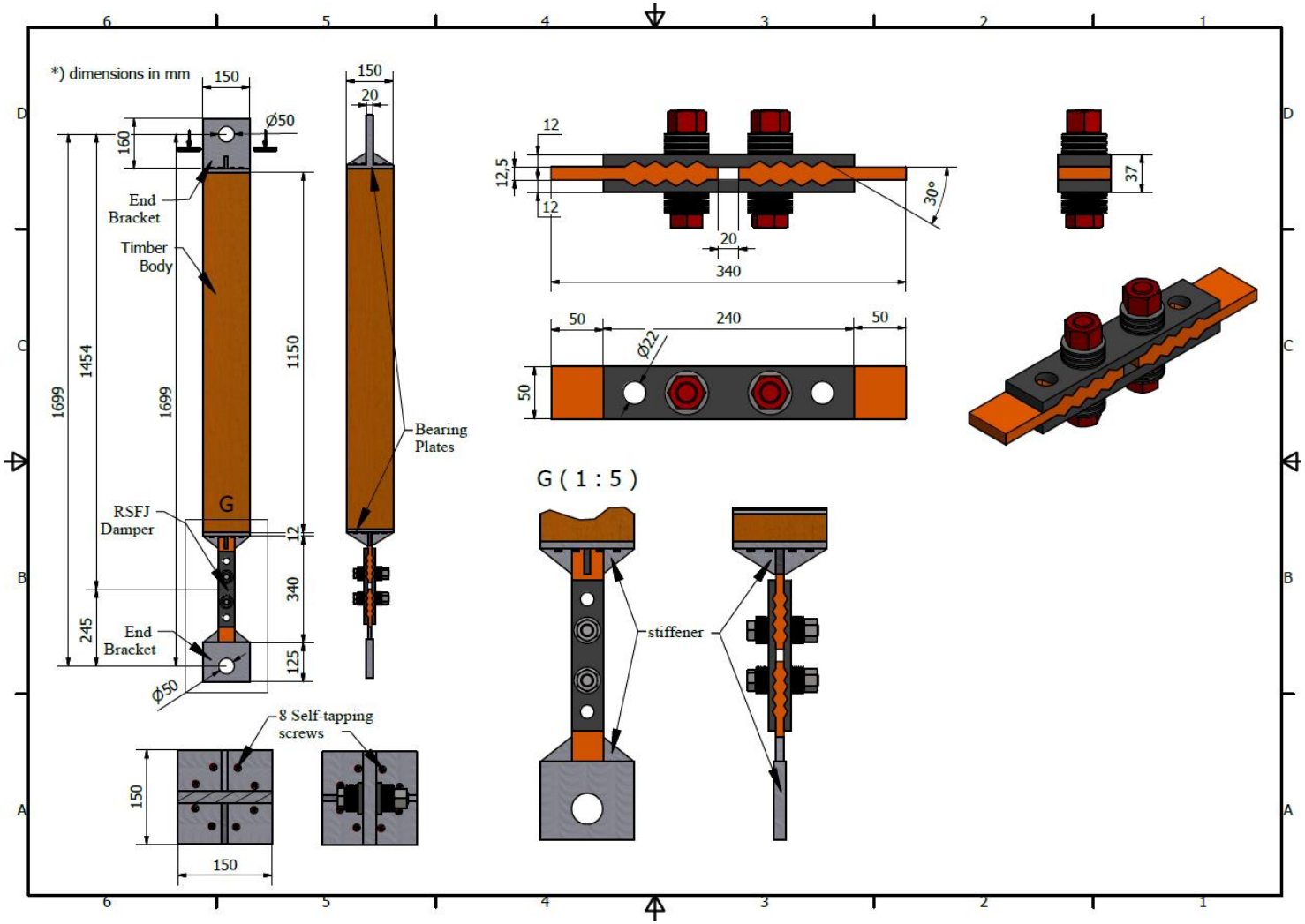

12.1.6. *Full-scale timber brace test (Chapter 4, 8 and 9)*

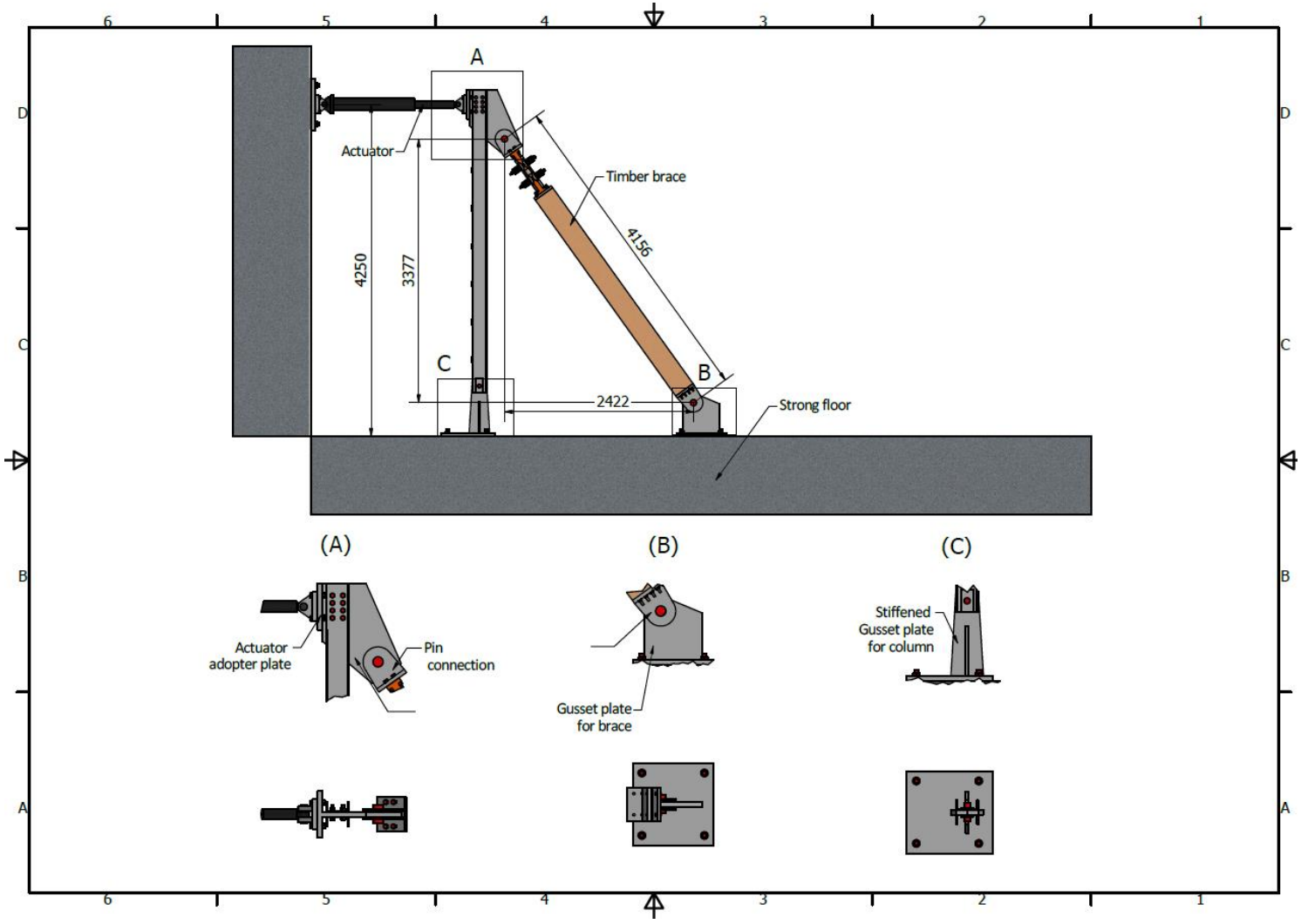

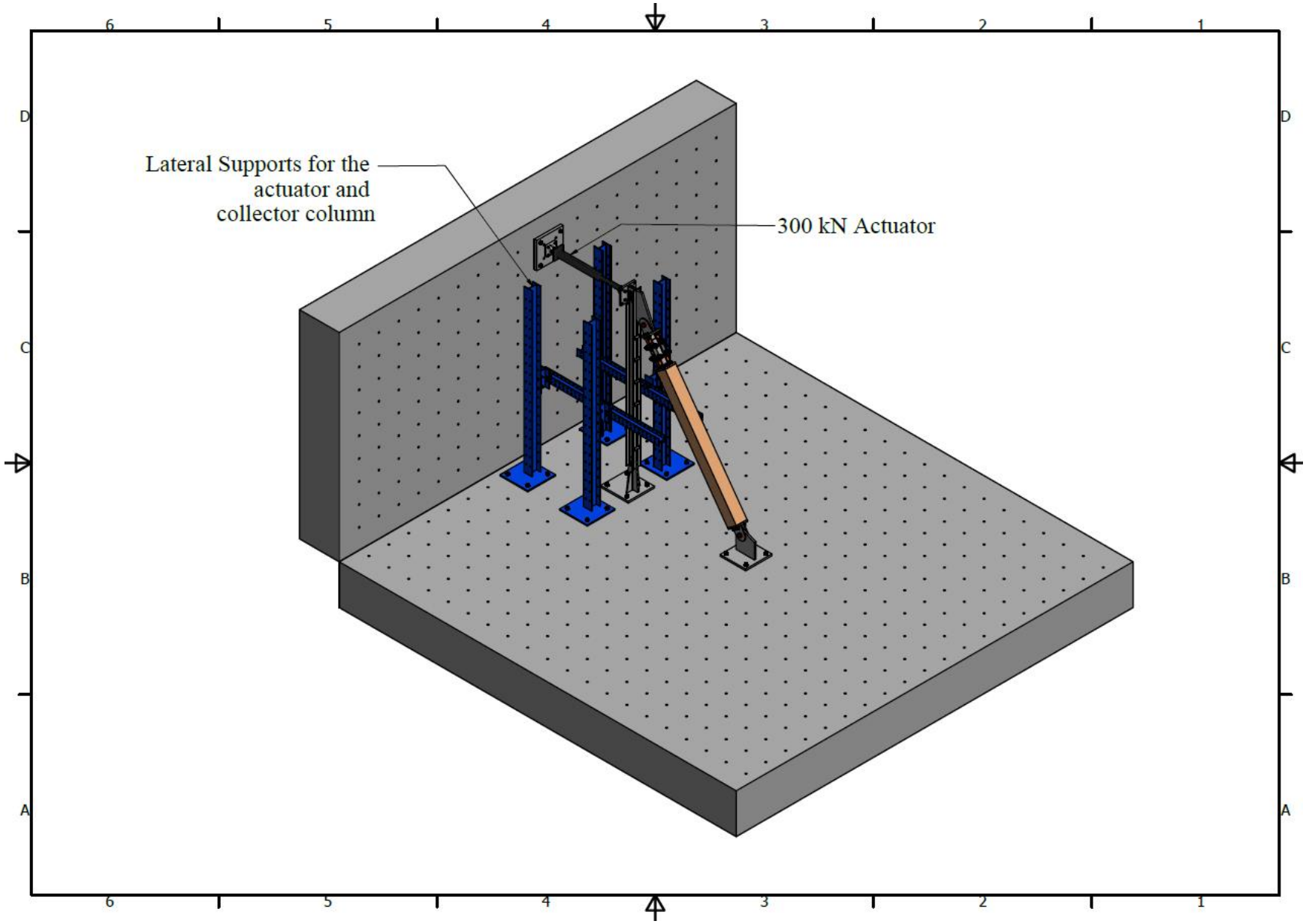
Lateral Supports for the actuator and collector column
300 kN Actuator
6
5
4
3
2
1
D
C
B
A

12.1.7. *Full-scale steel brace test (Chapter 5)*

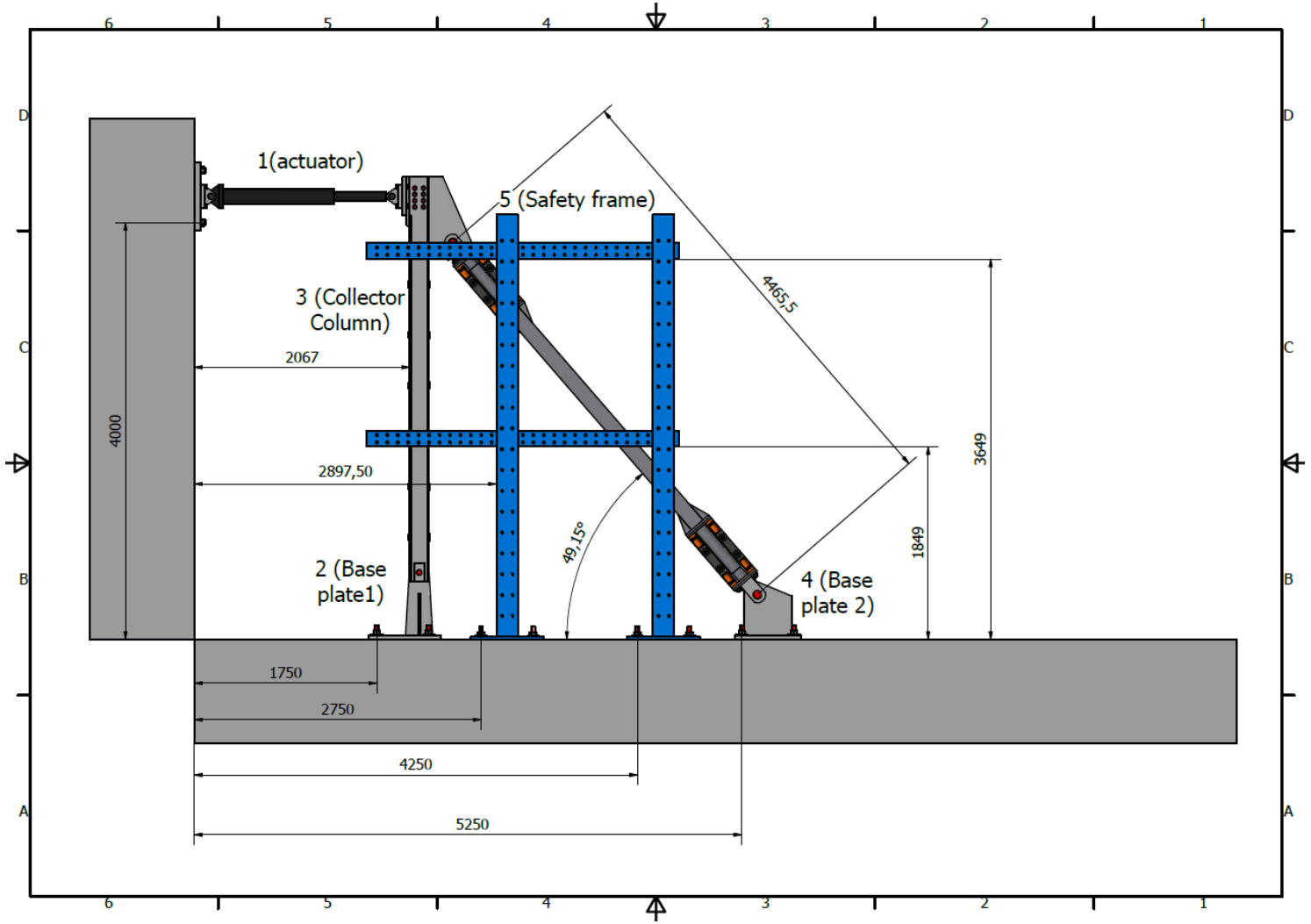

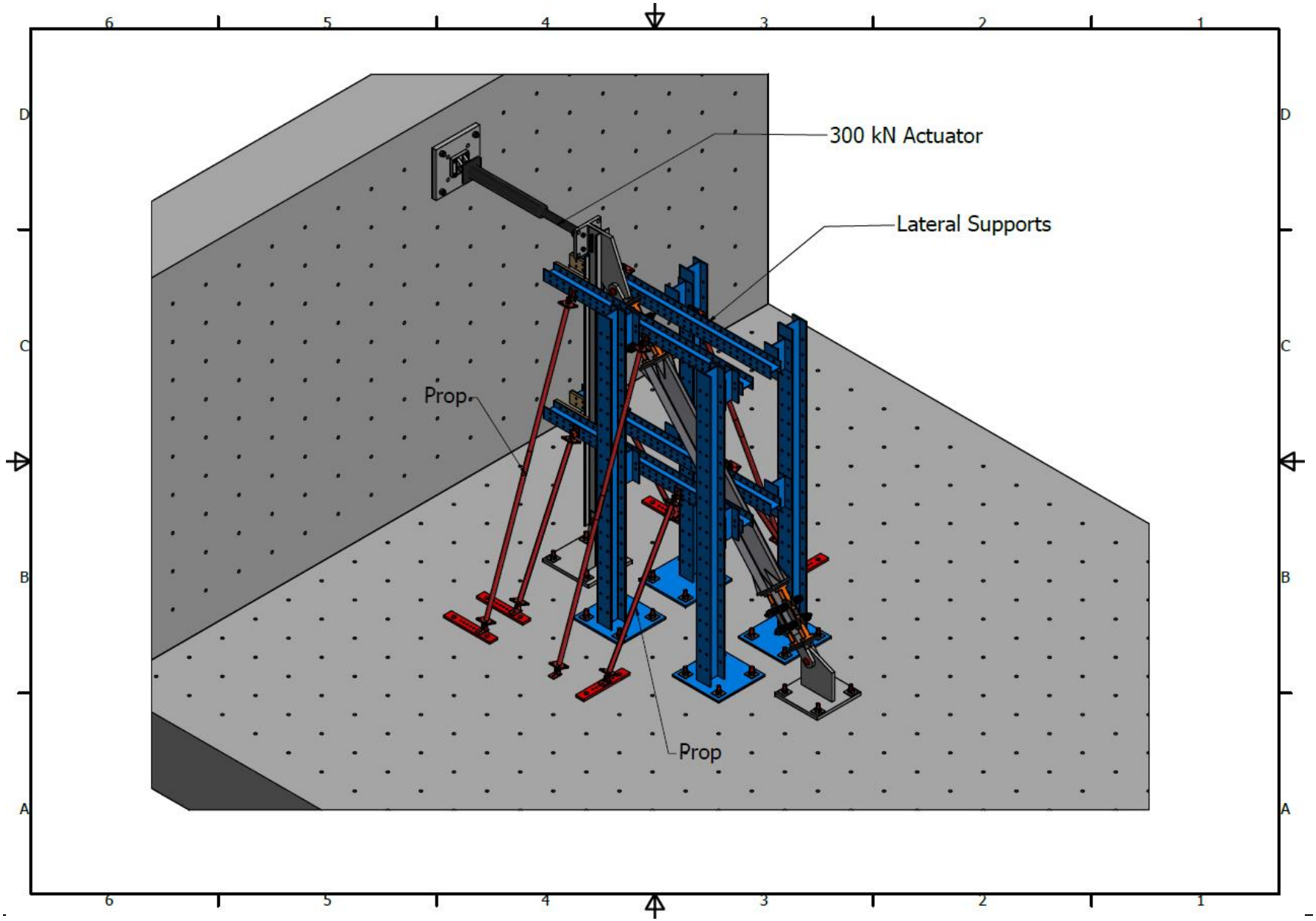
6
5
4
3
2
1
D
C
B
A
300 kN Actuator
Lateral Supports
Prop
Prop

12.2 Appendix B: Proofs

12.2.1. *Equilibrium path and internal actions for axially loaded RSFJ with out-of-plane rotation (Chapter 3)*

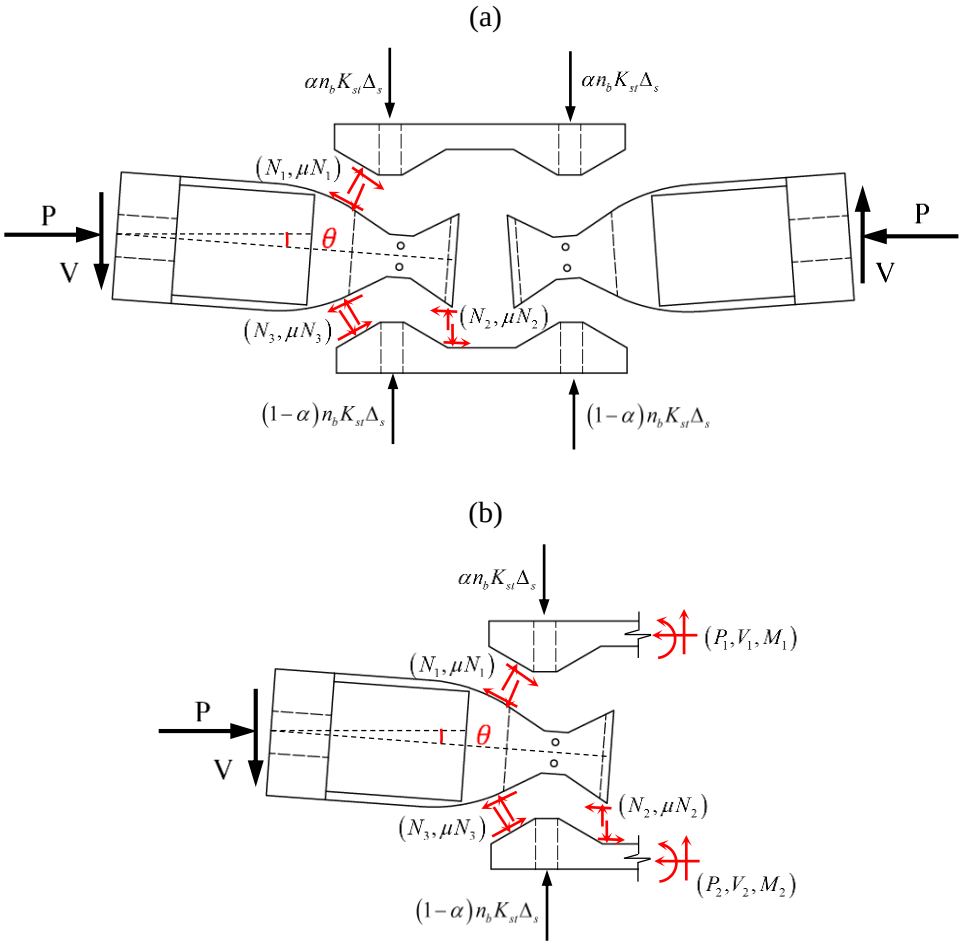

Figure 12.1: Free body diagram of the damper when subject to out-of-plane rotation, (a) Global, (b) Global + internal

In order to derive the equation mentioned in chapter 3.1.2, the free body diagram in the deformed shape should be available as shown in Figure 12.1 in which it is assumed that there are three contact points between a middle and two cap plates when the damper is subjected to out-of-plane deformation. In each contact point, two forces are acting namely: normal force and frictional force.

12.2.1.1. Equilibrium for Middle plate:

If the middle plate is taken out and the equilibrium is written for the acting forces, three equations will be given as follows:

$$\sum f_x = 0 \rightarrow N_1\, sin\theta_g + \mu N_1\, cos\theta_g + N_3\, sin\theta_g + \mu N_3\, cos\theta_g + \mu N_2 - P = 0 \quad \text{A.1}$$

$$\sum f_y = 0 \rightarrow N_2 + N_3\, cos\theta_g + \mu N_1\, sin\theta_g - N_1\, cos\theta_g - \mu N_3\, sin\theta_g - V = 0 \quad \text{A.2}$$

$$\begin{aligned}\sum_{pin} M \approx 0 \rightarrow & \left(N_1\, cos\theta_g - \mu N_1 sin\theta_g\right)\left(\frac{L}{2} - \frac{L_c}{2}\right) - N_2\left(\frac{L}{2} - \frac{L_c}{2} + L_e\right) \\ & - \left(N_3\, cos\theta_g - \mu N_3 sin\theta_g\right)\left(\frac{L}{2} - \frac{L_c}{2}\right) \\ & - \left(N_1\, sin\theta_g + \mu N_1\, cos\theta_g\right)\left[\left(\frac{L}{2} - \frac{L_c}{2}\right)\theta - \frac{t_{max}}{2}\right] \\ & + \left(N_3\, sin\theta_g + \mu N_3 cos\theta_g\right)\left[\left(\frac{L}{2} - \frac{L_c}{2}\right)\theta + \frac{t_{max}}{2}\right] \\ & + \mu N_2\left[\left(\frac{L}{2} - \frac{L_c}{2} + L_e\right)\theta + \frac{t_{max}}{2}\right]\end{aligned} \quad \text{A.3}$$

where N_i and μN_i are the normal and frictional force at each contact point. P and V are the axial and shear force at the pin supports. p_i , v_i and M_i are also the internal forces in the cap plates.

12.2.1.2. Equilibrium for top Cap plate:

If the top cap plate is taken out and the equilibrium is written for half of it, three equations will be given as follows:

$$\sum f_x = 0 \rightarrow N_1\, sin\theta_g + \mu N_1\, cos\theta_g - p_1 = 0 \quad \text{A.4}$$

$$\sum f_y = 0 \rightarrow N_1\, cos\theta_g - \mu N_1\, sin\theta_g + v_1 - \alpha n_b K_{st} \Delta_s = 0 \quad \text{A.5}$$

$$\sum_{middle} M \approx 0 \rightarrow M_1 + \alpha n_b K_{st} \Delta_s \left(\frac{L}{2} - l_b\right) - \left(N_1\, cos\theta_g - \mu N_1 sin\theta_g\right)\frac{L_c}{2} = 0 \quad \text{A.6}$$

in which:

$$\Delta_s = B(1 - cos\theta) + \frac{A\theta}{2} \quad \text{A.7}$$

12.2.1.3. Equilibrium for bottom Cap plate:

If the bottom cap plate is taken out and the equilibrium is written for half of it, three equations will be given as follows:

$$\sum f_x = 0 \rightarrow N_3\, sin\theta_g + \mu N_3\, cos\theta_g + \mu N_2 - p_2 = 0 \quad \text{A.8}$$

$$\sum f_y = 0 \rightarrow N_3\, cos\theta_g - \mu N_3\, sin\theta_g - (1-\alpha) n_b K_{st} \Delta_s + N_2 - v_2 = 0 \quad \text{A.9}$$

$$\sum_{middle} M \approx 0 \rightarrow M_2 + N_2\left(\frac{L}{2} - \frac{L_c}{2} + L_e\right) + \left(N_3\, cos\theta_g - \mu N_3 sin\theta_g\right)\frac{L_c}{2} - (1-\alpha) n_b K_{st} \Delta_s \left(\frac{L}{2} - l_b\right) = 0 \quad \text{A.10}$$

12.2.1.4. Global equilibrium:

If the global equilibrium is written for half of the RSFJ assembly, three equations will be given as follows:

$$\sum f_x = 0 \rightarrow p_1 + p_2 = P \quad \text{A.11}$$

$$\sum f_y = 0 \rightarrow v_1 + v_2 = V \quad \text{A.12}$$

$$\sum_{pin} M \approx 0 \rightarrow M_1 + M_2 + (p_2 - p_1)\frac{t_{max}}{2} - \frac{PL}{2} = 0 \quad \text{A.13}$$

After solving the system of equations with 12 variables ($\alpha, p, p_1, p_2, M_1, M_2, N_1, N_2, N_3, V_1, V_2, V$), the axial and internal load will be discovered.

12.2.2. *The characteristic equation for Stability of a Column with one intermediate rotational spring (Chapter 4 and 7)*

In order to calculate the characteristic equation of the system shown in Figure12.3, the deflected shape of each segment (two in total) can be assumed as following two expressions. For the simplicity of the solution, the normalized length is considered in the process:

$$y_1 = C_1\, sin\left(\sqrt{\alpha}x\right) + C_2\, cos\left(\sqrt{\alpha}x\right) + C_3 x + C_4, \qquad 0 \le \frac{x}{L} < a \tag{A.14}$$

$$y_2 = B_1\, sin\left(\sqrt{\alpha}x\right) + B_2\, cos\left(\sqrt{\alpha}x\right) + B_3 x + B_4, \qquad a \le \frac{x}{L} < L \tag{A.15}$$

in which $\alpha = {EI}/{PL^2}$

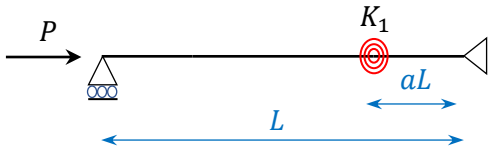

Figure12.2: Mathematical model

Each boundary condition of the system will put a constraint on the results. Therefore, all of them should be met based on the assumed deflection shape.

The first set of boundary conditions is the continuity of the shape necessitating to satisfy:

$$\begin{aligned} &y_1(0) = 0 \\ &y_1(a) = y_2(a) \\ &y_2(1) = 0 \end{aligned} \tag{A.17}$$

The second set is the continuity of the curvature and zero bendings at pin supports, which requires:

$$\begin{aligned} &\frac{d^2y_1}{dx^2}(0) = 0 \\ &\frac{d^2y_2}{dx^2}(1) = 0 \\ &\frac{d^2y_1}{dx^2}(a) = \frac{d^2y_2}{dx^2}(a) \end{aligned} \tag{A.18}$$

The third set of boundary conditions is the continuity of the shear at the locations where the rotational springs are installed, which necessitates:

$$\frac{d^3y_1}{dx^3}(a) + \alpha\frac{dy_1}{dx}(a) = \frac{d^3y_2}{dx^3}(a) + \alpha\frac{dy_2}{dx}(a) \quad \text{A.19}$$

The last one is the deformation compatibility and equilibrium at the location of rotational springs, which brings:

$$\frac{d^2y_1}{dx^2}(a) = k_1\left(\frac{dy_2}{dx} - \frac{dy_1}{dx}\right)(a) \quad \text{A.20}$$

in which

$$k_1 = \frac{K_1 L}{EI} \quad \text{A.21}$$

In order that all of the above-mentioned equations are satisfied, the determinant of the coefficient should be zero, which yields the characteristic equation as follows:

$$f(\alpha) = k_1 tan\left(a\sqrt{\alpha}\right) - tan\left(\sqrt{\alpha}(1-a)\right)\left[\sqrt{\alpha}tan\left(a\sqrt{\alpha}\right) - k_1\right] \quad \text{A.22}$$

The Euler load or elastic buckling load of the system, the minimum real root of the results of Eq.A.22 should be input in Eq.A.23:

$$P_{cr} = \alpha\frac{EI}{L^2} \quad \text{A.23}$$

where α should be bounded:

$$\alpha \in (0, \pi^2) \quad \text{A.24}$$

For the second mode of elastic buckling, α should be bounded:

$$\alpha \in (\pi^2, 4\pi^2) \quad \text{A.25}$$

If the brace body is relatively rigid compared to the rotational spring $K/EI \to 0$, Eq A.22 can be re-written as follows given that $\tan\theta \to \theta$ due to the flexibility of the system:

$$f(\alpha) = k_1 a\sqrt{\alpha} - \sqrt{\alpha}(1-a)\left[\sqrt{\alpha} * a\sqrt{\alpha} - k_1\right] \quad \text{A.26}$$

The root of the expression above is:

$$\alpha = \frac{k_1}{a(1-a)} \quad \text{A.27}$$

If Eq A.27 is replaced in Eq A.23, the following simplified expression would yield:

$$P_{cr} = \frac{K_1}{La(1-a)} \quad \text{A.28}$$

If the rotational spring is placed in the middle of the system then, the famous $4K_1/L$ formula would be achieved:

$$P_{cr} = \frac{4K_1}{L} \quad \text{A.29}$$

12.2.3. *The characteristic equation for Stability of a Column with two intermediate rotational springs (Chapter 5 and 7)*

In order to calculate the characteristic equation of the system shown in Figure12.3, the deflected shape of each segment (three in total) can be assumed as following three expressions. For the simplicity of the solution, the normalized length is considered in the process:

$$y_1 = C_1\, sin(\sqrt{\alpha}x) + C_2\, cos(\sqrt{\alpha}x) + C_3 x + C_4, \qquad 0 \le \frac{x}{L} < a \tag{A.30}$$

$$y_2 = B_1\, sin(\sqrt{\alpha}x) + B_2\, cos(\sqrt{\alpha}x) + B_3 x + B_4, \qquad a \le \frac{x}{L} < b \tag{A.31}$$

$$y_3 = E_1\, sin(\sqrt{\alpha}x) + E_2\, cos(\sqrt{\alpha}x) + E_3 x + E_4, \qquad b \le \frac{x}{L} < 1 \tag{A.32}$$

in which $\alpha = {EI}/{PL^2}$

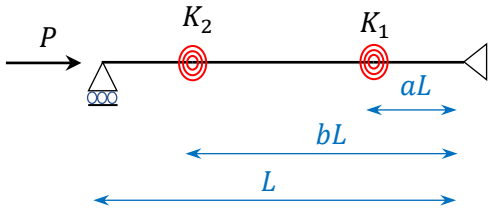

Figure12.3: Mathematical model

Each boundary condition of the system will put a constraint on the results. Therefore, all of them should be met based on the assumed deflection shape.

The first set of boundary conditions is the continuity of the shape necessitating to satisfy:

$$\begin{aligned} &y_1(0) = 0 \\ &y_1(a) = y_2(a) \\ &y_3(1) = 0 \\ &y_2(b) = y_3(b) \end{aligned} \tag{A.33}$$

The second set is the continuity of the curvature and zero bendings at pin supports, which requires:

$$\frac{d^2y_1}{dx^2}(0) = 0$$
$$\frac{d^2y_3}{dx^2}(1) = 0$$
$$\frac{d^2y_1}{dx^2}(a) = \frac{d^2y_2}{dx^2}(a) \qquad \text{A.34}$$
$$\frac{d^2y_2}{dx^2}(b) = \frac{d^2y_3}{dx^2}(b)$$

The third set of boundary conditions is the continuity of the shear at the locations where the rotational springs are installed, which necessitates:

$$\frac{d^3y_1}{dx^3}(a) + \alpha\frac{dy_1}{dx}(a) = \frac{d^3y_2}{dx^3}(a) + \alpha\frac{dy_2}{dx}(a)$$
$$\frac{d^3y_2}{dx^3}(b) + \alpha\frac{dy_2}{dx}(b) = \frac{d^3y_3}{dx^3}(b) + \alpha\frac{dy_3}{dx}(b) \qquad \text{A.35}$$

The last one is the deformation compatibility and equilibrium at the location of rotational springs, which brings:

$$\frac{d^2y_1}{dx^2}(a) = k_1\left(\frac{dy_2}{dx} - \frac{dy_1}{dx}\right)(a)$$
$$\frac{d^2y_2}{dx^2}(b) = k_2\left(\frac{dy_2}{dx} - \frac{dy_1}{dx}\right)(b) \qquad \text{A.36}$$

in which

$$k_1 = \frac{K_1 L}{EI}$$
$$k_2 = \frac{K_2 L}{EI} \qquad \text{A.37}$$

In order that all of the above-mentioned equations are satisfied, the determinant of the coefficient should be zero, which yields the characteristic equation as follows:

$$f(a, k_1, k_2) = 2\alpha\, sin\left(\sqrt{\alpha}(2a-1)\right) - \alpha\, sin\left(\sqrt{\alpha}(4a-1)\right) + \alpha\, sin\left(\sqrt{\alpha}\right) - 4k_1k_2\, sin\left(\sqrt{\alpha}\right) + 2\sqrt{\alpha}(k_1+k_2)\, cos\left(\sqrt{\alpha}(2a-1)\right) - 2\sqrt{\alpha}(k_1+k_2)\, cos\left(\sqrt{\alpha}\right) \qquad \text{A.38}$$

In Eq.A.38, if $k_1 = k_2$

$$f(a,k) = 2\alpha\, sin\left(\sqrt{\alpha}(2a-1)\right) - \alpha\, sin\left(\sqrt{\alpha}(4a-1)\right) + \alpha\, sin\left(\sqrt{\alpha}\right) - 4k^2\, sin\left(\sqrt{\alpha}\right) + 4\sqrt{\alpha}k\, cos\left(\sqrt{\alpha}(2a-1)\right) - 4\sqrt{\alpha}k\, cos\left(\sqrt{\alpha}\right) \quad \text{A.39}$$

The Euler load or elastic buckling load of the system, the minimum real root of the results of Eq.A.39 should be input in Eq.A.40:

$$P_{cr} = \alpha\frac{EI}{L^2} \quad \text{A.40}$$

where α should be bounded:

$$\alpha \in (0, \pi^2) \quad \text{A.41}$$

For the second mode of elastic buckling, α should be bounded:

$$\alpha \in (\pi^2, 4\pi^2) \quad \text{A.42}$$

12.2.3.1.1. Matlab code to solve the characteristic equation:

```
clc
clear
syms x

beta= #intended numeric value; %relative rotational stiffness
of the spring.

delta= #intended numeric value; %relative position of RSFJ.
(between 0 and 0.5)

for i=1:max(size(beta))
for n=1:20
 %two different rotational springs
%  equ(i,1)=2*x^2*sin(x*(2*delta - 1)) - x^2*sin(x*(4*delta -
1))+x^2*sin(x) - 4*beta(i,1)*beta2(i,1)*sin(x) +
2*x*(beta(i,1)+beta2(i,1))*cos(x*(2*delta - 1)) -
2*x*(beta(i,1)+beta2(i,1))*cos(x);
 %two identical rotational springs
equ(i,1)=2*x^2*sin(x*(2*delta - 1))- x^2*sin(x*(4*delta - 1))
+ x^2*sin(x) - 4*beta(i,1)^2*sin(x) +
4*x*beta(i,1)*cos(x*(2*delta - 1)) - 4*x*beta(i,1)*cos(x);
a(i,n)=(double(vpasolve(equ(i,1)==0,x, [0.001
3*pi],'random',true)));

end
end

aa=sort(a,2);
a1=aa.^2;
a1=min(a1');
a1
```

12.2.3.1.2. Calculating the mode shape:

Matlab code to derive mode shape:

```
clc
clear

syms a b alpha k k1 k2 c1 c2 c3 c4 b1 b2 b3 b4 e1 e2 e3 e4 x
real



b=1-a;
w1=c1*sin(alpha*x)+c2*cos(alpha*x)+c3*x+c4;
w2=b1*sin(alpha*x)+b2*cos(alpha*x)+b3*x+b4;
w3=e1*sin(alpha*x)+e2*cos(alpha*x)+e3*x+e4;
%_____________________________________________
% x belongs t0 (0,a)
w1_x=diff(w1,x);
w1_xx=diff(w1_x,x);
w1_xxx=diff(w1_xx,x);
w1_0=subs(w1,x,0);
w1_x_0=subs(w1_x,x,0);
w1_xx_0=subs(w1_xx,x,0);
w1_xxx_0=subs(w1_xxx,x,0);
w1_a=subs(w1,x,a);
w1_x_a=subs(w1_x,x,a);
w1_xx_a=subs(w1_xx,x,a);
w1_xxx_a=subs(w1_xxx,x,a);
% x belongs t0 (a,b)
w2_x=diff(w2,x);
w2_xx=diff(w2_x,x);
w2_xxx=diff(w2_xx,x);
w2_a=subs(w2,x,a);
w2_x_a=subs(w2_x,x,a);
w2_xx_a=subs(w2_xx,x,a);
w2_xxx_a=subs(w2_xxx,x,a);
w2_b=subs(w2,x,b);
w2_x_b=subs(w2_x,x,b);
w2_xx_b=subs(w2_xx,x,b);
w2_xxx_b=subs(w2_xxx,x,b);

% x belongs t0 (b,1)
w3_x=diff(w3,x);
w3_xx=diff(w3_x,x);
w3_xxx=diff(w3_xx,x);
w3_b=subs(w3,x,b);
w3_x_b=subs(w3_x,x,b);
w3_xx_b=subs(w3_xx,x,b);
w3_xxx_b=subs(w3_xxx,x,b);
w3_1=subs(w3,x,1);
w3_x_1=subs(w3_x,x,1);
```

```
w3_xx_1=subs(w3_xx,x,1);
w3_xxx_1=subs(w3_xxx,x,1);
%_____________________________________________
%boundry conditions:
eq1=w1_0;
eq2=w3_1;
eq3=w2_a-w1_a;
eq4=w2_b-w3_b;
eq5=w1_xx_0;
eq6=w3_xx_1;
eq7=w1_xx_a-w2_xx_a;
eq8=w2_xx_b-w3_xx_b;
eq9=w1_xxx_a+alpha^2*w1_x_a-w2_xxx_a-alpha^2*w2_x_a;
eq10=w2_xxx_b+alpha^2*w2_x_b-w3_xxx_b-alpha^2*w3_x_b;
eq11=k*(w2_x_a-w1_x_a)-w1_xx_a;
eq12=k*(w3_x_b-w2_x_b)-w2_xx_b;




[coeff,V]=equationsToMatrix([eq1==0,eq2==0,eq3==0,eq4==0,eq5==
0,eq6==0,eq7==0,eq8==0,eq9==0,eq10==0,eq11==0,eq12==0], [c1,
c2, c3, c4, b1, b2, b3, b4, e1, e2, e3, e4])
%_____________________________________________
equ_st1=simplify(expand(det(coeff)))
```

12.2.4. *Equivalent Rotational Stiffness of ABT (Chapter 5 and 7)*

12.2.4.1. One damper location along the brace

12.2.4.1.1. Second-order action from one side

The following expressions provide proof of the rotational stiffness of Anti-buckling Tubes (ABT) when the RSFJ brace is subjected to second-order action from one side. It should be noted that this formulation is for the RSFJ brace-assembly when there is one weakened location for the damper. In order to calculate the rotational stiffness, the method of virtual work (Structural Analysis Hibbeler 2008) is used, which involves putting a unit moment in a virtual system at the location where the rotational stiffness is required.

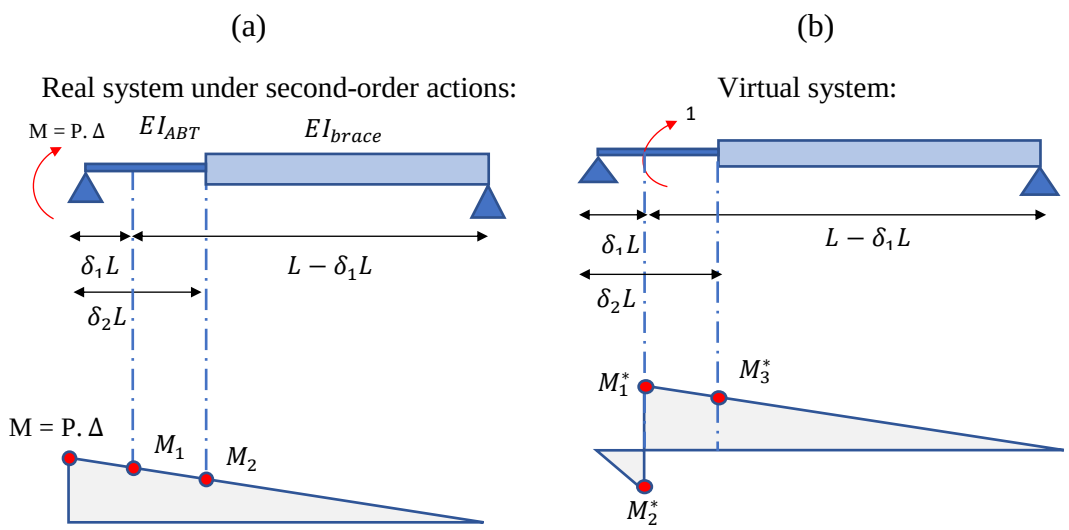

Bending moment at different points:

$M_1 = (1 - \delta_1)\, M$

$M_2 = (1 - \delta_2)\, M$

$M_1^* = (1 - \delta_1)$

$M_2^* = \delta_1$

$M_3^* = (1 - \delta_2)$

Figure 12.4: Bending diagram when the RSFJ brace is subjected to the second-order action from one side (a) Real system and (b) Virtual system

Method of Virtual Work (Structural Analysis Hibbeler 2008):

The rotation at the desired place according to the method of virtual work is:

$$1 * \theta = \int_0^L \frac{M^* M}{EI} = \frac{(1-\delta_2)^3 ML}{3EI_{brace}} + \frac{ML}{3EI_{ABT}}[(\delta_2-\delta_1)^3 - 3(\delta_2^2-\delta_1^2) + 3(\delta_2-\delta_1)] \quad \text{A.43}$$

The equivalent rotational stiffness of the desired location is:

$$\frac{M}{\theta} = \frac{3EI_{ABT}}{L} * \frac{1}{[\beta_b(1-\delta_2)^3 + (\delta_2-\delta_1)^3 - 3(\delta_2^2-\delta_1^2) + 3(\delta_2-\delta_1)]}$$

or A.44

$$K_{ABT} = \frac{3EI_{ABT}}{L} * m'$$

where:

$m'$is the modification factor and equals:

$$m' = \frac{1}{[\beta_b(1-\delta_2)^3 + (\delta_2-\delta_1)^3 - 3(\delta_2^2-\delta_1^2) + 3(\delta_2-\delta_1)]} \quad \text{A.45}$$

and

$$\beta_b = \frac{EI_{ABT}}{EI_{brace}} \quad \text{A.46}$$

The rotational stiffness can be rearranged based on the length of ABT:

$$K_{ABT} = \frac{3EI_{ABT}}{\delta_2 L} * m \quad \text{A.44}$$

where:

$$m = \frac{\delta_2}{[\beta_b(1-\delta_2)^3 + (\delta_2-\delta_1)^3 - 3(\delta_2^2-\delta_1^2) + 3(\delta_2-\delta_1)]} \quad \text{A.47}$$

12.2.4.1.2. Second-order action from both sides

The following expressions provide proof of the rotational stiffness of Anti-buckling Tubes (ABT) when the RSFJ brace is subjected to second-order action from both sides. It should be noted that this formulation is for the RSFJ brace-assembly when there is one weakened location for the damper. In order to calculate the rotational stiffness, the method of virtual work (Structural Analysis Hibbeler 2008) is used, which involves putting a unit moment in a virtual system at the location where the rotational stiffness is required.

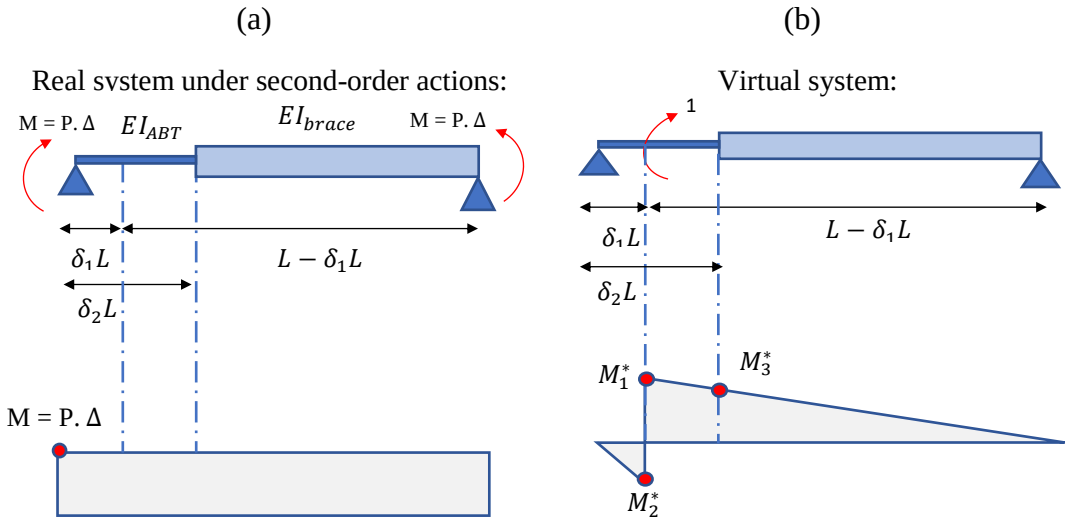

Bending moment at different points:

$$M_1^* = (1 - \delta_1)$$

$$M_2^* = \delta_1$$

$$M_3^* = (1 - \delta_2)$$

Figure 12.5: Bending diagram when the RSFJ brace is subjected to the second-order action from both sides

Method of Virtual Work (Structural Analysis Hibbeler 2008):

The rotation at the desired place according to the method of virtual work is:

$$1 * \theta = \int_0^L \frac{M^* M}{EI} = \frac{(-\delta_1)^2 ML}{2EI_{ABT}} + \frac{ML(\delta_2 - \delta_1)}{6EI_{ABT}}[3(2 - \delta_2 - \delta_1)] + \frac{ML(1 - \delta_2)^2}{2EI_{brace}} \quad \text{A.48}$$

The equivalent rotational stiffness of the desired location is:

$$\frac{M}{\theta} = \frac{2EI_{ABT}}{L} * \frac{1}{[2(\delta_2 - \delta_1) - (\delta_2)^2 + \beta_b(1 - \delta_2)^2]}$$

Or

A.49

$$K_{ABT} = \frac{2EI_{ABT}}{L} * m'$$

where m' is the modification factor and equals:

$$m' = \frac{1}{[2(\delta_2 - \delta_1) - (\delta_2)^2 + \beta_b(1 - \delta_2)^2]} \quad \text{A.50}$$

and

$$\beta_b = \frac{EI_{ABT}}{EI_{brace}} \quad \text{A.51}$$

The rotational stiffness can be rearranged based on the length of ABT:

$$K_{ABT} = \frac{2EI_{ABT}}{\delta_2 L} * m \quad \text{A.52}$$

where:

$$m = \frac{\delta_2}{[2(\delta_2 - \delta_1) - (\delta_2)^2 + \beta_b(1 - \delta_2)^2]} \quad \text{A.53}$$

12.2.4.2. Two damper locations along the brace

The following expressions provide the proof of the rotational stiffness of Anti-buckling Tubes (ABT) when the RSFJ brace is subjected to second-order action from both sides. It should be noted that this formulation is for the RSFJ brace-assembly when there are two weakened locations for damper. In order to calculate the rotational stiffness, the method of virtual work (Structural Analysis Hibbeler 2008) is used, which involves putting a unit moment in a virtual system at the location where the rotational stiffness is required.

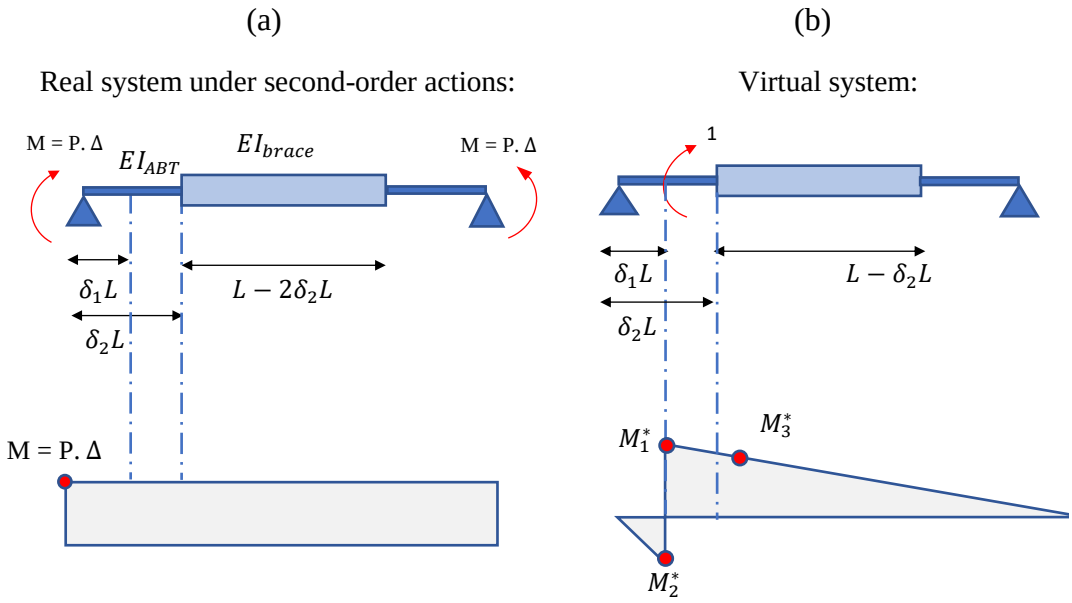

Bending moment at different points:

$$M_1^* = (1 - \delta_1)$$

$$M_2^* = \delta_1$$

$$M_3^* = (1 - \delta_2)$$

Figure 12.6: Bending diagram when the RSFJ brace is subjected to the second-order action from both sides with two weakened locations

Method of Virtual Work (Structural Analysis Hibbeler 2008):

The rotation at the desired place according to the method of virtual work is:

$$1 * \theta = \int_0^L \frac{M^* M}{EI} = \frac{(\delta_2 - \delta_1)ML}{EI_{ABT}} + \frac{ML(1 - 2\delta_2)}{2EI_{brace}} \quad \text{A.54}$$

The equivalent rotational stiffness of the desired location is:

$$\frac{M}{\theta} = \frac{2EI_{ABT}}{L} * \frac{1}{[2(\delta_2 - \delta_1) + \beta_b * (1 - 2\delta_2)]}$$

Or A.55

$$K_{ABT} = \frac{2EI_{ABT}}{L} * m'$$

where m' is the modification factor and equals:

$$m' = \frac{1}{[2(\delta_2 - \delta_1) + \beta_b * (1 - 2\delta_2)]} \quad \text{A.56}$$

and

$$\beta_b = \frac{EI_{ABT}}{EI_{brace}} \quad \text{A.57}$$

The rotational stiffness can be rearranged based on the length of ABT:

$$K_\theta = \frac{2EI_{ABT}}{\delta_2 L} * m \quad \text{A.58}$$

where:

$$m = \frac{\delta_2}{[2(\delta_2 - \delta_1) + \beta_b * (1 - 2\delta_2)]} \quad \text{A.59}$$

12.2.5. *Effect of imperfection on the column second-order performance – Stiffness decay (Chapter 5 and 7)*

This section discusses the effect of imperfection on the axial performance of a column. This will be referred to as stiffness decay or stiffness deterioration curve in the text and within the Simplified Collapse Mechanism Analysis (SCMA) in chapter 5. The aim is to derive the axial load as a function of elastic buckling load, imperfection and lateral displacement. Though the column (the brace) herein is assumed to be a prismatic column while it is not the case in reality due to the appearance of the ABTs and damper, it was observed in chapter 6 that it did not affect the ultimate capacity of the brace considerably. Therefore, in the interest of simplicity, the derivation of the following equations will be pursued based on this assumption.

To begin with, it is assumed the column is initially imperfect and bent where the maximum of imperfection at mid-span is δ_0 as shown in Figure 12.7. The second assumption is that the deflection of the column due to second-order actions is of sinusoidal shape as:

$$y = \delta \sin\left(\frac{\pi x}{L}\right) \quad \text{A.60}$$

and

$$y_0 = \delta_0 \sin\left(\frac{\pi x}{L}\right) \quad \text{A.61}$$

The total deflection of the column would be:

$$y_t = y_0 + y \quad \text{A.62}$$

The strain energy of the system would be:

$$U = \frac{EI}{2}\int_0^L \left(\frac{d^2y}{dx^2}\right) dx \rightarrow U = \frac{\pi^4 \delta^2 EI}{4L^3} \quad \text{A.63}$$

The work done due to external axial load would be:

$$W = \frac{P}{2}\int_0^L \left(\frac{dy_t}{dx}\right)^2 dx \rightarrow W = \frac{P\pi^2(\delta + \delta_0)^2}{4L} \quad \text{A.64}$$

The potential energy of the system is:

$$E = U - W \quad \text{A.65}$$

According to the stationary potential energy, the derivative of the potential energy will bring the critical state as:

$$\frac{dE}{d\delta} = 0 \rightarrow P = \frac{\pi^2 EI}{L^2}\left(\frac{\delta}{\delta + \delta_0}\right) \quad \text{A.66}$$

Or if re-formatted:

$$P = P_{cr}\left(\frac{\delta}{\delta + \delta_0}\right) \quad \text{A.67}$$

If Eq.A.67 is rearranged, the amplified deflection at mid-span due to second-order effect can be derived as:

$$\delta_t = \delta + \delta_0 \rightarrow \delta_t = \frac{\delta_0}{\frac{P}{P_{cr}} - 1} + \delta_0 = \frac{\delta_0}{1 - \frac{P}{P_{cr}}} \quad \text{A.68}$$

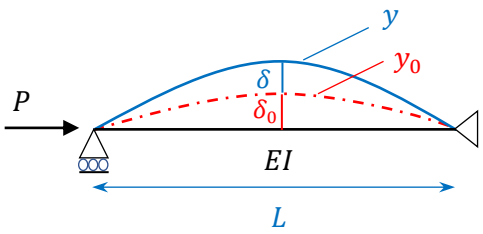

Figure 12.7: The deflected shape of the column due to second-order effect ($P - \Delta$)

12.2.6. *Simplified Collapse Mechanism Analysis (SCMA) method for indeterminate Systems*

As it was discussed in chapter 5, the strength deterioration curve for determinant systems is governed by the section strength mainly because only one plastic hinge is required so that the system becomes a mechanism and unstable. However, this is not the case for indeterminant systems. The fix-fix column, shown in Figure 12.8, with uniform a section can be taken as an example. There can be one mode of collapse for the system involving at least three plastic hinges. The potential energy of the system including the strain energy in the plastic hinges and the work done by the external axial load can be written as:

$$E = 4M_p\theta - PL(1 - cos\theta) \quad \text{A.69}$$

The first derivative of the potential energy determines the ultimate load (as a function of lateral displacement, which is referred to as strength deterioration curve) as:

$$\frac{dE}{d\theta} = 4M_p - PLsin\theta \quad \text{A.70}$$

Therefore, the strength deterioration curve of the system can be estimated as:

$$P = \frac{4\left(M_p\right)^*}{Lsin\theta} \sim \frac{2\left(M_p\right)^*}{\delta} \quad \text{A.71}$$

Where δ is the lateral displacement at midspan, measured from undeformed brace shape, L is the total length of the column and $\left(M_p\right)^*$ is the plastic capacity of the section, which, itself, is a function of axial load. If the effect of axial load on the flexural capacity of the section is conservatively assumed as shown in Eq.A.72 (ignoring any variation due to the shape), the strength deterioration curve can be further simplified to Eq.A.73:

$$\left(M_p\right)^* = M_p\left(1 - \frac{P}{P_n}\right) \quad \text{A.72}$$

$$P = \frac{2M_p}{\frac{2M_p}{P_n} + \delta} \quad \text{A.73}$$

Where P_n is the squash load ($A_g f_y$). Comparing Eq.A.73 with the strength curve of a pin-pin column in Eq.5.3, it can be concluded that the strength curve of the fix-fix column is more than the pin–pin case.

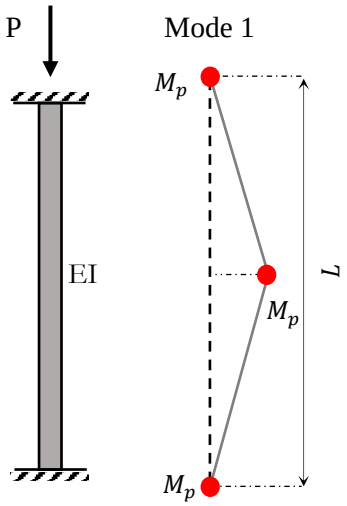

Figure 12.8: Collapse mode of a prismatic column with fix-fix end supports

If the stiffness deterioration curve is assumed as Eq.A.74 (see 5.1.2 or proof in Appendix B - section 12.2.4):

$$P = P_{cr}\frac{\delta}{\delta_0 + \delta} \qquad \text{A.74}$$

The intersection between two stiffness and strength deterioration curves will be determined as:

$$\delta_{int} = M_p\left[\frac{1}{P_{cr}} - \frac{1}{P_n} + \sqrt{\left(\frac{1}{P_{cr}} - \frac{1}{P_n}\right)^2 + \frac{2\delta_0}{M_p P_{cr}}}\right] \qquad \text{A.75}$$

And accordingly, the ultimate load of the system can be estimated as:

$$P_{ult} = P_{cr}\frac{\delta_{int}}{\delta_0 + \delta_{int}}$$

$$or \qquad \text{A.76}$$

$$P_{ult} = \frac{2M_p}{\frac{2M_p}{P_n} + \delta_{int}}$$

As a numerical example, a steel column with a square section – 100 mm * 100 mm – and length of 4000 mm is assumed and modelled in the ABAQUS software. The material had a modulus of elasticity of 200 GPa and yield strength of 340 Mpa. The same process explained in chapter 6 is followed to determine the performance curve of the model in ABAQUS software.

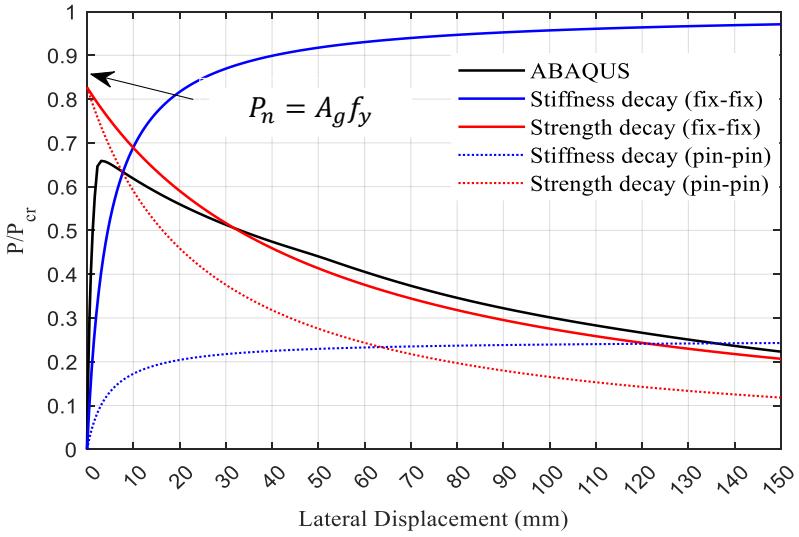

Figure 12.9: Inelastic buckling of the fix-fix column: SCMA Vs ABAQUS prediction

Figure 12.9 shows the comparative results of the SCMA method Vs ABAQUS software predictions (force axis has been calibrated with Euler load of fix-fix column). As can be seen, the red line shows the strength deterioration of the column while the blue curve shows the stiffness deterioration curve of the system. The intersection of these two curves can be taken as a good approximation of the ultimate load of the system. As can be seen, the ultimate load from SCMA ($0.7P_{cr}$) is very close to ABAQUS results ($0.66\ P_{cr}$). Another point to highlight here is the effect of boundary conditions. Imagine a situation with the same steel section and same length but with pin-pin end conditions. As can be seen in Figure 12.9, the ultimate capacity of the brace, in this case, would be around $0.25P_{cr}$ (fix-fix), which is almost 38% of the fix-fix situation. Thus, it can be concluded that the boundary conditions play a considerable role in the ultimate capacity of the system, which is largely due to bringing in *REDUNDANCY*. This implies that the system is well prepared to redistribute the nonlinearity demands and postpone the collapse!

In order to further validate the SCMA method for indeterminant (redundant) systems, a parametric comparative study has been conducted on the SHS (Square Hollow Section), UB (Universal Beams) and UC (Universal Columns) columns with different lengths in a way that the slenderness ratio falls within the range of 0 to 300. The result of the analysis is shown and compared with the different international steel standards code (AISC 360 and NZS 3404) in Figure 12.10 in which the ultimate force is calibrated with the gross cross-section area of the section (A_g) so that the results can be read and compared better in the context of stress (N/mm^2). It should be mentioned that while one curve is suggested for the all-column sections in AISC 360 while multiple curves are provided in NZS3101, and this is also reflected in the following curves. As can be observed, the SCMA (shown with red line) slightly overestimated the results for the

UC and UB. The overestimation was more considerable for the SHS section; however, the error was limited to 25%. The main reasons for overestimation lie in two phenomena. The first is that SCMA does not include the residual stress though according to literature, it might adversely affect the ultimate strength [121]. The second reason, which was previously discussed in chapter 6, is that the SCMA method always picks the intersection point between stiffness and strength decay curve while in reality, the ultimate strength always falls below this value.

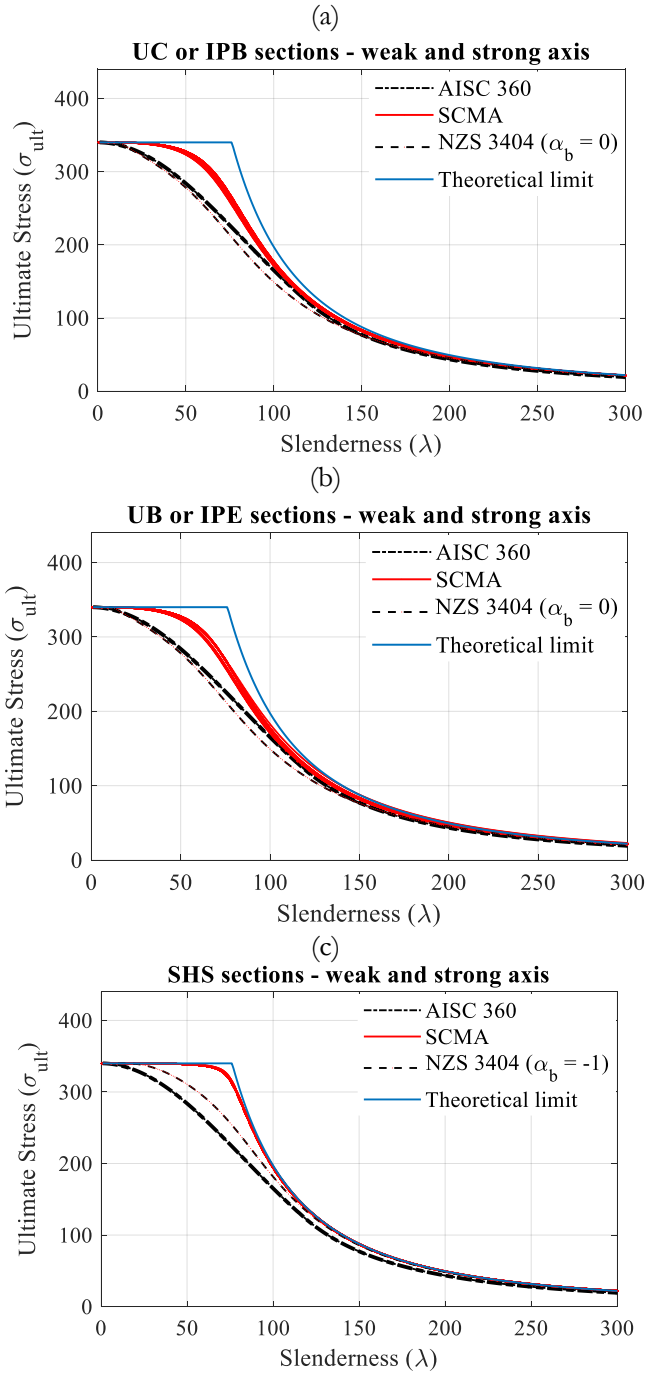

Figure 12.10: Parametric study on the effectiveness of SCMA for indeterminant systems (a, b) UC and UB section, (c) SHS section